Exciton diffusion and interactions with a two-dimensional Fermi sea

DISSERTATION ZUR ERLANGUNG DES DOKTORGRADES
DER NATURWISSENSCHAFTEN (DR. RER. NAT.)
DER FAKULTÄT FÜR PHYSIK
DER UNIVERSITÄT REGENSBURG

vorgelegt von

Koloman Wagner
aus Hallein (Österreich)

im Jahr 2022

Exciton diffusion and interactions with a two-dimensional Fermi sea

DISSERTATION ZUR ERLANGUNG DES DOKTORGRADES
DER NATURWISSENSCHAFTEN (DR. RER. NAT.)
DER FAKULTÄT FÜR PHYSIK
DER UNIVERSITÄT REGENSBURG

vorgelegt von

Koloman Wagner
aus Hallein (Österreich)

im Jahr 2022

Promotionsgesuch eingereicht am: 02.11.2022
Die Arbeit wurde angeleitet von: Prof. Dr. Alexey Chernikov

Prüfungsausschuss: Prof. Dr. Gunnar Bali
Prof. Dr. Alexey Chernikov
Prof. Dr. Christian Schüller
Prof. Dr. Franz Gießibl

Datum Promotionskolloquium: 31.01.2023

Abstract

Two-dimensional semiconductors such as monolayer transition metal dichalcogenides (TMDCs) evolved to a versatile platform to explore elementary optoelectronic phenomena. In these systems, excitons with firm light-matter coupling and spin-valley locking dominate the optical properties. Due to strong Coulomb forces, TMDCs are a particularly promising system to study the interplay between excitons, phonons and electrons at previously inaccessible conditions. In this thesis, exciton diffusion and interactions with a two-dimensional Fermi sea of free charge carriers are investigated. In carrier density-dependent reflectance spectra of electrically-tuneable hBN-encapsulated TMDC monolayers negatively- and positively-charged excited state trions are identified. Their binding energies and oscillator strengths are determined and autoionization is studied, a process which is typically associated with excited states in atomic systems. Exciton-carrier scattering rates are extracted from voltage-dependent reflectance and luminescence linewidth broadening and the interplay of exciton-phonon and exciton-carrier scattering is investigated. By analyzing the ground state low-energy recoil flank in time-resolved luminescence experiment, trion cooling times in monolayer $MoSe_2$ are determined. With increasing temperature and free charge carrier density an accelerated cooling is observed. Taking advantage of time-resolved microscopy, exciton propagation is investigated at cryogenic temperatures. Temperature-dependent diffusion experiments reveal mobile dark excitons and signatures of non-classical exciton propagation, contradicting the widely-used semiclassical description of exciton kinetics in TMDCs. In carrier density-dependent diffusion experiments, mobile trions and the impact of exciton-carrier scattering and trion formation on the quasiparticle propagation are explored.

Contents

Chapter 1

Introduction

The properties of matter are largely determined by the arrangement and interplay of atoms. An atom consists of a positively charged nucleus and is surrounded by an electron cloud. Ruled by the laws of quantum physics, mostly electronic interactions give rise to the versatile features of our physical world: they determine whether a material is gaseous, liquid or solid, whether it reflects or absorbs light or how it conducts heat and electricity. Electronic interactions can also be exploited for technological applications. Electrons play a central role in sensors, computers and energy transmission. Particularly interesting is the interaction between electrons and light. For example, in a LED (light emitting diode) light of a certain wavelength is generated by driving a current in a semiconductor p-n junction. The other way round, in a photodetector or in a solar cell, light is converted into an electric current. In the last decades, the field of opto-electronics experienced substantial progress. Laser systems, light emitters, sensors, photomultipliers and optical storage media have been pushed to the next level. Especially, because light can be clocked and transmitted on extremely short timescales, opto-electronic transistors are considered promising for future communication and computing technologies.

A novel playground to explore opto-electronic phenomena constitute systems with a limited degree of freedom. Diminishing the system's size to the nanometer regime manifests in stunning material properties which can drastically differ from its bulk form. By the introduction of molecular-beam epitaxy in the end of the 1960's [1], pristine two-dimensional systems became feasible. Most prominent, the realization of a two-dimensional electron gas in a metal-oxide-semiconductor field effect transistor lead to the observation of the quantum Hall effect by Klaus von Klitzing and co-workers in 1980 [2]. From the perspective of opto-electronics, gallium arsenide (GaAs) quantum wells established vibrant research activities [3].

In these systems, Coulomb-bound electron-hole pairs, so-called *excitons*, play a fundamental role. In principal, these quasiparticles can be generated, manipulated and detected both, optically and electrically and thus constitute an interesting interface between optics and electronics [4].

Excitons were already proposed by Yakov Frenkel in 1931 [5] and experimentally observed for the first time in bulk cuprous oxide by Gross and Karrjew in 1952 [6]. In quantum well systems, two-dimensional excitons exhibit binding energies on the order of 10 meV, much larger than in respective bulk crystals [7]. It has been demonstrated that these quasiparticles can be tuned by magnetic [8] and electric [9] fields, and are able to propagate through the crystal [10] if they are not localized on donors [11], acceptors [12] or disorder [13]. The ability to move through a two-dimensional plane renders excitons particularly suitable for information and energy transport. However, as excitons are effectively charge-neutral particles, they can not be efficiently accelerated by electric fields. Interestingly, in the presence of free charge carriers, excitons can bind to a free electron or hole resulting in a new composite quasiparticle: the so-called trion [14]. This charged quasiparticle has been experimentally observed for the first time in a modulation-doped GaAs quantum well by Kheng *et al.* in 1993 [15]. Trions were subsequently shown to propagate through the crystal [16, 17, 18] and indeed, allow for controlling their propagation direction by applying an in-plane electric field [19, 20, 21].

Fueled by the lively interest on quantum wells, the search for ever thinner systems led to the emergence of a new class of two-dimensional materials. In 2004, Konstantin Novoselov and Andre Geim demonstrated the ultimate limit of a thin-film crystal: the cleavage of an atomically-thin layer of graphite, or as it is named, graphene [22]. Most outstanding, the electronic properties of graphene comprise mass-less Dirac Fermions [23], unconventional superconductivity [24] and the quantum Hall effect at room temperature [25]. In the following years, single layers of van der Waals crystals emerged to a central pillar in semiconductor research. Next to metallic graphene, other air-stable monolayers have been cleaved, including insulating hexagonal boron nitride (hBN) and semiconducting transition-metal dichalcogenides (TMDCs) [26]. The emergence of a direct band gap in TMDC monolayers [27, 28] has sparked intense research activities due to their possible application in opto-electronic devices [29] and importance in fundamental research [30]. Two-dimensional TMDCs are characterized by strong spin-orbit and Coulomb interactions [31]. Importantly, the latter results in tightly-bound excitons, which are valley-polarized [32, 33, 34] and dominate the opto-electronic properties even at room temperature. Excitons in TMDCs were

demonstrated to be externally tuneable by strain [35], magnetic [36, 37] as well as electric [38, 39] fields and structuring dielectric surrounding [40].

Monolayer TMDCs particularly allow to study interactions between excitons, free charge carriers and phonons at previously inaccessible conditions. Inserting excitons in an electron- or hole-doped monolayer, trions with extremely high binding energies of up to 30 meV can form [41, 42]. This opens the possibility to study exciton-carrier complexes at elevated temperatures [43] and high carrier densities, far above the exciton ionization threshold in traditional quantum well systems [20]. In the high carrier density regime, the exciton-electron interactions are described by the Fermi polaron, a generalized quasiparticle where the exciton is dressed by Fermi sea excitations [44, 45, 46]. Furthermore, exotic higher-order particle states such as charged biexcitons [47, 48, 49, 50, 51, 52] and the emergence of hexcitons and oxcitons [53] are discussed. Particularly, due to the specific band structure of tungsten-based TMDCs, long-lived *dark* excitons and trions emerge, which allow to study their dynamics and interplay on a nanosecond time scale [54]. Due to strong exciton-phonon interactions [55, 56, 37], these dark states can be optically accessed e. g. via dominant phonon side bands [55, 56, 37]. In TMDCs, phonons play also an important role in spin-valley dynamics [57, 58, 59], lead to the formation of cascade effects [60] and intriguing exciton propagation phenomena [61, 62, 63]. Despite this much progress, the understanding of mobile excitons interacting with free charge carriers remains a challenging task. Particularly in doped TMDCs, the complex scenario including both, strong exciton-phonon and exciton-carrier interactions is expected to crucially determine the light-matter coupling and propagation behavior of excitonic quasiparticles.

In this thesis, the mechanisms of exciton diffusion and interactions with a two-dimensional Fermi sea are experimentally investigated in monolayer TMDCs. The first part of the investigations focuses on the identification and exploration of excited state trions in hBN-encapsulated WSe_2 monolayers. Although ground state trions have been intensively investigated [15, 64, 65, 41, 66, 42, 67, 36], the interaction of *excited* state excitons with a continuously-tuneable two-dimensional gas of free charge carriers has not been explored so far. In quantum wells, low binding energies and exciton ionization challenges the investigation of excited states at finite doping densities [68]. In non-encapsulated TMDCs, inhomogeneities due to adsorbates and dielectric disorder [69, 70] hampered an unambiguous identification of spectral features. Only recently, fingerprints of excited state trions have been reported in an hBN-encapsulated WS_2 monolayer with unknown doping density [71]. However, the microscopic structure and the interaction mechanisms of

excited state excitons in a two-dimensional Fermi sea remain elusive. In this thesis, the interaction of excited state excitons with the two-dimensional Fermi sea of free charge carriers is investigated in hBN-encapsulated WSe_2 monolayers, which allow to continuously tune the free electron and hole concentration. Signatures of positively and negatively-charged excited state trions are identified in an extended doping-regime up to free carrier densities of 10^{12} cm^{-2}. By extrapolating density-dependent resonance energies, their exact zero-density binding energies are determined. Interestingly, the experiments indicate that excited state trions efficiently autoionize, i. e., the excited state trion scatters into the exciton ground state while exciting an electron. This process is typically observed in atomic systems such as the doubly-excited H^- ion [72]. Due to the efficient autoionization process, the lifetime of the investigated states is estimated to be on the order of only few 10's of femtoseconds, much shorter than the lifetime of excited state excitons [73]. Furthermore, a rapid exchange of the oscillator strength from the excited state exciton to the excited state trion is observed. Signatures of excited state trions are also identified in luminescence experiments.

The strong exciton-carrier interaction in TMDCs does not only give rise to excited state trions, but also to strong exciton-carrier scattering which manifests in the carrier density-dependent exciton linewidth broadening. Understanding and controlling the scattering of optically-excited excitons with free electrons or holes is key for the quantitative investigation and manipulation of exciton relaxation, cooling and transport dynamics. While recent studies report a strong increase of the exciton linewidth with increasing free carrier density [74, 75], in a simple picture the scattering is expected to be hardly affected by the free carrier concentration in a degenerate Fermi sea. Due to Pauli blocking, the scattering is limited to electrons at the Fermi edge and the electrons inside the Fermi sea do not contribute to the scattering [76]. In a recent many-body approach, this apparent discrepancy to the experiments is resolved qualitatively by taking into account a finite dissipation, which effectively suppresses the Pauli blocking effect [45, 46]. In this thesis, exciton-carrier scattering rates are quantitatively determined in pristine hBN-encapsulated $MoSe_2$ and WSe_2 monolayers from reflectance contrast and PL spectroscopy. The findings demonstrate that due to the assistance of temperature-activated phonons, the exciton-carrier scattering rate coefficient increases. Interestingly, the efficiency of the scattering crucially depends on the trion linewidth. A larger trion linewidth corresponds to a larger dissipation and results in a stronger exciton-carrier scattering. This mechanism particularly allows to

estimate the intrinsic lower limit of exciton-carrier scattering in two-dimensional semiconductors by the intrinsic trion linewidth.

In contrast to the exciton, the trion linewidth hardly increases with free carrier density. In high-quality samples it is mostly determined by the scattering with phonons and a pronounced low-energy flank, which is attributed to the electron recoil effect [77]. While in some early studies on TMDC monolayers the recoil flank has been experimentally identified [66, 78, 43, 79] and theoretically investigated [80], in this thesis, a quantitative analysis of photoluminescence experiments on an electrically-tuneable hBN-encapsulated $MoSe_2$ monolayer gives access to non-equilibrium distributions and, most importantly, the trion temperature. In conventional quantum well systems, the quasiparticle temperature is typically determined by the plasma flank [68], which is, however, suppressed in monolayer TMDCs. Thus, the recoil analysis provides an alternative and comparably easy access to the effective quasiparticle temperature. Taking advantage of time-resolved photoluminescence spectroscopy, the transient recoil flank directly allows to track relaxation dynamics and provides characteristic cooling times. Both, the impact of phonons and free carriers on the cooling are investigated.

In the second part of this thesis, exciton propagation in monolayer semiconductors is investigated, focusing on the impact of phonons and free charge carriers. Excitons were demonstrated to be mobile [10, 81, 82, 83, 16, 17] and involve discussions on superfluidity [84, 85], condensation [86], phonon wind [87] and ring formation [88]. Particularly, in TMDCs, the valley-degree of freedom renders excitons promising for the investigation of the valley-Hall effect [89, 90, 91, 92, 93, 94]. Commonly, exciton propagation in TMDCs is described in a semiclassical picture where the quasiparticle freely moves through the crystal between two scattering events. In that case, the diffusion coefficient depends only on the free quasiparticle's properties, such as effective electron and hole masses and scattering times [4]. Although many studies demonstrated mobile excitons in TMDC monolayers [95, 96, 61, 97, 98, 99, 100] and their heterostructures [101, 102, 103, 104], the applicability of the semiclassical picture has not been tested so far. In previous room temperature experiments, the intrinsic exciton propagation mechanisms were covered by disorder [96, 61], non-linear density effects [95, 61], exciton ionization [105] or the complex interplay of neutral and charged quasiparticles [106]. In this thesis, the intrinsic mechanisms of exciton propagation are explored by spatio-temporal experiments in an hBN-encapsulated WSe_2 monolayer with suppressed dielectric disorder and flat energy landscapes [105]. Benefiting from long-lived [54] and thermalized [107, 108] dark states, exciton diffusion at cryogenic temper-

atures and a constant exciton temperature is investigated. By the combination of temperature-dependent diffusion experiments and independently-determined exciton scattering rates, a highly unusual non-classical exciton propagation behavior is observed which can neither be explained by hopping nor by semiclassical transport. The experimental results are discussed with respect to the Mott-Ioffe-Regel criterion and a first-order perturbation theory [109] approaching the impact of the exciton's wave-like nature on its propagation.

In order to investigate the influence of free charge carriers on the exciton transport, diffusion experiments on electrically-tuneable monolayer structures are performed. In many experiments it has been demonstrated that trions are able to propagate thorough the crystal [16, 17, 18, 20, 106]. Particularly, due to their effective charge, these quasiparticles are suitable for directed currents driven by in-plane electric fields, as previously demonstrated in quantum well systems [19, 21] and more recently in TMDCs [110, 111]. However, the mechanisms governing quasiparticle propagation in the presence of additional free charge carriers remains an open question. While strong exciton-carrier scattering [45, 46] is expected to lead to a drastic decrease of the diffusion, spatio-optical experiments at finite charge carrier densities indicate comparably high trion mobilities [106, 99]. In order to elucidate the mechanisms that govern exciton propagation in the presence of free charge carriers, in this work, the diffusion of dark excitons in an electrically-tuneable hBN-encapsulated WSe_2 monolayer is studied as a function of free electron and hole concentration. By continuously increasing the Fermi energy, a non-monotonic dependence of the diffusion is observed, demonstrating distinct propagation regimes of exciton-carrier scattering and quasiparticle formation. The findings reveal the competing mechanisms of increasing exciton-electron scattering and the role of trions, which are largely unaffected by the scattering with other electrons [45, 112]. Finally, in temperature-dependent experiments, free trion diffusion even at the lowest studied temperature of $T = 5$ K is observed.

This thesis is structured as following. In chapter 2, an introduction to the optoelectronic properties of TMDC monolayers is given. In chapter 3, the experimental techniques relevant for this thesis are described. The main experimental results are presented and discussed in chapter 4 and chapter 5. In chapter 4, the interactions of excitons immersed in a two-dimensional Fermi sea of charge carriers are explored. Based on these findings, in chapter 5, the investigations of exciton propagation in monolayer TMDCs are presented. In chapter 6, the main results are summarized, followed by an outlook to possible future research activities.

Chapter 2

Fundamentals: excitons in two-dimensional semiconductors

In this chapter an overview of the research field of semiconductor optics on monolayer structures is given. Highlighting major experimental discoveries and theoretical frameworks, the subsequent sections give an overview of the fundamentals decisive for the discussion of the main experimental results presented in chapter 4 and 5. To start with, the crystal and band structure of monolayer TMDCs as well as a Wannier-Mott exciton model is introduced, describing the major optical properties in this material system. Subsequently, exciton-electron interactions as well as trions and Fermi polarons are introduced. Specific exciton states, trion configurations and recombination pathways are discussed for monolayer WSe_2. The chapter is concluded with an overview of carrier transport regimes and recently proposed quantum corrections on the semiclassical exciton propagation in two-dimensional semiconductors.

2.1 Semiconducting monolayer transition metal dichalcogenides

Transition metal dichalcogenides (TMDCs) have attracted intense research activities. Particularly focusing on opto-electronic properties, many intriguing phenomena have been investigated with a broad range of possible applications including light emitters, photodetectors and opto-valleytronic devices [29, 113, 114, 115]. Although opto-electronic properties of TMDC bulk crystals have been explored already in the 1960s and 1970s [116, 117, 118, 119, 120], the emergence of graphene [22, 121] and the upcoming progress in fabrication of monolayer van der Waals

crystals was the starting point of a new chapter in the investigation of TMDCs [26]. Strong covalent bonds in the in-plane direction and weak interlayer van der Waals forces allow the separation of atomically-thin layers from bulk crystals by micro-mechanical cleavage (commonly referred to as exfoliation) [122, 123]. A typical monolayer crystal structure of the TMDC family of the form MX_2 is shown in Fig. 2.1(a). Here, M denotes the transition metal molybdenum (Mo) or tungsten (W) and X the chalcogene atoms which can be e. g. sulfur (S), selenide (Se) or tellurium (Te). A monolayer consists of a layer of transition metal atoms which is sandwiched between two laterally shifted layers of chalcogene atoms. The resulting hexagonal honeycomb lattice is characterized by the threefold D_{3h} symmetry point group [119]. The lattice constant ranges between 3.1 and 3.3 Å[118]. As demonstrated in 2010 by Splendiani *et al.* [27] and Mak *et al.* [28] this class of van der Waals crystals is a direct band-gap semiconductor in the monolayer limit with up to 20% absorption at the energetically lowest exciton resonance. The latter is in particular relevant for technological applications where devices with fast and efficient light emission are desired [115, 124, 29]. In Fig. 2.1(b) a typical TMDC band structure is presented along the high symmetry points of the first Brillouin zone shown in Fig. 2.1(c). The direct band gap occurs at the finite momentum K and the energetically equivalent K' valley and is in the visible to near-infrared spectral range [28, 31]. Valence band electrons at K and K' mostly stem from hybridized transition metal $d_{x^2-y^2} + d_{xy}$ orbitals and respective conduction band electrons from d_{z^2} orbitals [27, 125, 126].

In TMDCs, optical transitions are spin- and valley-selective. Due to strong spin-orbit coupling, stemming from the heavy transition metal atoms, the energetically lowest conduction and valence bands are spin-split. From the broken inversion symmetry of the crystal it follows that K and K' valleys are not equivalent. Time-reversal symmetry and Kramer's theorem demands $E_{s=+1/2}(k) = E_{s=-1/2}(-k)$ (with energy E and spin states $s = +1/2$ and $s = -1/2$). Importantly, the optically-allowed transitions are $\sigma+$ polarized at K and $\sigma-$ polarized at K' [127]. Optical excitation of a monolayer TMDC with $\sigma+$ polarized light lifts up an electron to the conduction band with spin $s = +1/2$ and valley index $\tau = +1$ leaving behind a hole with spin $s = -1/2$ and $\tau = -1$ [128, 129]. The resulting spin- and valley-selective band occupation is termed as *spin-valley locking* [32, 33, 34]. The latter renders TMDC monolayers a promising platform for information transport based on the valley degree of freedom. In this context often the term *valleytronics* is used, in close analogy to spintronics [130, 131]. While the valence band splitting at K and K' is on the order of 0.1 to 0.4 eV [132, 33, 133, 134],

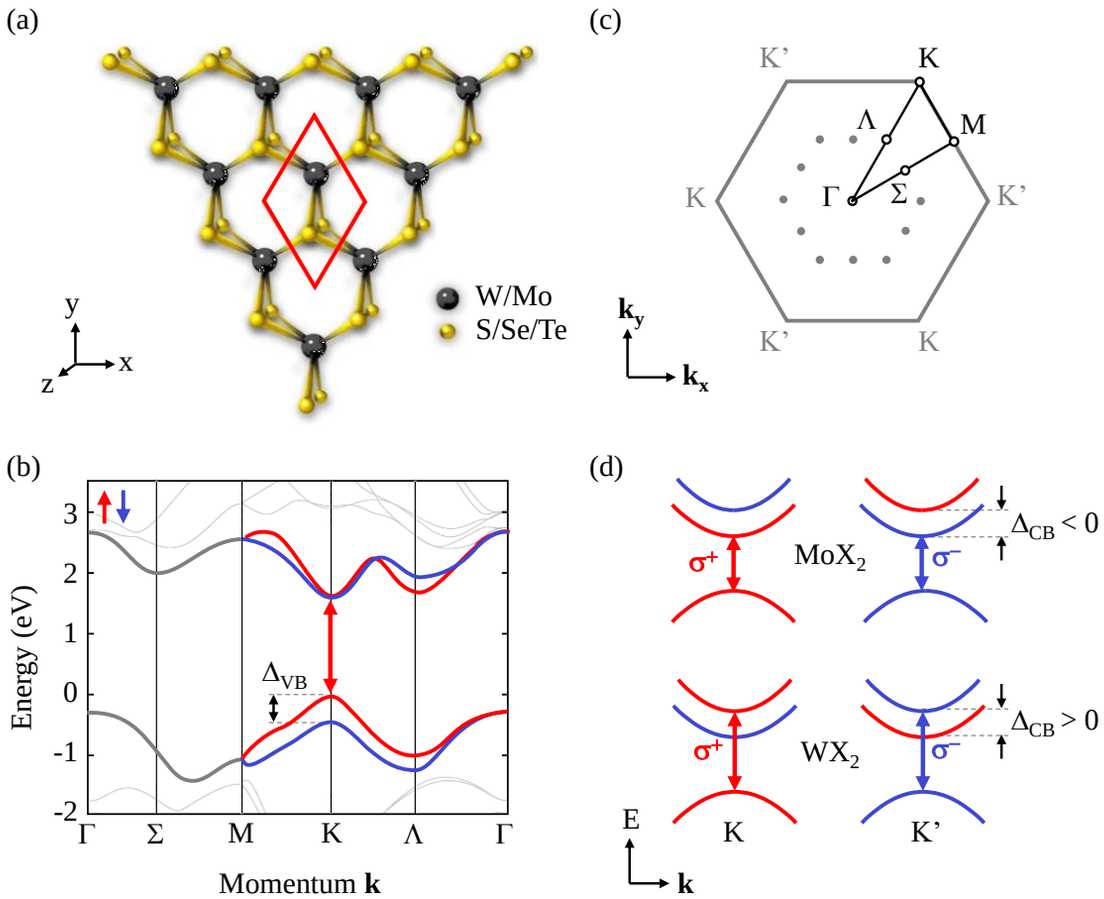

Figure 2.1: (a) Schematic illustration of the monolayer TMDC crystal structure with transition metal atoms (W/Mo) and chalcogene atoms (S/Se/Te). A cross-section of the unit cell is indicated in red. (b) Band structure of monolayer WSe_2 reproduced from Ref. [126] along the high symmetry points of the first Brillouin zone indicated in (c). At K, the energetically lowest conduction and valence bands are spin-split. The corresponding electron spin is indicated by red and blue color. The valence band splitting Δ_{VB} is indicated. (d) Schematic illustration of the lowest energy $\sigma+$ and $\sigma-$ polarized optical transitions in monolayer WX_2 and MoX_2 with positive and negative conduction band splitting Δ_{CB} at K and K'. The valence band splitting is omitted. The bands are colored according to the electron spin in red and blue for $s = +1/2$ and $s = -1/2$, respectively.

the conduction band splitting is only on the order of few to 10's of meV and can be either negative or positive, depending on the specific choice of the transition metal atom. As illustrated in Fig. 2.1(d), in monolayer MoX_2 the lowest energy optically-allowed transition involves the lower spin-split conduction band, whereas in monolayer WX_2 the upper conduction band is involved [135, 136, 126]. As a direct consequence, in monolayer WX_2 the lowest energy transition is dark, i. e., a dipole-forbidden transition [126, 54, 137, 138, 139, 140, 141].

2.2 Excitons – Coulomb-bound electron-hole pairs

Optical properties of many semiconductors are governed by Coulomb-bound electron-hole pairs, so-called excitons [142]. An exciton is a charge-neutral quasi-particle which possesses the ability to carry information and energy without transporting net electric charge. This elementary excitation has been studied in many materials, first of all in semiconductors and insulators [4]. Excitons can be created by optically exciting an electron from the valence band into the conduction band, which then binds to the remaining vacancy, i. e., the hole, in the valence band. Typically, ground state exciton binding energies range between a few 10's of meV in inorganic bulk crystals such as cuprous oxide [143] or quantum well systems [7], and up to few eV in organic crystals [144].

In monolayer TMDCs, exciton binding energies as large as several hundreds of meV have been observed [31]. These high values are traced back to the reduced dielectric screening which results in strong Coulomb interactions in the monolayer [145]. Consequently, excitons in TMDCs are tightly-bound and largely inert from thermal fluctuations even at room temperature [146]. Excitons in TMDCs are commonly described in a Wannier-Mott like picture [145, 31], implicating spatial extent of many lattice atoms and the possibility of free propagation through the crystal [147]. Herein, excitons are described by a modified hydrogen atom reduced to a two-dimensional plane [145]. The constituting electron and hole bind to hydrogen-like states ($n = 1, 2, 3, \dots$) with binding energies [4]

$$E_b^n = \frac{e^4 \mu_X}{2\hbar^2 \epsilon_0^2 \epsilon^2 (n - 1/2)^2}. \tag{2.1}$$

Here, e denotes the elementary charge, $\hbar$ the reduced Planck's constant and $\mu_X = m_e m_h/(m_e + m_h)$ the reduced exciton mass with m_e and m_h being the effective electron and hole masses. ϵ_0 is the vacuum permittivity. The dielectric constant ϵ accounts for the dielectric screening of the Coulomb interaction. As illustrated in Figure 2.2 (a), for a monolayer the electric field lines of the exciton extend into the surrounding, which, in general, exhibits a different dielectric constant than the monolayer, i. e., $\epsilon_{\text{surr.}} \neq \epsilon_{\text{ML}}$. In this case, ϵ in Equation 2.1 is not a constant and the potential deviates from the classical Coulomb potential $V(r) \propto 1/(\epsilon r)$ (r is the spatial coordinate). It is instead replaced by a thin-film Coulomb potential [148, 149, 145, 150, 151]

$$V(r) = -\frac{e^2}{8\epsilon_0 r_0} \left[H_0\left(\frac{r\epsilon_{\text{surr.}}}{r_0}\right) - Y_0\left(\frac{r\epsilon_{\text{surr.}}}{r_0}\right) \right]. \tag{2.2}$$

Here, H_0 and Y_0 denote the Struve and Neumann functions and r_0 is the screening length, i. e., the characteristic length scale where the potential deviates from the classical Coulomb potential.

Solving the Schrödinger equation with the thin-film Coulomb potential given by Equation 2.2, a modified relation of Equation 2.1 can be derived, consistent with experimentally determined binding energies [145, 4, 152, 153]. As the latter crucially depends on $\epsilon_{\text{surr.}}$, controlling and structuring the dielectric constant of the surrounding opens the possibility to tune the exciton's binding energy [40, 154, 155]. On the other hand, this also implies that in a bare monolayer excitons are affected by unintentional inhomogeneities due to surface adsorbates with varying dielectric constant [69]. To suppress such disorder effects, the monolayers are typically encapsulated in atomically-flat layers of hexagonal boron nitride (hBN) [156, 157, 158, 69, 105]. Due to a low dielectric constant [159] and transparency in the visible and near-infrared regime [160, 161], the influence of hBN on the intrinsic monolayer properties is considered to be otherwise negligible.

In Fig. 2.2(b), the 1s and 2s exciton radial probability is plotted as function of electron-hole separation for a hBN-encapsulated monolayer WS_2 considering the thin-film potential in Equation 2.2 with a screening length $r_0 = 4$ nm and $\epsilon_{surr.} = 4.5$. As initially confirmed in magneto-optic experiments, the exciton ground state exhibits a root-mean-square radius of ≈ 2.5 nm corresponding to a Bohr radius of ≈ 1 nm [150, 151], which is much larger than the inter-atomic distance, cf. Fig. 2.2(c). Recent angle-resolved photoemission spectroscopy measurements, presented in Fig. 2.2(d), directly show that the optical excitations are localized in momentum space [162], supporting the Wannier-Mott-like exciton picture.

The dynamical properties of the exciton are described by its total momentum $\mathbf{k}_X = \mathbf{k}_e + \mathbf{k}_h$ and translational mass $m_X = m_e + m_h$, with the effective electron and hole masses m_e and m_h, respectively. The kinetic energy of the exciton is given by [4]

$$E_{\text{kin}} = \frac{\hbar^2 \mathbf{k}_X^2}{2m_X}. \tag{2.3}$$

In a semiconductor with free particle band gap E_g the exciton dispersion reads

$$E_X^n = E_g - E_b^n + E_{\text{kin}}. \tag{2.4}$$

The exciton energy E_X^n is reduced with respect to the free particle band gap by the exciton binding energy E_b^n. In Fig. 2.2(e), the exciton dispersion with ground

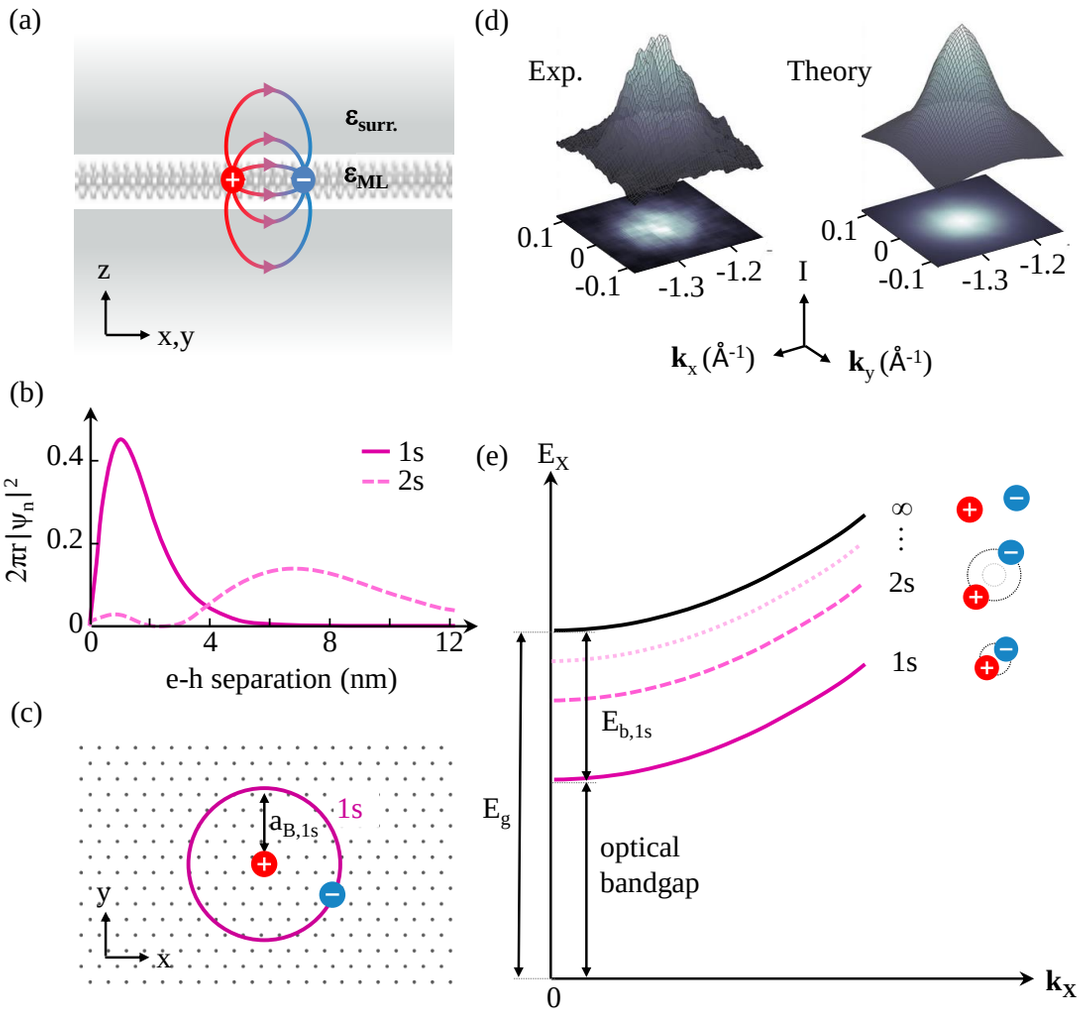

Figure 2.2: (a) Schematic cross-section of an exciton with electric field lines in a monolayer semiconductor embedded in a surrounding with dielectric constant $\epsilon_{\text{surr.}}$. (b) Radial probability of the 1s and 2s exciton in monolayer WS_2 as function of electron-hole separation. Reprinted figure with permission from Ref. [150]. Copyright (2022) by the American Physical Society. (c) Schematic representation of the 1s exciton with Bohr radius $a_{B,1s}$ from (b). (d) Direct measurement of the exciton wave function in k-space in a monolayer WSe_2 on hBN by angle-resolved photoemission spectroscopy. From Ref. [162]. Reprinted with permission from AAAS. (e) Two-particle dispersion with bound exciton states (n =1s, 2s, ...) and free electrons and holes ($n = \infty$). The free particle band gap E_g, optical band gap and ground state exciton binding energy $E_{b,1s}$ are indicated.

state 1s and excited states 2s, 3s,... is schematically illustrated. In absorption or reflectance spectroscopy, ground state excitons gives rise to a peak at an energy $E_X^{1s}(k_X \approx 0)$. The latter is often called the *optical band gap*. Also absorption peaks corresponding to higher-order exciton states can be observed [145, 152, 163, 153].

Due to their weaker oscillator strength ($f^n \propto (n-1/2)^{-3}$ [164]) their absorption strongly decreases with increasing quantum number.

2.3 Trions and Fermi polarons

In previous section the intrinsic optical excitations in a neutral semiconductor are introduced. Adding free charge carriers to the system, e. g. by electrically contacting the sample, exciton-carrier interactions result in significant changes in the optical properties of the material. In monolayer semiconductors, this scenario is typically approached by considering an exciton in a two-dimensional Fermi gas, i. e., a non-interacting two-dimensional electron (2DEG) or hole gas (2DHG). The ground state of the Fermi gas is called the Fermi sea. Here, electrons or holes occupy the conduction or valence band up to the Fermi energy. The interaction of excitons with free charge carriers leads to the formation of trions [41, 66, 42, 165, 67, 166], Fermi polarons [44, 45, 167, 168, 169, 170, 46] including dark state trions [37, 56, 171, 172] as well as higher order many-particle complexes such as charged biexcitons [47, 48, 49, 50, 51, 52]. In the following section, the basics of exciton-carrier interactions are outlined focusing on the low carrier density regime. Here, the spectroscopic observables are mainly described by trions and Fermi polarons.

In a simplified model, an exciton can bind to an electron and forms a trion, a three-particle complex in analogy to the H^- [72] ion. Depending whether an electron or a hole is considered, it is treated as a negatively or positively charged quasiparticle. While trions have been proposed already 1958 by Lampert *et al.* [14], their experimental observation in two-dimensional quantum wells such as CdTe [15], GaAs [64] and ZnSe [65] is dated back only to the 1990s. In cleaved monolayer semiconductors trions were first observed in 2013 [41, 66, 42]. In TMDC monolayers, experimentally observed trion binding energies are on the order of 10 to 30 meV [41, 66, 48, 50], much larger than in quantum well systems, with binding energies on the order of only few meV [15, 64, 65]. In TMDCs, this opens the possibility to study trions and their interaction and propagation mechanisms also at elevated temperatures [43] and charge carrier densities of several 10^{12} cm^{-2} [41, 173]. By contrast, in quantum well systems, typically at carrier densities of $\approx 10^{11}$ cm^{-2} excitons ionize [20].

Similar to an exciton, a trion can be described in an effective mass approach. Its kinetics are described by the momentum $\mathbf{k}_T = \mathbf{k}_X + \mathbf{k}_e$ and translational mass $m_T = m_X + m_e$ [4]. Trions can be optically injected in a semiconductor by exciting a Coulomb-bound electron-hole pair, i. e., an exciton, which simultaneously binds

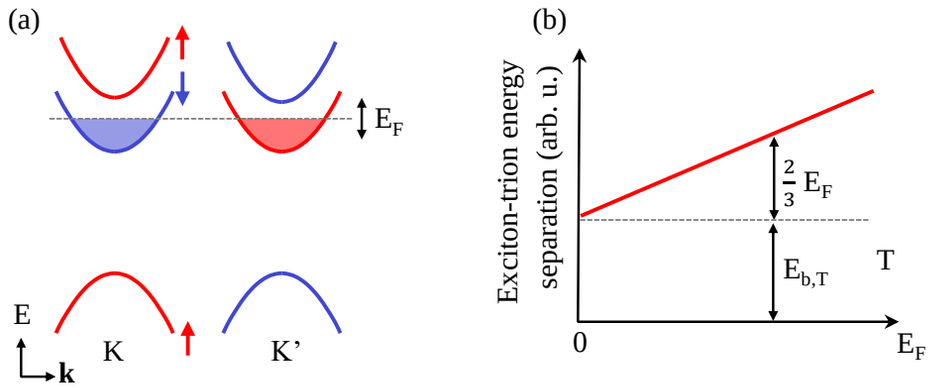

Figure 2.3: (a) Schematic band structure of monolayer WSe_2 with electron doping in the lowest spin-split conduction band at K and K'. E_F denotes the Fermi energy. Red and blue lines indicate electron spin states. (b) Exciton-trion energy separation as function of Fermi energy in the trion picture. The trion energy is lowered by the binding energy $E_{b,T}$. With increasing Fermi energy the exciton-trion energy separation increases linearly with $2/3E_F$.

an additional free carrier which already resides in the material. As the constituting optically-excited exciton exhibits negligible momentum $\mathbf{k}_X \approx \mathbf{k}_{photon} \approx 0$ (in the light cone), the momentum of the trion is approximately given by the electron momentum, i. e., $\mathbf{k}_T \approx \mathbf{k}_e$. Considering free charge carriers in a parabolic band structure, illustrated for TMDC monolayers in Fig. 2.3(a), an increase of the Fermi energy E_F (which scales linearly with the free carrier density in a two-dimensional parabolic dispersion [174]) leads to the occupation of higher momentum states. Taking into account energy and momentum conservation, yields $E_T^{kin} \approx m_e/m_T E_e^{kin}$ and the energy to optically create a trion is given by [173]

$$E_T^{opt} = E_X - E_{b,T} - (1 - m_e/m_T)E_e^{kin} \tag{2.5}$$

with exciton energy E_X and trion biding energy $E_{b,T}$. The exciton and trion transition energies are schematically illustrated in Fig. 2.3(b) as function of Fermi energy taking into account $E_e^{kin} \approx E_F$. At zero doping ($E_F = 0$), the trion is lowered with respect to the exciton energy by the constant trion binding energy $E_{b,T}$. The latter depends on the Coulomb interaction, effective electron and hole masses as well as spin- and valley indices. Similar to the excitons, the trion binding energy can be obtained from solving the Schrödinger equation [165, 166, 109, 67, 175, 168].

The presence of free charge carriers does not only result in the formation of trions, but also in modifications of the exciton. Due to screening of the exciton

binding energy, band gap renormalization [173] and face-space filling effects due to Pauli blocking, the exciton exhibits a pronounced blueshift [173]. In extended many-body approaches these phenomena are well captured resembling experimentally observed resonance energies, linewidth broadening and oscillator strengths, see e. g. Ref. [112].

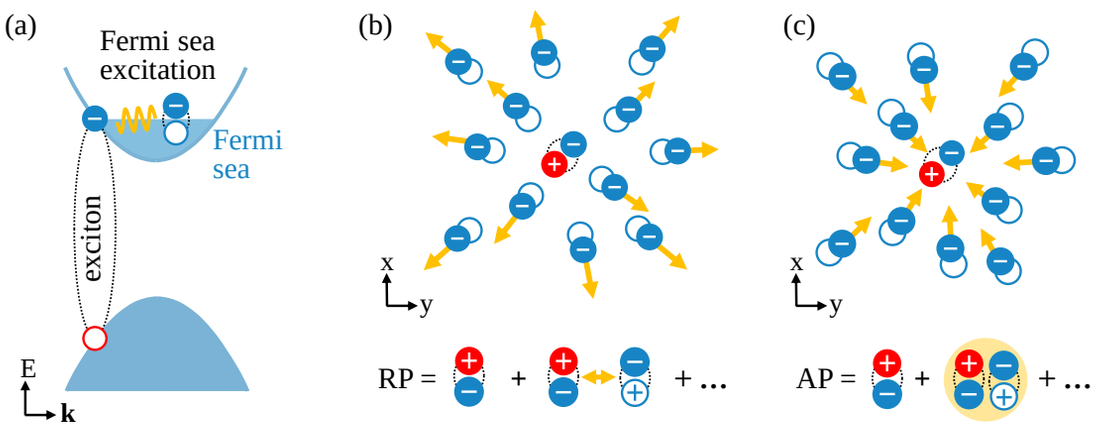

Figure 2.4: (a) Schematic illustration of an exciton represented in the electronic band structure interacting with a Fermi sea excitation. The exciton is generated by optically exciting an electron from the valence band into the conduction band which binds to the hole in the valence band. Similarly, the Fermi sea electron-hole pair corresponds to an electron which is excited out of the Fermi sea leaving behind a vacancy, i. e., the Fermi or conduction band hole. (b) Schematic illustration of the repulsive Fermi polaron (RP). Electrons are displaced from their equilibrium positions (empty circles). The RP is described by a linear combination of an exciton, an exciton scattering with one Fermi sea excitation and higher order contributions. (c) Illustration of the attractive Fermi polaron (AP). It corresponds to an exciton which binds to the Fermi sea excitations and is described by a linear combination of an exciton, an exciton which binds to one Fermi sea excitation (a tetron) and higher order contributions [176].

A many-body approach motivated from recent experiments with ultracold Fermi gases [177, 178, 179, 180, 181] describes the exciton-electron problem in monolayer semiconductors in the *Fermi polaron* or *exciton polaron* picture (sometimes also termed as exciton-Fermi-polaron) [44, 45, 167, 182, 168, 109, 170, 46, 183]. Different to a conventional polaron, which describes the interaction of an electron with a cloud of phonons, the Fermi polaron takes into account the correlation of an exciton with a cloud of Fermions, i. e., a gas of electrons or holes. Herein, the exciton interacts with excited Fermi sea electron-hole pairs (which are e. g. excited by the optically-generated exciton), schematically illustrated in Fig. 2.4(a). The interaction is described by a linear combination of an exciton, an exciton

dressed with one Fermi sea excitation, an exciton dressed with two Fermi sea excitations, etc. [183]. By this, the interplay of an exciton with many electrons is taken into account, particularly relevant in the case of a much larger carrier compared to exciton density. The Fermi polaron results in two branches in the absorption spectrum: the repulsive (RP) and attractive (AP) Fermi polaron. The repulsive and attractive exciton-electron interactions are schematically illustrated in Fig. 2.4(b) and (c), respectively. The repulsive branch corresponds to the renormalized exciton state, whereas the attractive branch corresponds to a bound state, similar to a trion [168]. It is noteworthy, that the repulsive polaron does not become a new particle when interacting with the electrons. Light-matter coupling, exciton binding energies or the wavefunction is only slightly modified in the presence of electrons. This is in stark contrast to the attractive Fermi polaron, which constitutes a new quasiparticle with qualitatively different properties.

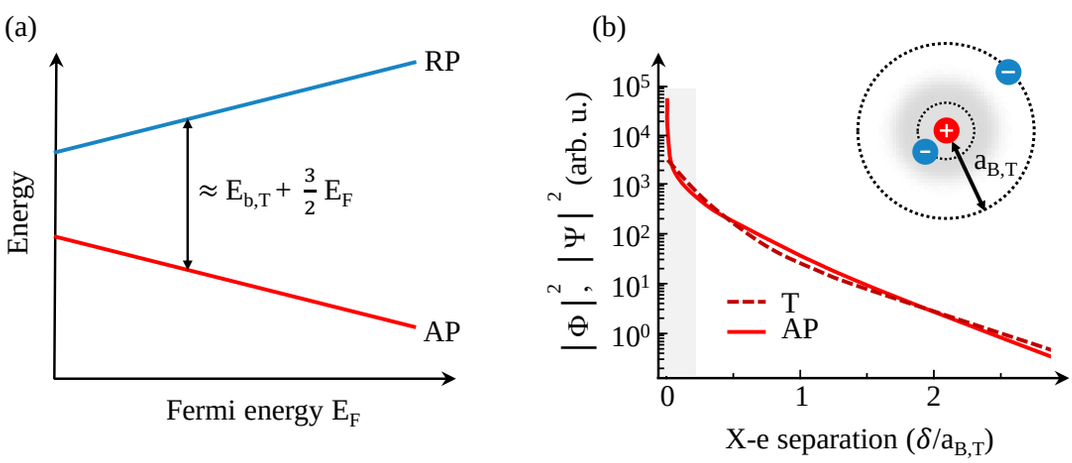

Figure 2.5: (a) Schematic illustration of attractive (AP) and repulsive (RP) Fermi polaron energies as function of Fermi energy E_F. The energy separation between RP and AP is approximately given by $E_{b,T} + 3/2E_F$. (b) Probability density $|\Phi|^2$ of the relative exciton-electron motion in the attractive Fermi polaron and trion wave function $|\Psi|^2$ representing the probability density of the extra electron with respect to its distance to the hole, reproduced from Ref. [169] with the permission of AIP Publishing. The trion Bohr radius is set to $a_{B,T} = 4a_{B,X}$. Grey area indicates region where Φ diverges and the description becomes inapplicable. The spatial extent of the trion is schematically illustrated in a hydrogen-like picture indicating the trion Bohr radius $a_{B,T}$

In addition to the trion, the attractive Fermi polaron takes into account the interaction with the collective Fermi sea, i. e., multiple Fermi sea excitations. In its simplest form, it can be understand as an exciton which binds to one Fermi sea excitation, resulting in an effective four-particle state which consists of two

electrons and two holes, one in the valence band and the other in the conduction band, the so-called conduction band or Fermi hole. This effectively charge-neutral quasiparticle has been introduced already in 2001 and is called a *tetron* [184]. In comparison to the trion, the additional Fermi sea hole leads to a further contribution in the attractive Fermi polaron binding energy, which increases with Fermi energy. In the limit of small carrier concentrations, the binding energy is equal to the bare trion binding energy, i. e., the Fermi hole becomes negligible. In Fig. 2.5(a), the qualitative energy dependence of the repulsive and attractive Fermi polaron is presented. While the repulsive polaron is lifted up in energy, the attractive Fermi polaron is lowered with respect to the bare exciton transition energy. The splitting of the two branches approximately scales linearly with the Fermi energy $E_{RP} - E_{AP} \approx E_{b,T} + 3/2E_F$ [45, 46] considering $m_e \approx m_h$ in monolayer TMDCs [126].

At high carrier densities, the binding to more than one Fermi sea excitation leads to an additional increase of the attractive Fermi polaron binding energy. Furthermore, the interaction with more than one distinguishable Fermi sea excitations can result in qualitatively new features in the absorption spectrum. For example, by electrically doping WSe_2 monolayers, the lower conduction band valleys at K and K' are occupied. At higher densities also the upper conduction band valleys fill up with electrons. Therefore, the exciton interacts with up to four distinguishable Fermi seas, each with a different spin and valley index. As discussed in Ref. [53], in this configuration an exciton can bind to two or three distinguishable Fermi sea excitations. The corresponding quasiparticles are termed as hexcitons or oxcitons.

Importantly, in the low carrier density regime, the Fermi polaron turns out to be equivalent to the trion picture. For the ground state, both models predict similar energy dependencies, linewidth broadenings and oscillator strengths [45, 112]. Therefore, in this thesis the terms "trion" and "attractive Fermi polaron" are used equivalently in the weak interaction regime. The applicability of the trion and Fermi polaron is further limited to the case where the exciton binding energy $E_{b,T}$ is much larger than the trion binding energy $E_{b,T}$, i. e., [109]

$$E_{b,X} \gg E_{b,T} \gg E_F. \tag{2.6}$$

The condition is fulfilled in monolayer TMDCs with ground state exciton binding energies in the range of several 100's of meV and trion binding energies of several 10's of meV considering free carrier densities $\lessapprox 10^{12}$ cm^{-2}. The majority of the experiments in this thesis are performed in this density regime.

It should be noted that the constituting electrons and holes within a trion or Fermi polaron are distinguishable, i. e., the two electrons in a negatively-charged trion are not "equal". Particularly, the electron-hole separation within the excitonic core is much smaller compared to the distance to the extra Fermi sea electron, i. e., $a_{B,X} \ll a_{B,T}$. In Fig. 2.5(b), the probability density of the relative exciton-electron motion δ in the trion picture using a variational approach and a simplified short-range model in the Fermi polaron picture is presented with $a_{B,T} = 4a_{B,X}$. In both pictures, the additional electron is bound similar to an electron in a hydrogen atom where the nucleus is replaced by an exciton.

2.4 Excitons and trions in monolayer WSe_2

Having outlined the general concept of excitons and trions, in this section the specific exciton dispersion of monolayer WSe_2 is discussed, focusing on the most important low-energy exciton and trion states. The choice for a tungsten-based TMDC monolayer is motivated by the inverted conduction band splitting ($\Delta_{CB} > 0$) at K/K', where the optically-accessible transition lies energetically above the spin-forbidden transition. In the scope of this thesis, the major advantage of this configuration are long-lived dark exciton reservoirs [54] which allow for diffusion experiments of thermalized states [107, 108]. In Fig. 2.6, the schematic exciton dispersion of hBN-encapsulated monolayer WSe_2 is presented along Γ-K focusing on the energetic minima where the excitations accumulate after relaxation (for an *ab initio* approach see Ref. [185]). For all excitonic states, the hole is considered to be located in the energetically lowest valence band K valley in the underlying electronic band structure. At zero momentum $\mathbf{k}_X = \Gamma$ the dispersion exhibits two minima which are separated by ≈ 40 meV mimicking the spin-split conduction band. The corresponding exciton states are called intra-valley K-K excitons, i. e., the constituting hole and electron are at K. There are two possible configurations: if the electron is located in the upper spin-split conduction band, the X^0 exciton forms. If the electron is in the lower spin-split conduction band, the D^0 exciton forms. Next to K-K excitons, the dispersion is characterized by further minima at higher momenta, where the constituting electron is located at Λ or K'. In the case that the electron is in the lower spin-split conduction band at K', the corresponding state is called the inter-valley I^0 exciton.

The characteristic properties of the introduced exciton states are mostly governed by their momentum and spin configuration. Due to equal electron and hole spin, the intra-valley D^0 exciton transition is *spin-forbidden* whereas transitions

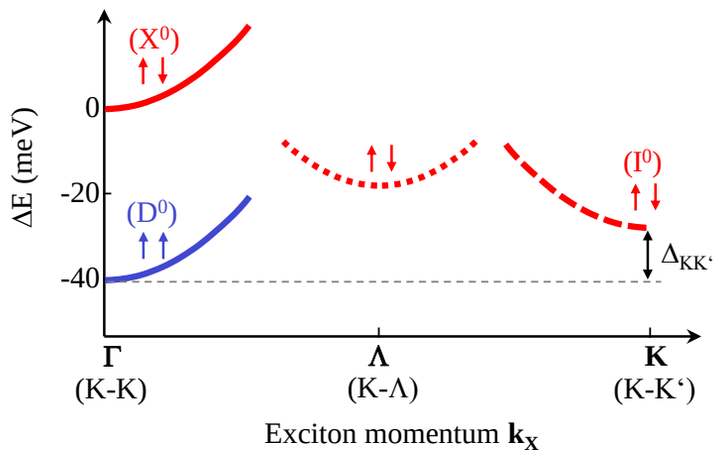

Figure 2.6: (a) Schematic low energy exciton dispersion as function of exciton momentum $\mathbf{k}_X$ in the direction of Γ-K in a hBN-encapsulated monolayer WSe_2 following Ref. [185]. The constituting hole (empty state in the valence band) is set to the K valley. The labels (K-K), (K-Λ) and (K-K') correspond to the constituting hole and electron valley configuration of the respective exciton states. Arrows indicate underlying electron and hole spin. X^0, D^0 and I^0 denote corresponding emission peaks in photoluminescence spectroscopy. The notation is adapted from Ref. [186]. The energy separation between intra-valley D^0 and inter-valley I_0 excitons is indicated by Δ_{KK}.

at K-Λ and K-K' are *momentum-forbidden*. The only low-energy dipole-allowed transition occurs for the upper K-K state, i. e., the intra-valley X^0 exciton. Excitons with a dipole-forbidden or dipole-allowed transition are called *dark* or *bright* excitons, respectively. While the properties and interplay of the individual states have been intensively studied [137, 187, 188, 189, 37, 107], their exact energetic alignment is part of an ongoing debate. Following recent interpretations based on photoluminescence spectroscopy, the I^0 exciton at K-K' lies $\Delta_{KK'} \approx 9$ meV above the D^0 ground state [37, 186], a consequence of the short-range electron-hole exchange interaction [190, 191, 192]. The heavier and three times degenerate K-Λ excitons are expected to be located energetically closer to the bright X^0 exciton at K-K [193, 194]. Fingerprints of K-Λ excitons have been observed in transient PL [107], strain-induced propagation dynamics [195] and in direct time- and angle-resolved photoemission spectroscopy experiments [196].

Inserting free charge carriers into the monolayer results in multiple bound trion (attractive Fermi polaron) states. For simplicity, only trion ground states in the effective mass approximation are considered [166]. The discussion is further restricted to the K and K' valley, i. e., neglecting trions with electrons or holes located at the Λ-valley. In Fig. 2.7, the low energy trion configurations in mono-

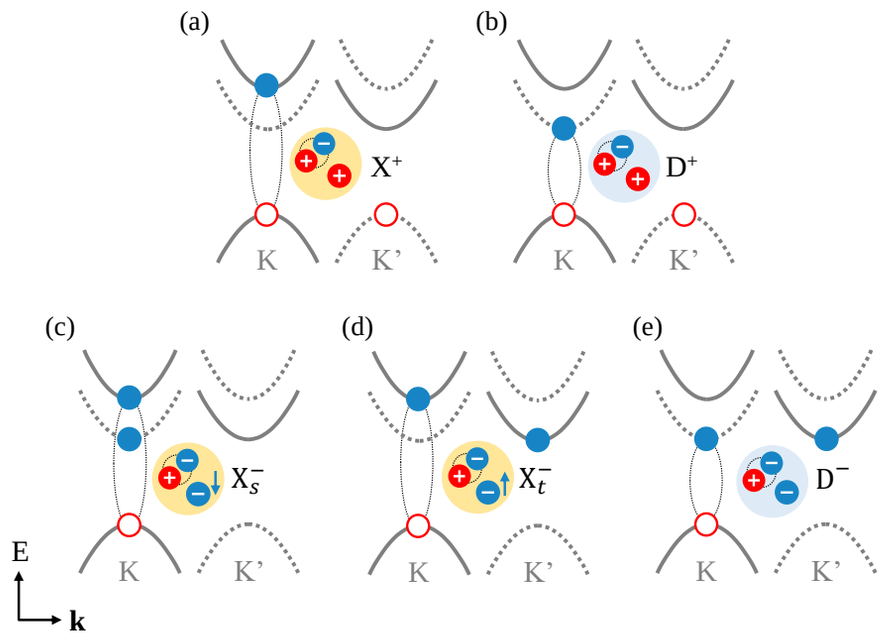

Figure 2.7: Schematic illustration of ground state trions with an excitonic core at K-K in the low-energy monolayer WSe_2 band structure. Solid and dashed lines indicate electron spin states. Filled blue circles denote conduction band electrons and empty red circles denote hole states in the valence band. (a,b) and (c,d,e) show positively and negatively-charged trion configurations considering doping in the energetically lowest valence and conduction band, respectively. Bright and dark trion states are denoted by $X^{\pm}$ and $D^{\pm}$ and indicated by yellow and blue colors, respectively. X_s^- and X_t^- denote the bright singlet and triplet trion.

layer WSe_2 are schematically represented in the electronic band structure. Fig. 2.7 (a) and (b) show configurations of positively charged trions where the holes are located in the K and K' valence band valleys. As outlined in section 2.3, the trion/attractive Fermi polaron is described by an excitonic core which additionally binds to a free carrier/a Fermi sea excitation. Depending on the excitonic core, the configurations are termed as bright (X^+) or dark (D^+) trions, respectively. It should be noted that no trions involving indirect I^0 (K-K') excitons are observed in photoluminescence. Due to exchange scattering between indirect I^0 excitons and free charge carriers which reside in the bottom-most K valley, I^0 excitons efficiently relax to D^0 [186] (see also Fig. 2.11(c)). Negatively charged trion configurations are presented in Fig. 2.7 (c-e) considering electron doping in the lowest spin-split conduction band at K and K'. The bright singlet trion X_s^- and triplet trion X_t^- involve the bright excitonic core at K-K and either an electron with opposite or equal spin at K and K', respectively. The two configurations split in energy due to short-range electron-electron exchange interaction [191, 36, 197]. In analogy to

the D^+ trion, the D^- trion forms due to the interaction of a D^0 exciton with an electron at K'.

2.5 Scattering and recombination pathways

As presented in previous section, tungsten-based TMDC monolayers such as WSe_2 exhibit extended excitonic landscapes with the prospect of a complex interplay of excitonic quasiparticles. In the following, the basics of exciton and trion scattering as well as selected recombination mechanisms are introduced. Fig. 2.8(a) schematically depicts exciton scattering channels in a semiconductor: intrinsic scattering with lattice vibrations, i. e., phonons (Γ_{phon}), scattering with other excitons (Γ_{X}), free carrier scattering (Γ_{carr}) and defect scattering at lattice vacancies or add-atoms (Γ_{defect}). The total scattering rate that an exciton experiences is given by [4]

$$\Gamma = \Gamma_{\mathrm{phon}} + \Gamma_{\mathrm{carr}} + \Gamma_{\mathrm{X}} + \Gamma_{\mathrm{defect}} \tag{2.7}$$

The exciton scattering rate translates to the scattering time $\tau_s = \hbar/\Gamma$ and is directly related to the spectroscopic linewidth broadening.

In this work, all experiments are performed at low exciton densities where the probability to scatter with other excitons Γ_X is negligible and thus, is not further considered. Most relevant in this thesis is the scattering with phonons and free charge carriers. First, the scenario of exciton scattering in an undoped semiconductor with $\Gamma_{\mathrm{carr}} = 0$ is discussed. As demonstrated in many two-dimensional semiconductors with sufficiently low defect scattering [198, 199, 200, 201, 202, 203, 204] and at low temperatures, the exciton scattering is governed by low-energy acoustic phonons and the homogeneous exciton linewidth approximately increases linearly with temperature, i. e., $\Gamma_{\mathrm{phon}} \approx \gamma T$ [205]. Here, γ is the material-characteristic strength of the electron-phonon coupling. In TMDCs, the latter is found to be on the order of several 10's of μeV/K [206, 207, 208, 209, 203, 156, 73], much stronger than in quantum wells, with values of only a few μeV/K [200, 201, 202]. At elevated temperatures the scattering with high-energy phonons becomes dominant, leading to a super-linear increase of the scattering rate. Approximately, in this regime the exciton linewidth is described by the Debye-Einstein relation [199]

$$\Gamma_{\mathrm{phon}}(T) = \Gamma_0 + \gamma T + \frac{\Gamma^*}{\exp(E^*/k_B T) - 1} \tag{2.8}$$

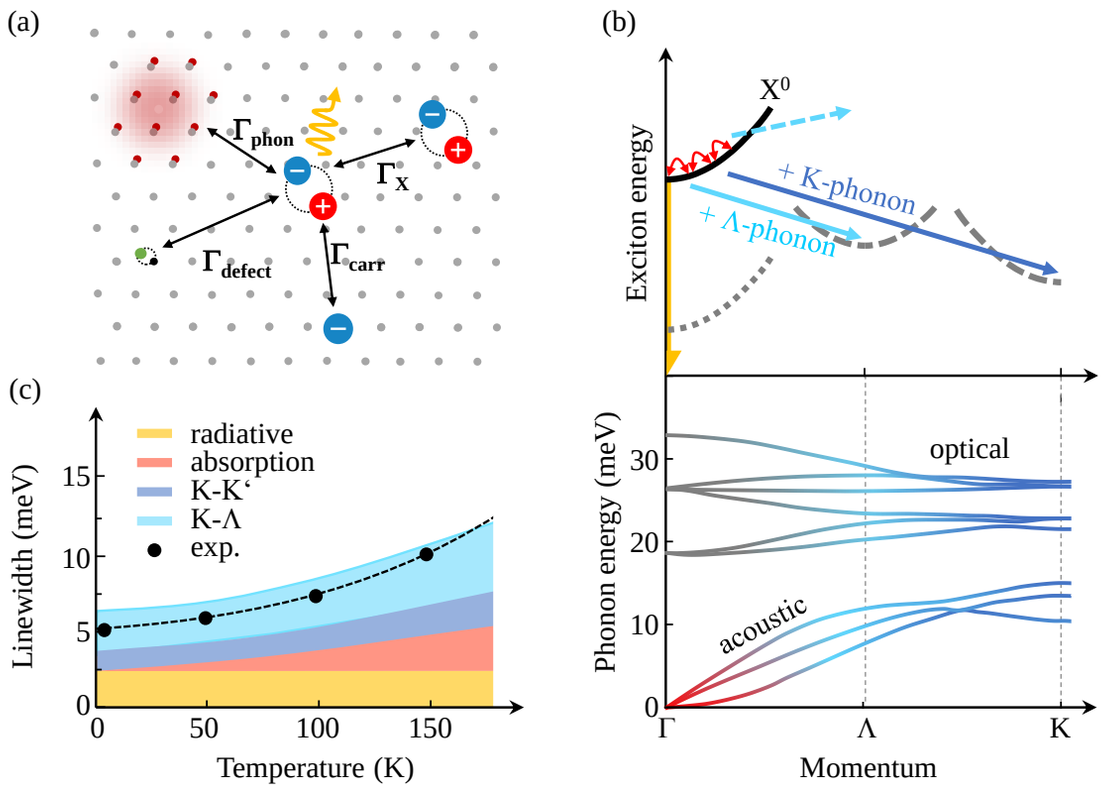

Figure 2.8: (a) Schematic illustration of exciton scattering mechanisms involving phonons, defects, other excitons and free charge carriers. (b) Schematic illustration of the exciton dispersion in tungsten-based TMDCs with indicated exciton-phonon scattering channels of the X^0 exciton at low temperatures. The intra-valley scattering is determined by the emission and absorption of acoustic phonons. The inter-valley scattering is predominantly determined by the emission of Λ- and K-phonons. At elevated temperatures also the absorption of temperature-activated acoustic Λ-phonons contribute to the inter-valley scattering (cyan dashed line). The lower panel shows the calculated phonon dispersion along Γ-K adapted from Ref. [37]. (c) Experimentally determined X^0 exciton linewidth broadening as function of temperature determined from reflectance contrast measurements of hBN-encapsulated monolayer WS_2. The figure is reproduced from Ref. [73]. The data is compared to the calculated exciton linewidth taking into account radiative dephasing and phonon scattering indicated in (b). Due to hBN-encapsulation, defect scattering and contributions from inhomogeneous broadening are considered to be small and are thus neglected.

with E^* being an effective average energy of the high-energy phonon modes and Γ^* is the strength of the coupling. Γ_0 is a phenomenological parameter and is often attributed to scattering with defects or radiative dephasing. For example, in case of the bright X^0 exciton in TMDCs, a radiative decay time on the order of 200 fs [210, 211] yields a constant radiative linewidth broadening on the order

of 2 meV. Depending on the local field effect, the radiative decay and thus the broadening can be tuned e. g. by the thickness of the surrounding hBN-layers [212]. By contrast, dark excitons exhibit a decay time on the order of several 100's of picoseconds [54], corresponding to a negligible radiative broadening in the μeV range. It should be noted that the Debye-Einstein relation is a simplified approach where the scattering with, in general, multiple acoustic and optical high-energy phonon modes is estimated by a single effective phonon with energy E^*.

For a quantitative understanding of exciton-phonon scattering in TMDCs, it is necessary to consider the complex multi-valley exciton dispersion, introduced in previous section. Following Ref. [73], low temperature phonon scattering of the bright X^0 exciton is divided into intra- and inter-valley scattering. In the case of intra-valley scattering, low-energy zone-center acoustic phonons are absorbed or emitted. In the case of inter-valley scattering, the exciton scatters between individual exciton states by the assistance of a high-momentum phonon, as illustrated in the upper panel of Fig. 2.8(b). At low temperatures, inter-valley scattering is mediated by the emission of high-momentum K- or Λ-phonons with energies on the order of 10 to 30 meV. For comparison, in the lower panel of Fig. 2.8(c), the phonon dispersion along Γ-K is presented, comprising longitudinal, traversal and out-of-plane (z-) polarized acoustic and optical phonon modes. By emitting a phonon with momentum $\mathbf{k}_{\mathrm{phon}} = \Delta\mathbf{k}_X$, the X^0 exciton can scatter into lower-laying exciton states separated by a finite momentum $\Delta\mathbf{k}_X$. At elevated temperatures, also the absorption of thermally-activated phonons can contribute to inter-valley scattering.

In Fig. 2.8(c), the experimentally measured X^0 exciton linewidth, determined from reflectance contrast measurements of hBN-encapsulated WSe_2 monolayer, is compared to a calculation based on the material-realistic multi-valley band structure [73]. The exciton linewidth is determined by several contributions. It is determined by a constant, temperature-independent radiative broadening on the order of 2.5 meV and a temperature-dependent contribution stemming from the absorption and emission of phonons. Approaching zero temperature, the absorption vanishes, as no thermally-activated phonons are available. Only the emission of K- and Λ-phonons determines the exciton-phonon scattering (X^0 excitons at K-K scatter into K-K' and K-Λ states) and results in a nearly temperature-independent scattering rate on the order of 4 meV. The temperature dependence is mainly determined by the absorption of acoustic phonons. At low temperatures, it results in an approximately linearly increasing contribution to the exciton scat-

tering rate on the order of $\approx 25\ \mu$eV/K. At elevated temperatures (T $\gtrapprox$ 100 K), the absorption of acoustic Λ-phonons leads to a (weak) super-linear increase.

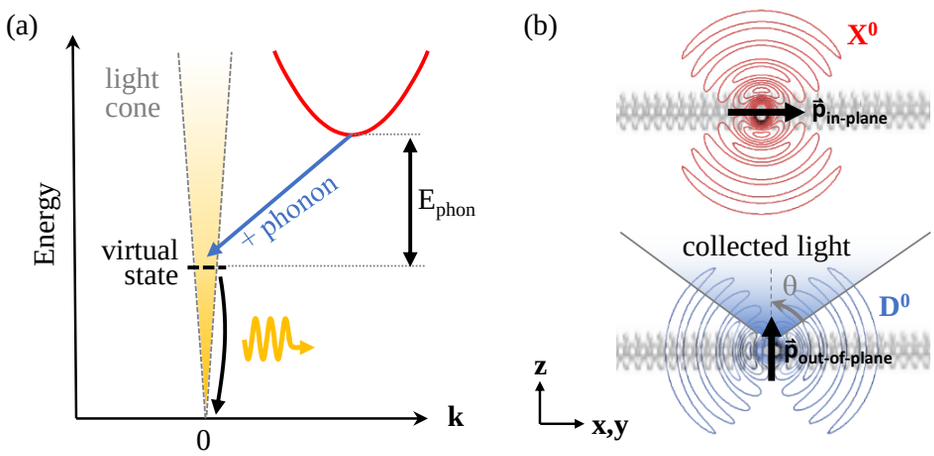

Figure 2.9: (a) Schematic illustration of phonon-assisted recombination of momentum dark excitons involving a virtual state in the light-cone. The emission energy is reduced by the phonon energy. (b) Schematic illustration of in-plane polarized X^0 exciton emission and out-of-plane polarized D^0 exciton emission. The emission intensity of the D^0 exciton is most strongest in x/y direction. In typical experiments, light is collected which emits in perpendicular direction to the sample surface. However, due to an objective with large numerical aperture NA $\propto \sin\theta$ (blue shaded area), stray light of the D^0 exciton can be observed.

As outlined in previous section, the majority of all exciton states are outside the light-cone and are thus momentum dark. The possibility of phonon-assisted inter-valley scattering turns out to be particularly crucial for the optical investigation of K-Λ or K-K' excitons. Momentum-dark excitons can become optically active by transferring their momentum to e. g. defects, other excitons, free carriers or phonons. Fig. 2.9(a) schematically illustrates the recombination of an exciton by transferring its momentum to a phonon (by creating a phonon) involving a virtual state at the light cone. In this case, the detected emission energy is lowered by the phonon energy, i. e., $E_{\mathrm{PSB}} \approx E_X - E_{\mathrm{phon}}$. Consequently, in photoluminescence spectroscopy a discrete low energy peak occurs, termed as *phonon side band* [4]. In the case that the recombination is assisted by two, three or more phonons, the phonon side band energy is reduced by $2E_{\mathrm{phon}}$, $3E_{\mathrm{phon}}$, ..., resulting in a progression of equally-spaced phonon side bands which decrease in intensity [4]. In principal, also the combination of phonon modes with different energies is possible. In tungsten-based monolayer TMDCs, particularly long-lived ground state excitons, i. e., intra-valley D^0 excitons and $D^{\pm}$ trions as well as inter-valley momentum-

forbidden I^0 excitons give rise to phonon side bands, dominating the low-energy photoluminescence spectrum [213, 37].

As outlined in section 2.4, the recombination of the D^0 exciton ad K-K is spin-forbidden (in in-plane polarization) due to equal electron and hole spin. However, it exhibits a finite transition matrix element in out-of-plane polarization [139]. Considering the specific orbital configuration in tungsten-based TMDCs, it can be shown that the D^0 state splits into two branches due to spin-orbit-induced spin mixing in the valence band. While one of the branches is optically inactive, the other one exhibits an out-of-plane polarized dipole-allowed transition. Despite of only a small expected oscillator strength, this mechanism gives rise to finite photoluminescence of the D^0 exciton [139]. Different to the X^0 emission, which is in-plane polarized and predominantly emits perpendicular to the sample surface in z-direction, the D^0 exciton emission is strongest in the direction parallel to the sample surface, i. e., in x/y direction, cf. Fig. 2.9(b). In the experiment, the emitted light is typically collected in z-direction and thus is most sensitive to in-plane polarized emissions. Using an objective with a large numerical aperture (NA), out-of-plane polarized light can be detected. In the lower panel of Fig. 2.9(b), the dashed lines indicate the maximum angle θ which an objective with NA $= n \times \sin\theta$ detects. Due to the dipole-like radiation of the D^0 emission, it exhibits a finite contribution in z-direction. Therefore, using large NA objectives (in this work NA $= 0.7$) allows to simultaneously detect the X^0 emission and stray light of D^0.

Furthermore, the intra-valley D^0 exciton can recombine via the assistance of the zero-momentum optical Γ_5-phonon mode. The Γ_5 mode exhibits a polarization vector which is denoted by in-plane and out of phase vibration of the chalcogene atoms and results in an in-plane polarized phonon-assisted emission [56]. Thus, although the direct D^0 recombination is out-of-plane polarized, its phonon side band is in-plane polarized.

In doped semiconductors, next to phonons, the scattering with free charge carriers needs to be taken into account. As outlined in previous sections, the presence of free electrons or holes can lead to the formation of bound trions or attractive Fermi polarons. However, excitons can also interact with electrons without forming a bound state. Particularly, the exciton-electron scattering manifests in the exciton/repulsive Fermi polaron linewidth. It should be noted, that due to comparably low trion oscillator strengths, the radiative broadening of the trion is negligible at low carrier densities. In Fig. 2.10 (a), the qualitative dependence of the exciton non-radiative linewidth broadening is plotted as function of Fermi energy at cryogenic temperatures [45, 46, 112]. At zero doping the linewidth is

determined by the scattering with phonons, defects or radiative broadening. With increasing density, the carrier-induced linewidth broadening is found to approximately linearly increase with the free electron or hole concentration. In stark contrast, the trion linewidth hardly depends on the free carrier concentration and only slowly increases at elevated carrier densities.

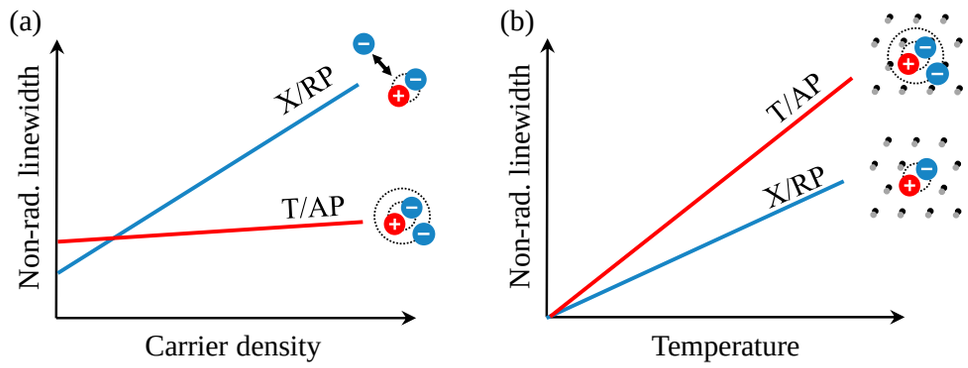

Figure 2.10: (a) Qualitative dependence of exciton/repulsive Fermi polaron (X/RP) and trion/attractive Fermi polaron (T/AP) non-radiative linewidth as function of free carrier density at cryogenic temperatures. (b) Qualitative dependence of the X/RP and T/AP non-radiative linewidth as function of temperature where the trion-phonon scattering is dominated by linear acoustic phonons ($T \lessapprox 50$ K).

The carrier-induced exciton linewidth comprises two major contributions: the scattering into a bound trion state and exciton-electron scattering where the exciton remains an exciton after the interaction. Both processes approximately linearly increase with the doping density and thus lead to an increase of the exciton linewidth. In the case of trions, the up-scattering to an excitonic state is suppressed due to large trion binding energies, i. e., at cryogenic temperatures and trion binding energy in the range of several 10's of meV the thermal energy of the trion is insufficient to ionize. Furthermore, trion-electron scattering is less efficient compared to exciton-electron scattering due to a larger trion mass. In an estimation based on energy and momentum conservation, the final kinetic energy $E_{\mathrm{X,kin'}}$ of an exciton with mass $m_X = m_e + m_h$ after scattering with an electron in rest with mass m_e, is given by

$$E_{\mathrm{X,kin'}} = \left(1 - \frac{2m_X m_e}{m_X^2 + m_e^2}\right) E_{\mathrm{X,kin}} \tag{2.9}$$

with the initial kinetic energy of the exciton $E_{\mathrm{X,kin}}$. In the limiting case of $m_X = m_e$, it follows that $E_{\mathrm{X,kin'}} = 0$, i. e., the total energy is transferred to the electron.

In the case of $m_X \gg m_e$, almost no energy is transferred, i. e., $E_{\mathrm{X,kin}'} \approx E_{\mathrm{X,kin}}$. Consequently, replacing the exciton by the heavier trion, less energy is transferred and the scattering is less efficient. In the particular case of TMDCs with $m_X \approx 2m_e$ and $m_T \approx 3m_e$, the final exciton kinetic energy is $E_{\mathrm{X,kin}'} = 0.2E_{\mathrm{X,kin}}$, whereas for the trion it is $E_{\mathrm{T,kin}'} = 0.4E_{\mathrm{T,kin}}$.

The suppressed trion-electron scattering can also be understand with respect to its effective charge. It is much less likely that an electron comes into the vicinity of a charged trion, as it gets repelled by long-range Coulomb interaction. Differently, the long-range Coulomb interaction between an effectively charge-neutral exciton and an electron is suppressed so that an electron can come comparably close to the exciton. Being close enough to the exciton, the electron strongly scatters with the exciton due to short-range Coulomb interaction.

While the carrier-induced trion linewidth broadening is negligible at low carrier densities, the trion linewidth is mostly governed by the interactions with phonons. As trion-phonon scattering roots in the coupling of the underlying electrons and holes to the phonons, the larger number of constituting particles in a trion results in a stronger trion-phonon coupling than in the case of excitons. As discussed above, the phonon coupling manifests in the temperature-dependent linewidth broadening (at low carrier densities the radiative broadening of the trion is negligible due to weak trion oscillator strengths). As schematically illustrated in Fig. 2.10 (b), the low-temperature linewidth increase $\propto \gamma T$ is stronger for the trion compared to the exciton [214].

Next to the symmetric broadening, the trion linewidth exhibits an additional low-energy flank attributed to the recombination of high-momentum trions. Similar to the phonon-assisted recombination of excitons, trions can recombine electron-assisted. Particularly, a high-momentum trion outside the light-cone can recombine by transferring its momentum to the remaining electron. This process results in a low-energy flank as the recombination energy is reduced by the energy transferred to the electron. This effect is called the *electron recoil effect* [77] and will be discussed in detail in chapter 4.

The electron-assisted recombination plays a particularly important role for dark states. In an electron-doped monolayer WSe_2, an exciton in the inter-valley K-K' state (I^0) can make a fast transition to the energetically favorable intra-valley spin-forbidden K-K exciton (D^0) due to exchange interaction [186], cf. Fig. 2.11 (a). By contrast, in a neutral semiconductor the transition between ground state K-K and K-K' excitons is strongly suppressed as a spin-flip is required. Particularly,

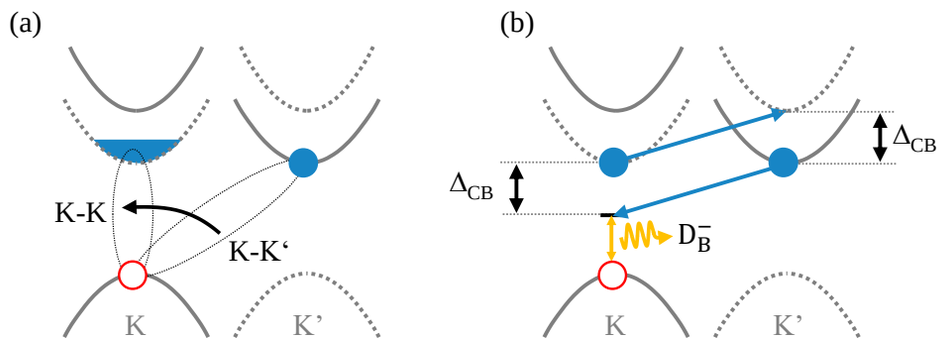

Figure 2.11: (a) Schematic illustration of the electronic band structure of monolayer WSe_2 indicating the inter-valley K-K' exciton state (I^0) consisting of an empty valence band state (hole) at K and an electron at the bottom K' valley. In the presence of electron doping in the lower K valley, the indirect K-K' exciton can scatter into the energetically favorable intra-valley K-K state (D^0) due to efficient exchange interaction. (b) Schematic illustration of the electron-assisted recombination process of dark D^- trions consisting of an empty electron in the valence band at K, a conduction band electron at K and the other one at K'. Fulfilling energy and momentum conservation, the indirect excitonic component can recombine leaving behind an electron at the upper conduction band at K' (inter-valley spin-conserving transition). The energy of the transition is reduced by the conduction band energy splitting Δ_{CB} compared to the direct transition of the D^- trion.

the formation of $I^{\pm}$ trions, i. e., trions consisting of an K-K' inter-valley excitonic core and an electron/hole at K are not observed [213, 37].

Another peculiar electron-assisted recombination pathway gives rise to the D_B^- emission, a replica of the D^- trion. The latter is composed of an intra-valley excitonic core at K-K and an electron at K'. One possibility to recombine is that the intra-valley excitonic core recombines in out-of-plane polarization (similar to the D^0 exciton). This recombination path gives rise to the D^- emission peak. Alternatively, the indirect component (the hole at K and the electron at K') recombines resulting in the D_B^- emission. In order to fulfill energy and momentum conservation the electron at K scatters to the upper K' valley [215, 216, 186], cf. Fig. 2.11 (d). Consequently, the emission energy of the D_B^- is reduced compared to the D^- emission by the energy splitting of the conduction band Δ_{CB}. This allows to estimate the conduction band splitting from photoluminescence experiments. In hBN-encapsulated monolayer WSe_2 the splitting is found to be $\approx$ 15 meV [186], consistent with an alternative analysis based on relative energy separations

between X^0, D^0 and I^0 and their estimated binding energies (taking into account effective masses and electron-hole exchange interaction) [186].

As the discussed phonon- and electron-assisted recombination processes are comparably inefficient, dark states exhibit lifetimes on the order of nanoseconds [54], much larger than directly recombining bright excitons. As a direct consequence, dark states allow for the investigation of exciton and trion dynamics on sufficiently long time scales. Importantly, it has been shown that the relaxation dynamics in monolayer TMDCs occur on much faster time scales [217, 218]. In particular, within the first picoseconds the excitons are intra-valley thermalized and can be approached by Boltzmann statistics, i. e., they are described by an effective exciton temperature. Within a few 10's of picoseconds the excitons cool down to lattice temperature [107, 108]. Consequently, dark excitons are at lattice temperature during the majority of their lifetime [107]. This opens the possibility to explore exciton dynamics at a well-defined, constant exciton temperature. Dark excitons allow for the investigation of Auger-recombination [219], brightening mechanisms [220], exciton to trion conversion [221], or to study propagation phenomena which are going to be introduced from a more general perspective in the next section.

2.6 Exciton propagation

In this section the fundamentals of exciton propagation are introduced. In this context, the diffusion coefficient D plays an important role. The diffusion coefficient is defined as a measure of the random motion of particles in space driven by their distribution gradient and gives access to their intrinsic ability to move. For example, exciting excitons by a focused laser, the larger concentration within the excitation area drives an effective exciton drift towards the area outside the excitation area where no excitons reside. In a simplified picture, the described scenario is approached by Fick's second law of thermodynamics

$$\frac{\partial n(\mathbf{x},t)}{\partial t} = D\nabla^2 n(\mathbf{x},t), \tag{2.10}$$

with the exciton distribution density $n(\mathbf{x},t)$, second spatial derivative ∇^2, spatial coordinates $\mathbf{x}$ and time t. The generalized differential equation describing exciton propagation in the presence of Auger-like recombination and external forces is presented in section 3.6.

For charged particles, the diffusion coefficient is directly connected to the mobility μ by the Einstein-Smoluchowski relation

$$\mu = \frac{qD}{k_b T} \tag{2.11}$$

with charge q, Boltzmann constant k_B and temperature T. In order to compare exciton dynamics determined from optical experiments to transport experiments, the mobility of an effectively charge-neutral exciton is often estimated by setting $q = e$ in Equation 2.11, with e being the elementary charge.

In two-dimensional TMDCs excitons exhibit strong binding energies rather typical for Frenkel-like excitons but are characterized by a wave function which spreads over many lattice atoms, a hallmark of Wannier-Mott like excitons (see also section 2.2). The propagation of Frenkel-like excitons is often characterized by localization and inter-site hopping [5, 222], whereas the spatial dynamics of Wannier-Mott-like excitons are often described in a band-like picture where the exciton freely moves between individual scattering events [223]. For an overview, the two conceptually opposing transport regimes are briefly outlined in the next section.

2.6.1 Hopping and band-like propagation

Various electronic coupling mechanisms enable excitons to move in a crystal by a finite microscopic increment resulting in a macroscopic, cascade-like long-range energy transport. The underlying mechanisms can be very different and largely depend on the individual material properties [224]. In many materials carriers are locally trapped e. g. on a molecule or defect site in a crystal. Due to high energy barriers, carriers reside on individual sites most of the time. Only occasional transitions termed as hopping contribute to an effective energy transport. Fig. 2.12(a) schematically illustrates hopping of excitons between neighboring sites separated by a distance d. The coupling between two sites is often mediated by Förster resonance energy transfer (FRET) [225], i. e., dipole-dipole electromagnetic interaction, Dexter coupling [226], where the carrier tunnels from one site to another or by phonons. Hopping-like transport has been observed most prominent in organic materials such as 3D metal halide perovskites [227] or colloidal quantum dot materials [228]. A similar transport behavior can be observed in inorganic semiconductors. Particularly, in low-dimensional systems with high defect densities and interface roughness scattering, carriers often localize [10]. Defect-assisted localization has been observed e. g. for excitons in many quantum well systems [10, 81, 82, 83].

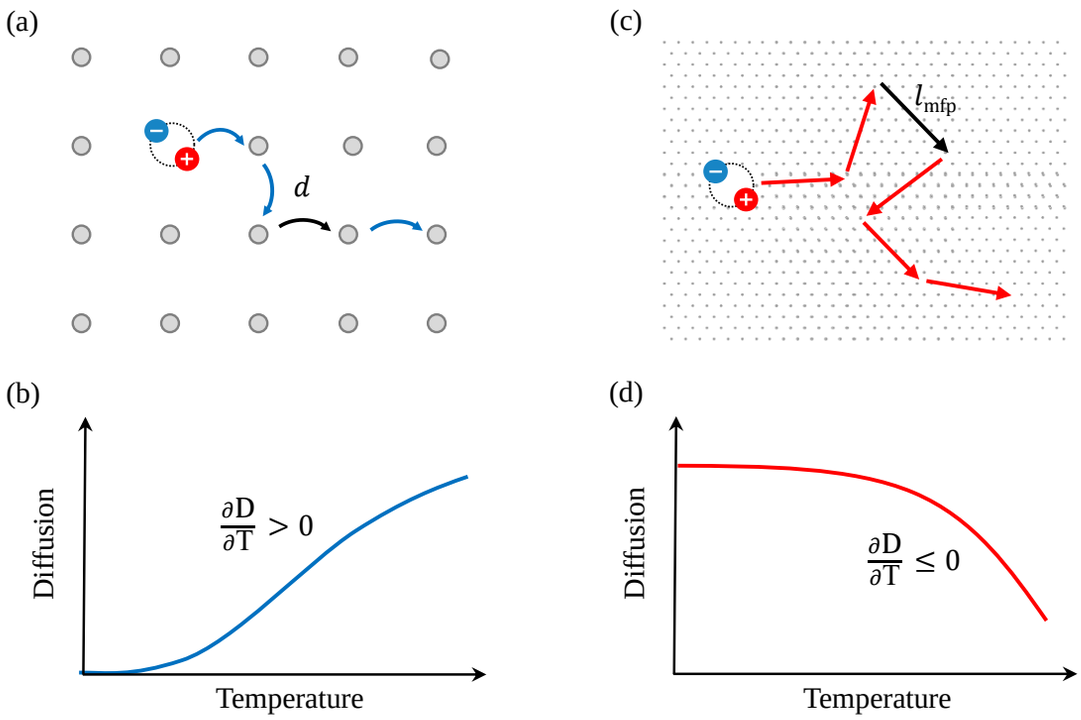

Figure 2.12: (a) Schematic illustration of exciton propagation in the regime of hopping. Excitons occasionally hop from one site to another. The transition rate depends on the inter-site distance d. (b) Qualitative dependence of the exciton diffusion coefficient as function of temperature if the propagation is mediated by hopping. The diffusion coefficient *increases* with temperature, i. e., $\partial D/\partial T > 0$. (c) Schematic illustration of semiclassical band-like diffusion. The exciton ballistically propagates between two scattering events. The average length between two scattering events is defined as the mean free path l_{mfp}. (d) Qualitative dependence of the semiclassical diffusion coefficient as function of temperature if the propagation is limited by scattering with temperature-activated phonons. The diffusion coefficient remains constant or *decreases* with temperature, i. e., $\partial D/\partial T \leq 0$.

By contrast, at elevated temperatures in most metals and inorganic semiconductors but also in some single molecule organic crystals [229], carrier transport is described in a semiclassical band-like (wave-like) picture. Herein, the particle freely propagates through the crystal between individual scattering events [224]. In Fig. 2.12(b), semiclassical exciton transport is schematically illustrated. The kinetics are characterized by a series of segments, where the particle ballistically moves in space on a length scale defined as the mean free path l_{mfp} between two scattering events. The semiclassical diffusion coefficient is given by

$$D_{sc} = \frac{k_B T}{m_X} \times \tau_s. \tag{2.12}$$

Here, m_X is the exciton mass, $\tau_s = \hbar/\Gamma$ is the scattering time and $k_B T$ is the thermal energy of the excitons.

While both, hopping and semiclassical free propagation leads to an effective energy transport, their dynamics are governed by an opposing temperature dependence [230]. In the case of localized states, the diffusion coefficient increases with temperature as qualitatively presented in Fig. 2.12(c). While at low temperatures the carriers hardly propagate, with increasing thermal activation energy it becomes more and more likely to overcome the energy barrier between neighboring sites and the diffusion coefficient increases. Depending on the specific properties of the underlying material system, various quantitative models have been derived to describe temperature-dependent hopping, e. g. presented in Refs. [231, 232, 233]. By contrast, in the semiclassical picture the diffusion coefficient is constant or decreases with temperature. Considering that the scattering time at cryogenic temperatures is determined by linear acoustic phonons, the scattering time inversely scales with temperature $\tau_s \propto T^{-1}$ (see also section 2.5) and the diffusion coefficient in Equation 2.12 becomes temperature-independent. At higher temperatures (T > 50 K), the additional scattering with high-energy phonons leads to a decrease of the diffusion coefficient. In this regime, experimentally observed diffusion coefficients scale with $D(T) \propto T\mu(T) \propto T^{-n+1}$ with n reaching values of up to 3 [230]. The qualitative temperature dependence of the diffusion coefficient in the semiclassical picture is presented in Fig. 2.12(d).

2.6.2 Weak localization and quantum interference

This section provides an intermediate propagation regime where the full quantum nature of the exciton is taken into account. The excitons are considered to freely propagate, but different to the above presented semiclassical picture, their wave-like behavior is explicitly taken into account. Due to constructive interference of the particle's wave function in space, the exciton effectively localizes. This effect is called weak localization [234, 235, 236, 237, 238, 88, 239] and is a precursor of strong Anderson localization [240, 241]. Following Ref. [109], the prerequisites for this transport phenomenon is outlined for excitons in two-dimensional TMDCs.

In the semiclassical picture the exciton is considered to be a point-like particle and the mean free path l_{mfp} exceeds the de Broglie wavelength λ_{dB}, i. e.,

$$l_{\mathrm{mfp}} \gg \lambda_{\mathrm{dB}}. \tag{2.13}$$

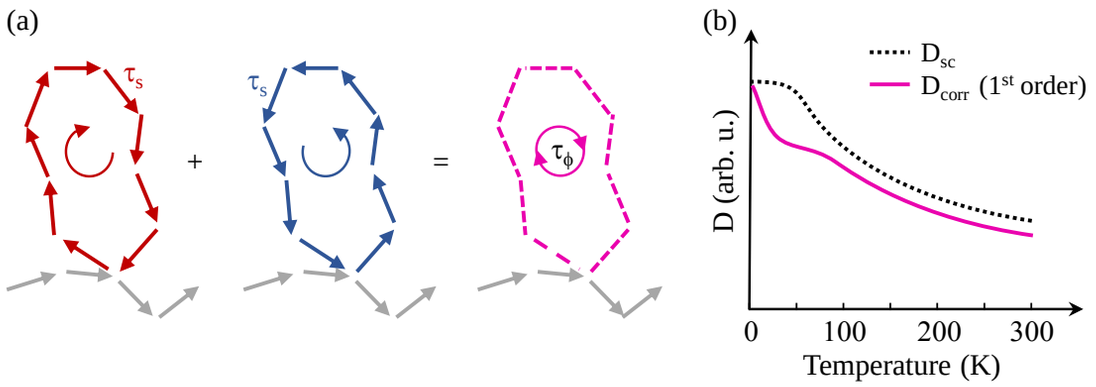

Figure 2.13: (a) Schematic illustration of constructive interference of clockwise and anti-clockwise propagating exciton wave packets. The arrows indicate propagation between two quasielastic scattering events. The strength of the interference is governed by the phase relaxation time τ_ϕ, i. e., the time after the interference is broken. $\tau_s \ll \tau_\phi$ is the scattering time. (b) Qualitative temperature-dependence of the diffusion coefficient considering a first order quantum correction of the semiclassical diffusion coefficient $D_{\text{corr}} = D_{\text{sc}} - \delta D$. D_{sc} is the semiclassical diffusion coefficient determined by the scattering with phonons and δD is the correction due to the wave-like nature of the exciton.

However, for excitons in monolayer TMDCs, Equation 2.13 is not strictly fulfilled. Recent experiments demonstrate mean free paths comparable to the exciton radius and the de Broglie wavelength [61]. In a first approximation, the impact of the wave-like nature of the exciton on its propagation is approximated by considering interference of the exciton's de Broglie waves in closed trajectories. If the interference of forward and backward traveling waves is constructive, a standing wave builds up. Thus, the exciton spends more time in the loop and effectively localizes. The scenario is schematically depicted in Fig. 2.13(a). The diffusion coefficient is reduced compared to its semiclassical value D_{sc} given by Equation 2.12. The interference depends on the phonon scattering time τ_s and phase relaxation time $\tau_\phi \gg \tau_s$. The phase relaxation time is the time after clockwise and anti-clockwise waves are out of phase. Importantly, it is not the dephasing time after (resonant) excitation which is typically given by the scattering time τ_s. In a first-order perturbation theory the corrected diffusion coefficient is given by [109]

$$D_{\text{corr}} = D_{\text{sc}} - \delta D = D_{\text{sc}} - \frac{\hbar}{2\pi m_X} \ln\left(\frac{\tau_\phi}{\tau_s}\right). \tag{2.14}$$

At low temperatures, the exciton-phonon interaction is determined by quasielastic acoustic phonons and the effective potential field created by the phonons

is almost static. Particularly in monolayer TMDCs, the mean exciton velocity between two scattering events is much larger than that of the phonons. While the exciton reaches a mean speed of ≈ 40 km/s ($v_{\mathrm{mfp}} = l_{\mathrm{mfp}}/\tau_s$) [61], the phonons travel with a velocity of 3.3 km/s [242]. In this case, τ_ϕ is basically limited by the energy uncertainty $\delta\epsilon(\tau_\phi) \times \tau_\phi \approx \hbar/2$. Here, $\delta\epsilon(\tau_\phi)$ denotes the exciton energy variation determined by the exciton-phonon scattering while propagating in the loop. It means that the phase is lost if the energy uncertainty over time τ_ϕ is similar to $\hbar/(2\tau_\phi)$. The phase relaxation time is given by [109]

$$\tau_\phi = \left(\frac{\hbar^2 \tau_0^2}{(k_B T)^2} \right)^{1/3} \tag{2.15}$$

with τ_0 being a constant related to the strength of the exciton-phonon coupling. Considering that the scattering time inversely scales with temperature in the case of acoustic phonon scattering (see section 2.5) the correction term δD increases with temperature $\propto \ln(T^{1/3})$. Despite both, the phase relaxation and scattering time decrease, their ratio and therefore the correction becomes larger with increasing temperature. Taking into account *inelastic* scattering with high-energy phonon modes at higher temperatures, the phase relaxation time reduces and the weak localization effect is hampered [243]. In Fig. 2.13(b), the qualitative temperature-dependent of the corrected diffusion coefficient D_{corr} is presented as function of temperature. The quantum correction is strongest at cryogenic temperatures where quasielastic scattering with acoustic phonons dominate [243]. Interestingly, it exhibits a qualitatively different temperature dependence compared to the semi-classical diffusion. At cryogenic temperatures T $<$ 50 K, the semi-classical diffusion coefficient is constant, while the corrected diffusion coefficient decreases with temperature.

In the presence of free charge carriers the quantum correction is expected to become negligible, as the exciton-electron scattering is highly inelastic. Due to the twice as high exciton mass compared to the free charge carrier mass, the exciton transfers the majority of its kinetic energy to the electron (see also Equation 2.9). Only at elevated temperatures and low electron densities quantum corrections on the exciton transport may be relevant [243].

Having outlined the prerequisites for quantum interference effects on exciton propagation, the pertinent question is whether these phenomena can be experimentally accessed. Electrically-tuneable hBN-encapsulated monolayer TMDCs fulfill all necessary conditions to study these effects. As outlined in this chapter, monolayer TMDCs

- are characterized tightly-bound excitons with strong light-matter coupling
- exhibit strong exciton-phonon and exciton-electron interactions
- comprise long-lived dark exciton and trion reservoirs which allow for the investigation of quasiparticle propagation in a thermalized system cooled down to lattice temperature

Following the current state of research, the main scope of this work is the experimental investigation of exciton-carrier interactions and their propagation dynamics which will be presented in chapter 4 and 5. In the subsequent chapter 3, the required experimental methods are introduced.

Chapter 3

Experimental methods: sample fabrication and time-resolved microscopy

In this chapter the experimental methods are described. First, a brief overview of the sample fabrication as well as an introduction to the spectroscopy setup is given, focusing on reflectance contrast and photoluminescence spectroscopy. Subsequently, a description of spatio-temporal monitoring of exciton diffusion is presented. The chapter is concluded by a basic characterization of the investigated electrically-tuneable TMDC structures.

3.1 Micro-mechanical exfoliation of van der Waals crystals

In this work, monolayer semiconductors are investigated which are embedded in heterostructures consisting of several thin layers of van der Waals crystals. The considered structures comprise single sheets of conductive few layer graphene (FLG), insulating hexagonal boron nitride (hBN) and semiconducting monolayer WSe_2 as well as monolayer $MoSe_2$. In a typical sample structure, a monolayer WSe_2 or $MoSe_2$ flake is sandwiched between two thin layers of hBN placed on a SiO_2/Si substrate (d_{SiO_2} = 290 nm). The graphite layers serve as electrical contacting. Electrically-tuneable samples are introduced in section 3.8. The individual layers are mechanically exfoliated from high-quality bulk crystals and subsequently stamped on top of each other, either by an all-dry visco-elastic polydimethylsiloxan-mediated (PDMS) stamping process or a polycarbonate (PC) pick-up transfer. The chemically synthesized WSe_2, $MoSe_2$ and graphite bulk crystals have been commercially purchased from *HQGraphene*. In case of hBN,

artificially grown crystals by Takashi Taniguchi and Kenji Watanabe from the National Institute of Materials Science in Tsukuba (Japan) are employed. The exfoliation and assembly was performed by Jonas David Ziegler.

The majority of the investigated structures are fabricated by a PDMS-mediated stamping process following Ref. [244]. In a first step, (atomically) thin layers are cleaved and exfoliated by pulling off an adhesive tape (Nitto Denko Corporation) from the considered bulk crystals. The individual layers are then transferred to visco-elastic PDMS from which they are subsequently stamped on top of each other on a cleaned and preheated 70°C SiO_2/Si substrate. Between each transfer step, the structure is annealed to 150°C for 1 to 3 hours. The stamping procedure is schematically illustrated in Fig. 3.1 (a). Alternatively, the individual layers are

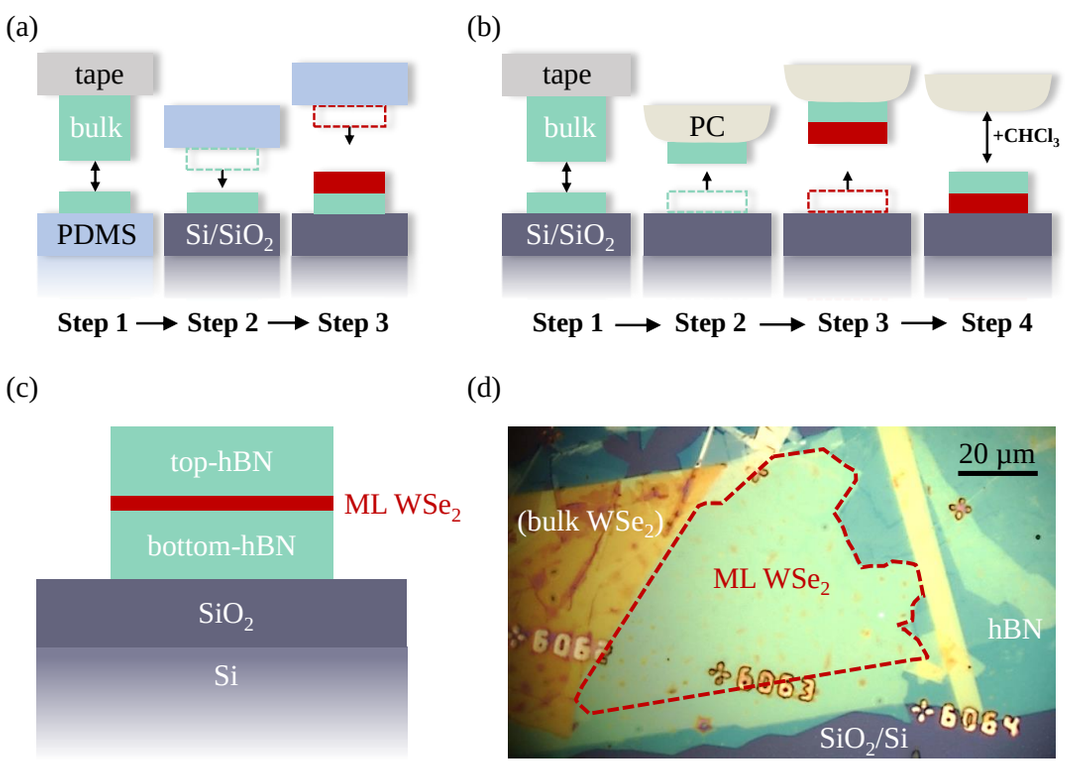

Figure 3.1: Step by step illustration of the exfoliation and transfer procedure in the (a) PDMS-mediated stamping transfer and (b) PC pick-up transfer. The process is depicted for a structure consisting of two layers. (c) Schematic cross-section of a hBN-encapsulated WSe_2 monolayer on a SiO_2/Si substrate. (d) Micrograph of an hBN-encapsulated WSe_2 monolayer on SiO_2/Si. The monolayer flake is indicated by the area surrounded by red dashed lines.

picked up by a PC-coated PDMS stamp at a temperature of 125°C following a slightly modified approach presented in Ref. [245]. The advantage of this method is that only the first layer gets in contact with the PC whereas all following layers

are directly picked up by the previous layers. Therefore, adsorbates between the individual layers are reduced. The complete stack, consisting of the multi-layer structure and the PC stamp is then released on the SiO_2/Si substrate. In a last step, the PC stamp is melted at 175°C and dissolved in chloroform. A schematic step-by-step illustration of the pick-up method is depicted in Fig. 3.1 (b). Fig. 3.1 (c) shows a schematic sample cross-section. In Fig. 3.1 (d), a micrograph of a hBN-encapsulated monolayer WSe_2 structure on a SiO_2/Si substrate is presented.

3.2 Spectroscopy setup

In this section, the spectroscopy setup is introduced. Fig. 3.2 shows a schematic overview of the setup which is structured in three units. The excitation sources on the left, the microscope with the sample in the center and the detection unit consisting of an imaging spectrometer with a CCD and a streak camera as detectors on the right. The sample is optically excited either by a broad-band quartz-tungsten halogen (QTH) lamp for reflectance measurements, a continuous wave (CW) diode-pumped solid state (DPST) laser with a wavelength of 532 nm for steady-state photoluminescence measurements, or a pulsed 140 fs Ti:Sapphire laser with a repetition rate of 80 MHz and continuously tuneable wavelength range for time-resolved measurements. In the microscope, the incident light is focused by a 60× objective (NA= 0.7) to a spot diameter of approximately 1 μm on the sample (in case of the QTH lamp the spot diameter is 2 μm). The sample is fixed in a continuous-flow microscope cryostat mounted on a x-y micrometer stage. During measurements, the sample is cooled down by liquid Helium to a nominal heat sink temperature of 4.2 K. The temperature at the sample is continuously adjusted up to room temperature by a built-in electric heater. The majority of the experiments discussed in this thesis are performed at temperatures between 5 and 50 K. After passing neutral density and spectral band pass filters, the reflected or emitted light is guided to the spectrometer. For spectral detection, the light is focused by a lens on a 300 gr/mm or 1200 gr/mm grating. For spatial imaging, the grating is replaced by a mirror. The light is finally detected by a Peltier-cooled CCD camera or a Hamamatsu streak camera. The latter is triggered by the oscillations of the Ti:Sapphire laser.

In the following sections the individual measurement procedures are presented in detail. In particular, an overview of reflectance and photoluminescence spectroscopy is given followed by the description of spatio-temporal measurements of exciton diffusion.

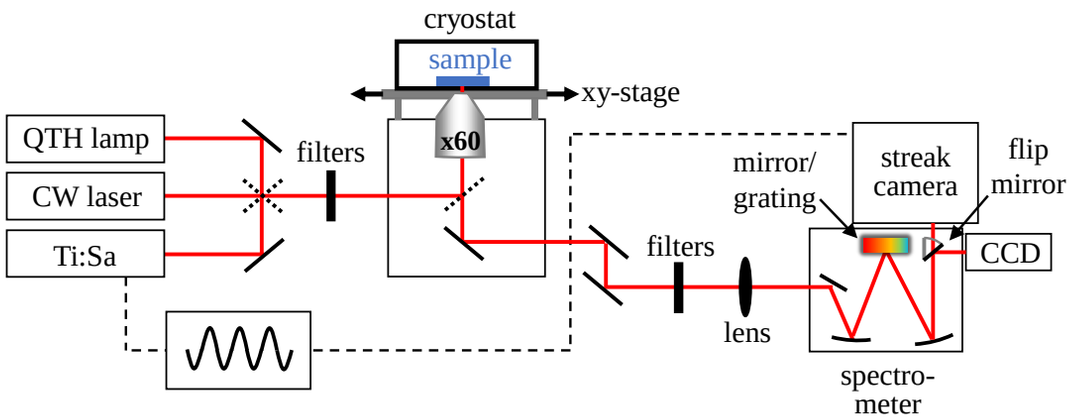

Figure 3.2: Schematic illustration of the spectroscopy setup. The excitation beam from a QTH lamp, CW laser or pulsed Ti:Sa laser is focused on the sample, which is fixed in the microscope cryostat mounted on a x-y stage. The reflected and/or emitted light is guided to the spectrometer and imaged by a CCD camera or a streak camera detector, which is synchronized by the oscillations of the Ti:Sa laser.

3.3 Reflectance spectroscopy

For the optical characterization of the investigated monolayer structures including the determination of exciton resonance energies, linewidths and oscillator strengths, reflectance experiments are performed. The sample structure is illuminated by a broad-band QTH lamp focused on a spot with full-width at half-maximum (FWHM) of ≈ 2 μm. The total incident power is set to few 100's of nW. At this power the linear response of the system is probed and non-linear density effects are excluded. The reflected light is dispersed by a grating and subsequently detected by the CCD camera. The integration time is set to 0.3 to 1.8 seconds per frame. In order to increase the signal-to-noise ratio, 100 individual frames are averaged for a single spectrum. Fig. 3.3 (a) shows a typical as-measured reflectance spectrum R_s of a hBN-encapsulated WSe_2 monolayer on a SiO_2/Si substrate (Si/SiO_2/hBN/WSe_2/hBN) in the energy range of the X^0 exciton at a nominal heat sink temperature of T = 5 K. While the overall shape is determined by multi-layer interference effects, the spectrum exhibits pronounced features around the exciton ground state (1s) at 1.72 eV and excited state (2s) at 1.86 eV. For comparison, a reference spectrum R_{ref} on a nearby position without the monolayer (Si/SiO_2/hBN) is recorded. In contrast to the spectrum with the monolayer, it does not show any excitonic features. In Fig. 3.3 (b), the reflectance contrast $R_c = (R_s - R_{\mathrm{ref}})/(R_{\mathrm{ref}} - \mathrm{BG})$ is plotted, with BG being the background

signal obtained while blocking the QTH lamp. In Fig. 3.3 (c), the derivative of the reflectance contrast $\partial R_c/\partial E$ is presented.

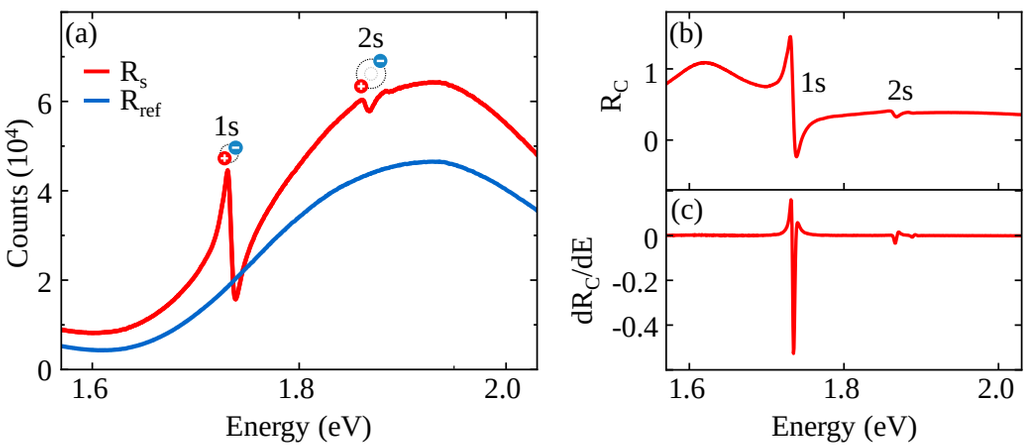

Figure 3.3: (a) Reflectance spectra R_s of hBN-encapsulated WSe_2 monolayer on SiO_2/Si and the reference spectrum R_{ref} without the monolayer on a nearby position with only one layer hBN on SiO_2/Si. The spectra are plotted in a typical energy range of the ground state 1s and excited state 2s, 3s, ... X^0 exciton at T = 5 K. (b) Reflectance contrast spectra calculated from the spectra presented in (a). (c) Derivative $\partial R_c/\partial E$ of the reflectance contrast spectrum shown in (b).

For a quantitative extraction of resonance energies, linewidths and oscillator strengths, the recorded reflectance contrast spectra are fitted by a transfer matrix model parameterized by individual Lorentzians for each resonance. The transfer matrix model is required as the sample structure consists of several layers with different refractive indices which lead to multi-layer interference between absorbed (A), transmitted (T) and reflected (R) light. In general, the interference results in modified spectral features, including variations in the resonance energies and linewidth broadening. To incorporate these effects, the reflectivity is modeled by a transfer matrix model based on a customized *MATLAB* (Mathworks) script which was developed by Steve Byrnes [246] and implemented by Jonas Zipfel [247]. The general approach is briefly outlined along the lines of Refs. [246] and [247].

Considering a multi-layer system which consists of N individual layers j, the forward traveling light amplitude v_j and backward traveling amplitude w_j at each layer boundary is calculated by

$$\begin{pmatrix} v_j \\ w_j \end{pmatrix} = M_j \begin{pmatrix} v_{j+1} \\ w_{j+1} \end{pmatrix}$$

with the transfer matrix M_j. Considering unpolarized light perpendicular to the sample structure (zero angle approximation), the transfer matrix for a boundary between two adjacent layers j and $j+1$ reads [246]

$$M_j = \begin{pmatrix} e^{-i\delta_j} & 0 \\ 0 & e^{i\delta_j} \end{pmatrix} \begin{pmatrix} 1 & \frac{2n_j}{n_j+n_{j+1}} \\ \frac{n_j-n_{j+1}}{n_j+n_{j+1}} & 1 \end{pmatrix} \frac{n_j+n_{j+1}}{2n_j}.$$

Here, n_j and n_{j+1} denote the individual refractive indices of two neighboring layers j and $j+1$. δ_j is the relative phase collected while propagating through the layer. Note that i is the imaginary unit and not an index. δ_j depends on the individual layer thickness d_j as well as wavelength λ and is determined by $\delta_j = 2\pi n_j d_j/\lambda$. For the semi-infinite first layer $\delta_1 = 0$ is considered. For the last semi-infinite layer $j = N$ no matrix is required. The total matrix of the structure is given by multiplying the individual matrices

$$M_{\mathrm{tot}} = M_1 \times M_2 \times M_3 \times ... \times M_{N-1}. \tag{3.1}$$

the total reflected light is given by

$$\begin{pmatrix} 1 \\ r_{\mathrm{tot}} \end{pmatrix} = M_{\mathrm{tot}} \begin{pmatrix} t_{\mathrm{tot}} \\ 0 \end{pmatrix}.$$

Here it is assumed that the initial amplitude $v_1 = 1$ and that no light is coming from the last layer. The total reflectance of the multi-layer stack is given by $R = |r_{\mathrm{tot}}|^2$. The total transmittance T is proportional to $|t_{\mathrm{tot}}|^2$. For an exact expression of T, the Poynting vector needs to be calculated, as e. g. demonstrated in Ref. [246].

In order to match the experimental spectra, the modeled reflectivity R with complex refractive indices from literature is adjusted by fitting the individual layer thicknesses d_j. The dielectric function of the monolayer $\epsilon_{\mathrm{ML}} = n_{\mathrm{ML}}^2$ is approximated by

$$\epsilon_{\mathrm{ML}} = \epsilon_\infty + \sum_k \frac{f_k}{E^2(\lambda) - E_k^2 - iE\Gamma_k}$$

consisting of Lorentzians in the range of optical transitions with e. g. exciton resonances $k = 1\mathrm{s}, 2\mathrm{s}, ...$, the background dielectric constant of the monolayer ϵ_∞, as well as resonance energies E_k, dephasing Γ_k (corresponding to the non-radiative linewidth) and oscillator strength f_k being free fit parameters.

The presented transfer matrix approach enables the accurate determination of resonance energies, non-radiative linewidths and oscillator-strengths and gives an estimate of the layer thicknesses d_j of the investigated structures. By fitting the measured reflectance contrast spectrum of a sample structure with known layer configuration, the extracted layer thicknesses agree with an accuracy of approximately 5 to 10 nm with layer thicknesses determined from atomic force microscopy (AFM) measurements. Furthermore, the model allows to calculate the absorption $A = 1 - R - T$, which is particularly relevant for the estimation of the optically-injected electron-hole pair density in photoluminescence experiments, discussed in the next section.

3.4 Photoluminescence spectroscopy

For continuous wave (CW) photoluminescence (PL) measurements, the sample is excited by a CW laser at a wavelength of 532 nm (2.331 eV). Similar to the reflectance measurements, the emitted PL is guided to the spectrometer where the light is dispersed and imaged on the CCD camera. To separate the emitted PL from the reflected and scattered laser light, a 550 nm long-pass filter is inserted in the optical path between microscope and spectrometer. For an individual spectrum, the integration time is set to a value between 10 to 400 seconds. The PL spectrum is obtained by subtracting the background signal with the laser source switched off from the sample spectrum.

The excitation power is adjusted by continuously-tuneable neutral density filters and determined by a wavelength-sensitive power meter. In this thesis, excitation powers range between 1 nW and 10 μW. The power density p is approximated by

$$p = P_0/(\pi r_{\text{eff}}^2) \tag{3.2}$$

with total (measured) power P_0 and effective excitation spot radius r_{eff}.

In the approximation in Equation 3.2 a cylindrical excitation profile is assumed. It particularly neglects the radial density dependence of the actual excitation profile of the focused laser, which exhibits a density maximum in the spot center and a decreasing density with increasing distance to the center. Depending on the definition of the effective radius, the actual density can be under- or overestimated. In literature, different definitions of r_{eff} are considered. In Fig. 3.4, three conventions rooting on a two-dimensional Gaussian density profile are compared. For example, setting the effective radius to the standard deviation $r_{\text{eff}} = \sigma$ would

result in an effective power density which is twice as high as the actual power density at the peak maximum. Also setting $r_{\mathrm{eff}} = \mathrm{FWHM}$ overestimates the maximum peak density by a factor of ≈ 1.5. A more realistic approximation yields the definition of the Gaussian beam waist, yielding an effective density half of the maximum peak density. In this work, the effective radius is chosen such that the effective density is *equal* to the maximum density at the spot center

$$r_{\mathrm{eff}} = \mathrm{FWHM}/(2\sqrt{ln(2)}). \tag{3.3}$$

Evaluating Equation 3.2 and Equation 3.3, an excitation power of 1 μW corresponds to a peak power density of 90 W/cm^2, taking into account an experimentally determined laser spot diameter of FWHM = 1 μm.

(a)

$\mathbf{r_{eff}}$	w	σ	$w_{Gb} = 2\sigma$
$n(r)$	$\frac{N_0}{\pi w^2}\exp(-\frac{r^2}{w^2})$	$\frac{N_0}{2\pi\sigma^2}\exp(-\frac{r^2}{2\sigma^2})$	$\frac{2N_0}{\pi {w_{Gb}}^2}\exp(-\frac{2r^2}{{w_{Gb}}^2})$
$\boldsymbol{n_{eff}/n_{max}}^*$	**1**	**2**	**0.5**
$\mathbf{FWHM/r_{eff}}$	$2\sqrt{\ln(2)}$ ≈ 1.6652	$2\sqrt{2\ln(2)}$ ≈ 2.3548	$\sqrt{2\ln(2)}$ ≈ 1.1744

*for $r_{\mathrm{eff}} = \mathrm{FWHM}/2$: $n_{\mathrm{eff}}/n_{\mathrm{max}} = 1/\ln(2) \approx 1.4427$

(b)

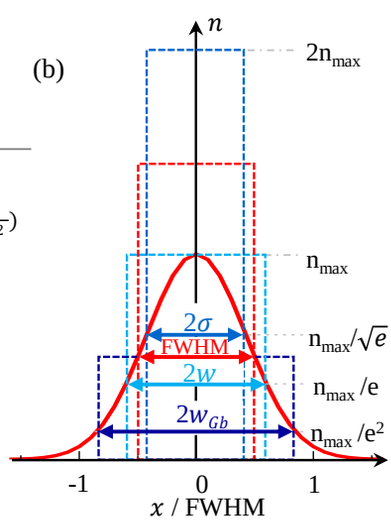

Figure 3.4: (a) Comparison of different definitions of the effective radius r_{eff} in a two-dimensional Gaussian function: the width w, the standard deviation σ and the beam waist w_{Gb}. The second row of the table shows the Gaussian distribution function $n(r) = n(\sqrt{x^2+y^2})$ represented by the different definitions of the effective radius. The profiles are normalized to $\iint n(\sqrt{x^2+y^2})dxdy = N_0$. In the third row, effective densities $n_{\mathrm{eff}}/n_{\mathrm{max}}$ in the cylindrical approximation $n_{\mathrm{eff}} = N_0/(\pi r_{\mathrm{eff}}^2)$ are summarized. $n_{\mathrm{max}} = n(x = 0, y = 0)$ is the maximum density in the peak center. In the fourth row, r_{eff} is compared to the FWHM. (b) Illustration of a two-dimensional Gaussian cross-section indicating the different definitions of r_{eff}. Dashed squares are cross-sections of the cylindrical profiles with radius r_{eff} normalized to $n_{\mathrm{eff}} \times \pi r_{\mathrm{eff}}^2 = N_0$.

Alternatively, the CW laser is replaced by a 140 fs pulsed Ti:sapphire laser with a repetition rate of $f_{\mathrm{rep}} = 80$ MHz. For most experiments on monolayer WSe_2 structures, the wavelength is tuned into resonance with the X^0 exciton at $E_{\mathrm{ph}} = 1.722$ eV. In analogy to Equation 3.2, the peak energy density per pulse is

given by $P_0/(f_{rep}\pi r_{eff}^2)$, with $r_{eff} = FWHM/(2\sqrt{ln(2)})$. The corresponding peak electron-hole pair density per pulse is approximated by

$$n_{eh} = \frac{P_0 \alpha^*}{f_{rep}\pi r_{eff}^2 E_{ph}} = \frac{4\ln(2) P_0 \alpha^*}{f_{rep}\pi FWHM^2 E_{ph}}, \tag{3.4}$$

with effective absorption α^*. As outlined in previous section, the energy-dependent absorption $A(E)$ is estimated from reflectance contrast measurements. Importantly, for the estimation in Equation 3.4, it is relevant to evaluate the absorption at the excitation energy E_{ph}. For example, at the ground state X^0 exciton resonance in hBN-encapsulated monolayer WSe_2, the absorption at the peak maximum can be as high as 60%, while exciting the sample 30 meV above, the absorption is only on the order of a few percent. The effective absorption is calculated by

$$\alpha^* = \frac{\int A(E)L(E)dE}{\int L(E)dE} \tag{3.5}$$

with the excitation profile $L(E)$, i. e., the spectral function of the laser. Notably, Equation 3.5 explicitly takes into account the spectral overlap of the excitation profile with the absorption $A(E)$.

For the measurements on monolayer WSe_2 structures presented in chapter 5, an effective absorption at the X^0 exciton of 30% is considered. Consequently, an excitation power of $P_0 = 1$ μW corresponds to a peak energy density of 1.1 $\mu J/cm^2$ and a peak electron-hole pair density of 1.2×10^{12} cm^{-2} per pulse (the spot diameter is set to FWHM = 1 μm). For the measurements on $MoSe_2$ structures presented in section 4.3, the excitation wavelength is tuned to 1.663 eV (slightly above the X^0 resonance at 1.642 eV) with an estimated effective absorption of 2%. Consequently, an excitation power of 1 μW corresponds to $n_{eh} = 8.3 \times 10^{10}$ cm^{-2}.

3.5 Asymmetric lineshape analysis

For the analysis of PL spectra, symmetric as well as asymmetric fit functions are applied. In the case of neutral excitons such as the bright X^0 and the dark D^0 emission, dephasing mechanisms such as radiative broadening, scattering with phonons and electrons result in a symmetric, homogeneous broadening which manifests in a Lorentzian emission profile. Inhomogeneities determined by e. g. local fluctuations of dielectric disorder or strain manifest in a Gaussian emission profile. To account for both, homogeneous and inhomogeneous broadening, a convolution of a Gaussian and a Lorentzian, i. e., a Voigt profile is applied.

Next to symmetric emission profiles, also asymmetric peaks are investigated. Particularly in this work, exciton phonon side bands and trions are fitted by a high- or low-energy exponential function convoluted with a Lorentzian profile. In case of phonon side bands, excitons with a finite center-of-mass momentum recombine via the assistance of high-energy phonons. Considering Boltzmann-distributed states, the phonon side band profile exhibits a *high*-energy flank. In case of high-momentum trions, the excitonic core radiatively recombines by transferring the momentum to the remaining electron (electron recoil effect) and the emission energy is reduced by the energy transferred to the electron. For Boltzmann-distributed trions the emission profile is characterized by a *low*-energy flank.

Consequently, the emission profiles of phonon side bands and trions are modeled by a convolution of an asymmetric exponential function, resembling Boltzmann-distributed high-energy states, and a symmetric Lorentzian, taking into account the symmetric broadening due to radiative dephasing and scattering. In case of a high-energy flank, the fit function is given by

$$\mathrm{PL}(E) = \mathrm{Lorentz}(E) \otimes \mathrm{Exponential}(E) \times \Theta(E - E_0) \tag{3.6}$$

$$= \frac{2A}{\pi} \frac{\Gamma}{4(E - E_0)^2 + \Gamma^2} \otimes \exp\left(-\frac{E - E_0}{\epsilon^*}\right) \Theta(E - E_0) \tag{3.7}$$

with amplitude A, center energy E_0, symmetric linewidth Γ and ϵ^* being a constant related to the asymmetry (for exciton phonon side bands it is $\epsilon^* = k_B T$). $\Theta(E - E_0)$ is the Heaviside function and $\otimes$ indicates the convolution. The function can be easily adjusted to the case of a low-energy flank by replacing $E \to -E$. Evaluating the convolution yields the following fit function

$$\mathrm{PL}(E) = \int_{-\inf}^{\inf} \mathrm{Lorentz}(\xi) \times \mathrm{Exponential}(E - \xi) \times \Theta(E - \xi - E_0) d\xi \tag{3.8}$$

$$= \int_{-\inf}^{E - E_0} \frac{2A}{\pi} \frac{\Gamma}{4(\xi - E_0)^2 + \Gamma^2} \exp\left(\frac{E - \xi - E_0}{\epsilon^*}\right) d\xi \tag{3.9}$$

The integral in equation 3.9 is evaluated numerically at each iteration step during the fit procedure. The latter is performed in an automatized *MATLAB* (Mathworks) script written by Jonas Zipfel. Compared to a simple Lorentzian or Gaussian function, the presented convolution fit exhibits only one additional free fit parameter ϵ^* (note that ξ is the integration variable due to the convolution and is not an additional fit parameter). Alternatively, the Lorentzian function entering in equation 3.9 can be replaced by a Voigt profile (which is equivalent to convo-

luting Equation 3.6 with an additional Gaussian function), relevant in the case of significant contributions of inhomogeneous broadening.

3.6 Time-resolved microscopy and diffusion

In this section, the procedure of time-resolved measurements is presented, considered for spectrally and spatially resolved studies. As an excitation source, the pulsed Ti:sapphire laser is applied, providing 140 femtosecond excitation pulses at a repetition rate of 80 MHz.

As in the above described CW PL experiments, the excitation laser is focused on the sample to a spot diameter of FWHM = 1 μm. The reflected and scattered laser light is blocked by a tuneable edge-pass filter and the excitonic emissions are guided to the spectrometer where the signal is either dispersed by a grating for spectral resolution, or reflected by a mirror for spatially-resolved diffusion experiments. Time-resolved detection is achieved by a streak camera which is synchronized to the excitation laser frequency. The principle of operation of a streak camera is briefly outlined as follows. First, incoming photons hit a photoscreen and are converted into electrons. Subsequently, the electrons are accelerated by a constant electric field. For a better signal to noise ratio, the amount of electrons is increased by a multi channel plate. In order to obtain time-resolution, the electrons are deflected by a time-dependent sinusoidal vertical electric field which matches the repetition rate of the Ti:sapphire excitation laser. As the electric field increases with time, earlier arriving electrons get less deflected than later arriving electrons. The electrons then hit a phosphor screen. Electrons which hit at the top and bottom correspond to earlier and later times. Finally, the phosphor screen is imaged by a C-MOS camera.

For spatially-resolved measurements, the light arriving in the spectrometer is reflected by the mirror and guided towards the streak camera detector. A slit before the streak camera collects the horizontal cross-section of the emitted PL. A lens is used to control the magnification, which is set to 7.2 pixel/μm on the C-MOS camera picture. In this configuration, the horizontal axis images the width of the emission cross-section and the vertical axis corresponds to its temporal evolution.

The time-resolved evolution of the PL cross section allows for direct monitoring of exciton propagation [61, 105]. As outlined in section 2.6, diffusive processes are described by Fick's second law of thermodynamics. For excitons in a real system, however, the evolution of the distribution density is more complex. The

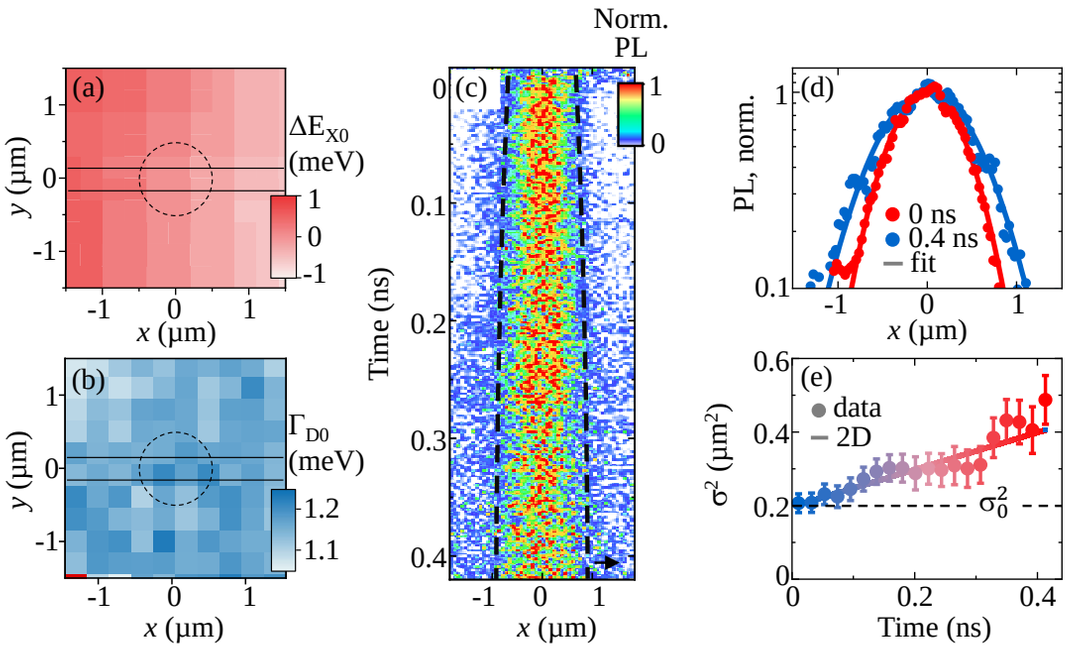

Figure 3.5: (a) Spatial mapping of the bright X^0 energy and (b) intra-valley dark exciton D^0 emission linewidth of a hBN-encapsulated WSe_2 monolayer in the area where diffusion measurements are performed. The excitation spot (dashed line) and the horizontal cross-section (solid line) considered for spatially-resolved measurements are schematically indicated. (c) Horizontal, normalized PL cross-section of dark exciton emissions in hBN-encapsulated monolayer WSe_2 as function of time, following pulsed excitation with a 140 fs Ti:sapphire laser at t = 5 K. The data is normalized at each time to the intensity maximum. The broadening is indicated by dashed lines (same data as in Fig. 5.2). (d) Normalized PL profiles at $t = 0$ and $t = 0.4$ ns extracted from (c). The data is fitted by Gaussians. (e) PL spot broadening as function of time represented by σ^2. The PL profile linearly broadens as function of time with respect to the initial spot size $\propto \sigma_0^2$. The diffusion coefficient D is determined from the slope divided by a factor of two.

generalized differential equation describing spatial exciton dynamics is given by [61, 62, 63, 248]

$$\frac{\partial n}{\partial t} = D\nabla^2 n - \frac{n}{\tau} - R_A n^2 - \alpha\nabla(\boldsymbol{f} n). \tag{3.10}$$

It contains four terms. The first term corresponds to Fick's second law and describes the spatial broadening due to the distribution gradient $\nabla^2 n$ which linearly scales with the diffusion coefficient D (see also Equation 2.10 in section 2.6). The second term takes into account a finite exciton lifetime τ. The third term considers Auger-like processes which scale with n^2 [61]. R_A is the Auger coefficient. The last term introduces a force $\boldsymbol{f}$ which additionally acts on the excitons. α is a

constant which typically depends on the temperature and diffusion coefficient D. The force can be external, e. g. due to a gradient, or induced by exciton interactions, e. g. due to exciton-exciton repulsion, particularly relevant for inter-layer excitons [249, 250, 104].

Different to interlayer excitons in heterostructures, where the constituting electrons and holes reside in different layers, in monolayer semiconductors exciton-exciton as well as trion-trion repulsion is negligible. Although trions are effectively charged particles, the Coulombic interaction between trions are not expected to contribute to a repulsion detectable in spatio-optical diffusion experiments. Trions are formed out of free charge carriers which are thermalized and evenly distributed in space and thus don't contribute to an additional drift.

In order to exclude external forces due to gradients, the diffusion experiments are performed at a sample position with flat energy landscapes. In Fig. 3.5 (a), the relative X^0 exciton energy fluctuation of a hBN-encapsulated monolayer WSe_2 is presented within a 3 x 3 μm^2 sample area where the majority of the diffusion measurements presented in section 5.1 are performed. The resonance energy shift of < 0.5 meV/μm indicates sufficiently flat energy landscapes with respect to thermal energies on the order of $k_B T \gtrapprox 0.5$ meV and expected exciton diffusion lengths on a sub μ-meter length scale. This is further confirmed by narrow emission linewidths of the D^0 exciton on the order of ≈ 1.1 meV, cf. Fig. 3.5 (b).

Evaluating Equation 3.10 in the absence of Auger-recombination, an initial Gaussian exciton distribution $\propto \exp(-r^2/(2\sigma_0^2))$ with radius σ_0 broadens with [61, 224]

$$\sigma^2 = 2Dt. \tag{3.11}$$

Here, D is the diffusion coefficient. Taking further into account a finite exciton lifetime τ, the diffusion length is given by $l_{\text{diff}} = \sqrt{2D\tau}$. Exemplary, in Fig. 3.5 (c) and (d), the temporal evolution of the emission cross-section of dark excitons in hBN-encapsulated monolayer WSe_2 at T = 5 K is presented. For a quantitative analysis, individual time intervals of $\Delta t = 20$ ps are fitted by Gaussian functions $f(x) \propto \exp(-x^2/(2\sigma^2))$. The corresponding area $\propto \sigma^2$ is plotted as function of time in Fig. 3.5 (e). Consistent with Equation 3.11, the distribution area increases linearly with time. The data is modeled by a line fit from which the diffusion coefficient is extracted by dividing the slope by a factor of two.

In Fig. 3.6(a), the spatial broadening of the emission cross-section, represented by the effective diffusion coefficient D_{eff}, is presented as function of the optically

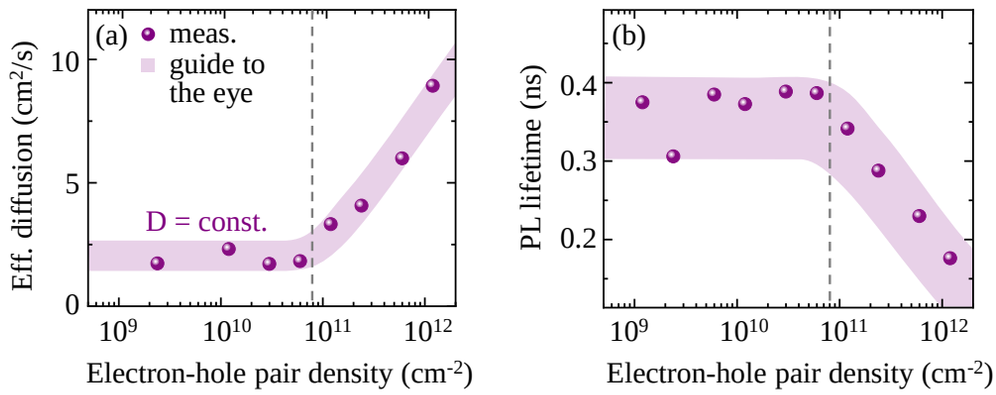

Figure 3.6: (a) Effective diffusion coefficient as function of injected electron-hole pair density collecting dark exciton emissions in a neutral, hBN-encapsulated WSe_2 monolayer. The sample is excited resonantly at the X^0 exciton. The lattice temperature is T = 5 K. (b) PL lifetimes τ_{PL} obtained from fitting dark exciton transients by mono-exponential fits within the first 200 ps. The linear regime where D = const. and τ_{PL} = const. is indicated for pump densities $\leq 8 \times 10^{10}$ cm^{-2}.

injected electron-hole pair density (by varying the excitation power). At low densities $\leq 8 \times 10^{10}$ cm^{-2}, the spatial broadening is constant whereas at elevated densities it rapidly increases. An analogous dependence is observed in the corresponding PL transients. At low carrier densities, the transients are characterized by a mono-exponential decay, whereas at elevated carrier densities a hyperbolic, non-exponential decay is observed. In Fig. 3.6(b), the extracted PL decay time is presented as function of the injected electron-hole pair density. At densities $\leq 8 \times 10^{10}$ cm^{-2} the decay time is constant, whereas at elevated densities it decreases. The observed behavior at elevated densities is attributed to Auger-like recombination of the excitons, studied e. g. in Refs. [61] and [219]. In this thesis, all experiments (apart from the measurements presented in Fig. 3.6) are performed at pump densities $\leq 6 \times 10^{10}$ cm^{-2} ensuring that contributions from non-linear density effects are excluded. Importantly, in this density regime the spatial broadening is determined by diffusive processes and D_{eff} is equal to the diffusion coefficient D in Equation 3.10.

3.7 Filtering of dark exciton emissions

Focusing on long-lived dark exciton reservoirs, their emissions are separated from bright excitons by *spectral* filtering, i. e., using adjustable band-pass filters,

or by *temporal* filtering, i. e., evaluating e. g. the diffusion coefficient at longer time scales.

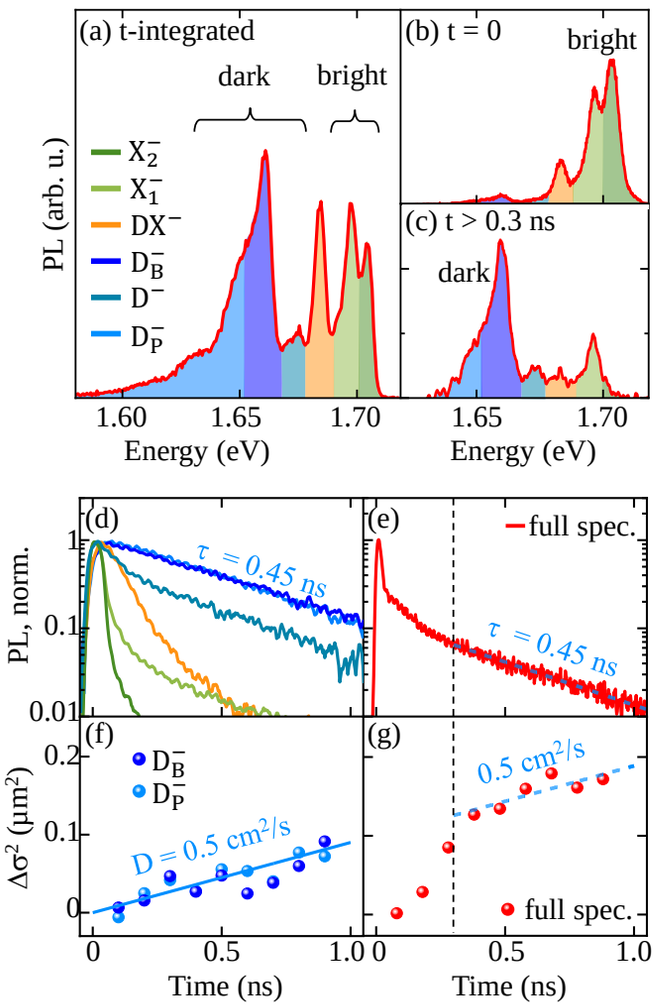

Figure 3.7: (a) Time-integrated PL spectrum of a hBN-encapsulated monolayer WSe_2 in the n-doped regime at T = 5 K under resonant excitation of the X^0 exciton at 1.722 eV. The spectrum shows several emission lines below the filtered X^0 emission (not shown) indicated by their common interpretations following Refs. [37, 186] (see also section 5.2). (b) Initial PL spectrum at $t = 0$. (c) Time-integrated PL spectrum for $t > 0.3$ ns. (d) Normalized PL transients of spectrally filtered emissions indicated in (a). The transients of the dark state emissions exhibit a 1/e decay time of 0.45 ns. (e) Energy-integrated PL transient of the spectrum shown in (a) yielding a 1/e decay time of 0.45 ps for $t > 0.3$ ns. (f) Spatial broadening of the PL cross-section collecting only D_B^- and D_P^- emissions. By fitting the data, a diffusion coefficient of 0.5 cm^2/s is determined. (g) Spatial broadening of the PL cross-section collecting all PL emissions energetically below X^0, yielding a diffusion coefficient of 0.5 cm^2/s for $t > 0.3$ ns.

In this work, temporal filtering is especially applied in the case of doping-dependent diffusion experiments, where the dark state emissions shift in energy with increasing free carrier concentration and thus spectral filtering becomes challenging. In Fig. 3.7, diffusion measurements applying both spectral and temporal filtering are presented. In Fig. 3.7 (a), a typical time-integrated WSe_2 monolayer spectrum in the n-doped regime is shown. The spectrum is characterized by several emission lines, i. e., the bright trion doublet X_1^-/X_2^-, charged biexcitons DX^-, as well as dark trion emissions D^-/D_B^- and their phonon side bands D_P^- . While the bright states dominate the initial spectrum at time $t = 0$, the emission is dominated by dark states at longer time scales, cf. Fig. 3.7 (b) and (c). *Bright* state emissions exhibit short lifetimes of only a few 10's of picoseconds, whereas *dark* state emissions are characterized by much longer decay times of several hundred picoseconds, cf. Fig. 3.7 (d). As illustrated in Fig. 3.7 (e–g), also the spatial long-term dynamics are dominated by dark excitons. Particularly, the propagation dynamics observed for the spectrally-filtered dark exciton emissions (Fig. 3.7 (f)) are equal to the long-term propagation dynamics of the total energy-integrated emission at $t > 0.3$ ns, cf. Fig. 3.7 (g).

3.8 Electrically-tuneable monolayer TMDC structures

Having described time-resolved spectroscopy and diffusion experiments, in this section, the fabrication and basic properties of the investigated electrically-tuneable TMDC structures are introduced. In order to study exciton-carrier interactions, electrically-contacted samples where the free carrier concentration can be varied are considered. Continuous tuneability of free electron or hole densities are achieved by integrating the monolayer in a plate capacitor. An out-of-plane field is applied between the contacted monolayer and a few layer graphene (FLG) flake which is separated by an insulating hBN layer. Applying a gate voltage V results in the accumulation of free carriers in the monolayer. In this geometry, the hBN layer acts as both, gate dielectric and encapsulating material to suppress disorder. As illustrated in Fig. 3.8 (a), the hBN/TMDC/hBN heterostructure introduced in section 3.1 is extended to an electrically-tuneable structure. The monolayer is contacted by two graphene contacts. Both contacts are equivalently used for doping. A list of all investigated structures and corresponding hBN thicknesses is presented in Fig. 3.8(b).

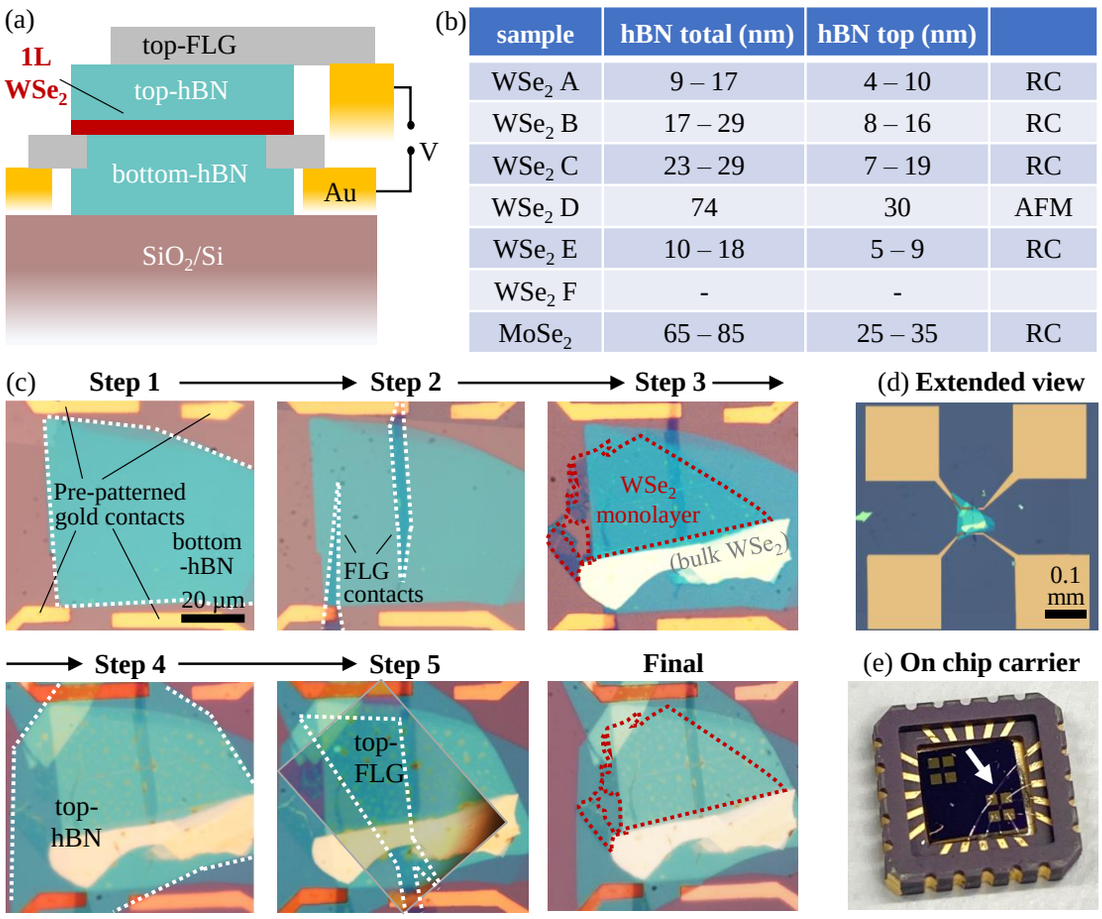

sample	hBN total (nm)	hBN top (nm)	
WSe_2 A	9 – 17	4 – 10	RC
WSe_2 B	17 – 29	8 – 16	RC
WSe_2 C	23 – 29	7 – 19	RC
WSe_2 D	74	30	AFM
WSe_2 E	10 – 18	5 – 9	RC
WSe_2 F	-	-	
$MoSe_2$	65 – 85	25 – 35	RC

Figure 3.8: (a) Schematic cross-section of an electrically-tuneable hBN-encapsulated monolayer WSe_2 structure. (b) Overview of investigated WSe_2 and $MoSe_2$ structures with hBN thicknesses estimated from reflectance contrast (RC) spectra or atomic force microscopy (AFM) measurements. AFM measurements were performed by Kaiqiang Lin. All samples allow for electrical control of the free carrier density in the monolayer but only sample WSe_2 E is an hBN-encapsulated structure without contacts. Sample WSe_2 F is listed for completeness although the hBN thickness was not determined. (c) Micrographs illustrating the individual stamping steps during the fabrication of a monolayer transistor. The structure exhibits charge-tuneable monolayer areas with a size of several 10's of μm^2. (d) Extended view with gold contacts and device structure in the center. (e) SiO_2/Si wafer with connected device structure fixed in a 20 pin chip carrier.

The electrically-tuneable TMDC structures are fabricated by subsequently stamping individually exfoliated layers on a SiO_2/Si substrate with pre-patterned gold contacts as depicted for a WSe_2 structure in Fig. 3.8 (c). First, the bottom-hBN layer is placed between the contacts followed by two thin FLG layers touching two gold contacts. The thin FLG contacts are aligned in parallel with a distance of 5 to 20 μm. Subsequently, the monolayer is stamped followed by a large top-

hBN layer covering the full monolayer area. In the last step, the top-FLG layer is stamped on top of the structure. The latter is connected to one of the remaining gold contacts. An extended view of the structure is presented in Fig. 3.8 (d).

For electrical control, the substrate is fixed with conductive silver lacquer in a 20 pin chip carrier where each pre-patterned gold contact is connected to one or two pins by aluminum wires, cf. Fig. 3.8 (e). The chip carrier is pressed to the cryostat cold finger by two screws. Thermal contact is provided by a conductive brass connection. In comparison to a sample which is directly fixed at the cold finger, the sample on the chip carrier exhibits a slightly worse thermal contact to the heat sink of the cryostat. However, differences in spectroscopic observables are hardly resolvable. In this work, the most sensitive spectroscopic observable of the actual (quasiparticle) temperature are the asymmetric emission flanks of trions and phonon side bands. In a sample on a chip carrier at a nominal heat sink temperature of T = 5 K, the trion temperature (by fitting the trion flank) after cooling ($t \leq 50$ ps) is estimated to be in the range of $\approx$ 10 K. For more details see section 4.3.

The sample is electrically controlled by a Keithley source measure unit. It provides a source voltage and simultaneously measures the current and/or resistance between two or more contacts. In a properly working device, the hBN layer completely isolates the gate contact from the sample, i. e., applying a voltage does not result in any currents. Typical resistances between monolayer and FLG gates are in the range of several 100's of GΩ.

In a typical structure, gate voltages of up to 0.3 V/nm hBN thickness can be applied before irreversible damage on the sample occur. It should be noted that multiple cooling cycles to liquid Helium temperatures can deteriorate the contacts between the aluminum bonds and the pre-patterned gold structure. In this case, the resistance of the aluminum bonds increase to a few kΩ (still in contact) to the GΩ range (no more contact) and the aluminum bonds need to be replaced.

Applying a gate voltage between the monolayer and the FLG flake leads to electrical doping of the monolayer. Successful injection of free charge carriers is evidenced in reflectance and photoluminescence spectroscopy by the voltage-dependent energy shift of the bright X^0 exciton and the emergence of the trions/ attractive Fermi polarons X^+ and X_1^-, X_2^-. Note that due to the specific band structure of monolayer WSe_2 and electron-electron exchange interaction, the n-side comprises two trion peaks [36, 166, 251]. Fig. 3.9 (a) shows the reflectance contrast derivative of an electrically-tuneable monolayer WSe_2 structure at T = 5 K as function of energy applying a gate voltage between the grounded monolayer

and the top-FLG flake between −1.5 and +2 V. Fig. 3.9 (b) shows the subsequent reflectance contrast derivative sweeping back from +2 V to −1.5 V exhibiting only a weak hysteresis. Positive and negative gate voltages correspond to n- and p-doping, respectively. At voltages between −0.2 and 0.3 V the system approaches charge-neutrality with an estimated free carrier density $\lessapprox 2\times10^{10}$ cm^{-2}. It should be noted that the observation of a charge-neutral regime which expands over a finite interval of gate voltages is a typical observation [49, 252]. In a perfect semiconductor without impurities and assuming T = 0 K, an energy larger than the band gap E_g is required to insert an electron into the conduction band. Thus, a finite voltage above a certain threshold value $\propto E_g/e$ is required for doping. In real systems, the doping onset is further determined by the interplay of the relative band alignment of the monolayer and the graphene, shallow impurities and Schottky barriers, lading to varying doping onsets between individual samples.

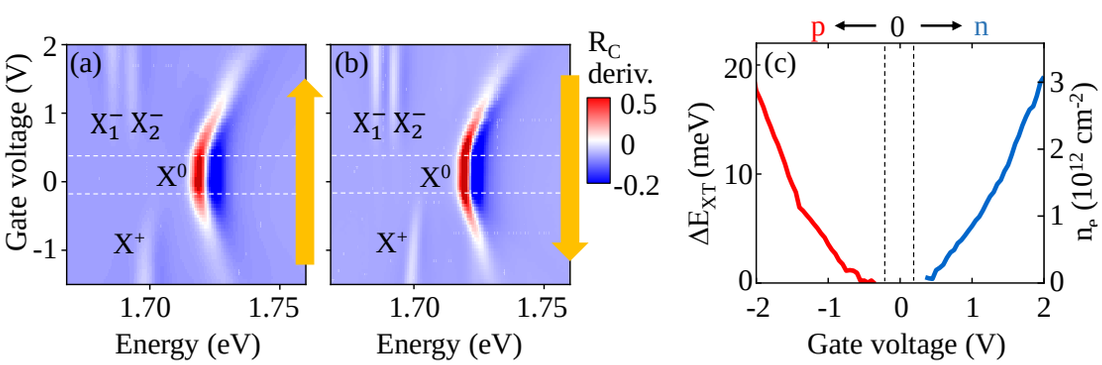

Figure 3.9: (a) Reflectance contrast as function of gate voltage in the energy range of the bright X^0 exciton in an electrically-tuneable monolayer WSe_2 (sample C) from −1.5 to 2.0 V and (b) backwards from 2.0 to −1.5 V. Dashed lines indicate the effective doping onset. (c) Relative X^0 – $X^\pm$ energy shift ΔE_{XT} obtained from an extended gate voltage sweep. The doping onset (zero-doping) is indicated by dashed lines. Right axis corresponds to the estimated electron doping density evaluating Equation 3.13.

In a first approximation, the free charge carrier density is estimated by a simple capacitor model

$$n_{e,h} = \frac{V\epsilon_0\epsilon_{\mathrm{hBN}}}{ed} \tag{3.12}$$

with gate voltage V, vacuum permittivity ϵ_0, dielectric constant of the hBN layer ϵ_{hBN}, hBN thickness d and elementary charge e. Considering an ideal structure with a $d = 10$ nm hBN spacer and $\epsilon_{\mathrm{hBN}} = 3.76$ [159], a gate voltage of 1 V corresponds to an injected charge carrier density of approximately 2×10^{12} cm^{-2}. However, in a real structure imperfections due to Schottky barriers, donor/acceptor-

doping caused by structural defects, or photo-doping leads to a non-linear scaling between applied voltage and free carrier density. This motivates for a carrier density scaling based on spectroscopic observables. At low doping, in both, the trion and Fermi polaron approach, resonance energies, linewidth broadening and oscillator strength scale approximately linearly with the free carrier density. Here, the effective free carrier density is estimated by the relative exciton-trion transition energy separation ΔE_{XT}. Among all carrier-density dependent observables, it is the most reliable and exhibits a well-known relation to the doping density. For a two-dimensional monolayer with parabolic electron dispersion and degenerate spin-states (doping at the lowest K and K' valleys) the carrier density is given by [174]

$$n_{e,h} = \Delta E_F \frac{m_{e,h}}{\pi \hbar^2} \tag{3.13}$$

with electron or hole mass $m_{e,h}$, elementary charge e and Planck constant $\hbar$. At low carrier densities, the Fermi energy shift ΔE_F is set equal to the relative exciton-trion shift ΔE_{XT}, yielding

$$n_{e,h} \approx \Delta E_{XT} \frac{m_{e,h}}{\pi \hbar^2} \tag{3.14}$$

As outlined in section 2.3, depending on whether the Fermi polaron ($\Delta E_{XT} \approx 3/2 E_F$) or the trion model ($\Delta E_{XT} \approx 2/3 E_F$) is considered, this estimation may leads to a constant error of up to 50%. In consideration of the two models, the choice of $\Delta E_{XT} \approx E_F$ seems appropriate, particularly, as in a recent many-body approach, quantitatively describing experimental observables, the scaling factor indeed is equal to unity [112].

In Fig. 3.9 (c), the relative exciton-trion energy separation $\Delta E_{XT} = E_X - E_{X^\pm} - E_{b,T^\pm}$ is plotted as function of gate voltage. The exciton and trion resonance energies are obtained by fitting the data by a parameterized transfer matrix model (see section 3.3). The trion binding energy $E_{b,T}$ corresponds to the extrapolated zero-doping energy separation

$$E_{b,T^+} = E_X(-0.2\,\mathrm{V}) - E_{X^+}(-0.2\,\mathrm{V}) = 19.4\,\mathrm{meV} \tag{3.15}$$

$$E_{b,T_1^-} = E_X(0.3\,\mathrm{V}) - E_{X_1^-}(0.3\,\mathrm{V}) = 34.6\,\mathrm{meV} \tag{3.16}$$

$$E_{b,T_2^-} = E_X(0.3\,\mathrm{V}) - E_{X_2^-}(0.3\,\mathrm{V}) = 27.8\,\mathrm{meV} \tag{3.17}$$

Considering an electron and hole mass of $m_e = 0.4\ m_0$ and $m_h = 0.36\ m_0$ [126], the scaling of the free carrier density in monolayer WSe_2 is

$$n_e/\Delta E_{XT} \approx n_e/\Delta E_{XT} = 1.7 \times 10^{11}\,\mathrm{cm}^{-2}/\mathrm{meV} \tag{3.18}$$

$$n_h/\Delta E_{XT} \approx n_h/\Delta E_{XT} = 1.5 \times 10^{11}\,\mathrm{cm}^{-2}/\mathrm{meV}. \tag{3.19}$$

Consequently, in Fig. 3.9 (c), an increase of the gate voltage of 1 V corresponds to an injected electron density of $n_e \approx 2 \times 10^{12}\ \mathrm{cm}^{-2}/V$. This value is in good agreement with the approximated charge carrier density obtained from the capacitor model in Equation 3.12, i. e., $n_e/\mathrm{V} = 1 - 3 \times 10^{12}\ \mathrm{cm}^{-2}/V$, considering a hBN thickness of $7 - 19$ nm, cf. Figure 3.8 (b), sample C. Considering an electron and hole mass of $m_e = 0.56\ m_0$ and $m_h = 0.6\ m_0$ [126] in monolayer $MoSe_2$, the scaling of the free carrier density is

$$n_e/\Delta E_{XT} \approx n_e/\Delta E_{XT} = 2.7 \times 10^{11}\,\mathrm{cm}^{-2}/\mathrm{meV} \tag{3.20}$$

$$n_h/\Delta E_{XT} \approx n_h/\Delta E_{XT} = 2.5 \times 10^{11}\,\mathrm{cm}^{-2}/\mathrm{meV}. \tag{3.21}$$

It should be noted that the considered electron mass in monolayer $MoSe_2$ is may be underestimated by up to a factor of two as indicated by recent experiments [253].

Equation 3.13 is only valid for doping of the lowest conduction or valence band at K and K'. In the case that also the upper spin-split conduction band is occupied by electrons, the number of relevant valleys increases from 2 to 4 and the right side of Equation 3.13 needs to be multiplied by an additional factor of 2 (assuming equal masses for upper and lower conduction band valleys). In hBN-encapsulated WSe_2 and $MoSe_2$ monolayers, the conduction band splitting is on the order of ≈ 15 meV [186] and ≈ 30 meV [254], respectively. Therefore doping of the upper spin-split valleys becomes only relevant at electron densities larger than 2.5×10^{12} cm^{-2} and $7 \times 10^{12}\ \mathrm{cm}^{-2}$, respectively (not investigated in this thesis). In case of hole doping, the valence band splitting is on the order of 100 meV [126] and thus irrelevant for electro-static doping. It should be noted, that in the case of elevated free charge carrier densities $\gtrapprox 10^{12}\ \mathrm{cm}^{-2}$, the assumption $\Delta E_{XT} \approx E_F$ and thus Equation 3.14 does not hold anymore and the carrier density given by Equation 3.12 should be considered.

Chapter 4

Exciton interactions in a two-dimensional Fermi sea

In this and the following chapter, the main experimental results are presented. This chapter focuses on exciton interactions in a two-dimensional gas of charge carriers and is structured in three sections. In the first section, a two-particle excitation termed as *excited state trion* is identified and explored in carrier density-dependent reflectance contrast and photoluminescence spectroscopy of WSe_2 monolayers. In the second section, the mechanisms of *exciton-electron scattering* are studied by analyzing the non-radiative exciton and trion linewidth broadening as function of free carrier density and different temperatures. In the third section, an electron-assisted radiative recombination process for trions, termed as *electron recoil effect*, is demonstrated in monolayer $MoSe_2$. This process is studied in time-resolved photoluminescence experiments giving access to the effective trion temperature and phonon- and free carrier-assisted cooling dynamics.

The contents presented in section 4.1 have been reported in a peer-reviewed publication "K. Wagner *et al.*, Phys. Rev. Lett., 125(26), 267401, 2020" [255]. The investigations presented in section 4.3 are performed with Jonas Zipfel (equally contributing) published as "J. Zipfel and K. Wagner *et al.*, Phys. Rev. B, 105, 075311, 2022" [251]. Figures are reprinted with permission. Copyright (2022) by the American Physical Society. The investigations presented in section 4.2 are part of an yet unpublished work (Ref. [256], under review) with theoretical support from Mikhail M. Glazov and Zakhar A. Iakovlev from the Ioffe Institute in Saint Petersburg.

4.1 Dressing of excited state excitons by free charge carriers

In this section, the dressing of excited excitons with a two-dimensional Fermi sea of free charge carriers in a monolayer semiconductor is investigated. By carrier density-dependent reflectance contrast and photoluminescence spectroscopy in electrically-tuneable hBN-encapsulated WSe_2 monolayers, positively- and negatively-charged excited state trions are identified and their interaction mechanisms are explored.

It should be noted that fingerprints of excted state trions have been recently reported in an unintentionally n-doped WS_2 monolayer [71] and parallel to this work, further studies on the topic of excited state trions have been published [74, 183, 75].

4.1.1 Identification of excited state trions in electircally-tuneable WSe_2 monolayers

In Fig. 4.1 (a), the reflectance contrast derivative $\partial R_c/\partial E$ of a hBN-encapsulated monolayer WSe_2 is presented in the energy range of 1s and 2s excitons as function of gate voltage. The free carrier concentration reaches a value of up $\approx 2 \times 10^{11}$ cm^{-2}. The temperature is set to T = 5 K. In Fig. 4.1 (b), selected spectra are presented in a waterfall plot.

At charge neutrality (0V), the spectrum exhibits a strong feature at 1.72 eV corresponding to the ground state X^0_{1s} exciton. At 1.85 and 1.88 eV excited state excitons X^0_{2s} and X^0_{3s} emerge. By applying a finite positive or negative gate voltage and thus inserting free electrons or holes, additional resonances energetically below the 1s exciton appear: the X^-_{1s} trion doublet and the X^+_{1s} trion. The trion doublet in the n-doped side is associated to the two non-degenerate bright trion configurations, characteristic for tungsten-based TMDCs [36, 166, 251]. The observed ground state resonances are in well agreement with previous reports [41, 66]. Interestingly, similar features appear for excited states. Both, for n- and p-doping, low energy features labeled by X^-_{2s} and X^+_{2s} emerge. These features are attributed to excited state trions, i. e., an exciton state dressed with a free charge carrier or, in the language of Fermi polarons, dressed by a Fermi sea excitation. It is excluded that the observed states stem from 2p excitons (which roughly fall in the same spectral range [258, 259, 129, 260]) due to a pronounced doping dependence of the observed features.

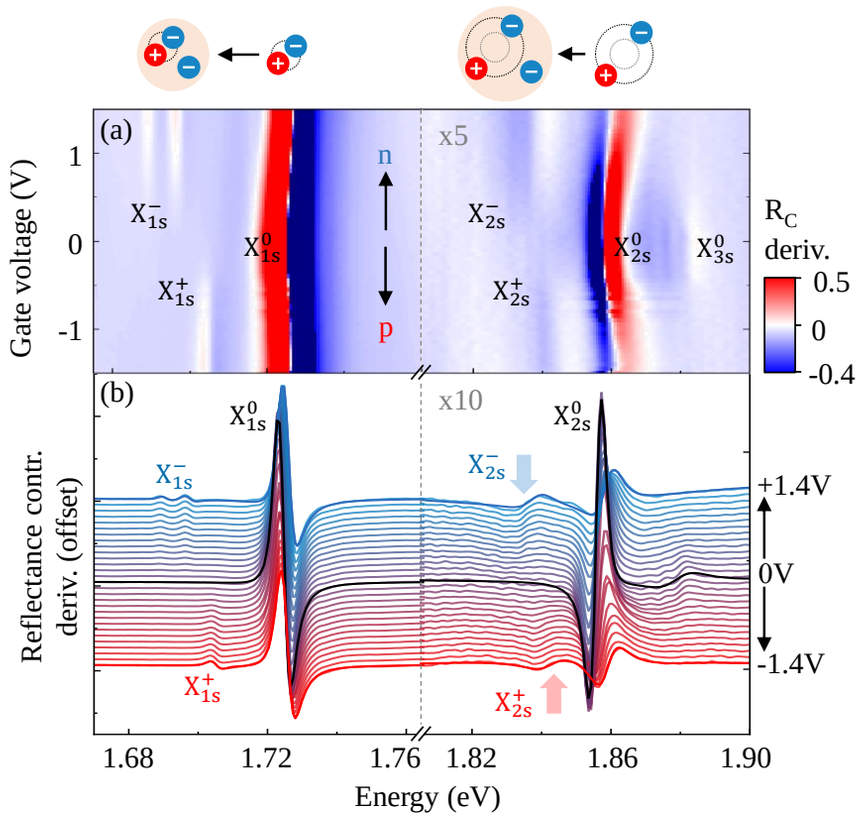

Figure 4.1: (a) Reflectance contrast derivative as function of gate voltage in the range of the ground state (1s) and excited state (2s, 3s) X^0 exciton in hBN-encapsulated monolayer WSe_2 at T = 5 K. A gate voltage of 1 V corresponds to a free carrier density of $\approx 10^{11}$ cm^{-2}. (b) Individual reflectance contrast spectra corresponding to (a) with exemplary fits for 0 and ±1.4 V.

The signatures of excited state trions are observed in three samples, i. e., WSe_2 A - C and different sample positions. For direct comparison, in Fig. 4.2 four different measurements are presented, including the data shown in Fig. 4.1. All measurements are characterized by a similar appearance of the 1s and 2s resonances. In two of the data sets no 3s resonances are resolvable. Most importantly, the emergence of the excited state trions $X^{\pm}_{2s}$ are observed in all measurements. Particularly, the findings are robust with respect to varying gate voltage to free carrier density scaling and linewidth broadening, which is e. g. slightly larger in sample B compared to sample A and C.

In Fig. 4.3(a), the energies determined from fitting individual reflectance contrast spectra by a parameterized multi-Lorentzian transfer matrix model are summarized as function of free carrier density n. Exemplary fits are shown in Fig. 4.1(b) and in the lower panels in Fig. 4.2. The carrier density is obtained from setting the exciton-trion energy separation equal to the Fermi energy (see section 3.8).

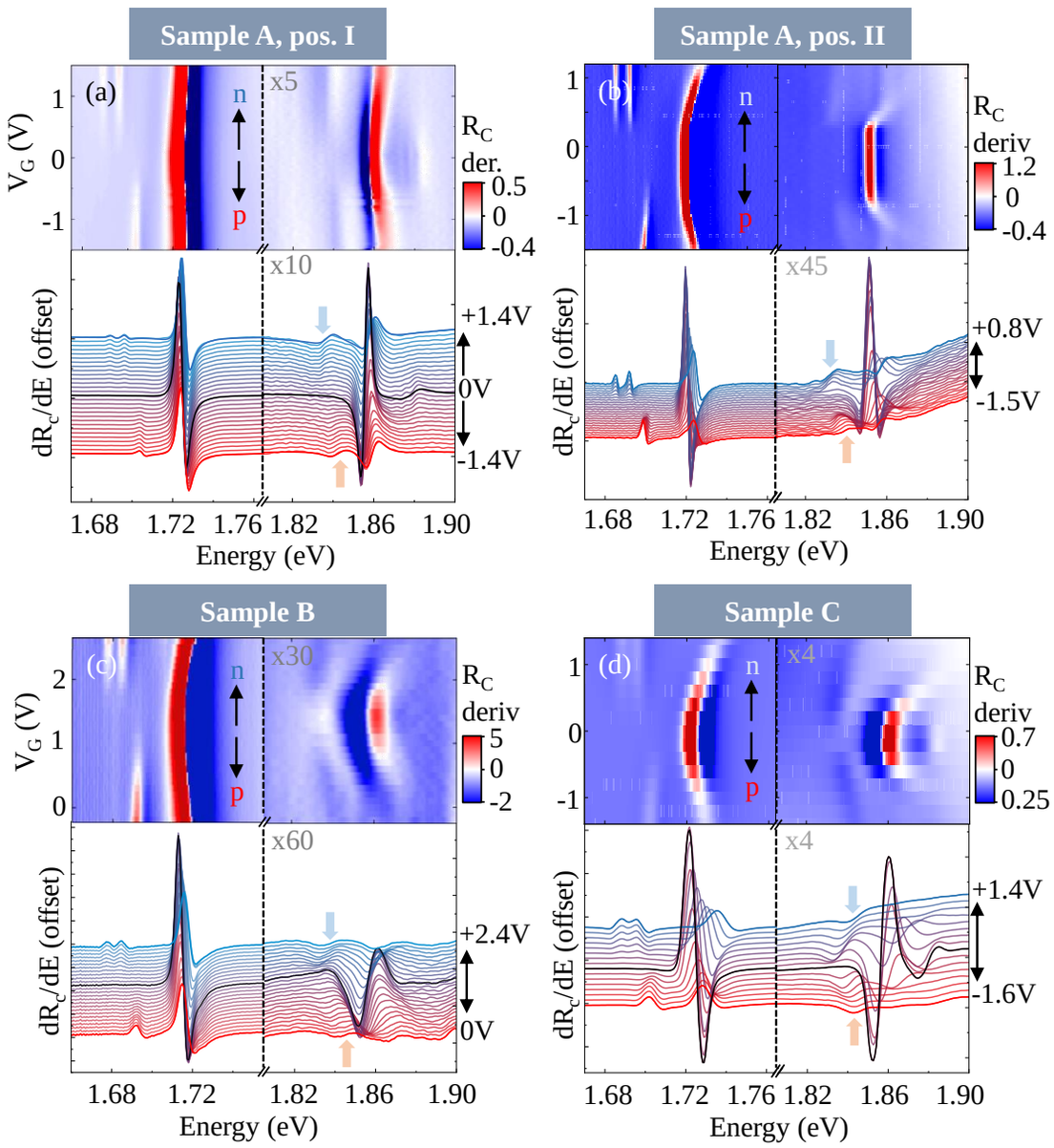

Figure 4.2: Comparison of measured reflectance contrast derivative as function of gate voltage in the range of the ground state (1s) and excited state (2s, 3s) X^0 exciton in hBN-encapsulated monolayer WSe_2. The lower panels show individual reflectance contrast spectra with exemplary fits. Panel (a) corresponds to the measurement presented in Fig. 4.1. In (b), a measurement on the same sample but on a different position is presented. (c) and (d) correspond to measurements on sample B and C, respectively. The the regime of excited state resonances, the data is corrected by subtracting a baseline with a tilt.

Similar to previous reports, the ground state exciton energy exhibits a blueshift with increasing carrier density and is typically associated with renormalization of the band gap and screening of the exciton binding energy [173]. The ground state trion energies are characterized by only a weak energy dependence. In the low

carrier density regime the trions slightly shift towards lower energies and their energy is mostly determined by the carrier-density dependent exciton-trion energy separation. A similar behavior is observed for the excited states. The exciton energy is characterized by a strong blueshift and the trion energies exhibit only a weak carrier density dependence. In Fig. 4.3(b), the exciton-trion energy separations $\Delta_{1s} = E_X^{1s} - E_{X\pm}^{1s}$ and $\Delta_{2s} = E_X^{2s} - E_{X\pm}^{2s}$ are plotted as function of carrier density. The energy separations increase linearly with free carrier density for 1s (which is determined by the definition of the carrier density, i. e., $\Delta_{1s} = \Delta E_F$) and 2s states.

Despite the overall similarity, there are two main differences between 1s and 2s states. First, the extrapolated zero-doping energy separation corresponding to the excited state trion binding energy is 14.1 and 18.6 meV for p- and n-type states, respectively, and thus smaller than the ground state binding energies, which are found to be 19.4 meV at the p-doped side and 27.9 and 34.7 meV for the two spin-split trion resonances at the n-doped side. Note, that the splitting of the negatively-charged 2s trion is may not resolved due to a larger linewidth broadening. Both, for 1s and 2s states the binding energies are larger at electron doping. The overall smaller values for excited state trions are consistent with their interpretation. Most strikingly, the 2s trion and 2s exciton binding energies are on a same order of magnitude. Similar to the estimation of the 1s exciton binding energy in Refs. [69, 261], the 2s exciton binding energy can be estimated by $E_{b,X}^{2s} \approx 0.3 \times (E_X^{2s} - E_X^{1s}) = 0.3 \times (1.86 \text{ eV} - 1.72 \text{ eV}) = 40$ meV (the scaling factor of 0.3 is obtained from Ref. [151] and includes dielectric screening effects due to the hBN-encapsulation). It follows that $E_{b,X}^{2s} \approx 2E_{b,T}^{2s}$, i. e., the 2s exciton binding energy is only twice as large as the 2s trion binding energies. This finding is in stark contrast to the conventional picture where the extra electron of the trion is much weaker bound than the excitonic core.

Second, the energy separation between trion and exciton increases almost twice as much with free carrier density for 2s compared to 1s states, i. e., $\Delta_{2s}/n > \Delta_{1s}/n$. The increasing energy separation can be e. g. approached in the Fermi polaron model [183]. Here, the energy separation is mostly determined by the binding energy of the exciton with the Fermi sea excitations. Due to the larger spatial extent of excited state excitons, the interaction with the Fermi sea is stronger. Consequently, by increasing the Fermi energy the energy separation increases stronger for excited states compared to the ground state.

Next, the efficiency of the investigated light-matter coupling, given by the oscillator strength, is discussed. In Fig. 4.4(a), the oscillator strength extracted from

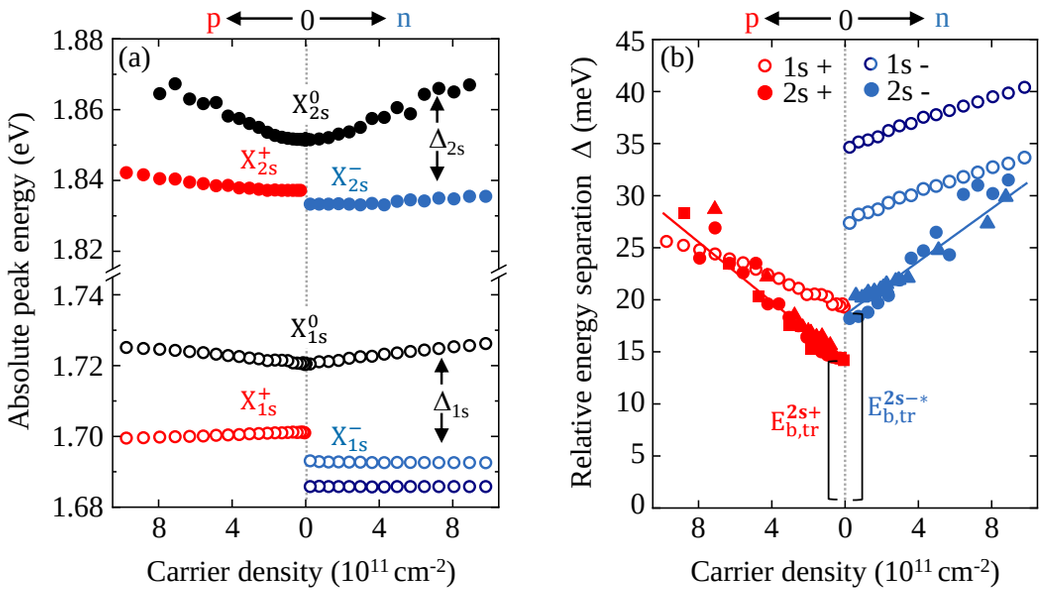

Figure 4.3: (a) Resonance energies as function of gate voltage for 1s and 2s states extracted from fitting data shown in Fig. 4.1. (b) Energy separation between trion and exciton resonances Δ_{1s} and Δ_{2s} as function of free carrier density. Triangles, squares and circles correspond to different measurements on different samples and positions.

Fig. 4.1 are presented as function of free carrier density. Both, 1s and 2s exciton oscillator strength decrease with increasing carrier density. Simultaneously, the trions gain oscillator strength with increasing carrier concentration. In the case of the 1s state, the sum of exciton and trion oscillator strength remains initially constant and only decreases slowly with increasing carrier density, whereas, in case of 2s states, it decreases more rapidly. Similarly, while the 1s oscillator strength is only slowly exchanged, i. e., ground state exciton and trion oscillator strengths are approximately similar at carrier densities as high as 2×10^{12} cm^{-2}, cf. Fig. 4.4 (b), for the 2s states the exchange occurs at almost an order of magnitude lower free carrier densities densities at about 3×10^{11} cm^{-2}. Interestingly, at carrier densities above 8×10^{11} cm^{-2}, the 2s state is fully dominated by the trion while the ground state is still governed by the exciton, i. e., 1s excitons coexist with 2s trions.

In a simple picture, the trion oscillator strength can be understand as the probability that an exciton binds an additional electron. In the weak interaction regime, it scales approximately linearly with the free electron density and the area in the vicinity of the exciton where the electron is bound, i. e., the area within the trion radius $a^2_{B,T}$ [169]. Particularly, the probability that an exciton forms to a

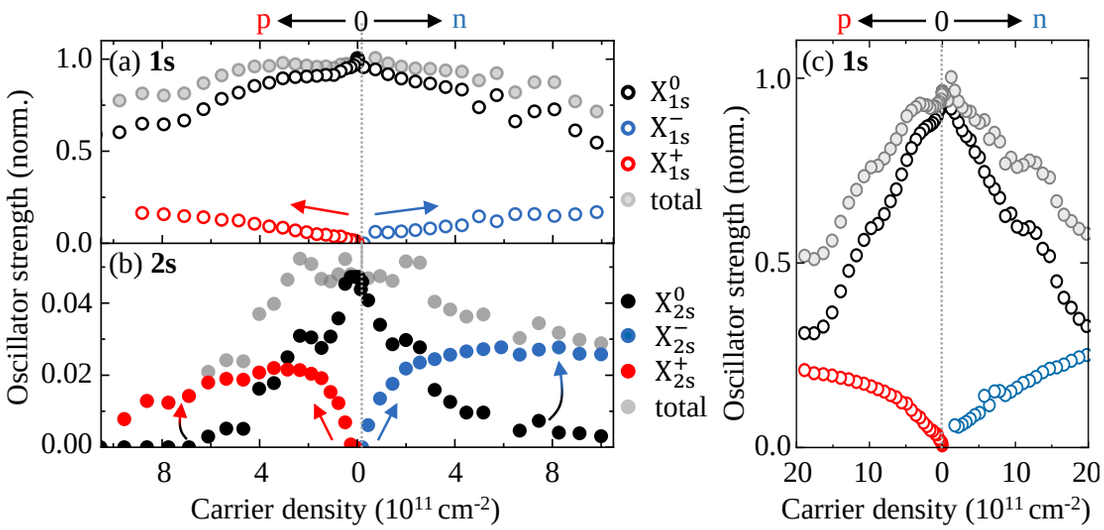

Figure 4.4: Extracted oscillator strength from Fig. 4.1 as function of carrier density for 1s (a) and 2s (b) states. In (c) the ground state oscillator strengths are shown in an extended carrier density range. In case of the n-type 1s trion, the oscillator strengths includes both spin-split resonances, i. e, the data refers to the total oscillator strength of the trion doublet. The oscillator strength is normalized to the 1s exciton at charge neutrality. The total 1s and 2s oscillator strength corresponds to the sum of the respective exciton and trion oscillator strengths.

trion is larger in case of a larger spatial extent. The observed faster oscillator strength exchange of excited states is thus consistent with their experimentally-observed 2 to 3 three times larger root-mean-square radii compared to ground states [151, 150, 183].

In Fig. 4.5(a), the non-radiative linewidths of the 1s and 2s resonances extracted from Fig. 4.1 are summarized as function of free carrier concentration. At zero doping, the non-radiative 1s exciton linewidth is on the order of 2.5 meV. It is mostly governed by phonon absorption and the scattering towards lower-laying dark states, cf. Figure 2.8 in section 2.5. Interestingly, the non-radiative linewidth of the 2s exciton at zero-doping is in a similar range although excited state excitons can additionally scatter into ground states. However, due to their larger spatial extent and therefore smaller size in k-space, the interaction of 2s excitons with phonons is less efficient and the scattering is even slightly reduced compared to 1s excitons [73]. In Fig. 4.5(b), the linewidth broadening is presented for sample B. By contrast, here, at zero doping, the 2s exciton linewidth is about 7 meV larger than the 1s exciton linewidth. As demonstrated in Ref. [69], this can be understand due to a larger degree of dielectric disorder in this sample. The 2s exciton state is much more sensitive to variations in the dielectric surround-

ing, manifesting in a pronounced additional inhomogeneous broadening γ_{disorder} of the 2s exciton resonance. This observation is consistent with an overall larger linewidth broadening of all resonances in sample B. In particular, the 1s exciton linewidth at $n = 0$ is 5 meV und about twice as large as in sample A with about 2.5 meV. In sample A, the almost equal linewidths of 1s and 2s excitons at $n = 0$ indicate suppressed dielectric disorder.

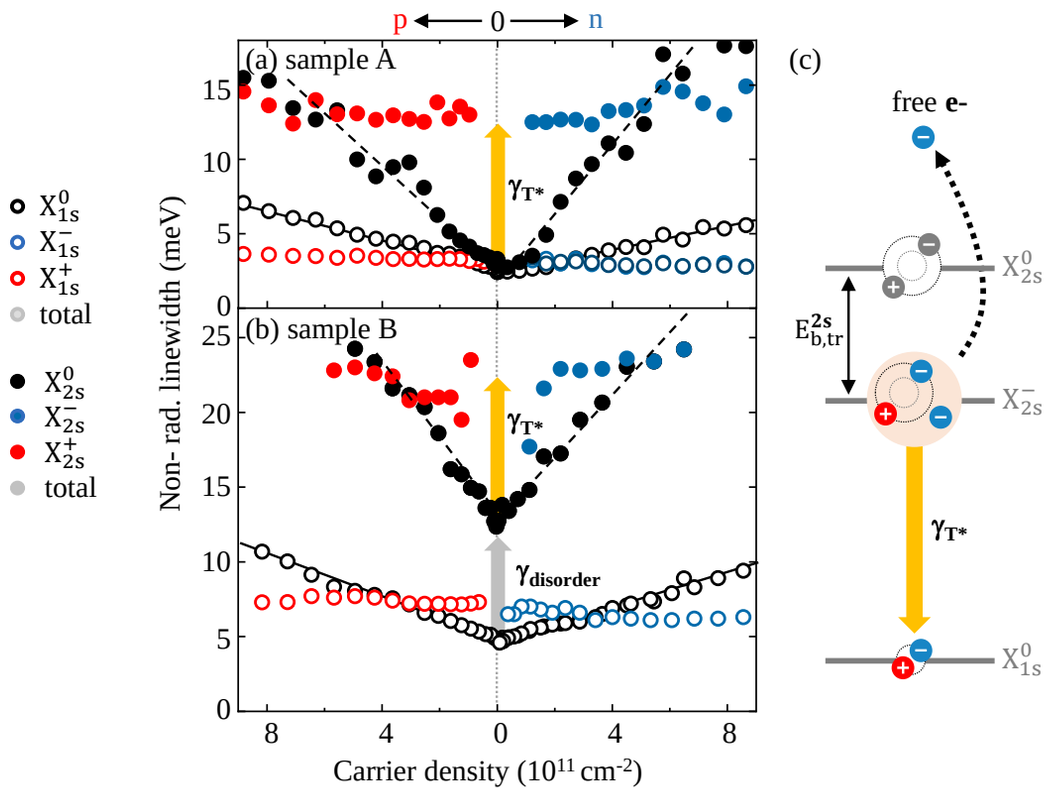

Figure 4.5: (a) Non-radiative linewidth broadening as function of carrier density extracted from the data in Fig. 4.1 (sample A). The data is determined by a parameterized multi-Lorentzian transfer matrix model fit, cf. section 3.3. (b) Same data obtained in sample B. γ_T^* indicate the additional 2s trion linewidth broadening due to autoionization. γ_{disorder} is the dielectric disorder-induced linewidth of the neutral 2s exciton. In sample A, γ_{disorder} is negligible due to suppressed dielectric disorder. (c) Schematic illustration of the autoionization process in an energy level diagram. The excitonic core within the 2s trion makes a transition to the 1s exciton state while leaving behind a free electron which is excited.

With increasing carrier density, first of all, the excitons are characterized by a strongly increasing linewidth broadening. The increase of the exciton linewidth is mostly determined by the increasing scattering with free carriers and the scattering into trion states. In Fig. 4.5 (a), the carrier-induced 1s exciton broadening is 0.5 meV/(10^{11} cm^{-2}) and 2 meV/(10^{11} cm^{-2}) for the 2s exciton. The larger linewidth

increase of the excited state exciton is consistent with its larger Bohr radius and therefore a stronger interaction with the Fermi gas. Differently, the trions hardly broaden with increasing carrier density. In Fig. 4.5 (a), the carrier-induced non-radiative linewidth broadening of the 1s trion is on the order of a few meV and increases with free hole density only about 0.05 meV/(10^{11} cm^{-2}). In case of electron doping, the trion shows no linewidth increase at all. Furthermore, the 1s trion linewidth is slightly larger compared to the 1s exciton at charge neutrality due to stronger phonon interactions, i. e., the trion consists of one more particle compared to the exciton which contributes to the phonon scattering [214]. Most remarkably, the 2s trion exhibits a non-radiative linewidth as high as 14 meV in sample A and 23 meV in sample B. Despite different absolute values, in both samples the 2s trion broadening is $\gamma_T^* \approx 10$ meV larger compared to the 2s exciton broadening at charge neutrality. As the relative broadening is observed equally in both samples, its origin is not connected to dielectric disorder effects. Similar to neutral excited state excitons, due to the larger spatial extent and therefore smaller size in k-space, the 2s trion-phonon scattering efficiency is expected to be rather weaker compared to the 1s trion and γ_T^* is unlikely to stem from enhanced phonon interactions.

The huge additional broadening indicates a scattering channel for excited states in the presence of free charge carriers. As γ_T^* hardly depends on the free carrier density, it is related to an intra-excitonic scattering process. In analogy to the doubly-excited H^- ion [72], the observed non-radiative broadening is attributed to autoionization

$$(2s + e^-)_{bound} \rightarrow 1s + e^{-\prime}.$$

In this process, an excited 2s exciton which binds to a free charge carrier (an excited state trion) can scatter to the 1s ground state by simultaneously exciting the bound electron, cf. schematic illustration in Fig. 4.5 (c). This process can also be understand as an intra-excitonic Auger-scattering.

Similar to the doubly-excited H^- ion [72], the 2s trion is characterized by an excited excitonic core (2s exciton), which interacts with free charge carriers resulting in a bound three-particle state, the 2s trion, cf. schematic illustration in Fig. 4.1. It means, that the excited state trion is an excited state exciton dressed by an additional, weakly bound electron or hole, i. e., both electrons are only weakly bound, i. e., both electrons are "excited".

The coupling of the 2s state to the Fermi gas can be e. g. approached within the Fermi polaron formalism [44, 45, 262, 184, 263], where the exciton-electron interaction is described in a short-range potential. In the following, this approach is outlined, focusing on the intra-excitonic transitions, i. e., the autoionization process. The model is derived by Marina M. Semina, Zakhar A. Iakovlev and Mikhail M. Glazov from the Ioffe Institute in Saint Petersburg [255].

The exciton is described by its Green's function at negligible damping (interactions with phonons, defects or other excitons are neglected)

$$G_j(\epsilon, \boldsymbol{k}) = \frac{1}{\epsilon - E_j - \frac{\hbar^2 k^2}{2m_X}}, \tag{4.1}$$

with translational mass $m_X = m_e + m_h$ and energy E_j. The subscripts $j = 1s, 2s$ denote the corresponding quantum state, e. g. ground state 1s and first excited state 2s. The Green's function is directly related to the absorption spectrum $\propto -\mathrm{Im}\mathcal{G}_X(\epsilon, 0)$. $\mathcal{G}_j(\epsilon, 0)$ represent the repulsive (trion) and attractive (exciton) polaron resonances. The energy-dependent scattering amplitudes are

$$\begin{aligned} &T_{ij}(\epsilon, \boldsymbol{k}) = V_{ij} \\ &+ \sum_l V_{il} \sum_{\boldsymbol{p}} (1 - n_{\boldsymbol{p}}) G_l \left(\epsilon - \frac{\hbar^2 p^2}{2m_e}, \boldsymbol{k} - \boldsymbol{p} \right) T_{lj}(\epsilon, \boldsymbol{k}). \end{aligned} \tag{4.2}$$

with the matrix elements V_{ij} corresponding to the scattering from state j to i ($j, i =$ 1s, 2s) and $\mathcal{D} = \mu_{eX}/(2\pi\hbar^2)$. $\mu_{eX}^{-1} = m_e^{-1} + m_X^{-1}$ is the reduced electron-exciton mass. In Equation 4.2 it is assumed that $|V_{ij}|\,\mathcal{D} \ll 1$. Considering only the coupling between ground and first excited state and negligible Pauli blocking, i. e., $(1 - n_{\boldsymbol{p}}) \approx 1$ the scattering amplitude T_{22} reads

$$T_{22} = (1 + S_2 T_{22}) \left[V_{22} + \frac{|V_{12}|^2 S_1}{1 - V_{11} S_1} \right] \tag{4.3}$$

with $S_2 = \sum_{\boldsymbol{p}} G_2(\epsilon, \boldsymbol{p})$. The excited state trion resonances are at

$$\varepsilon = E_{2s} - E_{b,T}^{2s} \left(1 + \mathrm{i} \tan\phi\right), \tag{4.4}$$

with the 2s resonance energy E_{2s} and excited state trion binding energy

$$E_{b,T}^{2s} \approx E_{b,X}^{2s} \exp\left(\frac{1}{\mathcal{D} V_{22}}\right) \cos\phi, \tag{4.5}$$

with phase ϕ. Interestingly, the 2s trion resonance exhibits a finite imaginary part, which originates from a finite 2s to 1s coupling (V_{12}). The phase can be approximated by

$$\phi \approx \pi \frac{|V_{12}|^2}{|V_{22}|^2}. \tag{4.6}$$

In this approach it is assumed that ϕ should not exceed $\pi/2$ otherwise the 2s trion binding energy becomes negative (see Equation 4.5), requiring $|V_{22}|^2 \geq 2 \times |V_{11}|^2$. As a direct consequence, depending on the values of the matrix elements, the 2s trion state may be present or not. Most importantly, as the resonance energy exhibits an imaginary part, the 2s trion is intrinsically damped, i. e., it exhibits an additional broadening which is given by

$$\gamma_T^* = E_{b,T}^{2s} \tan \phi. \tag{4.7}$$

This broadening is a direct consequence of the autoionization process, i. e., the scattering of the 2s state into the 1s ground state in the presence of free charge carriers. It should be emphasized that in the Green's function in Equation 4.1 explicitly no damping is considered (which would be otherwise introduced by a finite imaginary part in the denominator). It means, that γ_T^* is indeed an intrinsic broadening which only originates from the finite 2s to 1s coupling. This additional linewidth broadening depends on the 2s trion binding energy $E_{b,T}^{2s}$ and the phase ϕ which is basically given by the ratio of the matrix elements V_{22} and V_{12}. Both, the binding energy and the matrix elements are free parameters in this theory. According to Equation 4.5, it is crucial that $|V_{22}|$ is much larger than $|V_{11}|$ in order that the 2s trion is a bound state with a positive binding energy. In other words, it means that 2s trions form only in the case that the interaction of the 2s state are much stronger than the interactions of the 1s state. This is consistent with the experimental observations: the stronger relative exciton-trion energy separation Δ_{2s} and almost an order of magnitude faster oscillator strength exchange of the excited states and the about four times steeper linewidth increase of the 2s exciton compared to the 1s exciton indicate overall stronger interactions for the 2s state. Evaluating Equation 4.5, Equation 4.6, Equation 4.7 and the ground state binding energy $E_{b,T}^{1s} = E_{b,X}^{1s} \exp[1/(\mathcal{D}V_{11})]$, the following values for the matrix elements are

found:

$$V_{11} = 110\,\mathrm{eV/\AA}^2 \tag{4.8}$$

$$V_{12} = 90\,\mathrm{eV/\AA}^2 \tag{4.9}$$

$$V_{22} = 240\,\mathrm{eV/\AA}^2, \tag{4.10}$$

considering $E_{b,X}^{1s} = 180$ meV , $E_{b,T}^{1s} = 30$ meV, $E_{b,X}^{2s} = 40$ meV, $E_{b,T}^{2s} = 20$ meV, $\gamma_T^* = 10$ meV, $m_X = 0.76m_0$ and $m_e = 0.36m_0$. Consistently, the determined excited state matrix element V_{22} is more than twice as large as the matrix element of the ground state V_{11}. This finding is particularly in agreement with the larger spatial extent of excited states, observed in magneto-optic experiments [151, 261, 150]. As expected, the inter-state coupling matrix element V_{12} is very efficient and comparable with V_{11}. It should be noted, however, that the observed values also indicate the limit of the presented model, i. e., $|V_{ij}|\mathcal{D}$ reaching unity (cf. Equation 4.2).

4.1.2 Excited state trions in emission spectroscopy

In this section, signatures of excited state trions in photoluminescence are revealed. In this type of experiments, the sample is typically excited by photons with an energy above band gap. While the system relaxes towards lower energies, it emits light at certain energies, indicating a finite population of states associated with these transition energies. In principle, also high-energy states with a finite light-matter coupling such as excited state excitons can be observed in photoluminescence due to e. g. transient emission ("hot" PL), reabsorption or up-conversion [264].

Exciting the WSe_2 monolayer by a CW laser at an energy of 2.331 eV, in Fig. 4.6(a) and (b), the collected PL intensity is presented as function of energy and gate voltage in the range of ground state and excited state excitons. At charge neutrality, the 1s state is dominated by the neutral exciton X^0 at 1.722 eV and dark exciton emission D^0. The spectrum is cropped towards lower energies by a edge-pass filter (dark state emissions will be discussed in chapter 5). With increasing gate voltage, $X_{1s}^{\pm}$ trions emerge [41, 66, 265, 36, 166, 266]. At higher energies the spectrum is characterized by excited state emissions including X_{2s}^0 and X_{3s}^0 resonances. Due to more than an order of magnitude weaker radiative coupling [73], the 2s exciton emission is much less intense compared to the 1s emission, i. e., $I_{\mathrm{PL}}(1\mathrm{s}) \approx 30 I_{\mathrm{PL}}(2\mathrm{s})$. While the neutral excited exciton features immediately vanish with increasing carrier density, emerging features of excited

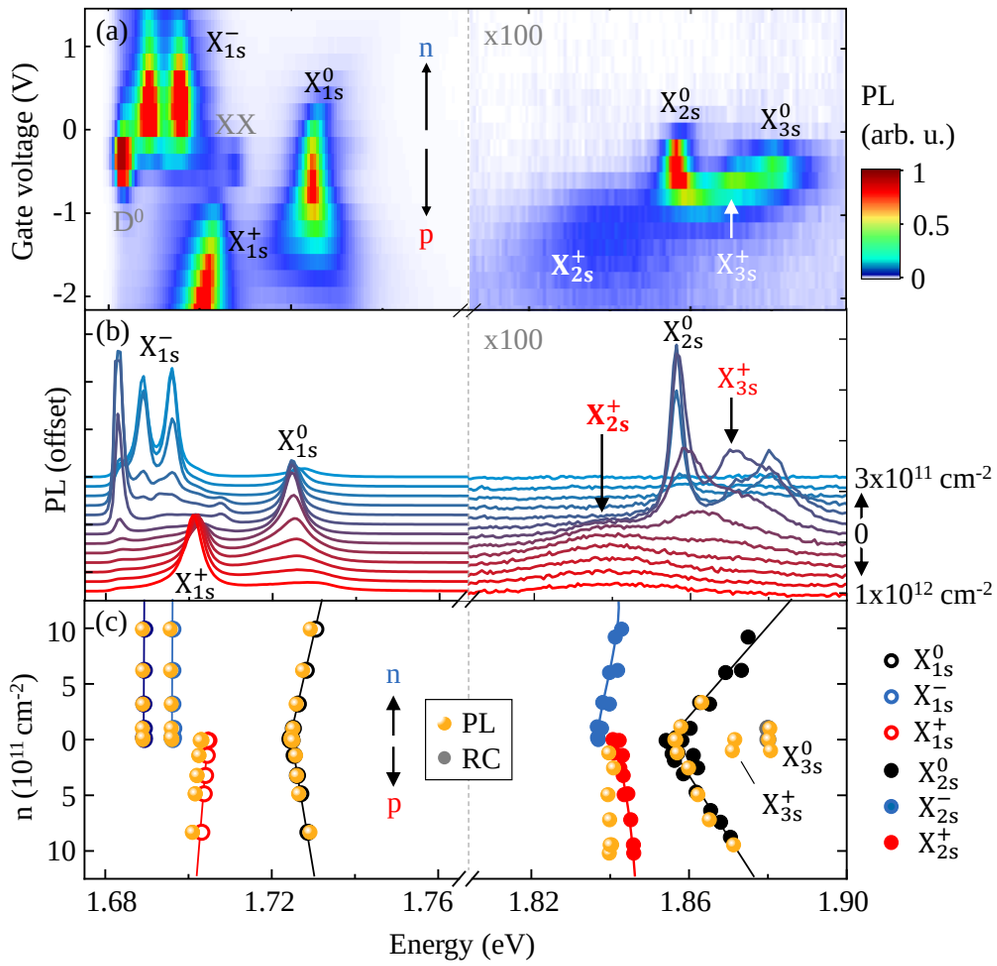

Figure 4.6: (a) Photoluminescence intensity as function of energy and gate voltage in the range of the ground state (1s) and excited state (2s, 3s) X^0 exciton in hBN-encapsulated monolayer WSe_2 at T = 5 K. (b) Selected, individual PL spectra from (a). (c) Comparison of resonance energies extracted from PL and and reflectance contrast spectra.

state trions are observed for both 2s and 3s states on the p-doped side. Similar to the reflectance measurements, the excited state trions are characterized by a large linewidth broadening on the order of $\geq$ 10 meV, governed by the autoionization process, introduced in previous section. A carrier-mediated 2s $\rightarrow$ 1s scattering rate on the order of 10 meV corresponds to an autoionization time of $\approx$ 30 fs ($\Delta E \Delta t \approx \hbar/2$), which is much shorter compared to the neutral 2s exciton non-radiative dephasing time of $\approx$ 130 fs [73]. This is also consistent with the observed lower intensity of the excited state trion emissions compared to the excited state excitons. In the n-doped side no features of excited state trions are observed. Different to monolayer $MoSe_2$ [74, 75], no n-type excited state trions have been observed in PL. Also in another report about excited state trions in monolayer

WSe_2, no n-type excited state trions are observed [183]. The exact mechanism of this electron-hole asymmetry is yet unclear.

In Figure 4.6(c), the emission energies are summarized and compared with the resonance energies from reflectance measurements. Particularly, the ground state exciton and trion emission energy closely follow the resonance energies from reflectance contrast. Also for the excited sate exciton, the extracted energies from PL and reflectance measurements closely match each other. Only for the excited state trion a small Stokes shift is observed. Note that at higher carrier densities an increasing Stokes shift is observed also for ground state trions (not investigated in this work) [44, 183].

To conclude with, the experimental observations demonstrate the existence of meta-stable negatively and positively-charged excited state trions. Importantly, excited state trions are characterized by autoionization, which manifests in an additional linewidth broadening of about 10 meV. Furthermore, excited states are characterized by overall stronger exciton-carrier interactions compared to the ground state, evidenced in the energy dependence, oscillator strength and linewidth broadening of excited state excitons and trions.

4.2 Exciton-carrier scattering in the presence of finite dissipation

In this section, the already mentioned exciton-carrier scattering will be investigated in more detail. In Fig. 4.7(a) the reflectance contrast spectra of p-doped hBN-encapsulated monolayer WSe_2 is presented at two temperatures T = 5 K and T = 30 K. In both measurements the doping is fixed to an equal value of $\approx 2\times10^{12}$ cm^{-2}. The spectrum is presented in the energy range of the ground state trion X^+ and exciton X^0. Due to the higher temperature, at T = 30 K the trion is slightly shifted towards lower energies. In Fig. 4.7(b), the reflectance contrast derivative $\partial R_c/\partial E$ of the two temperatures is compared at the trion resonance X^+. While the general lineshape is similar for both temperatures, the trion exhibits a slightly broader linewidth at T = 30 K compared to the trion at T = 5 K. The broadening is qualitatively illustrated by dashed lines. The increase of the linewidth mostly stems from temperature-activated scattering with linear acoustic phonons. As demonstrated in Ref. [214], the trion-phonon scattering in hBN-encapsulated monolayer WSe_2 is on the order of $\approx$ 70 μeV/K. Thus, a temperature increase of ΔT = 25 K should result in a broadening of $\approx$ 2 meV. Note that potential contributions from the electron recoil effect may lead to an additional increase of

the trion linewidth with increasing temperature. This effect will be discussed in detail in section 4.3.

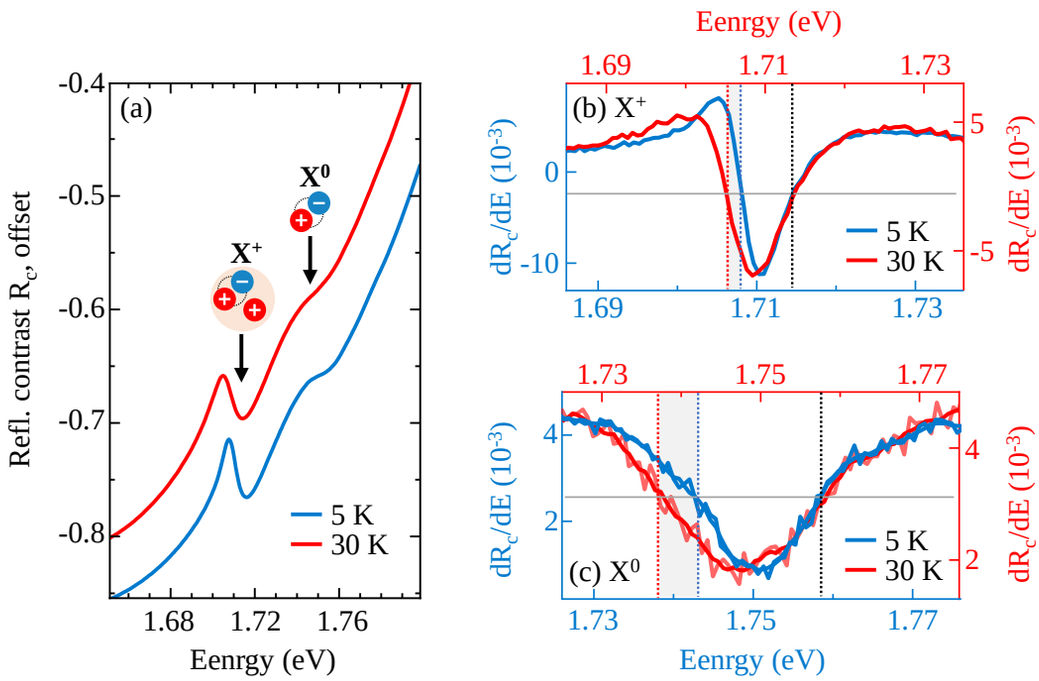

Figure 4.7: (a) Reflectance contrast spectrum R_c of a p-doped hBN-encapsulated monolayer WSe_2 at a temperature of 5 and 30 K in the energy range of the ground state exciton X^0 and trion X^+. The doping density is equal in both measurements and on the order of 2×10^{12} cm^{-2}. (b) Comparison of reflectance contrast derivative $\partial R_c/\partial E$ of the spectra presented in (a) in the energy range of the trion X^+. For better comparison, the two curves are relatively shifted in energy. Dashed lines qualitatively illustrate the broadening of the resonances. The grey shading illustrates the difference of the broadening between 5 and 30 K. Note that the illustrated broadening serves only as a qualitative illustration, as the derivatives of the spectra are shown. (c) Same data as in (b) in the energy range of the X^0 exciton.

While the trion linewidth is predominantly determined by phonon scattering, it is hardly affected by free carrier scattering, cf. Fig. 4.5. Differently, as demonstrated in previous section and other reports [252, 74, 75], the exciton linewidth strongly increases with free charge carrier density. Consistently, in Fig. 4.7(a), the exciton exhibits a much larger linewidth compared to the trion. The exciton broadening also increases with temperature, cf. Fig. 4.7(c). Interestingly, it broadens stronger than the trion linewidth, cf. grey shading in Fig. 4.7(b) and (c).

In Fig. 4.8(a), the non-radiative X^0 exciton linewidth Γ_X at T = 5 K and T = 30 K is presented as function of carrier density, represented by the relative exciton-trion separation $\Delta E_{XT} \approx E_F \propto n$. Correspondingly, the lower panel shows the

determined trion linewidths Γ_T. The linewidths are obtained by fitting the exciton and positively- as well as negatively-charged trion resonances in voltage-dependent reflectance contrast spectra in the n- and p-doped regime with a parameterized transfer matrix model. As discussed above, the trion linewidth hardly depends on the electron or hole concentration in this density regime. It is about 5 and 8 meV at 5 and 30 K, respectively. The difference of ≈ 3 meV between the two temperatures can be well explained by temperature-activated phonon-scattering [214]. By contrast, the exciton linewidth strongly increases with carrier density. Focusing on the p-doped side at T = 5 K, the exciton linewidth increases from about 4.5 meV at zero doping to about 15 meV at a relative exciton-trion energy separation of $\Delta E_{XT} = 10$ meV. At T = 30 K, the exciton linewidth increases much stronger. It increases from about 7 meV to about 20 meV at $\Delta E_{XT} = 10$ meV. Thus, at a temperature of 30 K the exciton linewidth is about 10 meV larger compared to 5 K at a free carrier concentration corresponding to $\Delta E_{XT} = 10$ meV. Furthermore, for both temperatures the exciton linewidth broadening depends on whether electrons or holes are doped. As indicated by dashed lines, the carrier-induced linewidth broadening is weaker for electron doping. At T = 30 K and $\Delta E_{XT} = 10$ meV, the exciton linewidth in the n-doped side is up to 25% smaller than in the p-doped side. By contrast, the trion linewidth does not depend on whether the system is electron- or hole-doped.

The observed differences in the exciton linewidth broadening indicate that the exciton-carrier scattering is crucially determined by a temperature-activated process. In the following, an analytical expression for the exciton linewidth is presented which roots on exciton-carrier interactions in the presence of an additional dissipation channel. The approach is based on a Fermi polaron formalism [169, 251], derived by Zakhar A. Iakovlev and Mikhail M. Glazov from the Ioffe Institute in Saint Petersburg. Similar to the model presented in section 4.1, the interaction of the exciton with the Fermi gas is calculated by the excitonic Green's function

$$\mathcal{G}_X(\epsilon, \boldsymbol{k}) = \frac{1}{\epsilon - \Sigma_X(\epsilon, \boldsymbol{k}) - \frac{\hbar^2 k^2}{2m_X} + i\delta/2}, \tag{4.11}$$

with energy ϵ, exciton wavevector $\boldsymbol{k}$- and, different from Equation 4.1, with a finite dissipation δ. $\Sigma_X(\epsilon, \boldsymbol{k})$ is the self energy describing the exciton interaction with the Fermi sea. The self energy is a $\boldsymbol{k}$ and ϵ-dependent potential mimicking the effect of the free electrons on the propagation of the exciton. The carrier-induced broadening of the individual resonances is given by $\Gamma = -2\mathrm{Im}\Sigma_X(\epsilon, 0)$. For low

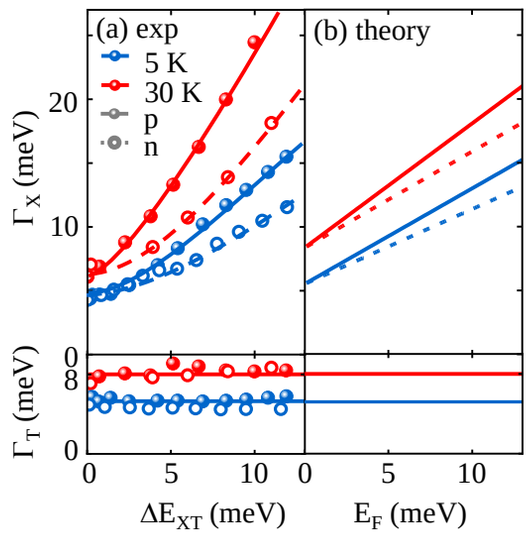

Figure 4.8: (a) Experimentally-determined non-radiative linewidth broadening Γ_X of the X^0 exciton (top panel) and Γ_T of trions $X^{\pm}$ (lower panel) as function of the relative exciton-trion separation $\Delta E_{XT} \approx E_F \propto n$ at T = 5 K and T = 30 K in hBN-encapsulated monolayer WSe_2. (b) Calculated non-radiative exciton linewidth as function of Fermi energy considering a finite dissipation $\delta = \Gamma_T$. Γ_T is set to the value determined in the experiment, i. e., in the lower panels in (a).

carrier densities, i. e., $E_F \to 0$, the trion and exciton linewidths are given by [256]

$$\Gamma_X = \delta + E_F \frac{m_T}{m_X} \frac{\pi}{\ln^2 \left[\delta/(2E_{b,T})\right] + \pi^2/4} \tag{4.12}$$

$$\Gamma_T = \delta. \tag{4.13}$$

with exciton and trion masses $m_X = m_e + m_h$, $m_T = m_X + m_e$ as well as trion biding energy $E_{b,T}$. In Equation 4.12, it is considered that $\delta \ll E_{b,T}$ and that the Fermi sea is degenerate.

Consistent with the experimental observation, the linewidth broadening of the trion is constant, i. e., it does not depend on the Fermi energy. In particular, it is given by the dissipation δ, which is typically dominated by the scattering with phonons in monolayer TMDCs [214]. Generally, δ is determined by all scattering process apart from the scattering with electrons, e. g. also the scattering with defects or other excitons, cf. Fig. 4.9(a). In this case the dissipation is given by

$$\delta = \Gamma_{\text{phon}} + \Gamma_{\text{defect}} + \Gamma_{\text{X}}. \tag{4.14}$$

By contrast, the exciton linewidth, which is directly related to the exciton-carrier scattering rate, linearly increases with Fermi energy, i. e., $\Gamma_X \propto E_F$. Importantly,

also Γ_X crucially depends on a finite dissipation. At $\delta = 0$ both, constant and carrier-induced scattering vanish in Equation 4.12. Thus, the dissipation δ is *necessary* for finite exciton-carrier scattering. The significance of the dissipation δ can be understand by considering a degenerate Fermi sea where e. g. the conduction band is occupied up to the Fermi energy $E_F \gg k_B$T. In the case of no dissipation, the exciton-carrier scattering is limited to electrons at the Fermi edge. Electrons inside the Fermi sea do not contribute to the scattering due to Pauli-blocking, i. e., there is no free final state inside the Fermi sea where the electron can scatter into. Consequently, increasing the free carrier concentration does not result in an enhanced exciton-carrier scattering and the exciton-carrier scattering is negligible. In the case of a finite dissipation, also electrons inside the Fermi sea contribute to the scattering. The dissipation effectively relaxes energy and momentum conservation and provides a free state where the electron can scatter into, cf. Fig. 4.9(b).

In Fig. 4.8(b), the theoretically expected exciton and trion linewidth broadening is presented as function of Fermi energy $E_F \approx \Delta E_{XT}$ considering Equation 4.12 for T = 5 and T = 30 K. δ is set to the trion linewidth observed in the experiment. Note that the temperature dependence in Equation 4.12 enters only through the trion linewidth. The model closely follows the experimental observation. In both, theory and experiment the carrier-induced exciton scattering rate increases stronger at T = 30 K in comparison to T = 5 K. The analytic approach also describes the slightly different slopes observed for n- and p-doping. Due to a higher binding energy of n-type trions, Equation 4.12 predicts a weaker increase in the presence of electrons compared to holes. The difference of exciton-electron and exciton-hole scattering is also consistent with an approximately 10% larger hole mass compared to the electron mass in monolayer WSe_2 [126], i. e., an exciton is stronger affected by the scattering with the heavier hole compared to the lighter electron (see also Equation 2.9 in section 2.5).

From Equation 4.12 it particularly follows that the exciton scattering is determined by the dissipation and thus by the trion linewidth. To test this, multiple measurements on different samples and positions are performed with slightly different trion linewidths Γ_T. In Fig. 4.9(c), the extracted slope of the exciton linewidth, i. e., the carrier-induced exciton scattering rate coefficient $\Gamma_X/\Delta E_{XT} \propto \Gamma_X/n$ is plotted as function of the trion linewidth normalized to the trion binding energy $\Gamma_T/E_{b,T}$. Each data point corresponds to a voltage-dependent reflectance contrast measurement at T = 5 K, i. e., each value corresponds to the slope of the carrier-induced exciton linewidth broadening obtained from multiple individually

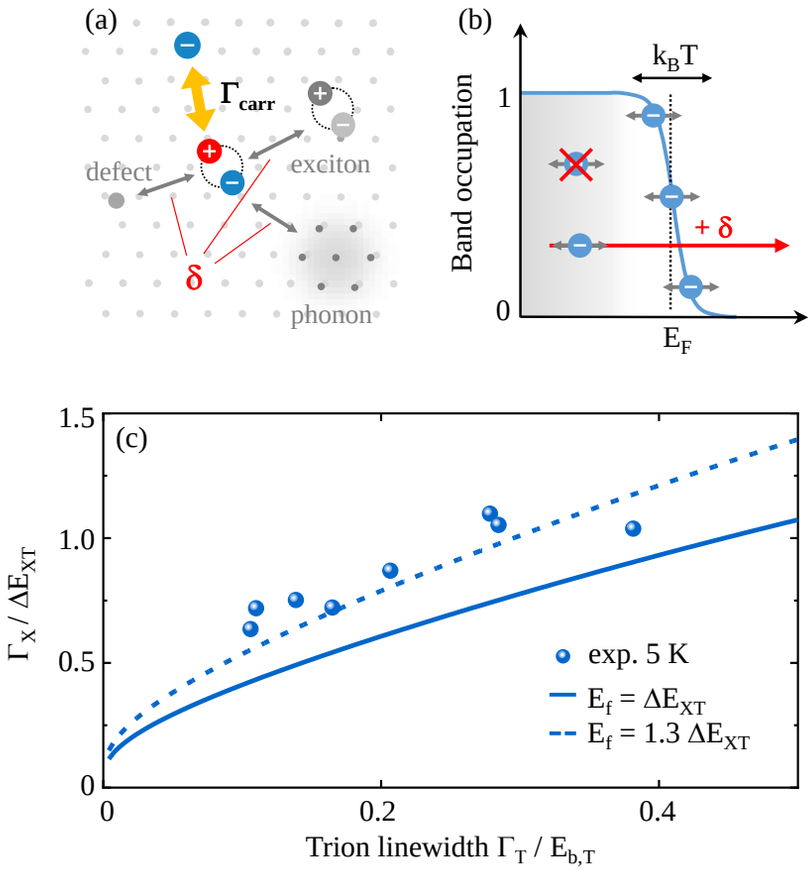

Figure 4.9: (a) Schematic illustration of exciton scattering channels in a semiconductor. The exciton-carrier scattering rate Γ_{carr} crucially depends on a finite dissipation δ, determined by e. g. scattering with phonons, defects or other excitons. (d) Illustration of electron band occupation at finite Fermi energies $\mathrm{E}_F > k_B\mathrm{T}$. Only with additional dissipation δ carriers inside the Fermi sea contribute to exciton-carrier scattering. (c) Exciton scattering rate $\Gamma_X/\Delta E_{XT}$ as function of $\Gamma_T/E_{b,T}$ at $\mathrm{T} = 5$ K. $\Gamma_X/\Delta E_{XT}$ is determined from linearly fitting carrier density-dependent reflectance contrast spectra in the free carrier density range $\Delta E_{XT} \lessapprox 6$ meV. Blue lines correspond to Equation 5.4 assuming $E_F = \Delta E_{XT}$ and $E_F = 1.3\Delta E_{XT}$.

fitted reflectance contrast spectra. The carrier-induced scattering rate coefficient increases with increasing dissipation (trion linewidth). In the best samples, with trion linewidths as small as 2.7 meV, carrier-induced scattering rate coefficients of 0.7 are observed, corresponding to a linewidth broadening of 0.4 meV/(10^{11} cm^{-2}). For a quantitative comparison, Equation 4.12 is plotted in Fig. 4.9(c). The experiment is best described by a scaling factor of 1.3 between E_F and ΔE_{XT} (In the Fermi polaron picture the scaling factor is ≈ 1.5, in the bare trion picture it is ≈ 0.7).

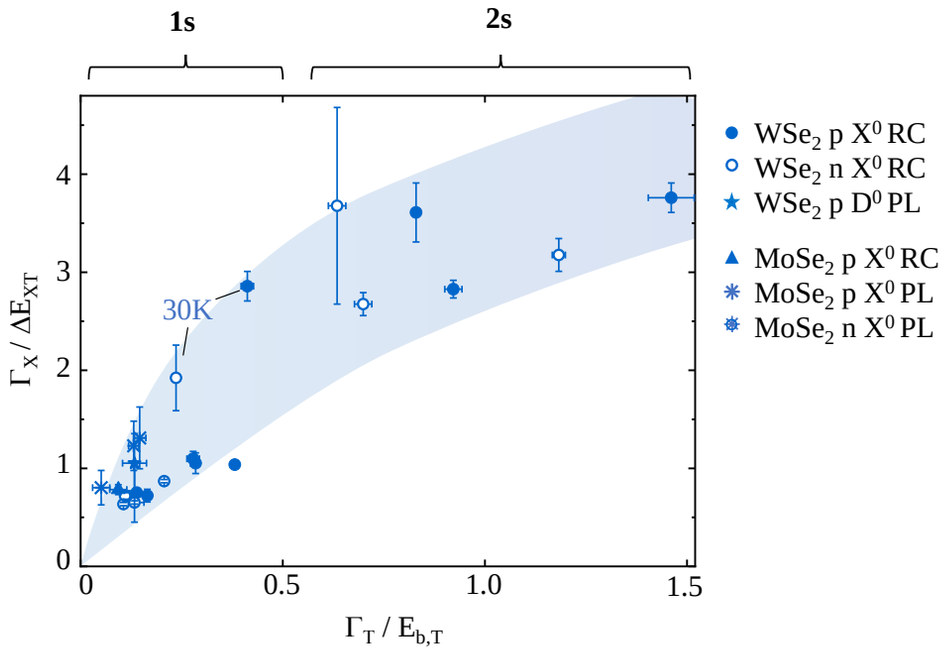

Figure 4.10: Experimentally determined exciton-carrier scattering rates $\Gamma_X/\Delta E_{XT}$ as function of $\Gamma_T/E_{b,T}$. The data is determined from voltage-dependent linewidth analysis of multiple reflectance contrast (RC) and PL measurements on monolayer WSe_2 and $MoSe_2$, including bright 1s and 2s X^0 excitons as well as dark excitons D^0. All data points correspond to measurements at T = 5 K except the two indicated measurements at T = 30 K. The blue shading is a guide to the eye.

For an extended overview, in Fig. 4.10 experimentally-determined carrier-induced scattering rate coefficients $\Gamma_X/\Delta E_{XT}$ are summarized as a function of $\Gamma_T/E_{b,T}$, including reflectance contrast as well as PL measurements of the bright exciton ground and first excited state of WSe_2 and $MoSe_2$ monolayer structures. Particularly, Fig. 4.10 includes the data presented in Fig. 4.9(c). Moreover, voltage-dependent PL linewidth broadenings of dark excitons (D^0) in monolayer WSe_2 are included. Similar to Fig. 4.9(c), the carrier-induced scattering rate coefficient increases with increasing trion linewidth. The largest values of ≈ 3.5 corresponds to excited state excitons with a slope of ≈ 2.5 meV/(10^{11} cm^{-2}) and are almost an order of magnitude larger compared to the smallest values obtained for ground states. Interestingly, the observed trend qualitatively follows Equation 4.12 although the above presented model is limited to $\delta \ll E_{b,T}$, i. e., $\Gamma_T/E_{b,T} < 1$. While for a quantitative description the distinct structure of the exciton should be considered, e. g., different interaction matrix elements for ground and excited states, the presented investigation demonstrates the general dependence of exciton-carrier scattering, which is crucially determined by the trion linewidth and

trion binding energy. As a practical consequence, reducing the trion linewidth, leads to a reduction of exciton-carrier scattering. Particularly, the findings provide a lower limit for the exciton-carrier scattering rate in doped two-dimensional semiconductors. In an ideal sample, the trion scattering rate is limited by the scattering with phonons. Considering a trion binding energy of 20 meV and a temperature-activated scattering rate due to acoustic phonon scattering of ≈ 50 μeV/K, the minimum exciton-carrier scattering rate coefficient is ≈ 0.2 at T = 5 K. In p-doped WSe_2 monolayers this corresponds to a carrier-induced linewidth of 0.13 meV/(10^{11} cm^{-2}). It means that for $n_h \approx 2 \times 10^{11}$ cm^{-2} the exciton-carrier scattering becomes comparable with the exciton-phonon scattering and the carrier-induced exciton linewidth reaches 1 meV only at a hole density of $n_h \approx 8 \times 10^{11}$ cm^{-2}.

4.3 Electron recoil effect and carrier-induced cooling dynamics

As outlined in section 2.3, trions can be created by optically exciting an electron-hole pair, which simultaneously binds to a resident free hole or electron. The other way around, the excitonic core within the trion can recombine radiatively leaving behind a free charge carrier. By transferring its center-of-mass momentum to the remaining free carrier, trions can recombine at finite momenta. This stands in stark contrast to the bare exciton, which is only optically accessible at small momentum, i. e., radiative exciton recombination is only possible within the light-cone. In optical spectroscopy, the free carrier-assisted recombination of finite-momentum trions manifests in a characteristic asymmetric low-energy flank in luminescence. The so-called electron recoil effect has been studied in 2D quantum wells [267, 268] and more recently observed in TMDCs [66]. While the asymmetric emission profile has been identified in several systems, including monolayer $MoSe_2$ [66, 78], MoS_2 [43] and WSe_2 [79], the effect has been exclusively addressed in steady-state experiments so far. In the following, the electron recoil effect is explored in time-resolved photoluminescence experiments giving direct access to relaxation and cooling dynamics in an electrically-tuneable $MoSe_2$ monolayer.

4.3.1 Electron recoil in monolayer $MoSe_2$

The electron recoil effect is studied in an electrically-tuneable hBN-encapsulated monolayer $MoSe_2$, which is characterized by narrow exciton linewidths of < 2

meV across large areas of many μm^2. For excitation, the pulsed 140 fs, 80 MHz Ti:Sapphire laser is tuned to an excitation energy of 1.657 eV slightly above the X^0 resonance. The injected electron-hole pair density is set to 4×10^{11} cm^{-2}. In Fig. 4.11(a) and (b) the PL intensity as function of energy and gate voltage is

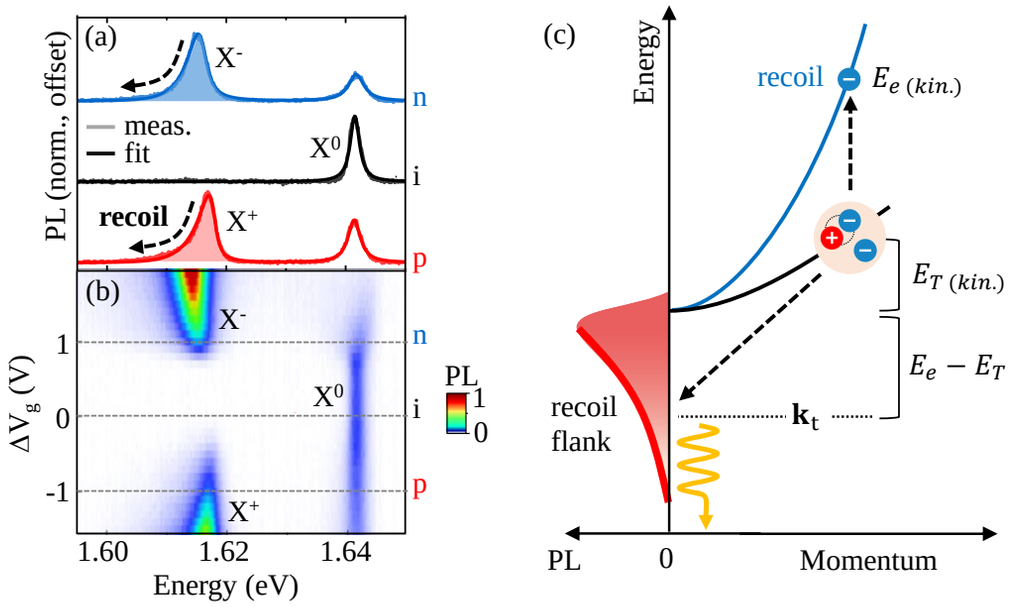

Figure 4.11: (a) Photoluminescence spectra of monolayer $MoSe_2$ at T = 5 K in the n- and p-doped as well as intrinsic regime of the ground state exciton X^0 and trions $X^{\pm}$. (b) PL intensity as function of energy and gate-voltage. Dashed lines correspond to spectra shown in (b). A voltage of ± 1 V corresponds to a change of the free carrier density of 1.6×10^{11} cm^{-2} and 2.9×10^{11} cm^{-2} in the p- and n-doped regime, respectively. (c) Schematic illustration of the electron recoil effect.

presented in the range of the ground state exciton X^0 at 1.642 eV at a temperature of T = 5 K. While the neutrality regime is characterized by a single exciton resonance, at finite doping the trion or attractive Fermi polaron resonance appears [66, 252, 269]. For p- and n-type trions the respective binding energies are 25 and 27 meV. Interestingly, the trion emission profiles exhibit pronounced low energy flanks [267], whereas the exciton is characterized by a symmetric emission line shape.

The low energy flank of the trion emission is a direct consequence of energy and momentum conservation during radiative recombination [268, 267]. Fig. 4.11(c) schematically illustrates the recombination of a trion with finite momentum. During the recombination of an electron-hole pair within the trion, i. e., the ex-

citonic core, the trion momentum $\mathbf{k}_\mathrm{T}$ is transferred to the remaining electron (vertical dashed line). Considering that the kinetic energy of the recoiled electron is $E_{\mathrm{e(kin.)}} = \hbar^2\mathbf{k}_\mathrm{T}^2/(2m_e)$ the detected trion emission energy is $E_\mathrm{T} + E_{\mathrm{T,(kin.)}} - E_{\mathrm{e(kin.)}}$. Here, E_T is the trion resonance energy at zero momentum and $E_{\mathrm{T(kin.)}} = \hbar^2\mathbf{k}_\mathrm{T}^2/(2m_\mathrm{T})$ is the trion's kinetic energy with $m_\mathrm{T} = m_X + m_e$. There are two main consequences. First, trions with $\mathbf{k}_\mathrm{T} > c\mathbf{k}$ can radiatively recombine by transferring their momentum to the remaining electron, i. e., trions can recombine radiatively outside the light-cone. Second, a trion with higher kinetic energy emits a photon at lower energies. Considering that high energy states are less occupied then low energy states, the emission lineshape is characterized by a *low*-energy flank observable in emission experiments [267].

For a quantitative approach a derivation of an analytic expression describing the asymmetric emission lineshape is given. The calculation is performed by Marina M. Semina and Mikhail M. Glazov form the Ioffe Institute [251]. Following Ref. [267], in the trion picture the recombination rate is given by a modified version of Fermi's golden rule

$$W^{tr}(\omega) = \frac{2\pi}{\hbar}\sum_{\boldsymbol{k}} f_{\boldsymbol{k}} |M^{T,opt}(\boldsymbol{k})|^2 \delta(\hbar\omega + E_{\mathrm{e(kin.)}} - E_\mathrm{T} - E_{\mathrm{T(kin.)}}). \tag{4.15}$$

Here, the delta function ensures energy conservation and $f_{\boldsymbol{k}}$ is the distribution function in the Boltzmann approximation

$$f_{\boldsymbol{k}} = \mathcal{N}\exp\left(-\frac{\hbar^2 k^2}{2m_T k_B T^*}\right) \tag{4.16}$$

with effective trion temperature T^* and normalization constant $\mathcal{N}$. The transition matrix element is given by [267, 169]

$$M^{T,opt}(\boldsymbol{k}) = \mathfrak{M}_r \int \varphi(0,\boldsymbol{\rho}) e^{-\mathrm{i}\boldsymbol{k}\boldsymbol{\rho}(m_X/m_T)} d\boldsymbol{\rho}. \tag{4.17}$$

with the trion envelope function $\varphi(\boldsymbol{\rho}_1, \boldsymbol{\rho}_2)$. $\boldsymbol{\rho}_{1,2}$ are the relative coordinates of the electrons with respect to the hole. The PL spectrum is calculated by

$$\begin{aligned} I_{PL} \propto W^{tr}(\omega) \propto \exp\left(\frac{\hbar\omega - E_T}{k_B T^*}\frac{m_e}{m_X}\right) \\ \times \left| M^{tr,opt}\left(\sqrt{\frac{2m_e m_{tr}(E_0^{tr} - \hbar\omega)}{m_X\hbar^2}}\right)\right|^2 \Theta(E_0^{tr} - \hbar\omega). \end{aligned} \tag{4.18}$$

The PL intensity is determined by two contributions: an exponential term resembling the Boltzmann distribution and the transition matrix element. To estimate the latter, a trion envelope wavefunction of the following form is used [257, 165, 166]

$$\varphi(\boldsymbol{\rho}_1, \boldsymbol{\rho}_2) = e^{-\rho_1/a_X} e^{-\rho_2/a_T} + e^{-\rho_2/a_X} e^{-\rho_1/a_T}, \tag{4.19}$$

with a_X and a_T being effective exciton and trion Bohr radii. Assuming low carrier densities with the Fermi energy being smaller than the trion binding energy and the thermal energy of the trion gas, i. e., $\hbar^2 N_e/m_e \ll E_{b,T}, k_B T_*$, Equation 4.17 is evaluated

$$\begin{aligned} M^{tr,opt}(\boldsymbol{k}) = & \frac{\mathfrak{M}_r}{\sqrt{a_T^2 a_X^2/8 + 2a_T^4 a_X^4/(a_T + a_X)^4}} \\ & \times \left(\frac{a_T^2}{[1 + a_T^2 k^2 (m_X/m_T)^2]^{3/2}} + \frac{a_X^2}{[1 + a_X^2 k^2 (m_X/m_T)^2]^{3/2}} \right), \end{aligned} \tag{4.20}$$

and plotted in Fig. 4.12 as function of the kinetic excess energy of the trion for material-realistic parameters. It exhibits a strong energy dependence which originates from the wavefunction overlap of the trion and free electron. For higher kinetic energies the overlap and thus the transition matrix element becomes rapidly smaller as schematically illustrated in the top panels of Fig. 4.12.

The above presented approach roots in the trion picture, namely a three-body problem. A similar result can be derived in the Fermi polaron picture [251]. Herein, the recombination is approached by considering the exciton being a rigid dipole interacting with Fermi sea excitations.

In close analogy to the trion approach, the recombination of a high momentum polaron results in a low energy emission flank. While the exciton recombines, the Fermi sea gets excited and the excess momentum is absorbed. Notably, in the Fermi polaron picture, both, the repulsive and attractive branch exhibit a low energy flank. However, for the repulsive branch, its influence on the emission shape is expected to be negligible at low carrier densities. The reason for this difference can be explained by the competition of two distinct recombination processes: first, the direct radiative recombination where the Fermi sea remains in an unperturbed state, and second, the indirect carrier-induced recombination where the Fermi sea is excited. Only in the case of small oscillator strengths, which is in the regime of $E_F \ll k_B T^*$ (T^* is the trion temperature), the carrier-induced recombination becomes dominant and results in a low energy tail. By contrast, for a large oscillator strength, the indirect recombination becomes negligible and the emission is

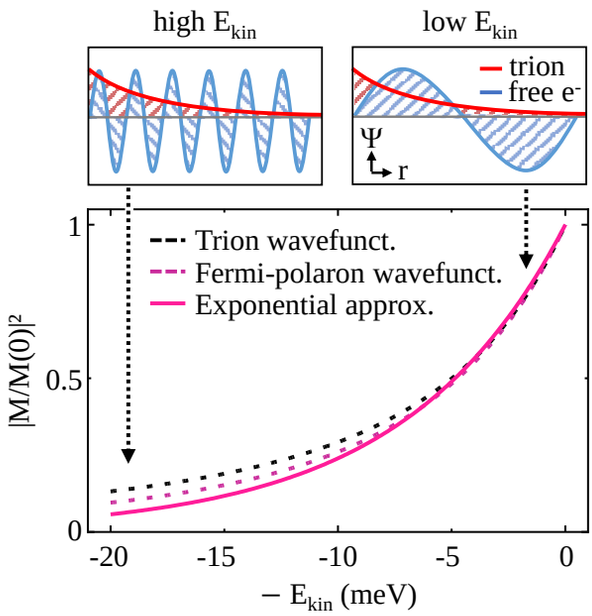

Figure 4.12: Dependence of the transition matrix element M on the kinetic energy considering a trion and Fermi Polaron wavefunction or an exponential approximation. The trion radius is $a_T = 3a_X$ and the obtained binding energy is $E_{b,T} = 17$ meV. For the Fermi polaron the binding energy is set to $E_{b,T} = 25$ meV. In the exponential approximation $\epsilon_1 = 7$ meV. Boxes in the top panel show schematic illustration of the trion/Fermi polaron and free-electron wavefunction overlap at high and low kinetic energies.

dominated by a symmetric profile. At low carrier densities, the repulsive Fermi polaron branch is characterized by a large oscillator strength and thus, the emission shape is symmetric. Differently, the attractive branch exhibits only a small oscillator strength and the emission is dominated by a low energy tail. For comparison, the transition matrix element in the Fermi polaron approach is plotted in Fig. 4.12(c) (for more details on the calculation refer to Ref. [251]). It closely follows the transition matrix element derived in the trion picture. Particularly, at low kinetic energies, the two functions coincide.

Having derived the transition matrix elements, Equation 4.18 can be evaluated. For simplicity, the transition matrix element is approximated by an exponential function [267]. Particularly, in the low energy regime the exponential approximation well agrees with both presented approaches, cf. solid purple line in Fig. 4.12(c). The PL spectrum simplifies to

$$I_{PL} = I_0(\epsilon) \otimes \exp(\epsilon/\epsilon^*)\Theta(-\epsilon), \tag{4.21}$$

with the convolution symbol $\otimes$ and $\epsilon = \hbar\omega - E_T$. The first term $I_0(\epsilon)$ is a Lorentzian and corresponds to the *symmetric* linewidth broadening Γ representing the dephasing, e. g. due to phonons. The second term is an exponential function resulting in a low-energy flank which originates from the carrier-assisted recombination assuming Boltzmann-distributed states. ϵ^* is given by [267]:

$$\frac{1}{\epsilon^*} = \frac{1}{\epsilon_1} + \frac{1}{k_B T^*}\frac{m_e}{m_X}. \tag{4.22}$$

Here, the first term accounts for the kinetic energy dependence of the light-matter coupling strength which is calculated from the dipole matrix element. Typically, the constant ϵ_1 is roughly on a similar order of magnitude as the trion binding energy. The second term resembles the trion distribution in the Boltzmann approximation and depends on the effective trion temperature T^*.

Focusing again on the experiment, in Fig. 4.13 (a), temperature-dependent PL spectra are presented in the range of the positively-charged trion. The free carrier density is set to 1×10^{11} cm^{-2}. Temperature-induced doping effects are compensated by manually adjusting the gate voltage at each temperature. The carrier density fluctuation determined by the relative exciton-trion energy shift remains below 6×10^{10} cm^{-2}, cf. Fig. 4.13(b). The emission lineshape is governed by the characteristic low-energy flank. With increasing lattice temperature, the low-energy tail becomes broader indicating an increased trion temperature. For a quantitative analysis, the data is fitted by Equation 4.21. To take realistic experimental conditions better into account, the described profiles are extended by additionally considering inhomogeneous broadening. Equation 4.21 is convoluted by a Gaussian profile with a fixed inhomogeneous broadening $\Gamma_{\text{inhom}} = 1$ meV. Free fit parameters are the amplitude, resonance energy E_T, symmetric broadening Γ and ϵ^*. The fitted values, represented by k_B/ϵ^*, are summarized in Fig. 4.13(c) as function of inverse lattice temperature. Approximating $T^* = T_{\text{lattice}}$, the slope of the line fit yields a mass ratio $m_h/m_X = 0.44$, consistent with similar electron and hole masses determined in *ab initio* calculations [126]. Moreover, the temperature-dependent recoil analysis gives access to the light-matter coupling strength ϵ_1, which is determined to be 7 meV. As illustrated in Fig. 4.12, the latter value is reasonable considering a trion binding energy of 25 meV.

4.3.2 Trion cooling dynamics

In order to gain access to time-resolved trion cooling dynamics, the emission is detected by a streak camera detector. In Fig. 4.14(a), PL spectra of the pos-

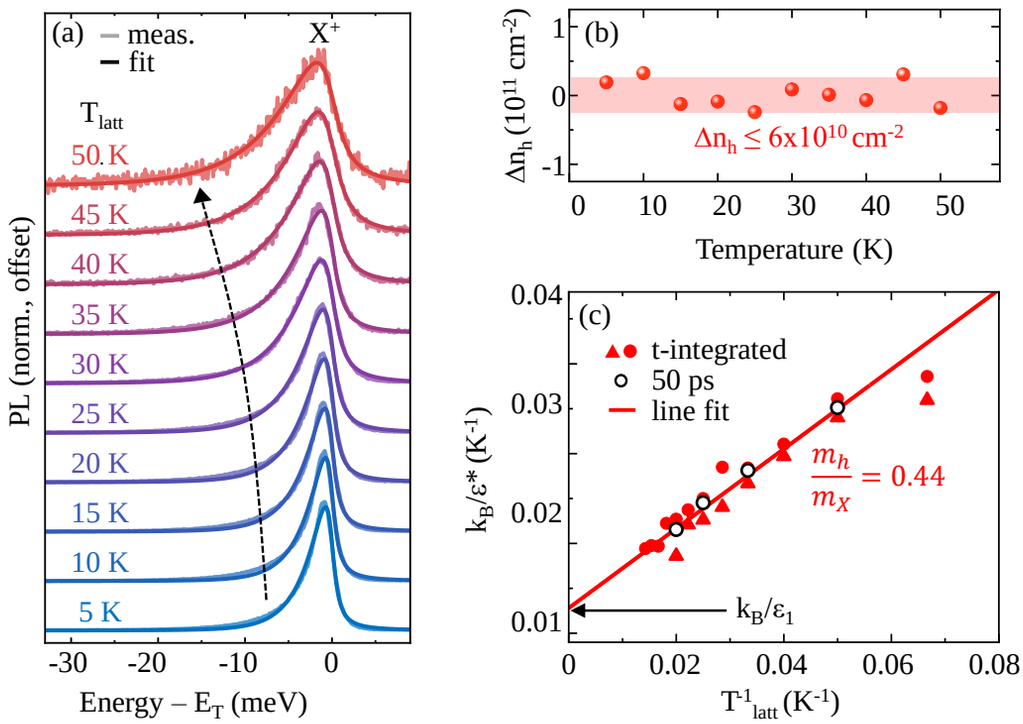

Figure 4.13: PL spectra of the trion/Fermi polaron X^+ as function of energy for selected temperatures in hBN-encapsulated monolayer $MoSe_2$. The free carrier density is tuned to 1×10^{11} cm^{-2} for all temperatures. Saturated lines correspond to the convolution fit presented in Equation 4.21. (b) Carrier density fluctuation in the measurement presented in (a) obtained by the relative exciton-trion separation. (c) Extracted low energy exponent k_B/ϵ^* as function of inverse lattice temperature T^{-1} for $T \geq 15$ K. Red triangles and dots correspond to measurements on two different sample positions. Solid line is a line fit considering Equation 4.22. The slope is $m_h/m_X = 0.44$. For comparison, open circles correspond to data obtained from time-resolved measurements at $t = 50$ ps.

itively charged trion are presented for selected time intervals extracted from the 2D streak camera image plotted in Figure 4.14(b). The low-energy recoil flank decreases with increasing time. Only in the very first spectrum indiations of non-equilibrium distributions can be resolved. At later times, the flank is well described by a Boltzmann distribution with an effective trion temperature. The evolution of the recoil flank directly gives access to the transient trion temperature. Fitting each PL spectrum with the fit function given by Equation 4.21 (fixing $m_h/m_X = 0.44$ and $\epsilon_1 = 7$ meV), in Fig. 4.14(c), the effective trion temperature T^* is plotted as function of time. The measurement is repeated for several lattice temperatures. Independently from the lattice temperature, each curve is characterized by an initial excess temperature of about 20 K, which then

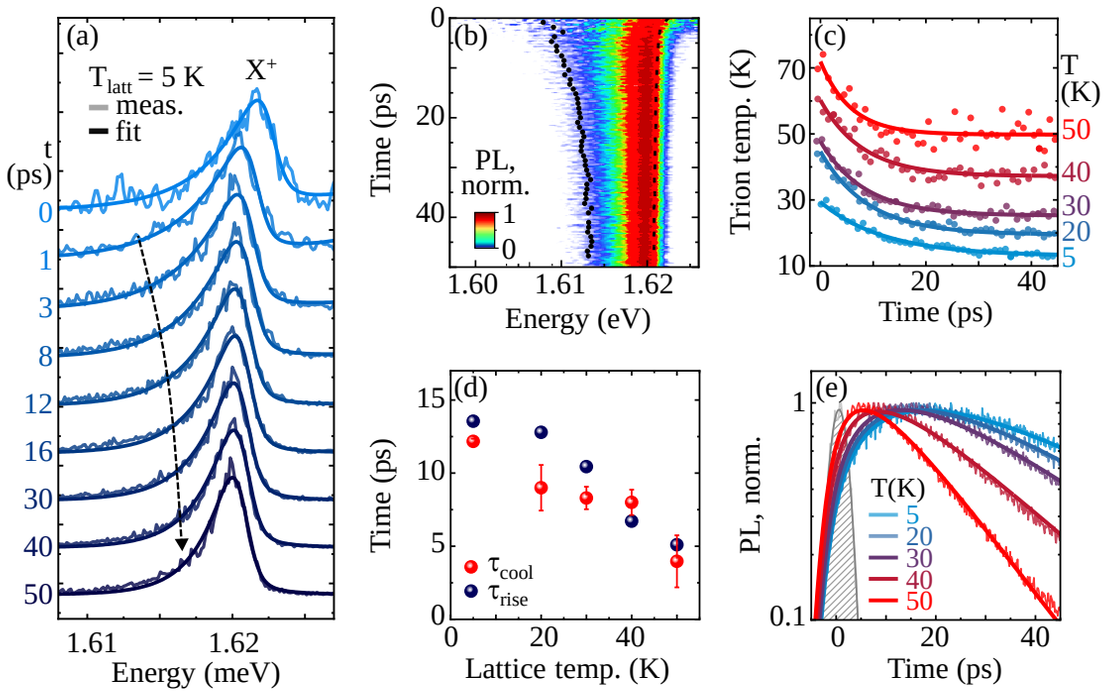

Figure 4.14: (a) PL spectra of the trion/Fermi polaron X^+ as function of energy at selected time intervals at T = 5 K lattice temperature after near-resonant excitation of the X^0 exciton at 1.663 eV in hBN-encapsulated monolayer $MoSe_2$. The estimated injected electron-hole pair density is 4.5×10^{11} cm^{-2}. The free carrier density is tuned to $\approx 7 \times 10^{10}$ cm^{-2}. (b) PL intensity as function of energy and time. Dashed line and dots corresponds to the extracted center energy $E_{T,0}$ and low energy exponent $E_T - 4\epsilon^*$, respectively. (c) Transient trion temperature for selected lattice temperatures. Solid lines correspond to mono-exponential fits. (d) $1/e$ cooling and rise times obtained from (c) and (e), respectively. (e) Normalized X^+ PL transients at selected lattice temperatures. Solid line corresponds to an exponential rise-decay model convoluted by the instrumental response function ($\Delta t_{\text{min}} = 4$ ps) indicated by the grey area.

decreases towards lattice temperature. The transient temperature is fitted by a mono-exponential fit. Fig. 4.14(d) shows the corresponding $1/e$ cooling times. At T = 5 K, the cooling times are in the range of 10 – 15 ps. With increasing temperature, the cooling becomes accelerated, reaching values of down to 5 ps at 50 K. For all measurements, the trion gas reaches lattice temperature after 50 ps. Note that the trion resonance exhibits a shift towards the low energy side within the first picoseconds. The energy shift is equally determined for the neutral exciton and is a typical observation related to the interplay of band gap and exciton renormalization at elevated pump densities [270, 271, 272].

Different to previous studies on exciton and trion dynamics in TMDCs, the recoil flank directly shows the energy distribution of the trions. This result is particularly interesting as it demonstrates that trions are thermalized within the first picoseconds, i. e., they can be approximated by Boltzmann-statistics. Most importantly, the analysis gives access to the trion temperature and cooling times. Typically, in quantum well systems carrier temperatures are determined by analyzing the plasma flank [68]. However, in TMDCs the latter is strongly suppressed. Therefore, the recoil analysis provides a novel and comparably easy tool (as it does not involve any pump-probe-like techniques) to determine the quasiparticle temperature.

The observed cooling times are on a similar order of magnitude as relaxation dynamics observed in other time-resolved studies on TMDC monolayers [107, 212]. At low temperatures and small doping $E_F \ll k_B T^*$, the cooling is dominated by the interaction with acoustic phonons and can be e. g. approximated via the deformation potential mechanism. Herein, the cooling time inversely scales with the trion mass and underlying carrier-phonon interactions. As the mechanism is expected to be similar for trions and excitons, the observed cooling times should approximately apply for excitons as well. However, due to less constituting particles and a lower total mass and therefore a weaker phonon coupling, exciton cooling is expected to be rather slower compared to trion cooling. From the same argument it follows that also free carrier cooling occurs on longer time scales. In pump-probe experiments on monolayer $MoSe_2$ electron cooling times are found to be on the order of 70 ps at T = 5 K [273], thus still in the same order of magnitude but longer compared to the observed trion cooling times of 10 to 15 ps.

The decrease of the cooling time with increasing temperature is related to the thermal activation of phonons. Within the first 10's of K only acoustic phonons contribute to the cooling. At higher temperatures more efficient high-energy phonons contribute and the cooling becomes much faster. As demonstrated in Refs. [203, 273], at T = 100 K, the cooling time is expected to be an order of magnitude faster compared to T = 5 K and is mostly governed by optical zone-edge phonons.

For comparison, in Fig. 4.14(e) the PL transients of the trion are presented. They are characterized by a short increase in the range of 10 ps and a subsequent decrease with a decay time on the order of 30 ps. *A priori* it is not clear whether the rise time belongs to the relaxation or recombination processes. For excitons in monolayer $MoSe_2$, it has been shown that the rise time corresponds to the radiative lifetime at T = 5 K [212]. Here, the rise time correlates with the determined

cooling time. The extracted $1/e$ PL rise times obtained from a bi-exponential approach $\propto (\tau_{decay} - \tau_{rise})^{-1}[\exp(-t/\tau_{decay}) - \exp(-t/\tau_{rise})]$ [78] are plotted in Fig. 4.14(d). The rise time closely follows the cooling time indicating that it is governed by the relaxation and cooling of the trion gas. It should be noted that in case of the trion, the rise time cannot be interpreted as radiative recombination time due to only a small trion oscillator strength, much smaller than that of the exciton (see e. g. data shown in Fig. 4.4).

So far, the investigations focus on the low carrier density regime where exciton-electron scattering is comparably weak. In order to explore the influence of free charge carriers on the trion cooling, a larger gate voltage is applied. In Fig. 4.15(a), trion PL spectra are presented at three distinct carrier densities. With increasing carrier density, the center energy shifts towards lower energies and the pronounced asymmetric profile at low densities (black curve) becomes a more and more symmetric profile (red curve). The latter can be explained by two effects. First, the symmetric linewidth, which is associated with the scattering rate, slightly increases with carrier density. Second, the trion/attractive polaron gains oscillator strength and the direct recombination increasingly dominates and the carrier-assisted recombination becomes comparably weaker.

To investigate the influence of the free carriers on the cooling dynamics, time-resolved PL measurements are preformed at T = 5 K as function of the free carrier density. As for the temperature-dependent dynamics, time-resolved profiles are analyzed by the fit based on Equation 4.21. In Fig. 4.15(b), the extracted transient trion excess temperature is plotted for a series of carrier densities from 5×10^{10} to 1.9×10^{12} cm^{-2}. The corresponding $1/e$ cooling times are summarized in Fig. 4.15(c). Similar to the temperature-dependent measurements, the excess temperature is about 20 K and independent from the carrier density. However, the cooling gets increasingly faster with increasing carrier density. While in the low carrier density regime $< 3 \times 10^{11}$ cm^{-2} the cooling is nearly constant, it drastically decreases at elevated densities. At 2×10^{12} cm^{-2} the cooling time accelerates to 5 ps. The carrier-mediated cooling rate is estimated to be 0.042 cm^2/s. It means that the contribution to the cooling time from carrier scattering is $\approx$ 200 ps at 1×10^{11} cm^{-2}, justifying that in this regime the cooling is dominated by phonon interactions and the carrier-scattering only dominates at elevated densities. For comparison, in Fig. 4.15(d), the PL rise times, extracted from Figure 4.15(c), are plotted. As in the temperature-dependent study, the PL rise time closely follows the cooling time, further justifying the interpretation of the PL rise time being associated with the cooling time.

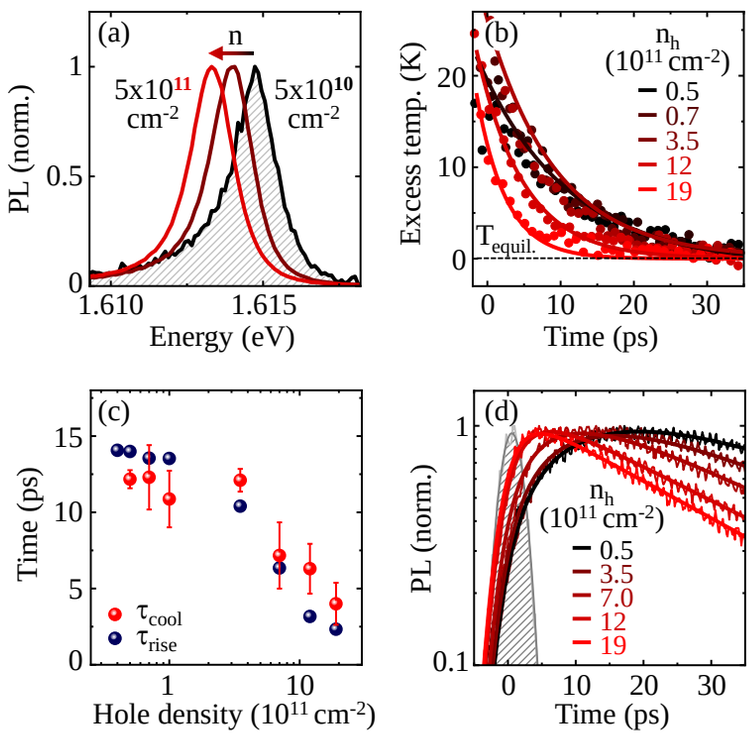

Figure 4.15: (a) PL spectra of the trion/Fermi polaron X^+ as function of energy at selected free carrier densities at T = 5 K. Excitation energy and injected electron-hole pair density are the same as for the measurements presented in Figure 4.14. (b) Transient trion excess temperature for selected free carrier densities at a fixed temperature of T = 5 K. Solid lines corresponds to mono-exponential fits. (c) $1/e$ cooling and rise times obtained from (c) and (e), respectively. (d) Normalized X^+ PL transients for selected free carrier densities. Solid lines correspond to exponential rise-decay fits.

Having investigated exciton-carrier interactions in TMDC monolayers including scattering and recombination mechanisms as well as first dynamical properties, in the next chapter, the propagation dynamics of excitons and trions are explored. The investigations particularly focus on the influence of phonons and free charge carriers, studied in temperature- and carrier density dependent diffusion experiments.

Chapter 5

Exciton propagation in two-dimensional semiconductors - impact of phonons and free carriers

In this chapter, the intrinsic mechanisms of exciton propagation in monolayer TMDCs are explored. The chapter is structured in two sections. In section 5.1, the diffusion of neutral dark excitons at cryogenic temperatures is studied. In section 5.2, the additional influence of exciton-carrier interactions on the exciton propagation is investigated in an electrically-tuneable monolayer. The contents presented in section 5.1 have been published in "K. Wagner *et al.*, Phys. Rev. Lett. 127(7), 076801, 2021" [274]. Figures are reprinted with permission. Copyright (2022) by the American Physical Society. The contents presented in section 5.2 are part of an yet unbublished article (Ref. [256], under review).

5.1 Non-classical exciton diffusion

Commonly, in monolayer TMDCs exciton propagation is described in a semi-classical picture, where the exciton propagates ballistically between two scattering events [106, 97, 105, 275, 276, 61]. In the semiclassical picture the diffusion coefficient is given by

$$D = \frac{k_B T^* \tau_s}{m_X}. \tag{5.1}$$

$m_X = m_e + m_h$ denotes the exciton mass, $k_B T^*$ is the thermal exciton energy with exciton temperature T^* and τ_s is the scattering time between two scattering events. In order to test Equation 5.1 experimentally, independent access to the

diffusion coefficient as well as exciton temperature, scattering time and exciton mass is required.

In the following two subsections, the intrinsic mechanisms of exciton propagation and the applicability of the semiclassical model in two-dimensional semiconductors is investigated by time-resolved microscopy of dark excitons in WSe_2 monolayers. In contrast to bright excitons, which only exhibit short lifetimes on a sub-picosecond time scale [277], ground state dark excitons are characterized by long lifetimes of several 100's of picoseconds [54]. As demonstrated in previous chapter and in other studies [107, 108] excitons quickly thermalize and cool down to lattice temperature after a few 10's of picoseconds. Thus, dark excitons exhibit a constant temperature during the majority of their lifetime, important for a quantitative comparison of their propagation behavior with Equation 5.1. Moreover, hBN-encapsulated monolayers with suppressed long-range disorder [69, 105] provide flat energy landscapes on a micrometer length scale, necessary to access the intrinsic exciton diffusion coefficient.

5.1.1 Mobile dark excitons in monolayer WSe_2

The photoluminescence spectrum of hBN-encapsulated monolayer WSe_2 at cryogenic temperatures exhibits multiple peaks, originating from bright and dark exciton reservoirs. Fig. 5.1(a) schematically illustrates the low-energy exciton dispersion in monolayer WSe_2 relevant for the interpretation of luminescence spectra. It includes the bright X^0 and spin-dark D^0 excitons at K-K as well as momentum-dark excitons I^0 at K-K'. After resonantly pumping the X^0 exciton, the system relaxes to the ground state K-K and K-K' states [54, 107]. The D^0 exciton emits either in out-of-plane polarization [139], or phonon-assisted as indicated in Fig. 5.1(a) by red and blue arrows. In Fig. 5.1(b), a characteristic PL spectrum of a hBN-encapsulated monolayer WSe_2 at $T = 5$ K is presented. At an emission energy of 1.722 eV the short-lived bright X^0 exciton emits. At lower energies the spectrum is dominated by dark state emissions. As the measurements are performed with a large objective aperture (NA = 0.7) the D^0 emission line dominates the spectrum 45 meV below X^0 [278]. The same exciton reservoir emits also via the assistance of homo-polar Γ_5 phonons, indicated by the $D^0_{\Gamma 5}$ peak [213]. K-K' excitons emit via I^0 as well as I^0_{K1} and I^0_{K3} by the assistance of zone-edge $K1$ and $K3$ phonons [37]. Emissions at lower energies are attributed to higher-order phonon side bands. Suppressed features of the bright negatively-charged trion doublet X_1^- and X_2^- indicate only very low intrinsic electron doping in the sample on the order of $\leq 2\times10^{10}$ cm^{-2}. As the recombination of dark states mostly occurs

via second order processes, or in the case of the D^0, via a weak oscillator strength in out-of-plane polarization, they exhibit comparably long lifetimes manifesting in $1/e$ PL decay times of 0.5 and 0.8 ns for K-K' and K-K excitons, cf. inset of Fig. 5.1(b). As shown in Refs. [107, 108], the excitons quickly cool down to lattice temperature within the first 50 ps allowing to monitor thermalized exciton diffusion at sufficiently long time scales.

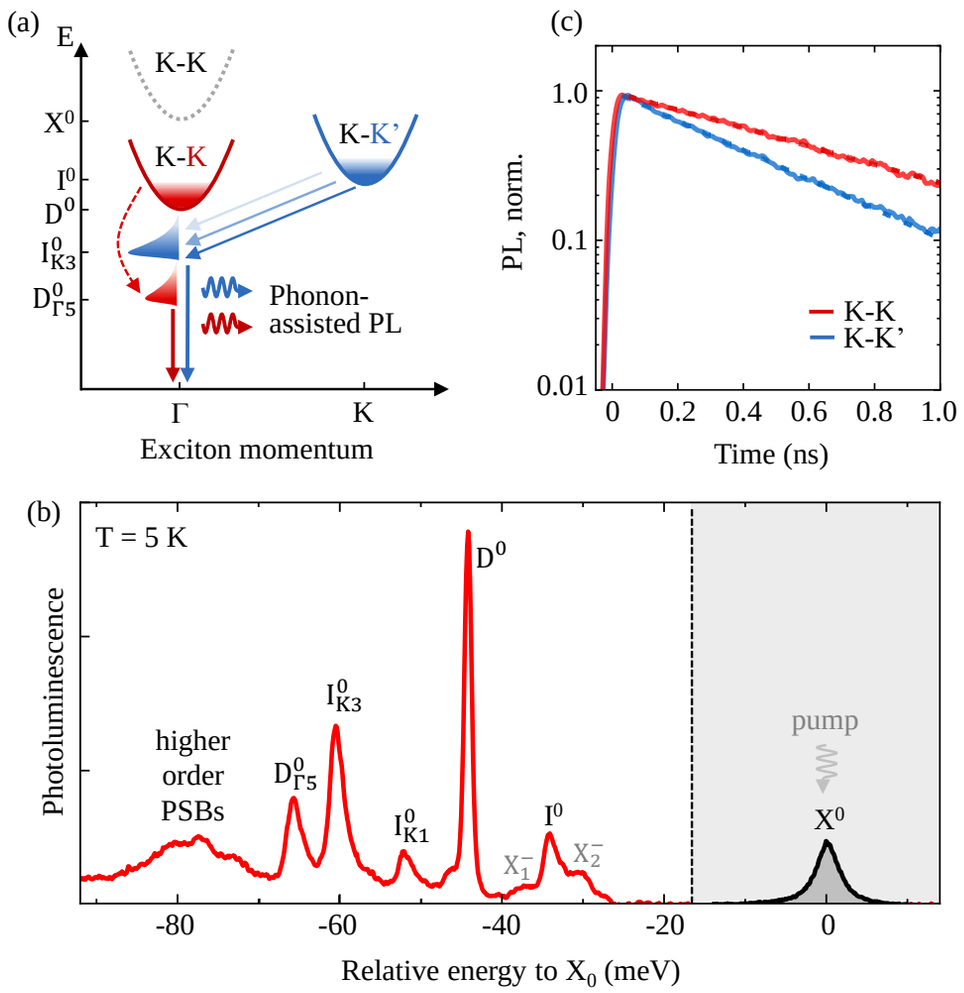

Figure 5.1: (a) Schematic illustration of the low-energy exciton dispersion in monolayer WSe_2 with characteristic phonon-assisted recombination pathways of dark K-K and K-K' excitons. (b) Typical PL spectrum of hBN-encapsulated monolayer WSe_2 at T = 5 K in the energy range of dark exciton emissions D^0 and I^0 and their phonon side bands after resonant excitation of the X^0 exciton at an optically-injected exciton density of 6×10^{10} cm^{-2}. The X^0 exciton is spectrally-cropped by a long-pass filter (grey area). The individual peaks are labeled according to their current interpretation adapted from Ref. [186]. (c) PL transients of the D^0 and I^0_{K3} emission.

For the investigation of dark exciton propagation the monolayer is excited resonantly at the X^0 exciton. The optically-injected exciton density is tuned to the

linear regime to 6×10^{10} cm^{-2} where non-linear density effects such as Auger-recombination are negligible, cf. section 3.6. By applying sharp spectral short- and long-pass filters, the diffusion coefficient of individual emission peaks is investigated: the D^0 and its phonon side band $D^0_{\Gamma 5}$, the I^0_{K3} emission and all phonon side band emission below I^0_{K1} (energy-integrated). The spectrally-filtered emission peaks are shown in Fig. 5.2 (a). For spatial monitoring, the central emission cross-section of the emission is monitored by a streak camera. In Fig. 5.2(b), a representative normalized streak camera image is presented. The vertical axes corresponds to the spatial coordinate and the horizontal axis to the temporal evolution. As schematically illustrated by the black dashed line, the normalized cross section broadens with time. In Fig. 5.2(c), the mean-squared-displacement σ^2 extracted from fitting temporal cuts in Fig. 5.2(b) by Gaussians is plotted as function of time. As expected for diffusive behavior, the mean-squared-displacement increases linearly with time [224]. The diffusion coefficient D is extracted by dividing the slope by a factor of 2. For all emissions, the measured diffusion coefficient is approximately equal. The average diffusion coefficient, determined from the individual slopes, is 2.4 ± 0.5 cm$^2/s$ corresponding to a diffusion length on the order of 0.5 μm. The approximately equal diffusion coefficients for emissions stemming from K-K and K-K' excitons is reasonable considering equal properties at K and K' valleys (apart from the spin and valley indey).

In order to quantitatively compare the measured diffusion coefficients to Equation 5.1, the exciton temperature T^* and scattering time τ_s needs to be determined. In the following, τ_s and the effective exciton temperature T^* is estimated from temperature-dependent linewidth analysis [199, 73] of the investigated dark exciton emissions. The exciton scattering time typically manifests in the symmetric (non-radiative) linewidth broadening $\Gamma \propto 1/\tau_s$ [73]. The effective exciton temperature can be e. g. determined by the low-energy recoil flank, as demonstrated in section 4.3 for trions, or in the case of excitons, by the high-energy flank of the phonon side bands [4, 279, 280, 194, 281].

In Fig. 5.3(a) and (b), PL spectra are presented in the energy range of phonon side bands $D^0_{\Gamma 5}$ and I^0_{K3} as well as in the range of the out-of-plane polarized D^0 emission for selected temperatures between 5 and 50 K. In order to quantitatively extract the linewidth, the D^0 emission is fitted by a symmetric Voigt profile. Considering thermalized states, the phonon side bands are fitted by a convolution of a Boltzmann distribution and a Voigt profile

$$I_{\mathrm{PL}}(E) \propto \exp[(E - E_0)/(k_B T^*)]\Theta(E - E_0) \otimes I_0(E, \Gamma). \tag{5.2}$$

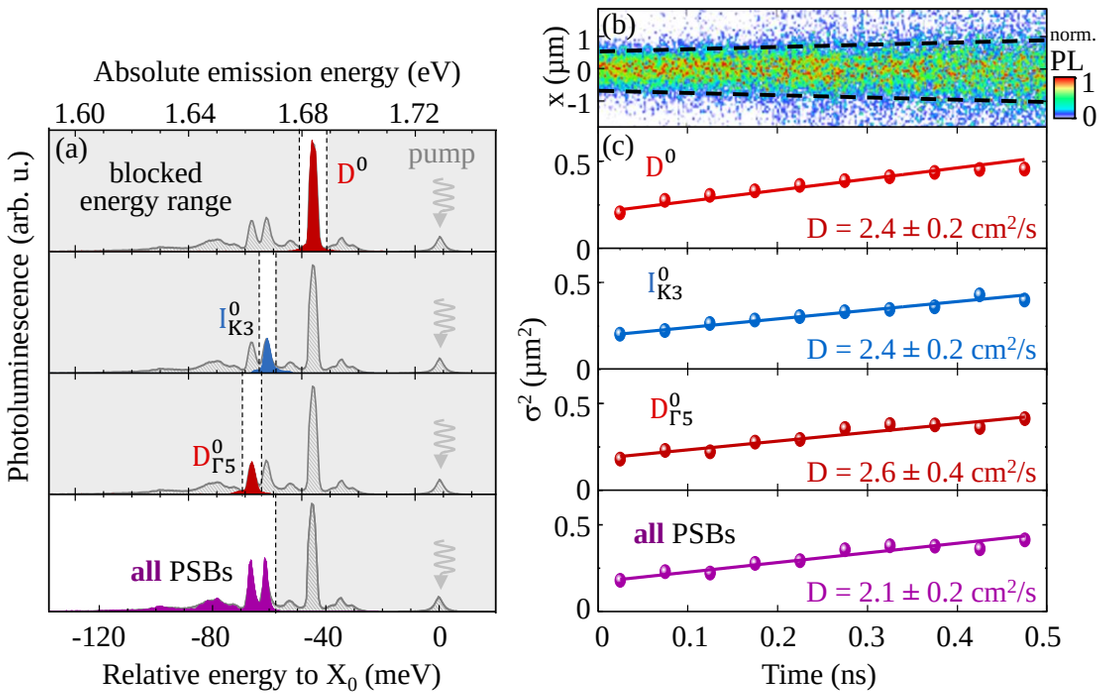

Figure 5.2: (a) Spectrally-cropped emission peaks in hBN-encapsulated monolayer WSe_2 at T = 5 K. (b) Normalized 2D streak camera image showing the temporal broadening of the spatial emission cross-section. For this data set the emission of all phonon side bands below I^0_{K1} are collected, cf. lowest panel in (a). Dashed line qualitatively illustrates the broadening with time. (c) Spatial broadening of the emission cross-section represented by the mean squared displacement as function of time for the individual emission lines highlighted in (a) after resonant excitation of X^0. The estimated injected electron-hole pair density is 6×10^{10} cm^{-2}. The average diffusion coefficient of all four measurements is 2.4 ± 0.5 cm^2/s.

Here, E_0 is the center emission energy and $\otimes$ denotes the convolution. Similar to the approximation of the low energy tail of the trion presented in section 4.3, the high-energy flank gives access the effective temperature T^* of the exciton gas. The symmetric profile $I_0(E, \Gamma)$ is the Voigt profile and accounts for the symmetric linewidth broadening Γ.

As demonstrated in Fig. 5.3(a), Equation 5.2 fits the data very well. In Fig. 5.3(c), the symmetric broadening obtained from D^0 as well as $D^0_{\Gamma 5}$ and I^0_{K3} phonon side bands are summarized. The symmetric linewidth broadening is nearly identical for all emissions. At T = 5 K it reaches values as small as 1 meV increasing to a value of $\approx$ 3 meV at T = 50 K. Due to the vanishing oscillator strength and therefore negligible radiative broadening of dark excitons, the remaining linewidth at T = 5 K is attributed to inhomogeneities. In order to estimate the pure *homogeneous* contribution, the data is deconvoluted by an inhomogeneous broadening of 0.9

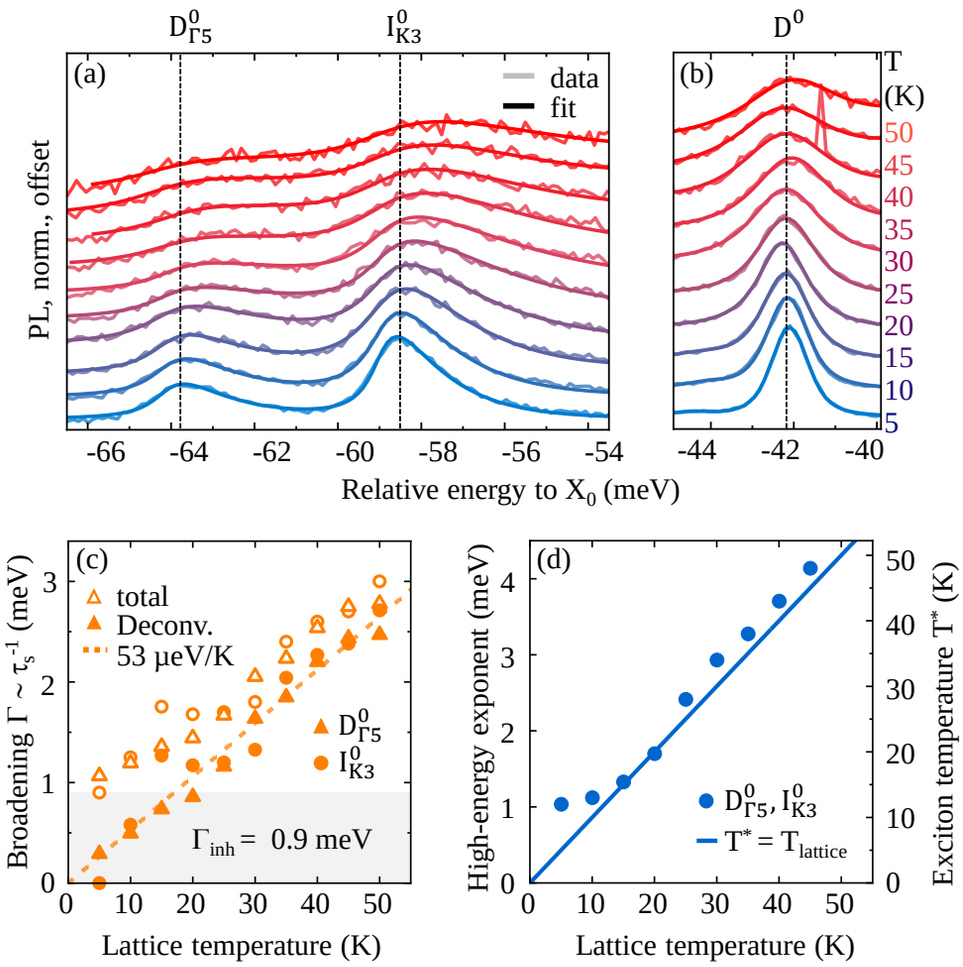

Figure 5.3: (a) PL spectra in the range of $D^0_{\Gamma5}$ and I^0_{K3} emissions as function of energy at different lattice temperatures. The experimental parameters are kept the same as in Figure 5.2, i. e., resonant X^0 excitation and an optically-injected exciton density of 6×10^{10} cm^{-2}. The data is fitted by asymmetric peak fits corresponding to Equation 5.2. (b) Same data for the D^0 emission. Here, the spectra are fitted by symmetric Voigt profiles. (c) From (a) and (b) obtained symmetric linewidth broadening as function of temperature. The data is deconvoluted by $\Gamma_{\text{inh}} = 0.9$ meV. (d) High-energy exponent determined from the asymmetric fits presented in (a) as function of lattice temperature. The right axis corresponds to the estimated exciton temperature setting the high-energy exponent equal to $k_B T^*$.

meV. The determined temperature-activated linewidth broadening is 53 μeV/K and is attributed to the scattering with linear acoustic phonons [205, 4, 73]. Importantly, the obtained scattering rate agrees with direct measurements of the homogeneous exciton broadening in four-wave mixing experiments [206].

In Fig. 5.3(d), the extracted exciton temperate T^* is plotted as function of lattice temperature. It closely follows the lattice temperature confirming that the excitons are thermalized and cooled down. Only at temperatures $\leq$ 10 K, the

exciton temperature is slightly higher than the lattice temperature. For a direct comparison to the effective trion temperature determined by the recoil flank in section 4.3, a hBN-encapsulated WSe_2 spectrum at a temperature of T = 5 K is presented with both, exciton and trion emissions. The spectrum is fitted by a multi-peak model including a symmetric profile for the D^0 emission, asymmetric profiles with a *high*-energy flank for exciton phonon side bands (X-PSBs) and asymmetric profiles with *low*-energy flanks for trions. Most importantly, the spectrum is well fitted by considering an equal exciton and trion temperature $T^*_{\text{X-PSB}} = T^*_{\text{T}}$.

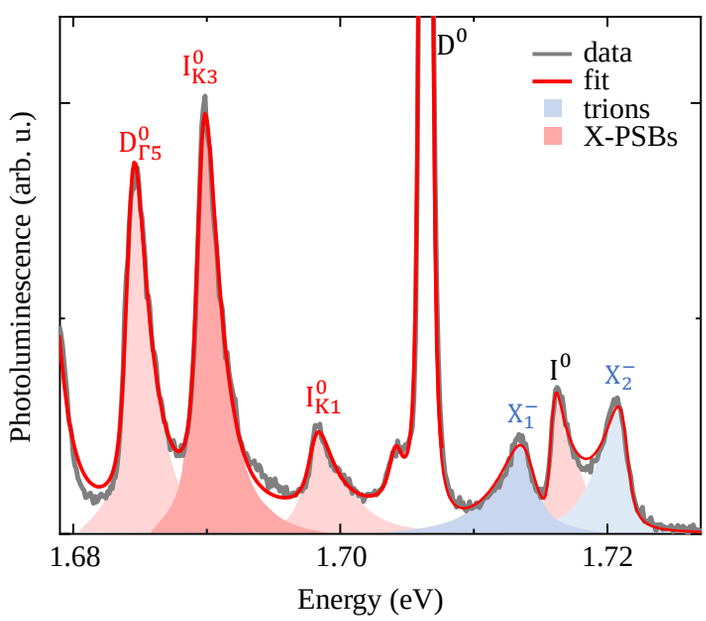

Figure 5.4: (a) Weakly n-doped PL spectrum of hBN-encapsulated monolayer WSe_2 at a nominal heat sink temperature of T = 5 K after CW excitation at an energy of 2.331 eV and a laser power of 0.5 μW. The data is fitted by a multi-peak model including a symmetric Voigt profiles for D^0 and the weak emission closely below D^0, asymmetric profiles with a *high*-energy Boltzmann flank according to Equation 5.2 for $D^0_{\Gamma 5}$, I^0_{K3}, I^0_{K1} and I^0, and asymmetric profiles with *low*-energy recoil flank for trions X^-_1/X^-_2 according to Equation 4.21. The exciton and trion temperature is fixed to $T^*_{\text{X-PSB}} = T^*_{\text{T}} = 12$ K. Following parameters are considered for the recoil flank: $\epsilon_1^{-1} = 7$ meV (same value as used in section 4.3) and $m_e/m_X = 0.5$. The inhomogeneous broadening is fixed to 0.6 meV. Center energies, symmetric linewidths ($\Gamma_{D_0} = \Gamma_{\text{X-PSBs}}$ and $\Gamma_{X_1^-} = \Gamma_{X_2^-}$) and amplitudes are free fit parameters. The colored areas qualitatively illustrate the profiles of trions, excitons and exciton phonon side bands.

Having determined the exciton temperature and scattering rate, the semiclassical diffusion coefficient given by Equation 5.1 is evaluated. Considering $T^* = T_{\text{lattice}}$, the measured broadening coefficient of $\Gamma/T = \hbar/(\tau_s T) = 53$ μeV/K and

$m_X = 0.75\ m_0$ [126], a diffusion coefficient of 2.5 cm^2/s is obtained. This value is in well in agreement with the experimentally observed value of 2.4 ± 0.5 cm^2/s at T= 5 K. It particularly highlights efficient exciton propagation which is only intrinsically limited by the scattering with linear acoustic phonons. As in the investigated temperature regime the scattering rate linearly scales with temperature $\Gamma \propto T$, the diffusion coefficient $D = k_B T\hbar/(\Gamma m_X)$ is particularly temperature-independent, motivating further time-resolved measurements of the exciton diffusion coefficient at temperatures T > 5 K.

5.1.2 Evidence of non-classical exciton propagation

In Fig. 5.5(a), the normalized spatial broadening of the PL cross-section is presented for a series of temperatures between 5 and 50 K. In Fig. 5.5(b), corresponding relative mean-squared-displacements $\Delta\sigma^2$ are shown. For a better signal-to-noise ratio, the accumulated signal of all phonon side bands below I^0_{K1} is evaluated. The excitation conditions are kept the same as before, i. e., resonant X^0 excitation at an optically-injected exciton density of 6×10^{10} cm^{-2}. The extracted diffusion coefficients are summarized in Fig. 5.5(c) (blue/red data points). At low temperatures the diffusion coefficient is close to the previously observed value of 2.5 cm^2/s. With increasing temperature the diffusion coefficient *decreases*. Already during the first 30 K the diffusivity reduces to a value below 1 cm^2/s. Surprisingly, the observed diffusivity does not remain constant as expected in the semiclassical model, nor it increases, as it would be expected in a disordered system, i. e., for hopping-like propagation [222] or defect-assisted scattering [10, 83].

In order to exclude any doping-related effects, in Fig. 5.5 (d), the observed exciton diffusion coefficient is presented at 5 and 40 K while slightly varying the free carrier density. At both studied temperatures the diffusion coefficient reaches its maximum at zero doping. With increasing doping, the diffusion coefficient decreases due to increasing exciton-carrier scattering (for more details on exciton diffusion in the presence of free charge carriers see section 5.2). Most importantly, at charge neutrality the diffusion coefficient is < 2 cm^2/s at T = 40 K and thus indeed smaller than ≈ 3 cm^2/s at T = 5 K. The measurements demonstrate, that the observed temperature-induced decrease of the diffusion is robust with respect to small doping variations.

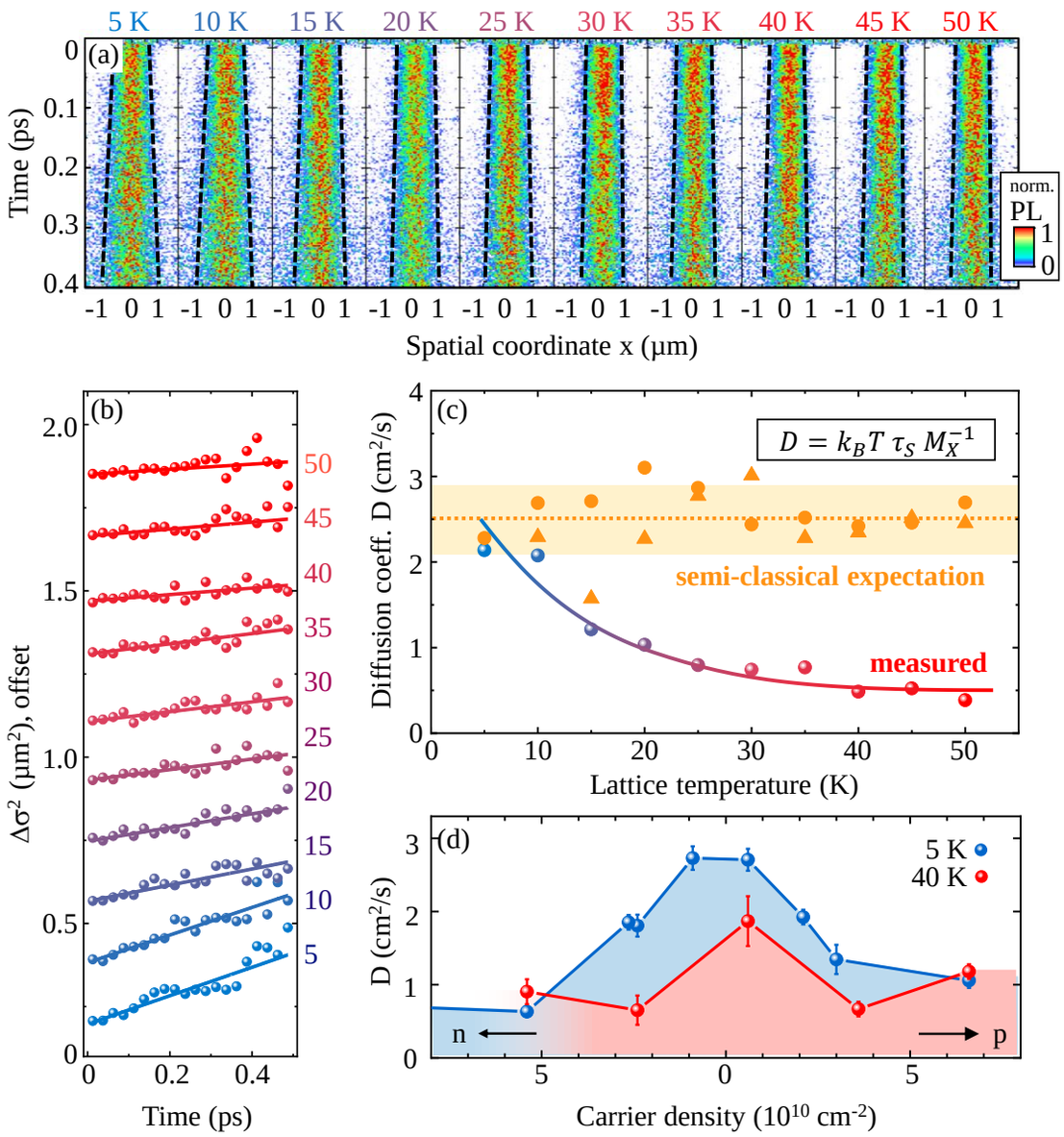

Figure 5.5: (a) Normalized streak camera images showing spatial broadening of the dark exciton emission cross-section at selected temperatures. The emission is spectrally cropped such that only dark exciton emissions below I^0_{K1} contribute to the signal. (b) Mean squared displacement as function of time extracted from (a). (c) Exciton diffusion coefficient as function of lattice temperature determined from (b). For comparison, the expected diffusion coefficient in the semiclassical model with exciton scattering rates obtained from Figure 5.3 is shown (orange data). (d) Exciton diffusion as function of free carrier density at 5 and 40 K measured in an electrically-tuneable sample.

The decreasing exciton diffusion coefficient with increasing temperature is observed in multiple measurements on different samples. In Fig. 5.6 (a), the extracted diffusion coefficients from two samples (including the data in Fig. 5.5(c)) are summarized as function of temperature. Despite variations in the absolute

numbers, all measurements exhibit a decrease of the diffusivity in the considered temperature range. In Fig. 5.6(b), the measurements at T = 5 and T = 50 K are summarized in two histograms. Consistent with the measurements discussed in Fig. 5.5 (c), the average diffusion coefficient is $D_{5K} = 2.4 \pm 0.5$ cm$^2/s$ and $D_{50K} = 0.84 \pm 0.6$ cm$^2/s$.

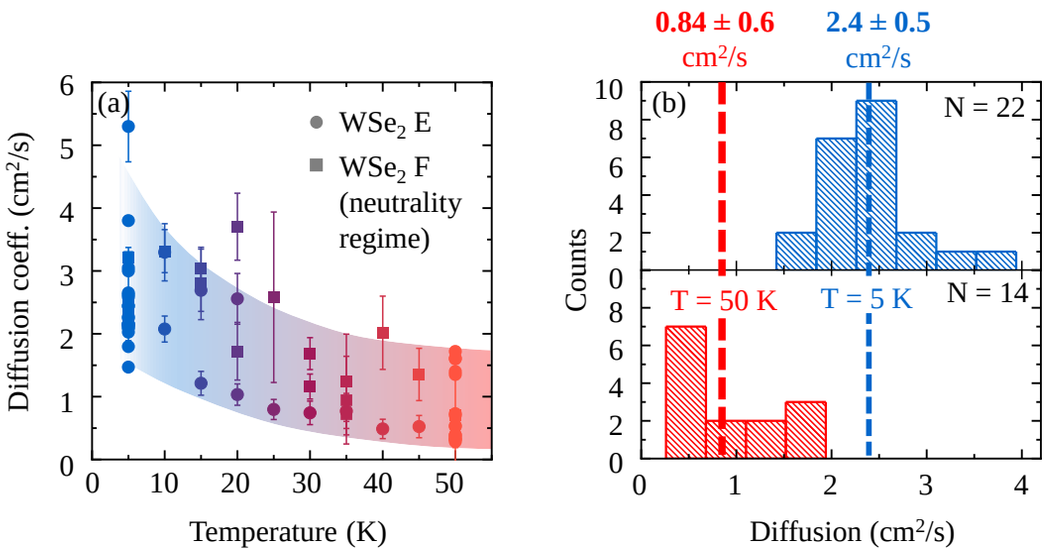

Figure 5.6: (a) Exciton diffusion coefficient as function of temperature for multiple measurements on two samples (WSe_2 E and the electrically-tuneable structure WSe_2 F at charge neutrality). Each data point corresponds to a time-resolved measurement. The values of up to 5 cm$^2/s$ at 5 K are observed in a measurement with larger pump power and thus contains contributions from Auger-like recombination [61]. (b) Statistics on diffusion measurements. The measured diffusion coefficient at 5 K averaged over 22 individual measurements is 2.4 ± 0.5 cm^2/s. At 50 K, an average value of 0.84 ± 0.6 cm^2/s is found evaluating 14 individual measurements.

This observation strongly contrasts the common semiclassical model where the diffusion coefficient is expected to be constant in this temperature regime. For direct comparison, in Fig. 5.5(c), the semiclassical diffusion coefficient is plotted by considering scattering rates from Fig. 5.3 and evaluating Equation 5.1 (orange data points). The decreasing diffusion coefficient within the first 30 K can neither be explained by nonequilibrium effects in the initial relaxation, as the diffusion is analyzed on much longer time scales, nor by density-dependent nonlinearities such as bimolecular processes [61, 282] or phonon-wind effects [63, 283] as the experiments are performed at low excitation powers in the linear density regime. Most importantly, any additional temperature-induced scattering channel would manifest in additional spectral broadening. This behavior is not observed and can thus be exclude [73].

Also in a multi-valley approach based on the material-realistic WSe_2 band structure, the diffusion coefficient is not expected to decrease within the first 30 K. Although, the possibility of temperature-activated scattering into heavier K-Λ excitons can lead to a decrease of the temperature-dependent diffusivity (depending on the exact energy separation between K-K and K-Λ excitons), this effect is expected to occur only at temperatures higher than 30 K. In this scenario the diffusion decreases due to the larger mass of K-Λ excitons [126, 194]. This process would not be observable in the temperature-dependent linewidth broadening. However, in this scenario the absorption of higher-energy Λ phonons are required which become populated only at elevated temperatures.

The semiclassical picture comes to its limit when its general assumption breaks down: that the exciton mean free path becomes similar or smaller than the spatial extent of the exciton wave packet. This condition is called the Mott-Ioffe-Regel criterion [284]. For a direct comparison, in Fig. 5.7(a), the ratio of the semiclassical mean free path $l_{\mathrm{mfp}} = \sqrt{2D\tau_s}$ and the de Broglie wavelength $\lambda_{dB} = \sqrt{2}\pi\hbar(m_X k_B T)^{-1/2}$ is plotted as function of temperature. The absolute value of the de Broglie wavelength is plotted in the inset. The ratio decreases with increasing temperature from 0.5 to a value smaller than 0.1. It means, while at T = 5 K the die Broglie wavelength and the mean free path are still on a similar order of magnitude, with increasing temperature the de Broglie wavelength becomes up to 10 times larger than the mean free path. For illustrative purposes, in Fig. 5.7(b), exciton propagation is schematically depicted in the semiclassical picture (top panel) where the length between two scattering events is much larger than the spatial extent $\propto \lambda_{dB}$ of the exciton. In the bottom panel the same scenario is depicted in the case where the Mott-Ioffe-Regel criterion is violated. The exciton wave packet by far exceeds the length of an individual segment between two scattering events.

In a recent theoretical work, the effect of the wave-like nature on the exciton transport is approached for monolayer TMDCs [109]. In Fig. 5.7(c), a first order quantum correction to the semiclassical exciton diffusion is presented [109]. For the calculation an exciton mass of 0.76 m_0 [126] and a sound velocity of 3.3 km/s [242] is considered. As outlined in subsection 2.6.2, the wave-like nature of the exciton is taken into account by considering closed exciton trajectories where a constructive interference of the clockwise and counter-clockwise propagating exciton wave occurs. Due to the constructive interference, the exciton spends effectively more time in the loop, resulting in weak localization of the exciton [234, 235, 236, 237, 238, 88, 239]. The key parameter in this approach is the phase

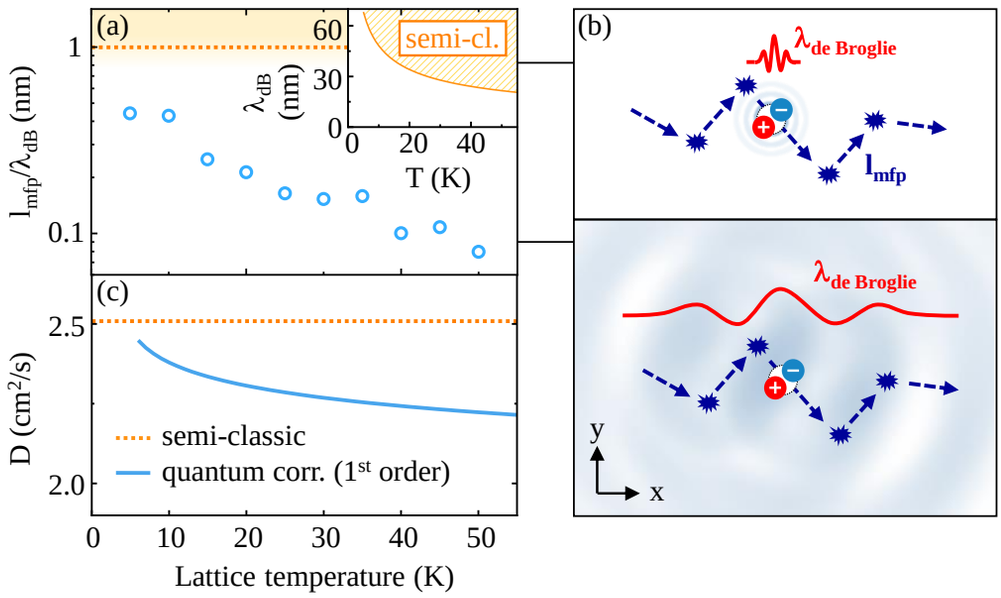

Figure 5.7: (a) $\lambda_{\mathrm{dB}}/l_{\mathrm{mfp}}$ and the mean free path as function of temperature. Dashed line corresponds to the semiclassical expectation considering Equation 5.1. Open circles are obtained from the independently measured scattering rate τ_s and diffusion coefficient D_{meas} considering $l_{\mathrm{mfp}} = \sqrt{2D_{\mathrm{meas.}}\tau_s}$. (b) Calculated diffusion coefficient considering 1st order quantum corrections according to Ref. [109]. (c) Schematic illustration of exciton propagation in the semiclassical picture. (d) Schematic illustration of exciton propagation in the case where the de Broglie wavelength is larger than the mean free path and interference effects need to be taken into account.

relaxation time τ_ϕ which governs the constructive interference, i. e., τ_ϕ is the time after which the constructive interference breaks down. It can be shown that the interplay of the energy loss rate and momentum scattering rate leads to an effective enhancement of the weak localization effect with increasing temperature, and thus to a decrease of the diffusion coefficient. Importantly, this process occurs due to the wave-like nature of the exciton and does not manifest in the temperature-dependent exciton linewidth.

The qualitative behavior of the first order quantum correction indeed resembles the experimental observation. In particular it demonstrates that at very low temperatures, e. g. at T = 5 K, the quantum nature leads to only minor deviations and the propagation is reasonably well described by the semiclassical model (justifying the analysis presented in subsection 5.1.1). With increasing temperature, interference effects become more dominant and the correction to the semiclassical diffusion increase (considering low temperatures where the scattering is dominated by linear acoustic phonons). However, the presented perturbative approach can

not quantitatively explain the experimental observation. It underestimates the effect by almost an order of magnitude. A full quantitative understanding of the observed non-classical propagation behavior, thus, remains an open question.

5.2 Exciton diffusion in the presence of free charge carriers

The investigations in previous section demonstrate that low temperature exciton diffusion in charge-neutral TMDCs is crucially determined by the scattering with phonons. In doped semiconductors, the scattering with free charge carriers is expected to additionally influence the propagation behavior. Importantly, in the presence of free electrons or holes excitons form to trions, which are expected to similarly propagate through the two-dimensional crystal [16, 106]. In this section, the propagation of both, excitons and trions in a continuously-tuneable two-dimensional Fermi sea of free charge carriers is explored.

5.2.1 Gate-tuneable exciton diffusion in monolayer WSe_2

The investigations focus on dark sates in electrically-tuneable hBN-encapsulated monolayer WSe_2. In Fig. 5.8(a), a characteristic PL spectrum of the studied sample is presented in the energy range below the resonantly excited X^0 exciton at 1.722 eV as a function of gate voltage. The temperature is set to T = 5 K. The neutrality regime at $\approx$ 0.7 V is characterized by K-K and K-K' emissions. As outlined in subsection 5.1.1, the dominant emission peaks are the D^0 and I^0 zero phonon lines and the associated phonon side bands $D^0_{\Gamma 5}$ and I^0_{K3} [278, 188, 187, 37]. By increasing or decreasing the gate voltage, free holes or electrons are injected, respectively. The doping results in the formation of bright trions $X^{\pm}$ as well as dark trions $D^{\pm}$ and associated phonon side bands, dominated by $D^{\pm}_{\Gamma 5}$ and $D^{\pm}_{K3}$ [37]. On the n-doped side, additionally the electron side band D^-_B of the dark trion D^- emerge, where the inter-valley K-K' electron-hole pair recombines and the electron at K is excited to the upper spin-split conduction band at K' [186] (see also Figure 2.11(b) in section 2.5). Furthermore, the n-doped side exhibits two bright trion emissions X^-_1 and X^-_2, which stem from the two possible trion configurations involving the bright K-K exciton in the spin-split conduction band [36, 166]. Ground state K-K and K-K' states are characterized by comparably weak light-matter coupling manifesting in $1/e$ PL lifetimes of up to 1 ns. By applying spectral filters and evaluating the spatial behaviour on longer time scales

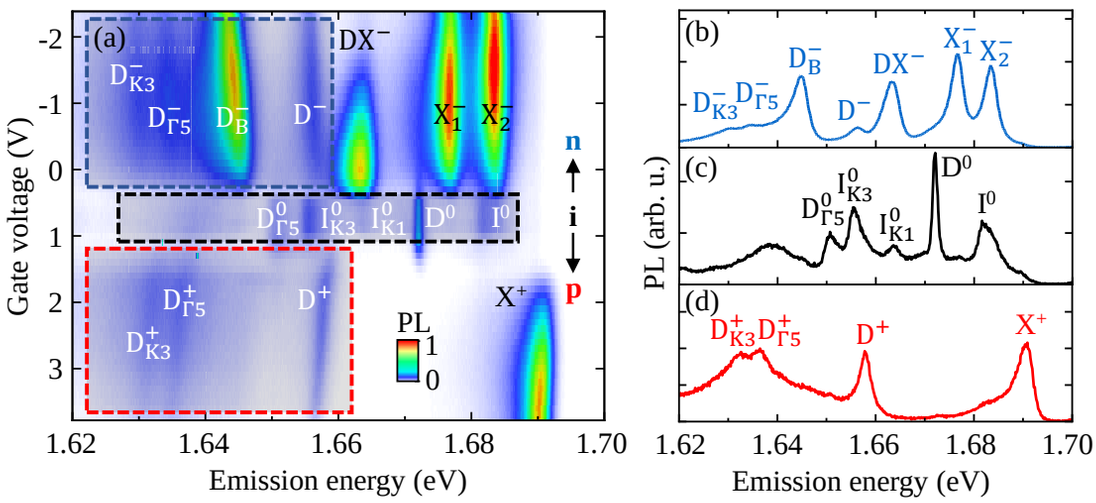

Figure 5.8: (a) PL intensity as function of emission energy and gate voltage in the energy range below the X^0 exciton at 1.722 eV in hBN-encapsulated monolayer WSe_2 at T = 5 K. The sample is excited resonantly at the X^0 exciton at 1.722 eV with an estimated injected electron-hole pair density of 4.5×10^{10} cm^{-2}. A gate voltage of 1 V corresponds to a free carrier density of 3×10^{11} cm^{-2}. Individual peaks are labeled according their current interpretation [186]. Spectral regions of dark exciton and trion emissions are marked by dashed rectangles. (b-d) Spectral cuts at −0.5, 0.7 and 1.8 V in the n-doped, neutrality, and p-doped regime, respectively.

(see also section 3.7), only dark state emissions which are highlighted in Fig. 5.8(a) by dashed rectangles are investigated.

In Fig. 5.9, the main observations of the diffusion experiment are presented. In Fig. 5.9(a), the relative mean-squared-displacement $\Delta\sigma^2$ as function of time is plotted for several fixed gate voltages in the weakly p-doped regime. The linear increase of $\Delta\sigma^2$ hallmarks diffusive propagation [224]. In Fig. 5.9(b), the extracted diffusion coefficients obtained from the slope of $\Delta\sigma^2(t)$ for n- and p-doping are summarized. The free carrier density is obtained from setting the relative exciton-trion separation equal to the Fermi energy. At charge-neutrality a diffusion coefficient of 2.7 cm^2/s is observed, consistent with the previous findings presented in section 5.1. With increasing free carrier density the diffusivity drastically decreases to a value of ≈ 1 cm^2/s. Surprisingly, further increasing the free carrier density leads to a reversed behavior. The propagation is accelerated up to 1.5 cm^2/s at a free carrier density of 1.5×10^{11} cm^{-2}. Then the diffusion coefficient remains comparably high and only slowly decreases towards 0.5 cm^2/s at 6×10^{11} cm^{-2}. A similar dependence is observed in the n-doped regime.

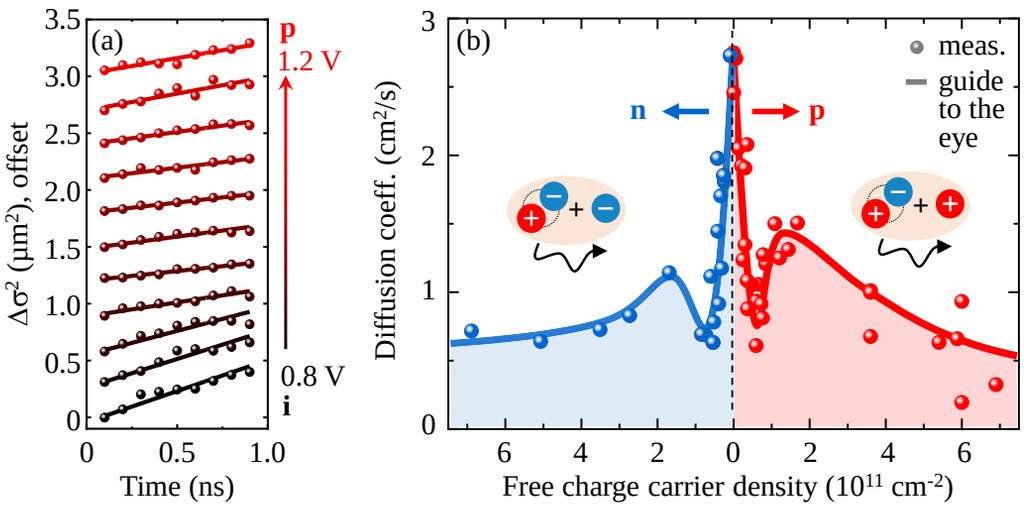

Figure 5.9: (a) Spatial broadening of the emission distribution $\Delta\sigma^2$ as function of time for selected gate voltages in the p-doped regime. Only emissions highlighted in Fig. 5.8(a) are considered. (b) Summarized exciton diffusion coefficients as function of free carrier density in the n- and p-doped regime. Solid lines are guides to the eye.

As demonstrated in section 5.1, the spatial propagation of neutral dark excitons is governed by the scattering with linear acoustic phonons and can be described in the semiclassical model at least at T = 5 K. Only at elevated temperatures non-classical effects need to be taken into account. The semiclassical diffusion coefficient is given by (equivalent to Equation 5.1)

$$D = \frac{k_B T^* \hbar}{\Gamma m} \tag{5.3}$$

with quasiparticle temperature T^*, quasiparticle mass m and scattering rate $\Gamma = \hbar/\tau_s$. In Equation 5.3, the charge carrier-dependence mainly enters via Γ. In the simplest scenario the scattering rate is given by exciton-carrier and exciton-phonon scattering

$$\Gamma = \Gamma_{\text{phon}} + \Gamma_{\text{carr}}. \tag{5.4}$$

Due to similar propagation behavior at electron- and hole-doping, the following discussion focuses on the hole-doped side. As demonstrated in section 4.2 and subsection 5.1.1, the free carrier and phonon scattering rates manifest in the non-radiative voltage- and temperature-dependent exciton linewidth broadening [45, 46, 112]. In Fig. 5.10(a), the fitted symmetric linewidth of the D^0 exciton and D^+ trion are presented as function of temperature. Similar to the analysis pre-

sented in Fig. 5.3, the data is deconvoluted by $\Gamma_{\text{inhom}} = 1.8$ meV such that the extrapolated zero-temperature value vanishes, cf. Fig. 5.10(b). The phonon-assisted

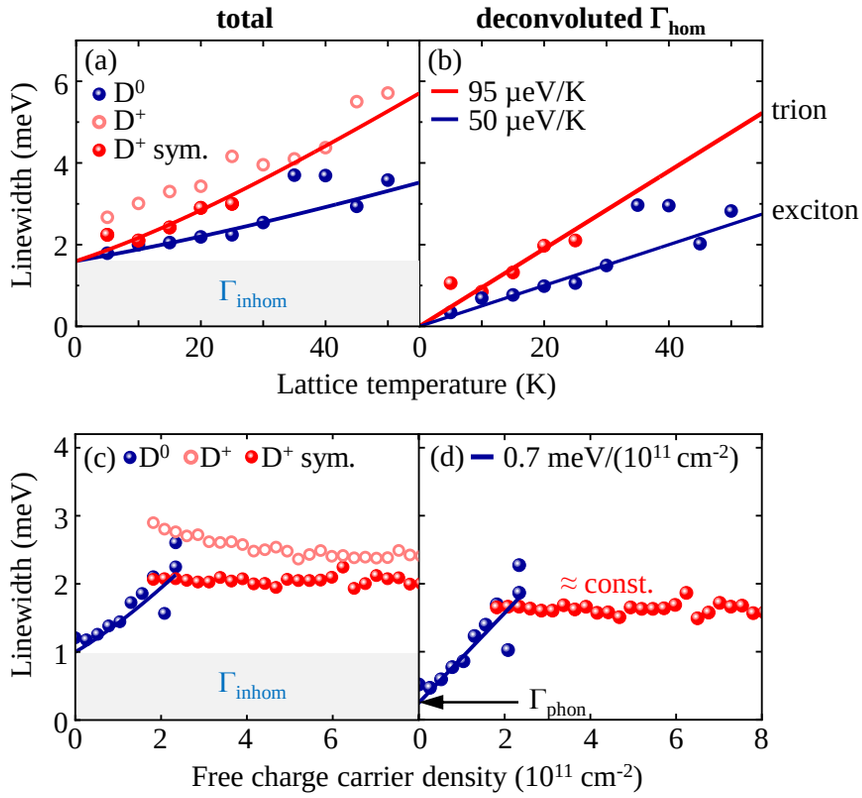

Figure 5.10: (a) D^0 and D^+ linewidth as function of lattice temperature in the neutrality and p-doped regime. Filled red circles correspond to the symmetric width fitting the trion emission by the recoil lineshape given by Equation 4.21. For comparison, open circles show the extracted FWHM fitting the emission by a symmetric Voigt profile. Solid lines correspond to convoluted line fits shown in (b) considering Γ_{inhom}. (b) Deconvoluted D^0 and D^+ linewidth. (c) D^0 and D^+ linewidth as function of free carrier density at T = 5 K. (d) Deconvoluted linewidth considering Γ_{inhom} indicated in (c). At zero doping the linewidth is set to the temperature-activated phonon-scattering rate $\Gamma_{\text{phon}} = 0.25$ meV (evaluating 50 μeV/K at T = 5 K).

scattering rates are $\Gamma_X/K = 50$ μeV/K and $\Gamma_X/K = 95$ μeV/K for the exciton and trion, respectively. The temperature-dependent scattering rate coefficient of the trion is slightly higher than that of the exciton, consistent with a theoretically expected larger trion-phonon scattering [214]. In Fig. 5.10(c) and (d), total and deconvoluted exciton and trion linewidths are presented as function of free charge carrier density determined from voltage-dependent PL measurements. In agreement with the data presented in section 4.2 and other reports [45, 285], the trion linewidth is constant while the exciton linewidth linearly increases with free car-

rier density yielding a density-dependent scattering rate coefficient of $\Gamma_X/n = 0.7$ meV/(10^{11} cm^{-2}).

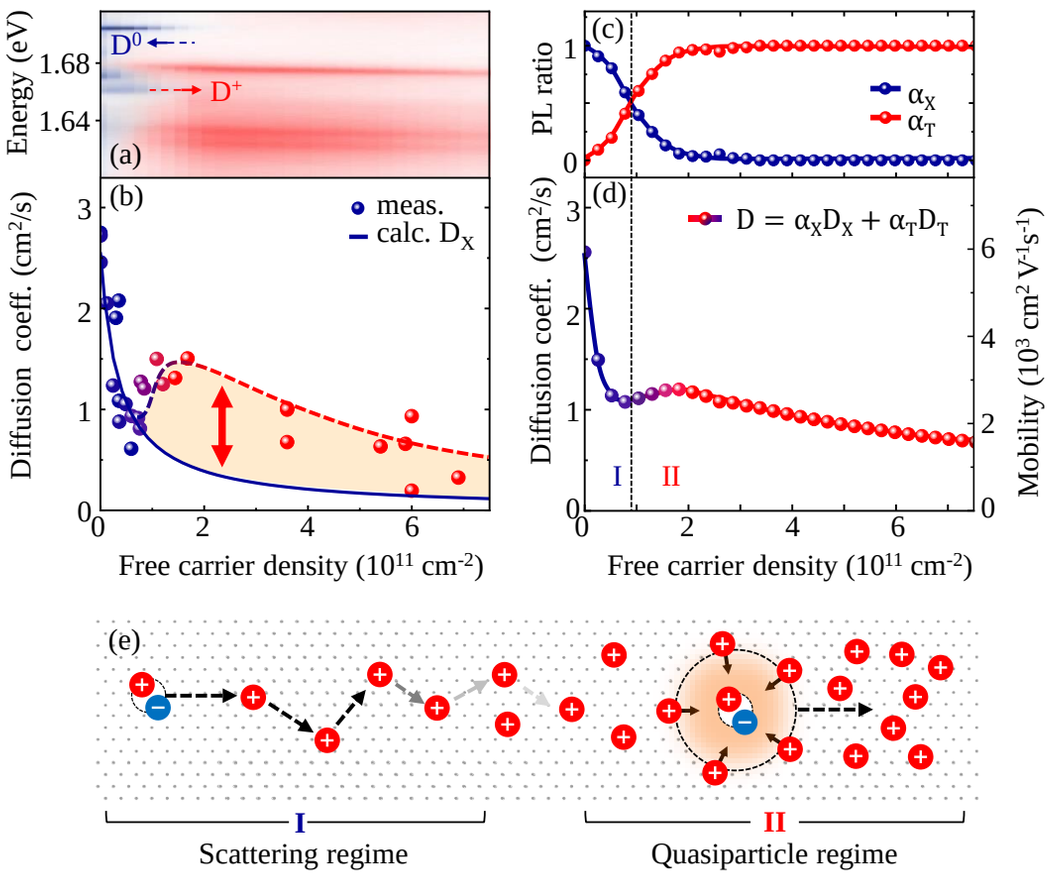

Figure 5.11: (a) Illustration of the carrier density-dependent PL spectrum presented in Fig. 5.8 in the energy range of D^0 and D^+ emissions. Exciton and trion emissions are colored in blue and red, respectively. (b) Diffusion coefficient as function of free carrier density (exp. data is reproduced from in Fig. 5.9). Solid line corresponds to the semiclassical exciton diffusion coefficient considering exciton-electron scattering rates presented in Fig. 5.10. (c) PL intensity ratio α_X =D^0/(D^0+D^+) and α_T =D^+/(D^0+D^+) determined from fitting voltage-dependent PL spectra shown in (a). (d) Calculated diffusion coefficient considering composite diffusion $D = \alpha_X D_X + \alpha_T D_T$ and setting the exciton-trion population ratio equal to the PL ratio shown in (c). (e) Schematic illustration of exciton propagation in the regime of (I) exciton-carrier scattering and (II) quasiparticle formation.

Having quantified the scattering rates, the observed non-monotonic propagation behavior can be explained. Considering the exciton scattering rate determined from D^0 and an exciton mass of $m_X = 0.76m_0$, the calculated exciton diffusion coefficient is plotted as function of free hole density in Fig. 5.11(b) (solid blue line). The calculation agrees with the initially observed strong decrease. However, at

elevated carrier densities the strong exciton-carrier scattering predicts a much lower diffusion coefficient as determined in the experiment.

While at charge neutrality, the spectrum is dominated by neutral exciton emissions, within the first 10^{11} cm^{-2} trion emissions emerge and the neutral exciton emissions quench, as illustrated by the carrier-density dependent PL spectrum in Fig. 5.11(a). To quantify this, in Fig. 5.11(c), the relative exciton and trion PL ratios $\alpha_X = \mathrm{D}^0/(\mathrm{D}^0+\mathrm{D}^+) = 1-\alpha_T$ are plotted. Considering that trions are characterized by a nearly carrier-independent linewidth broadening and thus effectively scatter much lass then excitons, their propagation is expected to hardly depend on the free carrier density. In Fig. 5.11(d), the calculated composite diffusion of excitons and trions is presented given by

$$D = \alpha_X D_X + \alpha_T D_T. \tag{5.5}$$

Here, the individual contributions D_X and D_T are determined by Equation 5.3 with $m_X = m_e + m_h$ and $m_T = m_X + m_h$. The exciton-phonon and exciton-carrier scattering rates are fixed to the values obtained from PL linewidth analysis, presented in Fig. 5.10. For the trion a weak carrier-induced scattering rate of 0.05 meV/(10^{11} cm^{-2}) is considered, consistent with the experimentally determined trion linewidht broadening. All parameters entering in Equation 5.5 are summarized in Table 5.1.

	parameter	value	Ref.
Temperature	T	5 K	set in experiment
Exciton mass	$m_X = m_e + m_h$	0.76 m_0	Ref. [126]
Trion mass	$m_T = M_X + m_h$	1.16 m_0	Ref. [126]
Exciton scattering rates	Γ_X/T	50 µeV/K	Temp.-dep. D^0 linewidth*
	Γ_X/n	0.7 meV/(10^{11}cm^{-2})	Volt.-dep. D^0 linewidth**
Trion scattering rates	Γ_T/T	95 µeV/K	Temp.-dep. D^+ linewidth
	Γ_T/n	0.05 meV/(10^{11}cm^{-2})	Volt.-dep. X^+ linewidth***

Table 5.1: Table with summarized parameters considered for modeling composite exciton-trion diffusion presented in Figure 5.11 and Figure 5.12. (*consistent with four-wave mixing experiments [206]. **consistent with Ref. [74]. ***for better reliability the bright trion linewidth is considered consistent with voltage-dependent linewidth broadening of the D^+ linewidth in PL, see also section 4.2)

The presented calculation closely resembles the experimental observations without any free fit parameters. It demonstrates the cross-over of neutral excitons to an interacting exciton-carrier mixture. In Fig. 5.11(d), the propagation is schematically illustrated within these two distinct regimes. While in the initial low density regime the exciton scatters with free carriers, leading to a drastic decrease of the diffusivity, the attractive exciton-carrier interaction leads to the formation of "protected" states, namely trions or attractive Fermi polarons, which are hardly affected by the increasing carrier concentration (quasiparticle regime). This mechanism facilitates efficient propagation even at elevated carrier densities of up to 10^{12} cm^{-2} with mobilities as high as 3×10^3 cm^2/(Vs).

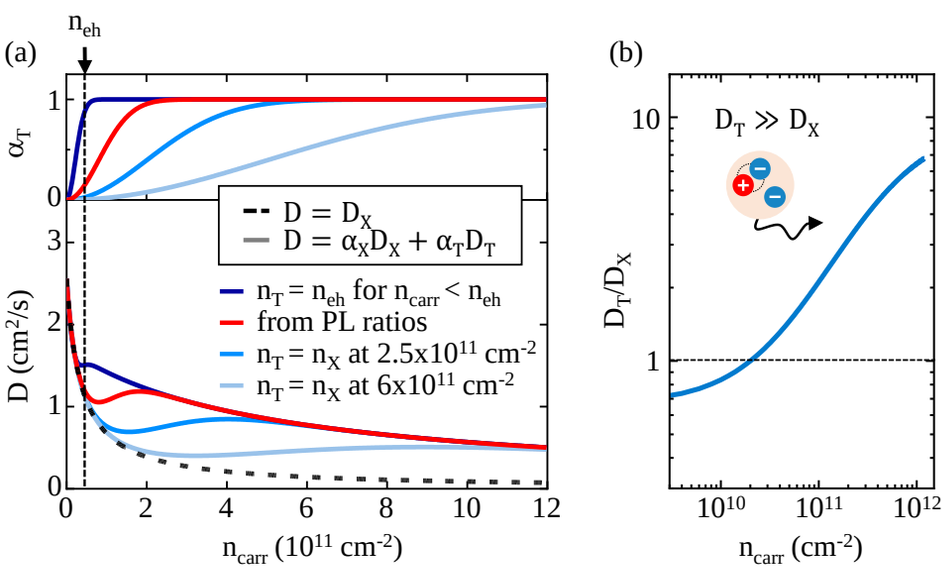

Figure 5.12: (a) Top panel: different scenarios of population ratios $\alpha_T = n_T/(n_T + n_X) = 1 - \alpha_X$ as function of free carrier density. Bottom panel: calculated average diffusion coefficients $D = \alpha_X D_X + \alpha_T D_T$ considering population ratios shown in the top panel. The scenario where no trions form and the diffusion coefficient is determined by only exciton-carrier (and exciton-phonon) scattering is plotted by a dashed black line. (b) D_T/D_X as function of free carrier density. Above the dashed line the trion diffusion coefficient is larger than the exciton diffusion coefficient.

It should be noted that the above presented model essentially roots on the exciton-trion population ratio. In general, the experimental determination of relative populations is a challenging problem. The curve shown in Fig. 5.11(d) is based on the exciton-trion population ratio estimated from PL ratios, i. e., from Fig. 5.11(c). By this, equal light-matter interaction strengths for both, D^0 and D^+ are assumed. This is supported by similar PL lifetimes and nearly constant total PL intensities, i. e., $I_{D0} + I_{D+} \approx$ const. The assumption also approximately

agrees with the scenario where each free electron binds to a trion, as long as the optically-injected electron-hole pair density is larger than the carrier density, i. e., $n_T = n_{\mathrm{carr}}$ for $n_{\mathrm{carr}} \leq n_{eh}$. In this case, the transition should occur at a free carrier density similar to the injected electron-hole pair density, i. e., at $n_{\mathrm{carr}} \approx n_{eh} = 4.5 \times 10^{10}$ cm^{-2}. For a comparison, in Fig. 5.12 (a), the diffusion as function of free carrier density is calculated for several modeled population ratios. Independent from the specific choice of the underlying exciton-trion population ratio, the diffusion coefficient strongly decreases in the initial low carrier density regime. At elevated carrier densities the diffusion coefficient remains comparably high and decreases only slowly. In almost all scenarios, in the intermediate regime a non-monotonic dependence of the diffusion coefficient is observed. Only at very low pump densities the non-monotonic behavior vanishes.

The investigations demonstrate that at elevated carrier densities trion propagation is much more efficient than exciton propagation. In order to illustrate the crucial role of trion formation for the transport, in Fig. 5.12(b), the ratio D_T/D_X is plotted as function of free charge carrier density. It strongly increases with free carrier concentration. Already at a carrier density o 3×10^{10} cm^{-2} the trion diffusion coefficient is larger than that of the excitons. At a carrier density of 10^{12} cm^{-2}, the trion diffusion coefficient is almost an order of magnitude larger.

5.2.2 Free trion propagation

In the above presented discussion trion propagation is described in analogy to exciton propagation. Particularly, it is assumed that both, excitons and trions can be described by the semiclassical diffusion equation considering respective masses and scattering rates. As demonstrated for neutral excitons in section 5.1, at elevated temperatures the wave-like nature of the propagating wave packet can lead to pronounced deviations to the semiclassical model. In the following, temperature-dependent trion diffusion experiments are performed. The free carrier density is tuned to $4 \pm 1 \times 10^{11}$ cm^{-2} in the p-doped regime. Thus, for an injected electron-hole pair density of 4.5×10^{10} cm^{-2} it is assumed that all excitons bind to trions. In Fig. 5.13 the measured temperature-dependent trion diffusion coefficient is presented. The diffusion coefficient remains largely constant. The average diffusivity is found to be in the order of 1 cm^2/s, consistent with the semiclassical model represented by Equation 5.3. It is illustrated by the red dashed line considering the trion scattering rate of $\Gamma/T = 95$ μeV/K, determined from temperature-dependent trion linewidth broadening, and a trion mass of $m_T = 1.16$ m_0.

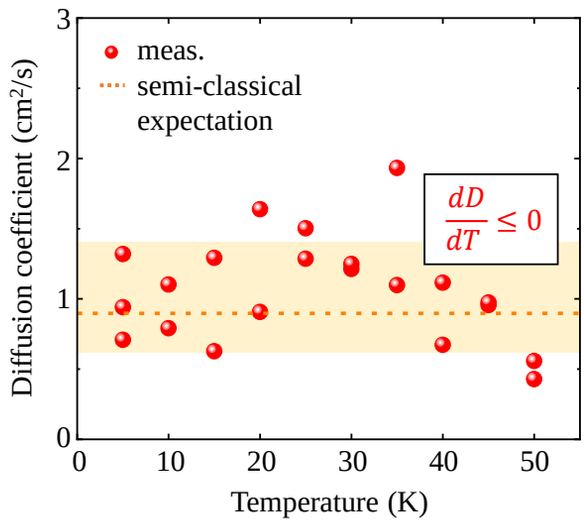

Figure 5.13: (a) Diffusion coefficient as function of temperature collecting emissions of dark trions D^+ and corresponding phonon side bands. The free carrier density is set to $4 \pm 1 \times 10^{11}$ cm^{-2}. Dashed line corresponds to the semiclassical expectation considering a trion scattering rate of $\Gamma_T/T = 95$ μeV/K obtained from Figure 5.10.

The observation demonstrates freely propagating trions which are well described by the semiclassical model. Particularly, the experiment does not show any substantial increase which would indicate hopping-like transport, nor it decreases within the first 30 K, as found for excitons. Thus, no indications for non-classical propagation behavior are found. Importantly, this finding is consistent with the above presented discussion of non-classical propagation of excitons at charge-neutrality which only scatter quasielastically with phonons. In the case of exciton-electron or trion-electron scattering, however, the scattering is highly inelastic. Due to comparably masses of excitons/trions and free carriers, energy and momentum conservation requires that the majority of the kinetic energy of the exciton/trion is transferred to the free carrier. At each trion-electron scattering event the phase of the trion wave packet is destroyed. Therefore, the formation of constructively interfering closed trajectories is suppressed compared to the case of only phonon scattering [243].

To conclude, in this chapter the mechanisms of exciton propagation in monolayer semiconductors in the presence of phonons and free charge carriers are investigated. First of all, the measurements demonstrate efficient quasiparticle propagation at cryogenic temperatures. At T = 5 K, the exciton diffusion can be well described in the semiclassical picture, revealing that the diffusion is only limited by the scattering with acoustic phonons. At elevated temperatures, an uncon-

ventional non-classical propagation behavior is observed, which is attributed to the wave-like nature of the exciton. Inserting free charge carriers to the system, no signatures of non-classical propagation are observed. Instead, the trions freely propagate through the two-dimensional crystal at all studied temperatures. While on the one hand, exciton-carrier scattering leads to a strong decrease of the exciton diffusion coefficient, on the other hand, the formation of trions enables efficient propagation even at free carrier densities on the order of 10^{12} cm^{-2}. In this density regime, the diffusion of trions is almost an order of magnitude larger compared to excitons.

Chapter 6

Summary and outlook

In the present work, the diffusion of excitons and their interaction with a two-dimensional Fermi sea of free charge carriers is explored. The experiments are performed on electrically-tuneable $MoSe_2$ and WSe_2 monolayers, taking advantage of reflectance and luminescence spectroscopy as well as time-resolved microscopy. The investigations reveal intriguing many-body interactions of optically-excited quasiparticles in a continuously tuneable, two-dimensional free carrier gas. The results include the identification and characterization of excited state trions and the quantitative determination and description of exciton-carrier scattering. In addition, by the electron recoil effect, the effective trion temperature is accessed and relaxation and cooling dynamics are studied. Based on these findings, the propagation mechanisms of the optical quasiparticles are investigated revealing signatures of non-classical exciton diffusion and a non-monotonic dependence of the diffusion coefficient on the free carrier density.

The main results of this work are discussed in chapter 4 and chapter 5. Chapter 4 begins with the investigations of exciton-carrier interaction in electrically-tuneable hBN-encapsulated WSe_2 monolayers. By means of reflectance contrast spectroscopy at liquid helium temperature, in section 4.1, the resonance energies, linewidth broadening and oscillator strength of ground and excited state excitons are determined. The experimental observations reveal meta-stable excited sate trions which are formed out of excited-state excitons attractively interacting with the Fermi sea of free charge carriers. Excited state trions are characterized by huge binding energies of $15 - 20$ meV and autoionization, an efficient recombination pathway which manifests in an additional density-independent linewidth broadening of ≈ 10 meV. Excited state trions are also observed in photoluminescence experiments. A theoretical model based on the Fermi polaron formalism qualitatively describes the experimental observations.

Subsequently, in section 4.2, exciton-carrier scattering is investigated by a quantitative linewidth analysis of exciton and trion resonances in temperature- and voltage-dependent reflectance contrast and PL spectroscopy of electrically-tuneable hBN-encapsulated WSe_2 and $MoSe_2$ monolayers. By increasing the temperature an increasing exciton linewidth broadening is observed. Furthermore, the exciton linewidth increases stronger with free carrier density in the case of a larger trion linewidth. Supported by an analytical model, the investigation demonstrates the crucial role of a finite dissipation on the carrier-induced exciton scattering rate: only in the presence of an additional dissipation, e. g. due to phonons, excitons efficiently scatter with electrons or holes also at elevated densities where the Fermi sea is degenerate. This is further supported by an extended study including multiple measurements on several sample structures and different measurement positions. The investigation provides a lower limit for the exciton-carrier scattering in two-dimensional semiconductors, which is basically determined by the trion linewidth.

In section 4.3, the relaxation and cooling dynamics of the exciton-carrier gas after excitation is investigated by the electron recoil effect. Employing electrically-tuneable hBN-encapsulated monolayer $MoSe_2$, the characteristic low energy flank of the ground state trion emission is analyzed at cryogenic temperatures between 5 and 50 K. Performing steady-state and time-resolved experiments allows to directly access the transient temperature of the trion gas. Immediately after excitation, the trion temperature exceeds the lattice temperature by at least 20 K. Subsequently, the trions cool down to lattice temperature. At low carrier densities, the 1/e cooling time is on the order of 15 ps and is dominated by the scattering with phonons. With both, increasing temperature and increasing free carrier density an accelerated cooling is observed. In all studied scenarios the trion gas cools down to lattice temperature after 50 ps.

Having discussed basic exciton-electron interactions, in chapter 5, exciton propagation mechanisms in two-dimensional TMDCs are investigated. By time- and spatially-resolved experiments on hBN-encapsulated WSe_2 monolayers, the diffusion of long-lived and thermalized dark excitons is explored at cryogenic temperatures. Despite being dark, these ground state excitons emit via phonon side bands or via a weak oscillator strength in out-of-plane polarization, characterized by PL lifetimes of up to 1 ns. At charge-neutrality, efficient exciton diffusion is observed, reaching values of up to 3 cm^2/s at a lattice temperature of $T = 5$ K. In combination with exciton scattering rates, determined from temperature-dependent PL linewidth analysis, this finding reveals intrinsically limited propagation, which is

governed by the scattering with linear acoustic phonons. Increasing the temperature, however, leads to a decrease of the diffusivity far below the onset of higher energy phonon modes. This observation can neither be explained by hopping nor by semiclassical free propagation. Considering that the exciton's de Broglie wavelength exceeds the mean free path, it follows that the semiclassical picture is not applicable in this temperature regime. Based on a recently proposed model calculation for TMDCs, the experiment is discussed in terms of the wave-like nature of the exciton. However, a first-order perturbation theory explains the observed unusual propagation behavior only qualitatively and underestimates the effect by an order of magnitude.

In order to investigate the impact of free charge carriers on the exciton propagation, the diffusion coefficient of the dark excitons is measured as a function of free charge carrier density. Increasing the electron or hole concentration up to $\approx 1\times10^{11}$ cm^{-2} leads to a decrease of the mobility, governed by enhanced exciton-carrier scattering. Remarkably, further increasing the carrier density results in an *increase* of the mobility, which then only slowly decreases over a wide range of carrier densities of up to 10^{12} cm^{-2}. The latter finding can be well described by attractive exciton-carrier interactions, leading to bound trion states which are largely unaffected from carrier scattering. Finally, temperature-independent trion diffusion is observed, demonstrating free trion propagation with effective mobilities of up to 3×10^{3} cm^2/(Vs). In particular, this finding implements that trions are not localized in hBN-encapsulated TMDC monolayers even at the lowest studied temperature at T = 5 K.

The presented studies constitute a solid contribution to the basic understanding of exciton-carrier interactions and quasiparticle propagation in electrically-tuneable two-dimensional semiconductors. The observed signatures of excited state trions in section 4.1 motivate for further studies in the regime of strong exciton-carrier interactions. At elevated carrier densities additional features in the absorption spectrum emerge which have been assigned to exotic high-density states, such as hexcitons and oxcitons [53]. There are also entirely unexplored low energy features in voltage-dependent emission spectra (see e. g. Ref. [49]). If the average distance between individual electrons becomes equal or smaller than the exciton Bohr radius, i. e., $n \geq 1/(\pi a_{B,X}^2)$, the picture of a rigid exciton interacting with the Fermi sea breaks down. In monolayer TMDCs, for ground state excitons this regime starts at free carrier densities of $\approx 10^{13}$ cm^{-2}. For 2s excited states it is expected to occur already an order of magnitude below, i. e., at experimentally accessible free carrier concentrations $n_{\mathrm{carr}} \approx 10^{12}$ cm^{-2}. In this regime the interac-

tion of the optically-excited electron with the Fermi sea becomes comparably with respect to the interaction with the hole in the conduction band. The consequences of this coupling regime on the optical and transport properties constitutes an open research field.

The investigated exciton-carrier scattering mechanisms in section 4.2 motivate for further magneto-optic experiments where the individual contributions from exciton scattering with spin up and spin down electrons or the scattering into trion states can be separated. By applying a magnetic field, the valleys of the electronic band structure at K and K' shift in energy and the doping of charge carriers with a fixed valley and spin quantum number becomes feasible [252]. For example, applying polarization-resolved voltage-dependent reflectance contrast spectroscopy at finite magnetic fields in monolayer $MoSe_2$, the scattering of K-K excitons with electrons at K (intra-valley exciton-electron scattering) can be studied in the absence of trion formation (as the bright exciton at K only forms to a trion with electrons at K').

The demonstrated analysis of the low-energy trion recoil flank in section 4.3 or the high energy shoulder of exciton phonon side bands in section 5.1 constitutes a powerful access to the quasiparticle temperature. The analysis of low- and high-energy flanks can be applied to other emissions as well. While the investigations in this work focus on the bright trion in monolayer $MoSe_2$, the analysis is applicable for dark trions as well. Particularly, the dark trions $D^{\pm}$ in monolayer WSe_2 exhibit a similar low-energy shoulder than the investigated bright trions. Furthermore, the electronic side band of the dark trion D^{-}, i. e., the D_B^- emission, is characterized by an even more pronounced low energy flank. Different to the conventional electron recoil effect, where the electron only compensates a comparably small intra-valley momentum, here, the electron makes a transition across the whole Brillouin zone. In principal, the recoil effect is not limited to trions. For example in the case of neutral or charged biexcitons, also asymmetric emission profiles are expected. In analogy to the electron recoil effect, the *exciton recoil effect* could give access to the underlying biexciton distribution and, for thermalized states, the biexciton temperature.

Regarding the observed highly-mobile dark excitons in hBN-encapsulated monolayer WSe_2, a versatile platform for the investigation of intrinsic exciton transport properties in monolayer semiconductors has been established. Subsequently followed studies have demonstrated that dark exciton propagation exhibits peculiar strain dependence [108, 286], non-linear phenomena [108, 287] and can be guided by quasi-1D channels [288]. Spin-valley lifetimes on the order of several nanosec-

onds [189] render dark excitons promising for the investigation of spin-transport with possible spin diffusion lengths of several micrometer. The observed non-classical propagation behavior challenges the widely-used semiclassical diffusion model and requires further theoretical and experimental investigations. For example, diffusion experiments in the presence of an external magnetic field would elucidate the weak localization effect on the exciton propagation. From a more general perspective, the observed non-classical exciton diffusion motivates to investigate other two-dimensional materials where the Mott-Ioffe-Regel criterion is violated such as two-dimensional hybrid perovskites [204].

The demonstration of freely propagating trions in section 5.2 is particularly encouraging for the deterministic control of electrically-driven and optically-detected trion currents, as demonstrated in Refs. [111, 110]. Furthermore, trions are suitable for the investigation of the valley-Hall effect. So far, the valley-Hall effect has been studied in TMDCs for excitons driven by temperature gradients and/or chemical potentials [90], as well as exciton-polaritons in a channel-like geometry [91]. However, the external control of a directed trion current by applying an in-plane electric field would allow for the deterministic, ambipolar investigation of the valley-Hall effect in a well-defined, thermalized system. Furthermore, the presented diffusion experiments are important for theoretical considerations of Fermi polaron [289] and, more general, biexciton propagation. As both, excitons and trions efficiently propagate, also bound exciton-exciton or exciton-trion pairs, i. e., neutral and charged biexcitons are expected to propagate. Due to their observed lifetime of about 100 ps, particularly charged biexcitons in monolayer WS_2 and WSe_2 are highly promising for diffusion experiments by means of time-resolved microscopy.

Bibliography

[1] John E. Davey and Titus Pankey. Epitaxial gaas films deposited by vacuum evaporation. *Journal of Applied Physics*, 39(4):1941–1948, 1968.

[2] K. v. Klitzing, G. Dorda, and M. Pepper. New method for high-accuracy determination of the fine-structure constant based on quantized hall resistance. *Phys. Rev. Lett.*, 45:494–497, Aug 1980.

[3] R. Dingle, W. Wiegmann, and C. H. Henry. Quantum states of confined carriers in very thin al_xga_{1-x}As-gaas-al_xga_{1-x}As heterostructures. *Phys. Rev. Lett.*, 33:827–830, Sep 1974.

[4] C. Klingshirn. *Semiconductor Optics*. Springer, Berlin Heidelberg New York, 3rd edition, 2007.

[5] J. Frenkel. On the transformation of light into heat in solids. i. *Phys. Rev.*, 37(1):17–44, 1931.

[6] E. F. Gross and N. A. Karrjew. *Dokl. Akad. Nauk SSSR*.

[7] R.C. Miller and D.A. Kleinman. Excitons in gaas quantum wells. *Journal of Luminescence*, 30(1):520–540, 1985.

[8] Yu.E Lozovik and A.M Ruvinsky. Magnetoexcitons in coupled quantum wells. *Physics Letters A*, 227(3):271–284, 1997.

[9] A. Von Lehmen, D. S. Chemla, J. E. Zucker, and J. P. Heritage. Optical stark effect on excitons in gaas quantum wells. *Opt. Lett.*, 11(10):609–611, Oct 1986.

[10] H. Hillmer, S. Hansmann, A. Forchel, M. Morohashi, E. Lopez, H. P. Meier, and K. Ploog. Two-dimensional exciton transport in GaAs/GaAlAs quantum wells. *Appl. Phys. Lett.*, 53(20):1937–1939, nov 1988.

[11] D. A. Kleinman. Binding energy of biexcitons and bound excitons in quantum wells. *Phys. Rev. B*, 28:871–879, Jul 1983.

[12] R.C. Miller, A.C. Gossard, W.T. Tsang, and O. Munteanu. Bound excitons in p-doped gaas quantum wells. *Solid State Communications*, 43(7):519–522, 1982.

[13] J. Hegarty, M. D. Sturge, C. Weisbuch, A. C. Gossard, and W. Wiegmann. Resonant rayleigh scattering from an inhomogeneously broadened transition: A new probe of the homogeneous linewidth. *Phys. Rev. Lett.*, 49:930–932, Sep 1982.

[14] Murray A. Lampert. Mobile and Immobile Effective-Mass-Particle Complexes in Nonmetallic Solids. *Phys. Rev. Lett.*, 1(12):450–453, dec 1958.

[15] K. Kheng, R. Cox, Merle d' Aubigné, Franck Bassani, K. Saminadayar, and S Tatarenko. Observation of negatively charged excitons X- in semiconductor quantum wells. *Phys. Rev. Lett.*, 71(11):1752–1755, sep 1993.

[16] H. W. Yoon, A. Ron, M. D. Sturge, and L. N. Pfeiffer. Diffusion of free trions in mixed type gaasalas quantum wells. *Solid State Communications*, 100(11):743–747, 1996.

[17] F Pulizzi, W.H.A Thijssen, P.C.M Christianen, J.C. Maan, D.R. Yakovlev, W Ossau, Wojtowicz, T. G. Karczewski, and J. Kossut. Motion of neutral and negatively charged excitons in high magnetic fields. *Physica B: Condensed Matter*, 298(1):397–401, 2001. International Conference on High Magnetic Fields in Semiconductors.

[18] M. T. Portella-Oberli, V. Ciulin, S. Haacke, J.-D. Ganière, P. Kossacki, M. Kutrowski, T. Wojtowicz, and B. Deveaud. Diffusion, localization, and dephasing of trions and excitons in cdte quantum wells. *Phys. Rev. B*, 66:155305, Oct 2002.

[19] Daniele Sanvitto, Fabio Pulizzi, Andrew J. Shields, Peter C. M. Christianen, Stuart N. Holmes, Michelle Y. Simmons, David A. Ritchie, Jan C. Maan, and Michael Pepper. Observation of charge transport by negatively charged excitons. *Science*, 294(5543):837–839, 2001.

[20] F. Pulizzi, D. Sanvitto, P.C.M. Christianen, A.J. Shields, S.N. Holmes, M.Y. Simmons, D.A. Ritchie, M. Pepper, and J.C. Maan. Optical imaging of trion diffusion and drift in gaas quantum wells. *Phys. Rev. B*, 68:205304, Nov 2003.

[21] Fumiyoshi Takano, Takashi Tokizaki, Hiro Akinaga, Shinji Kuroda, and Kôki Takita. Real-time observation of charged exciton drift in modulation-doped (Cd,Mn)Te quantum well. *Phys. Rev. B - Condens. Matter Mater. Phys.*, 71(12):1–5, 2005.

[22] Novoselov K.S., Geim A.K., Morozov S.V., Jiang D, Zhang Y, Dubonos S.V., Grigorieva I.V., Firsov, A.A. Electric Field Effect in Atomically Thin Carbon Films. *Science (80-.).*, 306:666–9, 2004.

[23] K. S. Novoselov, A. K. Geim, S. V. Morozov, D. Jiang, M. I. Katsnelson, I. V. Grigorieva, S. V. Dubonos, and A. A. Firsov. *Nature*, (30):197–200.

[24] Yuan Cao, Valla Fatemi, Shiang Fang, Kenji Watanabe, Takashi Taniguchi, Efthimios Kaxiras, and Pablo Jarillo-Herrero. Unconventional superconductivity in magic-angle graphene superlattices. *Nature*, 556(7699):43–50, apr 2018.

[25] K. S. Novoselov, Z. Jiang, Y. Zhang, S. V. Morozov, H. L. Stormer, U. Zeitler, J. C. Maan, G. S. Boebinger, P. Kim, and A. K. Geim. Room-temperature quantum hall effect in graphene. *Science*, 315(5817):1379–1379, 2007.

[26] A. K. Geim and I. V. Grigorieva. Van der Waals heterostructures. *Nature*, 499(7459):419–25, jul 2013.

[27] Andrea Splendiani, Liang Sun, Yuanbo Zhang, Tianshu Li, Jonghwan Kim, Chi-Yung Chim, Giulia Galli, and Feng Wang. Emerging photoluminescence in monolayer MoS2. *Nano Lett.*, 10(4):1271–1275, apr 2010.

[28] Kin Fai Mak, Changgu Lee, James Hone, Jie Shan, and Tony F. Heinz. Atomically thin MoS_2: A new direct-gap semiconductor. *Phys. Rev. Lett.*, 105(13):136805, sep 2010.

[29] Thomas Mueller and Ermin Malic. Exciton physics and device application of two-dimensional transition metal dichalcogenide semiconductors. *NPJ 3D Mater. Appl.*, 2:29, 2018.

[30] M M Fogler, L V Butov, and K S Novoselov. Indirect excitons in van der Waals heterostructures. *arXiv Prepr. arXiv1404.1418*, 5(May):5, 2014.

[31] Gang Wang, Alexey Chernikov, Mikhail M. Glazov, Tony F. Heinz, Xavier Marie, Thierry Amand, and Bernhard Urbaszek. Colloquium : Excitons in atomically thin transition metal dichalcogenides. *Rev. Mod. Phys.*, 90(2):021001, apr 2018.

[32] Ting Cao, Gang Wang, Wenpeng Han, Huiqi Ye, Chuanrui Zhu, Junren Shi, Qian Niu, Pingheng Tan, Enge Wang, Baoli Liu, and Ji Feng. Valley-selective circular dichroism of monolayer molybdenum disulphide. *Nat. Commun.*, 3(may):887, jan 2012.

[33] Di Xiao, Gui-Bin Liu, Wanxiang Feng, Xiaodong Xu, and Wang Yao. Coupled Spin and Valley Physics in Monolayers of MoS_2 and Other Group-VI Dichalcogenides. *Phys. Rev. Lett.*, 108(19):196802, may 2012.

[34] G. Sallen, L. Bouet, X. Marie, G. Wang, C. R. Zhu, W. P. Han, Y. Lu, P. H. Tan, T. Amand, B. L. Liu, and B. Urbaszek. Robust optical emission polarization in mos_2 monolayers through selective valley excitation. *Phys. Rev. B*, 86(8):081301, aug 2012.

[35] Rafael Roldán, Andrés Castellanos-Gomez, Emmanuele Cappelluti, and Francisco Guinea. Strain engineering in semiconducting two-dimensional crystals. *J. Phys. Condens. Matter*, 27(31):313201, aug 2015.

[36] Gerd Plechinger, Philipp Nagler, Ashish Arora, Robert Schmidt, Alexey Chernikov, Andrés Granados del Águila, Peter C.M. Christianen, Rudolf Bratschitsch, Christian Schüller, and Tobias Korn. Trion fine structure and coupled spin-valley dynamics in monolayer tungsten disulfide. *Nat. Commun.*, 7(May):12715, sep 2016.

[37] Minhao He, Pasqual Rivera, Dinh Van Tuan, Nathan P. Wilson, Min Yang, Takashi Taniguchi, Kenji Watanabe, Jiaqiang Yan, David G. Mandrus, Hongyi Yu, Hanan Dery, Wang Yao, and Xiaodong Xu. Valley phonons and exciton complexes in a monolayer semiconductor. *Nat. Commun.*, 11(1):618, 2020.

[38] J. Klein, J. Wierzbowski, A. Regler, J. Becker, F. Heimbach, K. Müller, M. Kaniber, and J. J. Finley. Stark effect spectroscopy of mono- and few-layer mos2. *Nano Letters*, 16(3):1554–1559, 2016. PMID: 26845085.

[39] Zefang Wang, Yi-Hsin Chiu, Kevin Honz, Kin Fai Mak, and Jie Shan. Electrical tuning of interlayer exciton gases in wse2 bilayers. *Nano Letters*, 18(1):137–143, 2018. PMID: 29240440.

[40] Archana Raja, Andrey Chaves, Jaeeun Yu, Ghidewon Arefe, Heather M. Hill, Albert F. Rigosi, Timothy C. Berkelbach, Philipp Nagler, Christian Schüller, Tobias Korn, Colin Nuckolls, James Hone, Louis E. Brus, Tony F. Heinz, David R. Reichman, and Alexey Chernikov. Coulomb engineering of the bandgap and excitons in two-dimensional materials. *Nat. Commun.*, 8(May):15251, may 2017.

[41] Kin Fai Mak, Keliang He, Changgu Lee, Gwan Hyoung Lee, James Hone, Tony F. Heinz, and Jie Shan. Tightly bound trions in monolayer mos_2. *Nature Materials*, 12:207–211, dez 2013.

[42] Aaron M Jones, Hongyi Yu, Nirmal J Ghimire, Sanfeng Wu, Grant Aivazian, Jason S Ross, Bo Zhao, Jiaqiang Yan, David G Mandrus, Di Xiao, Wang Yao, and Xiaodong Xu. Optical generation of excitonic valley coherence in monolayer WSe2. *Nat. Nanotechnol.*, 8(9):634–8, sep 2013.

[43] Jason W. Christopher, Bennett B. Goldberg, and Anna K. Swan. Long tailed trions in monolayer MoS2: Temperature dependent asymmetry and resulting red-shift of trion photoluminescence spectra. *Sci. Rep.*, 7(1):14062, 2017.

[44] Meinrad Sidler, Patrick Back, Ovidiu Cotlet, Ajit Srivastava, Thomas Fink, Martin Kroner, Eugene Demler, and Atac Imamoglu. Fermi polaron-polaritons in charge-tunable atomically thin semiconductors. *Nat. Phys.*, 13(3):255–261, mar 2017.

[45] Dmitry K. Efimkin and Allan H. MacDonald. Many-body theory of trion absorption features in two-dimensional semiconductors. *Phys. Rev. B*, 95(3):035417, jan 2017.

[46] Dmitry K. Efimkin, Emma K. Laird, Jesper Levinsen, Meera M. Parish, and Allan H. MacDonald. Electron-exciton interactions in the exciton-polaron problem. *Phys. Rev. B*, 103:075417, Feb 2021.

[47] Yumeng You, XiaoXiao Zhang, Timothy C. Berkelbach, Mark S. Hybertsen, David R. Reichman, and Tony F. Heinz. Observation of biexcitons in monolayer WSe2. *Nat. Phys.*, 11(6):477–481, may 2015.

[48] Gerd Plechinger, Philipp Nagler, Julia Kraus, Nicola Paradiso, Christoph Strunk, Christian Schüller, and Tobias Korn. Identification of excitons, trions and biexcitons in single-layer WS 2. *Phys. status solidi - Rapid Res. Lett.*, 9(8):457–461, aug 2015.

[49] Ziliang Ye, Lutz Waldecker, Eric Yue Ma, Daniel Rhodes, Abhinandan Antony, Bumho Kim, Xiao-Xiao Zhang, Minda Deng, Yuxuan Jiang, Zhengguang Lu, Dmitry Smirnov, Kenji Watanabe, Takashi Taniguchi, James Hone, and Tony F. Heinz. Efficient generation of neutral and charged biexcitons in encapsulated WSe2 monolayers. *Nat. Commun.*, 9(1):3718, dec 2018.

[50] Zhipeng Li, Tianmeng Wang, Zhengguang Lu, Chenhao Jin, Yanwen Chen, Yuze Meng, Zhen Lian, Takashi Taniguchi, Kenji Watanabe, Shengbai Zhang, Dmitry Smirnov, and Su-Fei Shi. Revealing the biexciton and trion-exciton complexes in BN encapsulated WSe2. *Nat. Commun.*, 9(1):3719, 2018.

[51] Shao-Yu Chen, Thomas Goldstein, Takashi Taniguchi, Kenji Watanabe, and Jun Yan. Coulomb-bound four- and five-particle intervalley states in an atomically-thin semiconductor. *Nat. Commun.*, 9(1):3717, 2018.

[52] Matteo Barbone, Alejandro R.-P. Montblanch, Dhiren M. Kara, Carmen Palacios-Berraquero, Alisson R. Cadore, Domenico De Fazio, Benjamin Pingault, Elaheh Mostaani, Han Li, Bin Chen, Kenji Watanabe, Takashi Taniguchi, Sefaattin Tongay, Gang Wang, Andrea C. Ferrari, and Mete Atatüre. Charge-tuneable biexciton complexes in monolayer WSe2. *Nat. Commun.*, 9(1):3721, 2018.

[53] Dinh Van Tuan, Su-Fei Shi, Xiaodong Xu, Scott A. Crooker, and Hanan Dery. Hexcitons and oxcitons in monolayer wse_2, 2022.

[54] Xiao-Xiao Zhang, Yumeng You, Shu Yang Frank Zhao, and Tony F. Heinz. Experimental Evidence for Dark Excitons in Monolayer WSe_2. *Phys. Rev. Lett.*, 115(25):257403, 2015.

[55] Dominik Christiansen, Malte Selig, Gunnar Berghäuser, Robert Schmidt, Iris Niehues, Robert Schneider, Ashish Arora, Steffen Michaelis de Vasconcellos, Rudolf Bratschitsch, Ermin Malic, and Andreas Knorr. Phonon Sidebands in Monolayer Transition Metal Dichalcogenides. *Phys. Rev. Lett.*, 119(18):187402, nov 2017.

[56] Erfu Liu, Jeremiah van Baren, Takashi Taniguchi, Kenji Watanabe, Yia-Chung Chang, and Chun Hung Lui. Valley-selective chiral phonon replicas of dark excitons and trions in monolayer WSe_2. *Phys. Rev. Res.*, 1(3):032007, 2019.

[57] G. Kioseoglou, a. T. Hanbicki, M. Currie, a. L. Friedman, D. Gunlycke, and B. T. Jonker. Valley polarization and intervalley scattering in monolayer MoS2. *Appl. Phys. Lett.*, 101(22):221907, 2012.

[58] G. Wang, M. M. Glazov, C. Robert, T. Amand, X. Marie, and B. Urbaszek. Double resonant raman scattering and valley coherence generation in monolayer wse_2. *Phys. Rev. Lett.*, 115:117401, Sep 2015.

[59] Bastian Miller, Jessica Lindlau, Max Bommert, Andre Neumann, Hisato Yamaguchi, Alexander Holleitner, Alexander Högele, and Ursula Wurstbauer. Tuning the fröhlich exciton-phonon scattering in monolayer mos_2. *Nat. Commun.*, 10:807, 2019.

[60] Ioannis Paradisanos, Gang Wang, Evgeny M. Alexeev, Alisson R. Cadore, Xavier Marie, Andrea C. Ferrari, Mikhail M. Glazov, and Bernhard Urbaszek. Efficient phonon cascades in wse_2 monolayers. *Nature*, 12:538, 2021.

[61] Marvin Kulig, Jonas Zipfel, Philipp Nagler, Sofia Blanter, Christian Schüller, Tobias Korn, Nicola Paradiso, Mikhail M. Glazov, and Alexey Chernikov. Exciton Diffusion and Halo Effects in Monolayer Semiconductors. *Phys. Rev. Lett.*, 120(20):207401, may 2018.

[62] Raul Perea-Causin, Samuel Brem, Roberto Rosati, Roland Jago, Marvin Kulig, Jonas D. Ziegler, Jonas Zipfel, Alexey Chernikov, and Ermin Malic. Exciton Propagation and Halo Formation in Two-Dimensional Materials. *Nano Lett.*, 19(10):7317–7323, oct 2019.

[63] M. M. Glazov. Phonon wind and drag of excitons in monolayer semiconductors. *Phys. Rev. B*, 100(4):045426, jul 2019.

[64] I. Finkelstein, G.and Bar-Joseph. Charged excitons in gaas quantum wells. *Il Nuovo Cimento D*, 17:1239–1245, 2016.

[65] G. Astakhov, D. Yakovlev, V. Kochereshko, W. Ossau, J. Nürnberger, W. Faschinger, and G. Landwehr. Charged excitons in ZnSe-based quantum wells. *Phys. Rev. B*, 60(12):R8485–R8488, 1999.

[66] Jason S Ross, Sanfeng Wu, Hongyi Yu, Nirmal J Ghimire, Aaron M Jones, Grant Aivazian, Jiaqiang Yan, David G Mandrus, Di Xiao, Wang Yao, and Xiaodong Xu. Electrical control of neutral and charged excitons in a monolayer semiconductor. *Nat. Commun.*, 4:1474, jan 2013.

[67] Bogdan Ganchev, Neil Drummond, Igor Aleiner, and Vladimir Fal'ko. Three-Particle Complexes in Two-Dimensional Semiconductors. *Phys. Rev. Lett.*, 114(10):107401, mar 2015.

[68] H. W. Yoon, D. R. Wake, and J. P. Wolfe. Effect of exciton-carrier thermodynamics on the gaas quantum well photoluminescence. *Phys. Rev. B*, 54:2763–2774, Jul 1996.

[69] Archana Raja, Lutz Waldecker, Jonas Zipfel, Yeongsu Cho, Samuel Brem, Jonas D. Ziegler, Marvin Kulig, Takashi Taniguchi, Kenji Watanabe, Ermin Malic, Tony F. Heinz, Timothy C. Berkelbach, and Alexey Chernikov. Dielectric disorder in two-dimensional materials. *Nat. Nanotechnol.*, 14(9):832–837, sep 2019.

[70] Daniel Rhodes, Sang Hoon Chae, Rebeca Ribeiro-Palau, and James Hone. Disorder in van der Waals heterostructures of 2D materials. *Nat. Mater.*, 18(6):541–549, jun 2019.

[71] Ashish Arora, Thorsten Deilmann, Till Reichenauer, Johannes Kern, Steffen Michaelis de Vasconcellos, Michael Rohlfing, and Rudolf Bratschitsch.

Excited-State Trions in Monolayer WS_2. *Phys. Rev. Lett.*, 123(16):167401, oct 2019.

[72] A R P Rau. The Negative Ion of Hydrogen. *J. Astrophys. Astr.*, 17:113–145, 1996.

[73] Samuel Brem, Jonas Zipfel, Malte Selig, Archana Raja, Lutz Waldecker, Jonas D. Ziegler, Takashi Taniguchi, Kenji Watanabe, Alexey Chernikov, and Ermin Malic. Intrinsic lifetime of higher excitonic states in tungsten diselenide monolayers. *Nanoscale*, 11(25):12381–12387, apr 2019.

[74] Thomas Goldstein, Yueh-Chun Wu, Shao-Yu Chen, Takashi Taniguchi, Kenji Watanabe, Kalman Varga, and Jun Yan. Ground and excited state exciton polarons in monolayer $MoSe_2$. *J. Chem. Phys.*, 153(7):071101, 2020.

[75] Ke Xiao, Tengfei Yan, Qiye Liu, Siyuan Yang, Chiming Kan, Ruihuan Duan, Zheng Liu, and Xiaodong Cui. Many-body effect on optical properties of monolayer molybdenum diselenide. *The Journal of Physical Chemistry Letters*, 12(10):2555–2561, 2021. PMID: 33683894.

[76] Matthew R. Carbone, Matthew Z. Mayers, and David R. Reichman. Microscopic model of the doping dependence of linewidths in monolayer transition metal dichalcogenides. *The Journal of Chemical Physics*, 152(19):194705, 2021/07/02 2020.

[77] A. Esser, E. Runge, R. Zimmermann, and W. Langbein. Trions in GaAs Quantum Wells: Photoluminescence Lineshape Analysis. *Phys. Stat. Sol.*, 178(1):489, mar 2000.

[78] Sangjun Park, Bo Han, Caroline Boule, Daniel Paget, Alistair C H Rowe, Fausto Sirotti, Takashi Taniguchi, Kenji Watanabe, Cedric Robert, Laurent Lombez, Bernhard Urbaszek, Xavier Marie, and Fabian Cadiz. Imaging Seebeck drift of excitons and trions in MoSe 2 monolayers. *2D Mater.*, 8(4):045014, 2021.

[79] T. P. Lyons, S. Dufferwiel, M. Brooks, F. Withers, T. Taniguchi, K. Watanabe, K. S. Novoselov, G. Burkard, and A. I. Tartakovskii. The valley Zeeman effect in inter- and intra-valley trions in monolayer WSe2. *Nat. Commun.*, 10(1):2330, 2019.

[80] Yaroslav V. Zhumagulov, Alexei Vagov, Dmitry R. Gulevich, Paulo E. Faria Junior, and Vasili Perebeinos. Trion induced photoluminescence of a doped MoS_2 monolayer. *J. Chem. Phys.*, 153(4):1–11, 2020.

[81] L M Smith, D R Wake, J P Wolfe, D. Levi, M. V. Klein, J. Klem, T. Henderson, and H. Morkoç. Picosecond imaging of photoexcited carriers in quan-

tum wells: Anomalous lateral confinement at high densities. *Phys. Rev. B*, 38(8):5788–5791, sep 1988.

[82] K. T. Tsen, O. F. Sankey, and H. Morkoc. Transport properties of excitons in gaas quantum wells-time-resolved raman probe. *Applied Physics Letters*, 57(16):1666–1668, 1990.

[83] D. Oberhauser, K.-H. Pantke, J. M. Hvam, G. Weimann, and C. Klingshirn. Exciton scattering in quantum wells at low temperatures. *Phys. Rev. B*, 47(11):6827–6830, mar 1993.

[84] A. Mysyrowicz, E. Benson, and E. Fortin. Directed Beam of Excitons Produced by Stimulated Scattering. *Phys. Rev. Lett.*, 77(5):896–899, 1996.

[85] E. Benson, E. Fortin, and A. Mysyrowicz. Anomalous exciton transport in Cu2O: Excitonic superfluidity or phonon-wind effect? *Solid State Commun.*, 101(5):313–317, 1997.

[86] S. A. Moskalenko and D. W. Snoke. *Bose-Einstein condensation of excitons and biexcitons*. Cambridge University Press, 2005.

[87] S.G. Tikhodeev, G.A. Kopelevich, and N.A. Gippius. Exciton Transport in Cu2O: Phonon Wind versus Superfluidity. *physica status solidi (b)*, 206(1):45–53, mar 1998.

[88] L. V. Butov, L. S. Levitov, A. V. Mintsev, B. D. Simons, A. C. Gossard, and D. S. Chemla. Formation Mechanism and Low-Temperature Instability of Exciton Rings. *Physical Review Letters*, 92(11):117404, mar 2004.

[89] K F Mak, K L McGill, J Park, and P L McEuen. The valley Hall effect in MoS2 transistors. *Science (80-.).*, 344:1489–1492, 2014.

[90] Masaru Onga, Yijin Zhang, Toshiya Ideue, and Yoshihiro Iwasa. Exciton Hall effect in monolayer MoS2. *Nat. Mater.*, 16(12):1193–1197, oct 2017.

[91] Nils Lundt, Łukasz Dusanowski, Evgeny Sedov, Petr Stepanov, Mikhail M. Glazov, Sebastian Klembt, Martin Klaas, Johannes Beierlein, Ying Qin, Sefaattin Tongay, Maxime Richard, Alexey V. Kavokin, Sven Höfling, and Christian Schneider. Optical valley Hall effect for highly valley-coherent exciton-polaritons in an atomically thin semiconductor. *Nat. Nanotechnol.*, 14(8):770–775, aug 2019.

[92] Zefei Wu, Benjamin T. Zhou, Xiangbin Cai, Patrick Cheung, Gui-Bin Liu, Meizhen Huang, Jiangxiazi Lin, Tianyi Han, Liheng An, Yuanwei Wang, Shuigang Xu, Gen Long, Chun Cheng, Kam Tuen Law, Fan Zhang, and Ning Wang. Intrinsic valley hall transport in atomically thin mos2. *Nat. Commun.*, 10:611, 2019.

[93] M. M. Glazov and L. E. Golub. Skew Scattering and Side Jump Drive Exciton Valley Hall Effect in Two-Dimensional Crystals. *Phys. Rev. Lett.*, 125(15):157403, oct 2020.

[94] A. Hichri and S. Jaziri. Trion fine structure and anomalous hall effect in monolayer transition metal dichalcogenides. *Phys. Rev. B*, 102:085407, Aug 2020.

[95] Nardeep Kumar, Qiannan Cui, Frank Ceballos, Dawei He, Yongsheng Wang, and Hui Zhao. Exciton-exciton annihilation in $MoSe_2$ monolayers. *Phys. Rev. B*, 89(12):125427, mar 2014.

[96] Long Yuan, Ti Wang, Tong Zhu, Mingwei Zhou, and Libai Huang. Exciton Dynamics, Transport, and Annihilation in Atomically Thin Two-Dimensional Semiconductors. *J. Phys. Chem. Lett.*, 8(14):3371–3379, jul 2017.

[97] F. Cadiz, C. Robert, E. Courtade, M. Manca, L. Martinelli, T. Taniguchi, K. Watanabe, T. Amand, A. C. H. Rowe, D Paget, B Urbaszek, and X Marie. Exciton diffusion in WSe 2 monolayers embedded in a van der Waals heterostructure. *Appl. Phys. Lett.*, 112(15):152106, apr 2018.

[98] Yang Fu, Dawei He, Jiaqi He, Ang Bian, Lu Zhang, Shuangyan Liu, Yongsheng Wang, and Hui Zhao. Effect of Dielectric Environment on Excitonic Dynamics in Monolayer WS 2. *Adv. Mater. Interfaces*, page 1901307, oct 2019.

[99] Shiekh Zia Uddin, Hyungjin Kim, Monica Lorenzon, Matthew Yeh, Der-Hsien Lien, Edward S. Barnard, Han Htoon, Alexander Weber-Bargioni, and Ali Javey. Neutral Exciton Diffusion in Monolayer MoS 2. *ACS Nano*, 14(10):13433–13440, 2020.

[100] Roberto Rosati, Samuel Brem, Raul Perea-Causin, Robert Schmidt, Iris Niehues, Steffen Michaelis de Vasconcellos, Rudolf Bratschitsch, and Ermin Malic. Strain-dependent exciton diffusion in transition metal dichalcogenides. *2D Mater.*, 8(1):015030, 2021.

[101] P. Rivera, K. L. Seyler, H. Yu, J. R. Schaibley, J. Yan, D. G. Mandrus, W. Yao, and X. Xu. Valley-polarized exciton dynamics in a 2D semiconductor heterostructure. *Science (80-.).*, 351(6274):688–691, feb 2016.

[102] E. V. Calman, M. M. Fogler, L. V. Butov, S. Hu, A. Mishchenko, and A. K. Geim. Indirect excitons in van der Waals heterostructures at room temperature. *Nat. Commun.*, 9(1):1895, dec 2018.

[103] Dmitrii Unuchek, Alberto Ciarrocchi, Ahmet Avsar, Kenji Watanabe, Takashi Taniguchi, and Andras Kis. Room-temperature electrical control of exciton flux in a van der Waals heterostructure. *Nature*, 560(7718):340–344, aug 2018.

[104] Long Yuan, Biyuan Zheng, Jens Kunstmann, Thomas Brumme, Agnieszka Beata Kuc, Chao Ma, Shibin Deng, Daria Blach, Anlian Pan, and Libai Huang. Twist-angle-dependent interlayer exciton diffusion in WS_2/WSe_2 heterobilayers. *Nat. Mater.*, 19(6):617–623, 2020.

[105] Jonas Zipfel, Marvin Kulig, Raul Perea-Causin, Samuel Brem, Jonas D. Ziegler, Roberto Rosati, Takashi Taniguchi, Kenji Watanabe, Mikhail M. Glazov, Ermin Malic, and Alexey Chernikov. Exciton diffusion in monolayer semiconductors with suppressed disorder. *Phys. Rev. B*, 101(11):115430, 2020.

[106] Toshiaki Kato and Toshiro Kaneko. Transport Dynamics of Neutral Excitons and Trions in Monolayer WS 2. *ACS Nano*, 10(10):9687–9694, oct 2016.

[107] Roberto Rosati, Koloman Wagner, Samuel Brem, Raul Perea-Causin, Edith Wietek, Jonas Zipfel, Jonas D. Ziegler, Malte Selig, Takashi Taniguchi, Kenji Watanabe, Andreas Knorr, Alexey Chernikov, and Ermin Malic. Temporal Evolution of Low-Temperature Phonon Sidebands in Transition Metal Dichalcogenides. *ACS Photonics*, 7(10):2756–2764, oct 2020.

[108] Roberto Rosati, Koloman Wagner, Samuel Brem, Raul Perea-Causin, Jonas D. Ziegler, Jonas Zipfel, Takashi Taniguchi, Kenji Watanabe, Alexey Chernikov, and Ermin Malic. Non-equilibrium diffusion of dark excitons in atomically thin semiconductors. *Nanoscale*, 13:19966–19972, 2021.

[109] M. M. Glazov. Quantum Interference Effect on Exciton Transport in Monolayer Semiconductors. *Phys. Rev. Lett.*, 124(16):166802, apr 2020.

[110] Pedro Soubelet, Julian Klein, Jakob Wierzbowski, Riccardo Silvioli, Florian Sigger, Andreas V. Stier, Katia Gallo, and Jonathan J. Finley. Charged exciton kinetics in monolayer mose2 near ferroelectric domain walls in periodically poled linbo3. *Nano Letters*, 21(2):959–966, 2021. PMID: 33428406.

[111] Guanghui Cheng, Baikui Li, Zijing Jin, Meng Zhang, and Jiannong Wang. Observation of diffusion and drift of the negative trions in monolayer ws2. *Nano Letters*, 21(14):6314–6320, 2021. PMID: 34250802.

[112] Florian Katsch and Andreas Knorr. Doping-induced non-markovian interference causes excitonic linewidth broadening in monolayer wse_2. *Phys. Rev. B*, 105:L041401, Jan 2022.

[113] Rob Thew, Thomas Jennewein, and Masahide Sasaki. Focus on quantum science and technology initiatives around the world. *Quantum Science and Technology*, 5(1):010201, dec 2019.

[114] Pulickel Ajayan, Philip Kim, and Kaustav Banerjee. Two-dimensional van der waals materials. *Physics Today*, 69(9):38–44, sep 2016.

[115] Oriol Lopez-Sanchez, Dominik Lembke, Metin Kayci, Aleksandra Radenovic, and Andras Kis. Ultrasensitive photodetectors based on monolayer mos_2. *Nat. Nanotechnol.*, 8:497–501, 2013.

[116] R.F. Frindt. The optical properties of single crystals of wse2 and mote2. *Journal of Physics and Chemistry of Solids*, 24(9):1107–1108, 1963.

[117] B L Evans and P A Young. Exciton spectra in thin crystals: the diamagnetic effect. *Proc. Phys. Soc.*, 91(2):475–482, jun 1967.

[118] J.A. Wilson and A.D. Yoffe. The transition metal dichalcogenides discussion and interpretation of the observed optical, electrical and structural properties. *Adv. Phys.*, 18(73):193–335, may 1969.

[119] P. G. Harper and D. R. Edmodson. Electronic band structure of the layer-type crystal mos2 (atomic model). *physica status solidi (b)*, 44(1):59–69, 1971.

[120] R A Neville and B L Evans. The Band Edge Excitons in 2H MoS_2. *Phys. status solidi*, 73(2):597–606, feb 1976.

[121] K S Novoselov, D Jiang, F Schedin, T J Booth, V V Khotkevich, S V Morozov, and A K Geim. Two-dimensional atomic crystals. *Proc. Natl. Acad. Sci. USA*, 102(30):10451–10453, jul 2005.

[122] Pramoda Kumar Nayak, editor. *Two-dimensional Materials - Synthesis, Characterization and Potential Applications*. InTech, aug 2016.

[123] Yuerui Lu. *Two-Dimensional Materials in Nanophotonics: Developments, Devices, and Applications*. Jenny Stanford Publishing, 2019.

[124] F. K. Perkins, A. L. Friedman, E. Cobas, P. M. Campbell, G. G. Jernigan, and B. T. Jonker. Chemical vapor sensing with monolayer mos_2. *Nano Lett.*, 13:668–673, 2013.

[125] Hualing Zeng, Gui-Bin Liu, Junfeng Dai, Yajun Yan, Bairen Zhu, Ruicong He, Lu Xie, Shijie Xu, Xianhui Chen, Wang Yao, and Xiaodong Cui. Optical signature of symmetry variations and spin-valley coupling in atomically thin tungsten dichalcogenides. *Sci. Rep.*, 3:1608, jan 2013.

[126] Andor Kormányos, Guido Burkard, Martin Gmitra, Jaroslav Fabian, Viktor Zólyomi, Neil D. Drummond, and Vladimir Fal'ko. k · p theory for two-dimensional transition metal dichalcogenide semiconductors. *2D Mater.*, 2(2):022001, oct 2015.

[127] Wang Yao, Di Xiao, and Qian Niu. Valley-dependent optoelectronics from inversion symmetry breaking. *Phys. Rev. B*, 77:235406, Jun 2008.

[128] M. M. Glazov, T. Amand, X. Marie, D. Lagarde, L. Bouet, and B. Urbaszek. Exciton fine structure and spin decoherence in monolayers of transition metal dichalcogenides. *Phys. Rev. B*, 89(20):201302, may 2014.

[129] M. M. Glazov, L. E. Golub, G. Wang, X. Marie, T. Amand, and B. Urbaszek. Intrinsic exciton-state mixing and nonlinear optical properties in transition metal dichalcogenide monolayers. *Phys. Rev. B*, 95:035311, Jan 2017.

[130] K. Behnia. Polarized light boosts valleytronics. *Nat. Nanotech.*, 7:488–489, 2012.

[131] John R. Schaibley, Hongyi Yu, Genevieve Clark, Pasqual Rivera, Jason S. Ross, Kyle L. Seyler, Wang Yao, and Xiaodong Xu. Valleytronics in 2D materials. *Nat. Rev. Mater.*, 1(11):16055, nov 2016.

[132] Z. Y. Zhu, Y. C. Cheng, and U. Schwingenschlögl. Giant spin-orbit-induced spin splitting in two-dimensional transition-metal dichalcogenide semiconductors. *Phys. Rev. B*, 84(15):153402, oct 2011.

[133] Chendong Zhang, Amber Johnson, Chang-Lung Hsu, Lain-Jong Li, and Chih-Kang Shih. Direct imaging of band profile in single layer mos2 on graphite: Quasiparticle energy gap, metallic edge states, and edge band bending. *Nano Letters*, 14(5):2443–2447, 2014. PMID: 24783945.

[134] Jill A. Miwa, Søren Ulstrup, Signe G. Sørensen, Maciej Dendzik, Antonija Grubiši ć Čabo, Marco Bianchi, Jeppe Vang Lauritsen, and Philip Hofmann. Electronic structure of epitaxial single-layer mos_2. *Phys. Rev. Lett.*, 114:046802, Jan 2015.

[135] K. Kośmider and J. Fernández-Rossier. Electronic properties of the MoS2-WS2 heterojunction. *Phys. Rev. B*, 87(7):075451, feb 2013.

[136] Gui Bin Liu, Wen Yu Shan, Yugui Yao, Wang Yao, and Di Xiao. Three-band tight-binding model for monolayers of group-VIB transition metal dichalcogenides. *Phys. Rev. B*, 88(8):085433, aug 2013.

[137] C Robert, T Amand, F Cadiz, D Lagarde, E Courtade, M Manca, T Taniguchi, K Watanabe, B Urbaszek, and X Marie. Fine structure and life-

time of dark excitons in transition metal dichalcogenide monolayers. *Phys. Rev. B*, 96(15):155423, 2017.

[138] Xiao-Xiao Zhang, Ting Cao, Zhengguang Lu, Yu-Chuan Lin, Fan Zhang, Ying Wang, Zhiqiang Li, James C. Hone, Joshua A. Robinson, Dmitry Smirnov, Steven G. Louie, and Tony F. Heinz. Magnetic brightening and control of dark excitons in monolayer WSe2. *Nat. Nanotechnol.*, 12(9):883–888, sep 2017.

[139] G Wang, C Robert, M M Glazov, F Cadiz, E Courtade, T Amand, D Lagarde, T Taniguchi, K Watanabe, B Urbaszek, and X Marie. In-Plane Propagation of Light in Transition Metal Dichalcogenide Monolayers : Optical Selection Rules. *Phys. Rev. Lett.*, 047401(July):1–7, 2017.

[140] You Zhou, Giovanni Scuri, Dominik S. Wild, Alexander A. High, Alan Dibos, Luis A. Jauregui, Chi Shu, Kristiaan De Greve, Kateryna Pistunova, Andrew Y. Joe, Takashi Taniguchi, Kenji Watanabe, Philip Kim, Mikhail D. Lukin, and Hongkun Park. Probing dark excitons in atomically thin semiconductors via near-field coupling to surface plasmon polaritons. *Nat. Nanotechnol.*, 12:856–860, 2017.

[141] K. Park, T Jiang, Geneviave Clark, Xiaodong Xu, and Markus B. Raschke. Radiative control of dark excitons at room temperature by nano-optical antenna-tip purcell effect. *Nat. Nanotechnol.*, 13:59–64, 2018.

[142] R. S. Knox. *Introduction to Exciton Physics*, pages 183–245. Springer US, Boston, MA, 1983.

[143] T. Kazimierczuk, D. Fröhlich, S. Scheel, H. Stolz, and M. Bayer. Giant Rydberg excitons in the copper oxide Cu_2O. *Nature*, 514(7522):343–347, oct 2014.

[144] M. Knupfer. Exciton binding energies in organic semiconductors. *Appl. Phys. A*, 77:623–626, 2003.

[145] Alexey Chernikov, Timothy C. Berkelbach, Heather M. Hill, Albert Rigosi, Yilei Li, Ozgur Burak Aslan, David R. Reichman, Mark S. Hybertsen, and Tony F. Heinz. Exciton binding energy and nonhydrogenic Rydberg series in monolayer WS2. *Phys. Rev. Lett.*, 113(7):076802, aug 2014.

[146] A. Steinhoff, M. Florian, M. Rösner, G. Schönhoff, T. O. Wehling, and F. Jahnke. Exciton fission in monolayer transition metal dichalcogenide semiconductors. *Nat. Commun.*, 8(1):1166, dec 2017.

[147] Gregory H. Wannier. The structure of electronic excitation levels in insulating crystals. *Phys. Rev.*, 52:191–197, Aug 1937.

[148] N. S. Rytova. Screened potential of a point charge in a thin film. *Proc. MSU, Phys., Astron.*, 3:30, 1967.

[149] L. V. Keldysh. Coulomb interaction in thin semiconductor and semimetal films. *JETP Lett*, 29(11):658–661, 1979.

[150] Jonas Zipfel, Johannes Holler, Anatolie A Mitioglu, Mariana V Ballottin, Philipp Nagler, Andreas V Stier, Takashi Taniguchi, Kenji Watanabe, Scott A Crooker, Peter C M Christianen, Tobias Korn, and Alexey Chernikov. Spatial extent of the excited exciton states in WS2 monolayers from diamagnetic shifts. *Phys. Rev. B*, 98(7):075438, aug 2018.

[151] A. V. Stier, N. P. Wilson, K. A. Velizhanin, J. Kono, X. Xu, and S. A. Crooker. Magnetooptics of Exciton Rydberg States in a Monolayer Semiconductor. *Phys. Rev. Lett.*, 120(5):057405, feb 2018.

[152] Keliang He, Nardeep Kumar, Liang Zhao, Zefang Wang, Kin Fai Mak, Hui Zhao, and Jie Shan. Tightly bound excitons in monolayer WSe_2. *Phys. Rev. Lett.*, 113(2):026803, jul 2014.

[153] Miguel M Ugeda, Aaron J Bradley, Su-Fei Shi, Felipe H. da Jornada, Yi Zhang, Diana Y Qiu, Wei Ruan, Sung-kwan Mo, Zahid Hussain, Zhi-Xun Shen, Feng Wang, Steven G Louie, and Michael F Crommie. Giant bandgap renormalization and excitonic effects in a monolayer transition metal dichalcogenide semiconductor. *Nat. Mater.*, 13(12):1091–1095, aug 2014.

[154] Philipp Steinleitner, Philipp Merkl, Alexander Graf, Philipp Nagler, Kenji Watanabe, Takashi Taniguchi, Jonas Zipfel, Christian Schüller, Tobias Korn, Alexey Chernikov, Samuel Brem, Malte Selig, Gunnar Berghäuser, Ermin Malic, and Rupert Huber. Dielectric Engineering of Electronic Correlations in a van der Waals Heterostructure. *Nano Lett.*, 18(2):1402–1409, feb 2018.

[155] Zidong Li, Darwin F. Cordovilla Leon, Woncheol Lee, Kanak Datta, Zhengyang Lyu, Jize Hou, Takashi Taniguchi, Kenji Watanabe, Emmanouil Kioupakis, and Parag B. Deotare. Dielectric engineering for manipulating exciton transport in semiconductor monolayers. *Nano Lett.*, 21:8409–8417, 2021.

[156] F. Cadiz, E. Courtade, C. Robert, G. Wang, Y. Shen, H. Cai, T. Taniguchi, K. Watanabe, H. Carrere, D. Lagarde, M. Manca, T. Amand, P. Renucci, S. Tongay, X. Marie, and B. Urbaszek. Excitonic Linewidth Approaching the Homogeneous Limit in MoS2-Based van der Waals Heterostructures. *Phys. Rev. X*, 7(2):021026, may 2017.

[157] Colin M. Chow, Hongyi Yu, Aaron M. Jones, Jiaqiang Yan, David G. Mandrus, Takashi Taniguchi, Kenji Watanabe, Wang Yao, and Xiaodong Xu. Unusual Exciton-Phonon Interactions at van der Waals Engineered Interfaces. *Nano Lett.*, 17(2):1194–1199, feb 2017.

[158] Johannes Holler, Lorenz Bauriedl, Tobias Korn, Andrea Seitz, Furkan Özyigit, Michaela Eichinger, Christian Schüller, Kenji Watanabe, Takashi Taniguchi, Christoph Strunk, and Nicola Paradiso. Air tightness of hBN encapsulation and its impact on Raman spectroscopy of van der Waals materials. *2D Mater.*, 7(1):015012, nov 2019.

[159] Akash Laturia, Maarten L. Van de Put, and William G. Vandenberghe. Dielectric properties of hexagonal boron nitride and transition metal dichalcogenides: from monolayer to bulk. *NPJ 2D Mater. Appl.*, 2:6, 2018.

[160] A. Zunger, A. Katzir, and A. Halperin. Optical properties of hexagonal boron nitride. *Phys. Rev. B*, 13:5560–5573, Jun 1976.

[161] Yoichi Kubota, Kenji Watanabe, Osamu Tsuda, and Takashi Taniguchi. Deep ultraviolet light-emitting hexagonal boron nitride synthesized at atmospheric pressure. *Science*, 317(5840):932–934, 2007.

[162] Michael K. L. Man, Julien Madéo, Chakradhar Sahoo, Kaichen Xie, Marshall Campbell, Vivek Pareek, Arka Karmakar, E Laine Wong, Abdullah Al-Mahboob, Nicholas S. Chan, David R. Bacon, Xing Zhu, Mohamed M. M. Abdelrasoul, Xiaoqin Li, Tony F. Heinz, Felipe H. da Jornada, Ting Cao, and Keshav M. Dani. Experimental measurement of the intrinsic excitonic wave function. *Science Advances*, 7(17):eabg0192, 2021.

[163] Ziliang Ye, Ting Cao, Kevin O'Brien, Hanyu Zhu, Xiaobo Yin, Yuan Wang, Steven G. Louie, and Xiang Zhang. Probing excitonic dark states in single-layer tungsten disulphide. *Nature*, 513(7517):214–218, aug 2014.

[164] Masaki Shinada and Satoru Sugano. Interband optical transitions in extremely anisotropic semiconductors. i. bound and unbound exciton absorption. *Journal of the Physical Society of Japan*, 21(10):1936–1946, 1966.

[165] Timothy C Berkelbach, Mark S Hybertsen, and David R Reichman. Theory of neutral and charged excitons in monolayer transition metal dichalcogenides. *Phys. Rev. B*, 88(4):045318, jul 2013.

[166] E. Courtade, M. Semina, M. Manca, M. M. Glazov, C. Robert, F. Cadiz, G. Wang, T. Taniguchi, K. Watanabe, M. Pierre, W. Escoffier, E. L. Ivchenko, P. Renucci, X. Marie, T. Amand, and B. Urbaszek. Charged

excitons in monolayer WSe2 : Experiment and theory. *Phys. Rev. B*, 96(8):085302, aug 2017.

[167] Yia-Chung Chang, Shiue-Yuan Shiau, and Monique Combescot. Crossover from trion-hole complex to exciton-polaron in n -doped two-dimensional semiconductor quantum wells. *Phys. Rev. B*, 98(23):235203, dec 2018.

[168] Christian Fey, Peter Schmelcher, Atac Imamoglu, and Richard Schmidt. Theory of exciton-electron scattering in atomically thin semiconductors. *Phys. Rev. B*, 101(19):195417, may 2020.

[169] M. M. Glazov. Optical properties of charged excitons in two-dimensional semiconductors. *J. Chem. Phys.*, 153(3):034703, jul 2020.

[170] Ovidiu Cotlet, Dominik S. Wild, Mikhail D. Lukin, and Atac Imamoglu. Rotons in optical excitation spectra of monolayer semiconductors. *Phys. Rev. B*, 101(20):205409, may 2020.

[171] Zhipeng Li, Tianmeng Wang, Zhengguang Lu, Mandeep Khatoniar, Zhen Lian, Yuze Meng, Mark Blei, Takashi Taniguchi, Kenji Watanabe, Stephen A. McGill, Sefaattin Tongay, Vinod M. Menon, Dmitry Smirnov, and Su-Fei Shi. Direct observation of gate-tunable dark trions in monolayer wse_2. *Nano Lett.*, 19:6886–6893, 2019.

[172] Erfu Liu, Jeremiah van Baren, Zhengguang Lu, Mashael M. Altaiary, Takashi Taniguchi, Kenji Watanabe, Dmitry Smirnov, and Chun Hung Lui. Gate tunable dark trions in monolayer wse_2. *Phys. Rev. Lett.*, 123:027401, Jul 2019.

[173] Alexey Chernikov, Claudia Ruppert, Heather M. Hill, Albert F. Rigosi, and Tony F. Heinz. Population inversion and giant bandgap renormalization in atomically thin WS2 layers. *Nat. Photonics*, 9(7):466–470, jul 2015.

[174] Rudolf Gross and Achim Marx. *Festkörperphysik*. Oldenbourg Wissenschaftsverlag, 2012.

[175] R. Combescot. Trion ground-state energy: Simple results. *Phys. Rev. B*, 100:245201, Dec 2019.

[176]

[177] André Schirotzek, Cheng-Hsun Wu, Ariel Sommer, and Martin W. Zwierlein. Observation of fermi polarons in a tunable fermi liquid of ultracold atoms. *Phys. Rev. Lett.*, 102:230402, Jun 2009.

[178] C. Kohstall, M. Zaccanti, M. Jag, A. Trenkwalder, P. Massignan, G. M. Bruun, F. Schreck, and R. Grimm. Metastability and coherence of repulsive polarons in a strongly interacting fermi mixture. *Nature*, 485:615–618, 2012.

[179] Marco Koschorreck, Daniel Pertot, Enrico Vogt, Bernd Fröhlich, Michael Feld, and Michael Köhl. Attractive and repulsive fermi polarons in two dimensions. *Nature*, 485:619–622, 2012.

[180] Richard Schmidt, Tilman Enss, Ville Pietilä, and Eugene Demler. Fermi polarons in two dimensions. *Phys. Rev. A*, 85:021602, 2012.

[181] Pietro Massignan, Matteo Zaccanti, and Georg M Bruun. Polarons, dressed molecules and itinerant ferromagnetism in ultracold fermi gases. *Reports on Progress in Physics*, 77(3):034401, feb 2014.

[182] Dmitry K. Efimkin and Allan H. MacDonald. Exciton-polarons in doped semiconductors in a strong magnetic field. *Phys. Rev. B*, 97:235432, Jun 2018.

[183] Erfu Liu, Jeremiah van Baren, Zhengguang Lu, Takashi Taniguchi, Kenji Watanabe, Dmitry Smirnov, Yia-Chung Chang, and Chun Hung Lui. Exciton-polaron Rydberg states in monolayer $MoSe_2$ and WSe_2. (1), 2021.

[184] R.A. Suris, V.P. Kochereshko, G.V. Astakhov, D.R. Yakovlev, W. Ossau, J. Nürnberger, W. Faschinger, G. Landwehr, T. Wojtowicz, G. Karczewski, and J. Kossut. Excitons and trions modified by interaction with a two-dimensional electron gas. *physica status solidi (b)*, 227(2):343–352, 2001.

[185] Thorsten Deilmann and Kristian Sommer Thygesen. Finite-momentum exciton landscape in mono- and bilayer transition metal dichalcogenides. *2D Mater.*, 6(3):035003, apr 2019.

[186] Min Yang, Lei Ren, Cedric Robert, Dinh Van Tuan, Laurent Lombez, Bernhard Urbaszek, Xavier Marie, and Hanan Dery. Relaxation and darkening of excitonic complexes in electrostatically doped monolayer wse_2: Roles of exciton-electron and trion-electron interactions. *Phys. Rev. B*, 105:085302, Feb 2022.

[187] Erfu Liu, Jeremiah van Baren, Takashi Taniguchi, Kenji Watanabe, Yia-Chung Chang, and Chun Hung Lui. Valley-selective chiral phonon replicas of dark excitons and trions in monolayer WSe_2. *Phys. Rev. Research*, 1:032007, Oct 2019.

[188] Zhipeng Li, Tianmeng Wang, Chenhao Jin, Zhengguang Lu, Zhen Lian, Yuze Meng, Mark Blei, Shiyuan Gao, Takashi Taniguchi, Kenji Watanabe, Tianhui Ren, Sefaattin Tongay, Li Yang, Dmitry Smirnov, Ting Cao,

and Su-Fei Shi. Emerging photoluminescence from the dark-exciton phonon replica in monolayer WSe2. *Nat. Commun.*, 10(1):2469, 2019.

[189] Yanhao Tang, Kin Fai Mak, and Jie Shan. Vlong valley lifetime of dark excitons in single-layer wse_2. *Nat. Commun.*, 10:4047, 2019.

[190] Diana Y. Qiu, Ting Cao, and Steven G. Louie. Nonanalyticity, valley quantum phases, and lightlike exciton dispersion in monolayer transition metal dichalcogenides: Theory and first-principles calculations. *Phys. Rev. Lett.*, 115:176801, Oct 2015.

[191] J. P. Echeverry, B. Urbaszek, T. Amand, X. Marie, and I. C. Gerber. Splitting between bright and dark excitons in transition metal dichalcogenide monolayers. *Phys. Rev. B*, 93:121107, Mar 2016.

[192] Thorsten Deilmann and Kristian Sommer Thygesen. Dark excitations in monolayer transition metal dichalcogenides. *Phys. Rev. B*, 96:201113, Nov 2017.

[193] Ermin Malic, Malte Selig, Maja Feierabend, Samuel Brem, Dominik Christiansen, Florian Wendler, Andreas Knorr, and Gunnar Berghäuser. Dark excitons in transition metal dichalcogenides. *Phys. Rev. Materials*, 2:014002, Jan 2018.

[194] Samuel Brem, August Ekman, Dominik Christiansen, Florian Katsch, Malte Selig, Cedric Robert, Xavier Marie, Bernhard Urbaszek, Andreas Knorr, and Ermin Malic. Phonon-Assisted Photoluminescence from Indirect Excitons in Monolayers of Transition-Metal Dichalcogenides. *Nano Lett.*, 20(4):2849–2856, apr 2020.

[195] Roberto Rosati, Robert Schmidt, Samuel Brem, Raul Perea-Causin, Iris Niehues, Johannes Kern, Johann A. Preuß, Robert Schneider, Steffen Michaelis de Vasconcellos, Rudolf Bratschitsch, and Ermin Malic. Dark exciton anti-funneling in atomically thin semiconductors. *Nat. Commun.*, 12:7221, 2021.

[196] Julien Madeo, Michael K. L. Man, Chakradhar Sahoo, Marshall Campbell, Vivek Pareek, E. Laine Wong, Abdullah Al-Mahboob, Nicholas S. Chan, Arka Karmakar, Bala Murali Krishna Mariserla, Xiaoqin Li, Tony F. Heinz, Ting Cao, and Keshav M. Dani. Directly visualizing the momentum-forbidden dark excitons and their dynamics in atomically thin semiconductors. *Science*, 370(6521):1199–1204, 2020.

[197] Jonas Zipfel, Koloman Wagner, Jonas D. Ziegler, Takashi Taniguchi, Kenji Watanabe, Marina A. Semina, and Alexey Chernikov. Light–matter cou-

pling and non-equilibrium dynamics of exchange-split trions in monolayer ws2. *The Journal of Chemical Physics*, 153(3):034706, 2020.

[198] Johnson Lee, Emil S. Koteles, and M. O. Vassell. Luminescence linewidths of excitons in gaas quantum wells below 150 k. *Phys. Rev. B*, 33:5512–5516, Apr 1986.

[199] S. Rudin, T. Reinecke, and B. Segall. Temperature-dependent exciton linewidths in semiconductors. *Phys. Rev. B*, 42(17):11218–11231, dec 1990.

[200] T. Ruf, J. Spitzer, V. F. Sapega, V. I. Belitsky, M. Cardona, and K. Ploog. Interface roughness and homogeneous linewidths in quantum wells and superlattices studied by resonant acoustic-phonon raman scattering. *Phys. Rev. B*, 50:1792–1806, Jul 1994.

[201] D. Gammon, S. Rudin, T. Reinecke, D. Katzer, and C. Kyono. Phonon broadening of excitons in GaAs/AlxGa1-xAs quantum wells. *Phys. Rev. B*, 51(23):16785–16789, 1995.

[202] P. Borri, W. Langbein, J. M. Hvam, and F. Martelli. Well-width dependence of exciton-phonon scattering in $in_xga_{1-x}As$/GaAs single quantum wells. *Phys. Rev. B*, 59:2215–2222, Jan 1999.

[203] Malte Selig, Gunnar Berghäuser, Archana Raja, Philipp Nagler, Christian Schüller, Tony F Heinz, Tobias Korn, Alexey Chernikov, Ermin Malic, and Andreas Knorr. Excitonic linewidth and coherence lifetime in monolayer transition metal dichalcogenides. *Nat. Commun.*, 7(May):13279, nov 2016.

[204] Jonas D. Ziegler, Jonas Zipfel, Barbara Meisinger, Matan Menahem, Xiangzhou Zhu, Takashi Taniguchi, Kenji Watanabe, Omer Yaffe, David A. Egger, and Alexey Chernikov. Fast and Anomalous Exciton Diffusion in Two-Dimensional Hybrid Perovskites. *Nano Lett.*, 20(9):6674–6681, 2020.

[205] Lucio Claudio Andreani and Alfredo Pasquarello. High exciton binding energies in GaAs/GaAlAs quantum wells. *Superlattices Microstruct.*, 9(1):1–4, jan 1991.

[206] Galan Moody, Chandriker Kavir Dass, Kai Hao, Chang-Hsiao Chen, Lain-Jong Li, Akshay Singh, Kha Tran, Genevieve Clark, Xiaodong Xu, Gunnar Berghäuser, Ermin Malic, Andreas Knorr, and Xiaoqin Li. Intrinsic homogeneous linewidth and broadening mechanisms of excitons in monolayer transition metal dichalcogenides. *Nat. Commun.*, 6(May):8315, 2015.

[207] Tomasz Jakubczyk, Valentin Delmonte, Maciej Koperski, Karol Nogajewski, Clément Faugeras, Wolfgang Langbein, Marek Potemski, and Jacek Kasprzak. Radiatively limited dephasing and exciton dynamics in mose2

monolayers revealed with four-wave mixing microscopy. *Nano Letters*, 16(9):5333–5339, 2016. PMID: 27517124.

[208] P. Dey, J. Paul, Z. Wang, C. E. Stevens, C. Liu, A. H. Romero, J. Shan, D. J. Hilton, and D. Karaiskaj. Optical coherence in atomic-monolayer transition-metal dichalcogenides limited by electron-phonon interactions. *Phys. Rev. Lett.*, 116:127402, Mar 2016.

[209] Caroline Boule, Diana Vaclavkova, Miroslav Bartos, Karol Nogajewski, Lukas Zdražil, Takashi Taniguchi, Kenji Watanabe, Marek Potemski, and Jacek Kasprzak. Coherent dynamics and mapping of excitons in single-layer <math> <msub> <mi>MoSe</mi> <mn>2</mn> </msub> </math> and <math> <msub> <mi>WSe</mi> <mn>2</mn> </msub> </math> at the homogeneous limit. *Phys. Rev. Mater.*, 4(3):034001, 2020.

[210] C. Poellmann, P. Steinleitner, U. Leierseder, P. Nagler, G. Plechinger, M. Porer, R. Bratschitsch, C. Schüller, T. Korn, and R. Huber. Resonant internal quantum transitions and femtosecond radiative decay of excitons in monolayer WSe2. *Nat. Mater.*, 14(9):889–893, jul 2015.

[211] C. Robert, R. Picard, D. Lagarde, G. Wang, J. P. Echeverry, F. Cadiz, P. Renucci, A. Högele, T. Amand, X. Marie, I. C. Gerber, and B. Urbaszek. Excitonic properties of semiconducting monolayer and bilayer MoTe2. *Phys. Rev. B*, 94(15):155425, oct 2016.

[212] H. H. Fang, B. Han, C. Robert, M. A. Semina, D. Lagarde, E. Courtade, T. Taniguchi, K. Watanabe, T. Amand, B. Urbaszek, M. M. Glazov, and X. Marie. Control of the Exciton Radiative Lifetime in van der Waals Heterostructures. *Phys. Rev. Lett.*, 123(6):067401, 2019.

[213] Can Liu, Hao Hong, Qinghe Wang, Ping Liu, Yonggang Zuo, Jing Liang, Yang Cheng, Xu Zhou, Jinhuan Wang, Yun Zhao, Jie Xiong, Bin Xiang, Jin Zhang, and Kaihui Liu. Strong-coupled hybrid structure of carbon nanotube and MoS 2 monolayer with ultrafast interfacial charge transfer. *Nanoscale*, 11(37):17195–17200, 2019.

[214] Raul Perea-Causin, Samuel Brem, and Ermin Malic. Trion-phonon interaction in atomically thin semiconductors, 2022.

[215] Mark Danovich, Viktor Zólyomi, and Vladimir I Fal'ko. Dark trions and biexcitons in ws_2 and wse_2 made bright by e-e scattering. *Scientific Reports*, 7(6):45998, 2017.

[216] Jhih-Sian Tu, Sven Borghardt, Detlev Grützmacher, and Beata E Kardynał. Experimental observation of a negative grey trion in an electron-rich wse2 monolayer. *Journal of Physics: Condensed Matter*, 31(41):415701, jul 2019.

[217] Malte Selig, Gunnar Berghäuser, Marten Richter, Rudolf Bratschitsch, Andreas Knorr, and Ermin Malic. Dark and bright exciton formation, thermalization, and photoluminescence in monolayer transition metal dichalcogenides. *2D Mater.*, 5(3):035017, may 2018.

[218] Satoshi Kusaba, Kenji Watanabe, Takashi Taniguchi, Kazuhiro Yanagi, and Koichiro Tanaka. Role of dark exciton states in the relaxation dynamics of bright 1s excitons in monolayer wse2. *Applied Physics Letters*, 119(9):093101, 2021.

[219] Daniel Erkensten, Samuel Brem, Koloman Wagner, Roland Gillen, Raul Perea-Causin, Jonas D. Ziegler, Takashi Taniguchi, Kenji Watanabe, Janina Maultzsch, Alexey Chernikov, and Ermin Malic. Dark exciton-exciton annihilation in monolayer wse_2. *Phys. Rev. B*, 104:L241406, Dec 2021.

[220] Maja Feierabend, Samuel Brem, August Ekman, and Ermin Malic. Brightening of spin- and momentum-dark excitons in transition metal dichalcogenides. *2D Materials*, 8(1):015013, oct 2020.

[221] Moshe G. Harats, Jan N. Kirchhof, Mengxiong Qiao, Kyrylo Greben, and Kirill I. Bolotin. Dynamics and efficient conversion of excitons to trions in non-uniformly strained monolayer WS2. *Nat. Photonics*, 14(5):324–329, 2020.

[222] Oleksandr V. Mikhnenko, Paul W. M. Blom, and Thuc-Quyen Nguyen. Exciton diffusion in organic semiconductors. *Energy Environ. Sci.*, 8(7):1867–1888, 2015.

[223] S. Grosse, R. Arnold, G. von Plessen, M. Koch, J. Feldmann, V. M. Axt, T. Kuhn, R. Rettig, and W. Stolz. Relaxation Dynamics of Electron-Hole Pairs Studied by Spatiotemporal Pump and Probe Experiments. *Phys. status solidi*, 204(1):147–150, 1997.

[224] Naomi S. Ginsberg and William A. Tisdale. Spatially Resolved Photogenerated Exciton and Charge Transport in Emerging Semiconductors. *Annu. Rev. Phys. Chem.*, 71(1):1–30, apr 2020.

[225] Th. Förster. Zwischenmolekulare energiewanderung und fluoreszenz. *Annalen der Physik*, 437(1-2):55–75, 1948.

[226] D. L. Dexter. A theory of sensitized luminescence in solids. *The Journal of Chemical Physics*, 21(5):836–850, 1953.

[227] Milan Delor, Hannah L. Weaver, QinQin Yu, and Naomi S. Ginsberg. Imaging material functionality through three-dimensional nanoscale tracking of energy flow. *Nat. Mater.*, 19(1):56–62, jan 2020.

[228] Rachel H Gilmore, Elizabeth M Y Lee, Mark C Weidman, Adam P Willard, and William A Tisdale. Charge carrier hopping dynamics in homogeneously broadened pbs quantum dot solids. *Nano letters*, 17(2):893—901, February 2017.

[229] Yulia Krupskaya, Marco Gibertini, Nicola Marzari, and Alberto F. Morpurgo. Band-like electron transport with record-high mobility in the tcnq family. *Advanced Materials*, 27(15):2453–2458, 2015.

[230] Alexander Heck, Julian J. Kranz, and Marcus Elstner. Simulation of temperature-dependent charge transport in organic semiconductors with various degrees of disorder. *Journal of Chemical Theory and Computation*, 12(7):3087–3096, 2016. PMID: 27224054.

[231] R. A. Marcus. On the theory of oxidation-reduction reactions involving electron transfer. i. *The Journal of Chemical Physics*, 24(5):966–978, 1956.

[232] Allen Miller and Elihu Abrahams. Impurity conduction at low concentrations. *Phys. Rev.*, 120:745–755, Nov 1960.

[233] N. F. Mott. Charge transport in non-crystalline semiconductors. In *Festkörper Probl. IX*, pages 22–45. Elsevier, 1969.

[234] Gerd Bergmann. Weak localization in thin films: a time-of-flight experiment with conduction electrons. *Physics Reports*, 107(1):1–58, 1984.

[235] Michael J. Stephen. Weak localization and the conductivity of nondegenerate electrons. *Phys. Rev. B*, 36:5663–5664, Oct 1987.

[236] V. V. Afonin, Yu. M. Galperin, V. L. Gurevich, and A. Schmid. Weak localization of electrons in a classical gas. *Phys. Rev. A*, 36:5729–5741, Dec 1987.

[237] A.M. Dyakonov and Ya. V. Kopelevich. Weak localization of electrons in cds at 77 k observed by the acoustoelectronic amplification method. *JETP Lett.*, 47:213–216, 1988.

[238] P. I. Arseev and A. B. Dzyubenko. Exciton magnetotransport in two-dimensional systems: Weak-localization effects. *J. Exp. Theor. Phys.*, 87(1):200–209, 1998.

[239] V. V. Belykh, A. Yu. Kuntsevich, M. M. Glazov, K. V. Kavokin, D. R. Yakovlev, and M. Bayer. Quantum interference controls the electron spin dynamics in n-gaas. *Phys. Rev. X*, 8:031021, Jul 2018.

[240] Ferdinand Evers and Alexander D. Mirlin. Anderson transitions. *Rev. Mod. Phys.*, 80(4):1355–1417, 2008.

[241] L. Gorkov, A. Larkin, and D. Khmelnitski. Particle conductivity in a two-dimensional random potential. *JETP Lett.*

[242] Zhenghe Jin, Xiaodong Li, Jeffrey T. Mullen, and Ki Wook Kim. Intrinsic transport properties of electrons and holes in monolayer transition-metal dichalcogenides. *Phys. Rev. B*, 90(4):045422, 2014.

[243] M. M. Glazov, Z. A. Iakovlev, and S. Refaely-Abramson. Phonon-induced exciton weak localization in two-dimensional semiconductors, 2022.

[244] Andres Castellanos-Gomez, Leonardo Vicarelli, Elsa Prada, Joshua O. Island, K. L. Narasimha-Acharya, Sofya I. Blanter, Dirk J. Groenendijk, Michele Buscema, Gary a. Steele, J. V. Alvarez, Henny W. Zandbergen, J. J. Palacios, and Herre S. J. van der Zant. Isolation and characterization of few-layer black phosphorus. *2D Mater.*, 1(2):025001, jun 2014.

[245] P. J. Zomer, M. H. D. Guimarães, J. C. Brant, N. Tombros, and B. J. van Wees. Fast pick up technique for high quality heterostructures of bilayer graphene and hexagonal boron nitride. *Applied Physics Letters*, 105(1):013101, 2014.

[246] Steven J. Byrnes. Multilayer optical calculations. mar 2016.

[247] Jonas Zipfel. *Excitons in monolayer semiconductors in complex environments and under external fields.* Dissertationsschrift, Universität Regensburg, Regensburg, 2020.

[248] Daniel Erkensten, Samuel Brem, Raul Perea-Causin, and Ermin Malic. Microscopic origin of anomalous interlayer exciton transport in van der waals heterostructures. *Phys. Rev. Materials*, 6:094006, Sep 2022.

[249] Ronen Rapaport, Gang Chen, and Steven H. Simon. Nonlinear dynamics of a dense two-dimensional dipolar exciton gas. *Phys. Rev. B*, 73:033319, Jan 2006.

[250] F. Fedichkin, P. Andreakou, B. Jouault, M. Vladimirova, T. Guillet, C. Brimont, P. Valvin, T. Bretagnon, A. Dussaigne, N. Grandjean, and P. Lefebvre. Transport of dipolar excitons in (al,ga)n/gan quantum wells. *Phys. Rev. B*, 91:205424, May 2015.

[251] Jonas Zipfel, Koloman Wagner, Marina A. Semina, Jonas D. Ziegler, Takashi Taniguchi, Kenji Watanabe, Mikhail M. Glazov, and Alexey Chernikov. Electron recoil effect in electrically tunable $mose_2$ monolayers. *Phys. Rev. B*, 105:075311, Feb 2022.

[252] T. Smoleński, O. Cotlet, A. Popert, P. Back, Y. Shimazaki, P. Knüppel, N. Dietler, T. Taniguchi, K. Watanabe, M. Kroner, and A. Imamoglu. Interaction-Induced Shubnikov-de Haas Oscillations in Optical Conductivity of Monolayer MoSe2. *Phys. Rev. Lett.*, 123(9):097403, 2019.

[253] Stefano Larentis, Hema C. P. Movva, Babak Fallahazad, Kyounghwan Kim, Armand Behroozi, Takashi Taniguchi, Kenji Watanabe, Sanjay K. Banerjee, and Emanuel Tutuc. Large effective mass and interaction-enhanced zeeman splitting of k-valley electrons in $mose_2$. *Phys. Rev. B*, 97:201407, May 2018.

[254] G Wang, I C Gerber, L Bouet, D Lagarde, A Balocchi, M Vidal, T Amand, X Marie, and B Urbaszek. Exciton states in monolayer mose2: impact on interband transitions. *2D Materials*, 2(4):045005, nov 2015.

[255] Koloman Wagner, Edith Wietek, Jonas D. Ziegler, Marina A. Semina, Takashi Taniguchi, Kenji Watanabe, Jonas Zipfel, Mikhail M. Glazov, and Alexey Chernikov. Autoionization and Dressing of Excited Excitons by Free Carriers in Monolayer WSe_2. *Phys. Rev. Lett.*, 125(26):267401, 2020.

[256] Koloman Wagner, Zahkhar A. Iakovlev, Jonas D. Ziegler, Marzia Cuccu, Takashi Taniguchi, Kenji Watanabe, Mikhail M. Glazov, and Alexey Chernikov.

[257] R. A. Sergeev and R. A. Suris. Ground-state energy of x^- and x^+ trions in a two-dimensional quantum well at an arbitrary mass ratio. *Phys. Solid State*, 43(4):746–751, apr 2001.

[258] Ajit Srivastava, Meinrad Sidler, Adrien V Allain, Dominik S Lembke, Andras Kis, and A. Imamoglu. Valley Zeeman effect in elementary optical excitations of monolayer WSe2. *Nat. Phys.*, 11(2):141–147, jan 2015.

[259] Jianhui Zhou, Wen-Yu Shan, Wang Yao, and Di Xiao. Berry phase modification to the energy spectrum of excitons. *Phys. Rev. Lett.*, 115:166803, Oct 2015.

[260] Gunnar Berghäuser, Andreas Knorr, and Ermin Malic. Optical fingerprint of dark 2p-states in transition metal dichalcogenides. *2D Mater.*, 4(1):015029, dec 2016.

[261] M. Goryca, J. Li, A. V. Stier, T. Taniguchi, K. Watanabe, E. Courtade, S. Shree, C. Robert, B. Urbaszek, X. Marie, and S. A. Crooker. Revealing

exciton masses and dielectric properties of monolayer semiconductors with high magnetic fields. *Nat. Commun.*, 10(1):4172, dec 2019.

[262] J. Heckötter, M. Freitag, D. Fröhlich, M. Aßmann, M. Bayer, M. A. Semina, and M. M. Glazov. Scaling laws of Rydberg excitons. *Phys. Rev. B*, 96:125142, Sep 2017.

[263] Ovidiu Cotlet, Falko Pientka, Richard Schmidt, Gergely Zarand, Eugene Demler, and Atac Imamoglu. Transport of Neutral Optical Excitations Using Electric Fields. *Phys. Rev. X*, 9(4):041019, oct 2019.

[264] M. Manca, M. M. Glazov, C. Robert, F. Cadiz, T. Taniguchi, K. Watanabe, E. Courtade, T. Amand, P. Renucci, X. Marie, G. Wang, and B. Urbaszek. Enabling valley selective exciton scattering in monolayer WSe2 through upconversion. *Nat. Commun.*, 8:14927, apr 2017.

[265] Shinichiro Mouri, Yuhei Miyauchi, and Kazunari Matsuda. Tunable Photoluminescence of Monolayer MoS 2 via Chemical Doping. *Nano Lett.*, 13(12):5944–5948, dec 2013.

[266] D Vaclavkova, J Wyzula, K Nogajewski, M Bartos, A O Slobodeniuk, C Faugeras, M Potemski, and M R Molas. Singlet and triplet trions in WS 2 monolayer encapsulated in hexagonal boron nitride. *Nanotechnology*, 29(32):325705, aug 2018.

[267] Axel Esser, Erich Runge, Roland Zimmermann, and Wolfgang Langbein. Photoluminescence and radiative lifetime of trions in GaAs quantum wells. *Phys. Rev. B*, 62(12):8232–8239, 2000.

[268] A. Esser, R. Zimmermann, and E. Runge. Theory of Trion Spectra in Semiconductor Nanostructures. *Phys. status solidi*, 227(2):317–330, oct 2001.

[269] Gabriella D. Shepard, Jenny V. Ardelean, Obafunso A. Ajayi, Daniel Rhodes, Xiaoyang Zhu, James C. Hone, and Stefan Strauf. Trion-species-resolved quantum beats in mose2. *ACS Nano*, 11(11):11550–11558, 2017. PMID: 29035552.

[270] H. Haug and S. W. Koch. *Quantum theory of the optical and electronic properties of semiconductors*. World Scientific, Singapore, 5th edition, 2009.

[271] A Steinhoff, M Rösner, F Jahnke, T O Wehling, and C Gies. Influence of excited carriers on the optical and electronic properties of MoS_2. *Nano Lett.*, 14(7):3743–3748, jul 2014.

[272] Robert Schmidt, Gunnar Berghäuser, Robert Schneider, Malte Selig, Philipp Tonndorf, Ermin Malić, Andreas Knorr, Steffen Michaelis de Vasconcellos,

and Rudolf Bratschitsch. Ultrafast Coulomb-Induced Intervalley Coupling in Atomically Thin WS 2. *Nano Lett.*, 16(5):2945–2950, may 2016.

[273] Tommaso Venanzi, Malte Selig, Stephan Winnerl, Alexej Pashkin, Andreas Knorr, Manfred Helm, and Harald Schneider. Terahertz-Induced Energy Transfer from Hot Carriers to Trions in a MoSe 2 Monolayer. *ACS Photonics*, page acsphotonics.1c00394, 2021.

[274] Koloman Wagner, Jonas Zipfel, Roberto Rosati, Edith Wietek, Jonas D. Ziegler, Samuel Brem, Raul Perea-Causin, Takashi Taniguchi, Kenji Watanabe, Mikhail M. Glazov, Ermin Malic, and Alexey Chernikov. Nonclassical Exciton Diffusion in Monolayer WSe_2. *Phys. Rev. Lett.*, 127(7):076801, 2021.

[275] V Shahnazaryan, O Kyriienko, and H Rostami. Exciton routing in the heterostructure of a transition metal dichalcogenide monolayer on a paraelectric substrate. *Phys. Rev. B*, 100(16):165303, oct 2019.

[276] Shinichiro Mouri, Yuhei Miyauchi, Minglin Toh, Weijie Zhao, Goki Eda, and Kazunari Matsuda. Nonlinear photoluminescence in atomically thin layered WSe_2 arising from diffusion-assisted exciton-exciton annihilation. *Phys. Rev. B*, 90(15):155449, oct 2014.

[277] Philipp Steinleitner, Philipp Merkl, Philipp Nagler, Joshua Mornhinweg, Christian Schüller, Tobias Korn, Alexey Chernikov, and Rupert Huber. Direct Observation of Ultrafast Exciton Formation in a Monolayer of WSe_2. *Nano Lett.*, 17(3):1455–1460, mar 2017.

[278] Haining Wang, Changjian Zhang, and Farhan Rana. Ultrafast Dynamics of Defect-Assisted Electron-Hole Recombination in Monolayer MoS 2. *Nano Lett.*, 15(1):339–345, 2015.

[279] D. Hägele, R. Zimmermann, M. Oestreich, M. R. Hofmann, W. W. Rühle, B. K. Meyer, H. Amano, and I. Akasaki. Cooling dynamics of excitons in GaN. *Phys. Rev. B*, 59(12):R7797–R7800, 1999.

[280] M. Kozhevnikov, B.M. Ashkinadze, E. Cohen, and Arza Ron. LO phonon sideband photoluminescence in pure GaAs and QWs. *J. Lumin.*, 72-74:312–313, 1997.

[281] Victor Funk, Koloman Wagner, Edith Wietek, Jonas D. Ziegler, Jonathan Förste, Jessica Lindlau, Michael Förg, Kenji Watanabe, Takashi Taniguchi, Alexey Chernikov, and Alexander Högele. Spectral asymmetry of phonon sideband luminescence in monolayer and bilayer wse_2. *Phys. Rev. Research*, 3:L042019, Nov 2021.

[282] J. T. Warren, K. E. O'Hara, and J. P. Wolfe. Two-body decay of thermalized excitons in CuO_2. *Phys. Rev. B*, 61(12):8215–8223, mar 2000.

[283] L. M. Smith, J. S. Preston, J. P. Wolfe, D. R. Wake, J. Klem, T. Henderson, and H. Morkoç. Phonon-wind-driven transport of photoexcited carriers in a semiconductor quantum well. *Phys. Rev. B*, 39(3):1862–1870, 1989.

[284] L. Landau and E. Lifshitz. *Physical Kinetics*. Butterworth-Heinemann, Oxford, 1981.

[285] G. V. Astakhov, V. P. Kochereshko, D. R. Yakovlev, W. Ossau, J. Nürnberger, W. Faschinger, and G. Landwehr. Oscillator strength of trion states in ZnSe-based quantum wells. *Phys. Rev. B*, 62(15):10345, oct 2000.

[286] Roberto Rosati, Frank Lengers, Christian Carmesin, Matthias Florian, Tilmann Kuhn, Frank Jahnke, Michael Lorke, and Doris E. Reiter. Electron dynamics in a two-dimensional nanobubble: A two-level system based on spatial density. *Nano Letters*, 21(23):9896–9902, 2021. PMID: 34812637.

[287] Shiekh Zia Uddin, Naoki Higashitarumizu, Hyungjin Kim, Jun Yi, Xiang Zhang, Daryl Chrzan, and Ali Javey. Enhanced neutral exciton diffusion in monolayer ws2 by exciton–exciton annihilation. *ACS Nano*, 16(5):8005–8011, 2022. PMID: 35467828.

[288] Florian Dirnberger, Jonas D. Ziegler, Paulo E. Faria Junior, Rezlind Bushati, Takashi Taniguchi, Kenji Watanabe, Jaroslav Fabian, Dominique Bougeard, Alexey Chernikov, and Vinod M. Menon. Quasi-1d exciton channels in strain-engineered 2d materials. *Science Advances*, 7(44):eabj3066, 2021.

[289] Beatriz Ferreira, Roberto Rosati, and Ermin Malic. Microscopic modeling of exciton-polariton diffusion coefficients in atomically thin semiconductors. *Phys. Rev. Materials*, 6:034008, Mar 2022.

Acknowledgements

I gratefully thank our colleagues for fruitful collaborations and discussions.

1. *Ioffe Institute, Saint Petersburg, Russian Federation*
   Zakhar A. Iakovlev
   Marina Semina
   Mikhail M. Glazov

2. *Department of Physics, Philipps-Universität Marburg, Marburg, Germany*
   Roberto Rosati
   Daniel Erkensten
   Raül Perea-Causin
   Samuel Brem
   Ermin Malic

3. *International Center for Materials Nanoarchitectonics, National Institute for Materials Science, Tsukuba, Japan*
   Takashi Taniguchi

4. *Research Center for Functional Materials, National Institute for Materials Science, Tsukuba, Japan*
   Kenji Watanabe

5. *Institute of Theoretical Physics, Technical University Berlin, Berlin, Germany*
   Malte Selig
   Andreas Knorr

6. *Department of Physics, Friedrich-Alexander-Universität Erlangen-Nürnberg, Erlangen-Nürnberg, Germany*
Roland Gillen
Jana Maultsch

7. *Fakultät für Physik, Munich Quantum Center, and Center for NanoScience (CeNS), Ludwig-Maximilians-Universität, München, Germany*
Victor Funk
Jonathan Förste
Jessica Lindlau
Michael Förg
Alexander Högele

List of publications

1. **Koloman Wagner**, Edith Wietek, Jonas D. Ziegler, Marina A. Semina, Takashi Taniguchi, Kenji Watanabe, Jonas Zipfel, Mikhail M. Glazov, and Alexey Chernikov. Autoionization and Dressing of Excited Excitons by Free Carriers in Monolayer WSe_2. *Phys. Rev. Lett.*, 125(26), 267401, 2020.

2. **Koloman Wagner**, Jonas Zipfel, Roberto Rosati, Edith Wietek, Jonas D. Ziegler, Samuel Brem, Raül Perea-Causin, Takashi Taniguchi, Kenji Watanabe, Mikhail M. Glazov, Ermin Malic, and Alexey Chernikov. Nonclassical Exciton Diffusion in Monolayer WSe_2. *Phys. Rev. Lett.*, 127(7), 076801, 2021.

3. Jonas Zipfel*, **Koloman Wagner***, Marina A. Semina, Jonas D. Ziegler, Takashi Taniguchi, Kenji Watanabe, Mikhail M. Glazov, and Alexey Chernikov. Electron recoil effect in electrically tunable $MoSe_2$ monolayers. *Phys. Rev. B*, 105, 075311, 2022.

4. Roberto Rosati, **Koloman Wagner**, Samuel Brem, Raül Perea-Causin, Edith Wietek, Jonas Zipfel, Jonas D. Ziegler, Malte Selig, Takashi Taniguchi, Kenji Watanabe, Andreas Knorr, Alexey Chernikov, and Ermin Malic. Temporal Evolution of Low-Temperature Phonon Sidebands in Transition Metal Dichalcogenides. *ACS Photonics*, 7(10), 2756–2764, 2020.

5. Roberto Rosati, **Koloman Wagner**, Samuel Brem, Raül Perea-Causin, Jonas D. Ziegler, Jonas Zipfel, Takashi Taniguchi, Kenji Watanabe, Alexey Chernikov, and Ermin Malic. Non-equilibrium diffusion of dark excitons in atomically thin semiconductors. *Nanoscale*, 13, 19966–19972, 2021.

6. Victor Funk, **Koloman Wagner**, Edith Wietek, Jonas D. Ziegler, Jonathan Förste, Jessica Lindlau, Michael Förg, Kenji Watanabe, Takashi Taniguchi, Alexey Chernikov, and Alexander Högele. Spectral asymmetry of phonon sideband luminescence in monolayer and bilayer WSe_2. *Phys. Rev. Research*, 3, L042019, 2021.

7. Jonas Zipfel, **Koloman Wagner**, Jonas D. Ziegler, Takashi Taniguchi, Kenji Watanabe, Marina A. Semina, and Alexey Chernikov. Light-matter coupling and non-equilibrium dynamics of exchange-split trions in monolayer Ws_2. *J. Chem. Phys.*, 153, 034706, 2020.

8. Daniel Erkensten, Samuel Brem, **Koloman Wagner**, Roland Gillen, Raul Perea-Causin, Jonas D. Ziegler, Takashi Taniguchi, Kenji Watanabe, Janina Maultzsch, Alexey Chernikov, and Ermin Malic. Dark exciton-exciton annihilation in monolayer WSe_2. *Phys. Rev. B*, 104, L241406, 2021.

Under revision (unpublished):

Koloman Wagner, Zakhar A. Iakovlev, Jonas D. Ziegler, Marzia Cuccu, Takashi Taniguchi, Kenji Watanabe, Mikhail M. Glazov, and Alexey Chernikov. Diffusion of excitons immersed in a two-dimensional Fermi sea of free charges.

* equally contributing authors.

Words of gratitude

At this point, I would like to express my gratitude once again to everyone who supported me in the preparation of this thesis. A special thanks goes to all my colleagues and collaborators. Thank you for the great cooperation, the fruitful discussions and your confidence.

I would also like to express my sincere thanks to the examination commission. Special thanks goes to the second examiner Prof. Dr. Christian Schüller and the chairman Prof. Dr. Gunnar Bali. Furthermore, many thanks to Prof. Dr. Franz Gießibl.

The following people I would like to thank in particular.

First of all, I would like to gratefully thank my adviser *Alexey Chernikov*. Thank you very much for giving me the opportunity to graduate in your group! Thank you for the great supervision, your support and your motivating words. I really appreciated your always transparent communication, that you involved us PhD students in so many discussions and that you always warned us rightly against futile efforts. I would like to thank you for introducing me so openhearted to the scientific community. It was a great pleasure to meet so many open-minded people, living for science all over the world!

A very special thanks goes to *Jonas David Ziegler* my colleague from first day on. Thank you so much for all your vigorous support and your benevolent and helpful way and all the time and nerves you spend! At this point, I would like to say a very special thank you once again for providing me with your extraordinary samples which led to the investigation of so much cool physics! I will miss our wide-ranging discussions, scientific debates, coffee breaks, your creative impulses and convincing arguments. Thank you for this wonderful time together! You have been the best colleague to work with!

I would also like to thank my colleague *Jonas Zipfel* for welcoming me to the group and introducing me to the experiments. Special thanks for the technical assistance and programming of sophisticated Matlab scripts that made our lives so much easier! It was a pleasrure working with you. I would like to particularly thank you for our shared project about the electron recoil effect! Thank you for your helpfulness and your good humor.

Thank you, *Edith Wietek* for the support in the lab, for technical discussions, for updating me with the latest publications and our conversations about art!

Thank you *Marzia Cuccu* for the support in the lab and for giving me so many opportunities to improve my Italian language skills. And a very special thanks for granting us a place to stay during our time in Dresden!

I would also like to thank my colleague *Sophia Terres* for the support and especially for the great time we had together. Your cheerful nature really improved our everyday life!

Thank you very much *Barbara Meisinger*, *Jan Marius Markl* and *Marvin Kulig*. You have contributed to the pleasant atmosphere in our group. Thank you for your support and helpfulness!

Furthermore I would like to thank (in no particular order):

- *Chrsitan Haimerl* and *Thomas Solleder* for the helium supply. Without you my experiments would not have been possible.
- *Martin Furthmeier*, *Ignaz Laepple*, *Andreas Schützenmeier* and *Sebastian Bange* for technical support.
- *Anna Lavkova*, *Ulla Franzke* and *Edeltraud Schlagbauer* for impeccable organization and handling of administrative matters.
- *Viola Zeller, Dieter Riedl, Christian Bäuml, Nicola Paradiso* and *Imke Gronwald* for support in the fabrication of electrically-tuneable sample structures.
- *Simon Raiber* for the many conversations about physics and science or just about God and the world. Thank you for carefully proofreading this thesis. I will miss our times sitting together and drinking coffee and talking. It was always a very very nice time with you. I hope we stay in contact after successfully finishing our PHDs.
- *Andreas Beer* and *Philipp Parzefall* for scientific and non-scientific discussions, lunch breaks, and the overall very nice atmosphere.
- *Yaroslav Zhumagulov* for the patient explanation of the fundamentals of many-body theory.

- *Kaiqiang Lin* for fruitfull discussions and sharing hBN thicknesses determined from AFM measurements.
- *Matthias Kronseder* and *Florian Dirnberger* for the fruitful discussions.
- *Christoph Butzhammer* and *Veit Iblacker* for carefully proofreading this thesis.
- *Prof. Dr. Christian Schüller* for providing a work space during the time I wrote this thesis. I really enjoyed the atmosphere in your group!
- *Fritz Wünsch* for the always reliable IT support.
- *Prof. Dr. Jörg Wunderlich* and especially *Magdalena Pfleger* for providing and organizing the coffee kitchen.
- *Prof. Dr. Rupert Huber* for providing the laboratory infrastructure.
- *Prof. Dr. Dieter Weiß* for the kind permission to work in the clean room.

Finally, I would like to thank my friends and family for supporting me in my work at all times. Thank you very much for your motivating words and your confidence! Especially I thank my wife *Franziska* and my mother *Karin Eline*. Thanks also to *Jan, Dorothea* and *Andreas*. *Resi*, thank you very much for careful proofreading.